

**A NUCLEAR MAGNETIC RESONANCE SPECTROSCOPIC INVESTIGATION
OF THE MOLECULAR STRUCTURE AND AGGREGATION BEHAVIOR OF
ASPHALTENES**

RUDRAKSHA DUTTA MAJUMDAR
B. Tech., West Bengal University of Technology, India, 2010

A Thesis
Submitted to the School of Graduate Studies
of the University of Lethbridge
in Partial Fulfilment of the
Requirements for the Degree

DOCTOR OF PHILOSOPHY

Department of Chemistry and Biochemistry
University of Lethbridge
LETHBRIDGE, ALBERTA, CANADA

© Rudraksha Dutta Majumdar, 2015

A NUCLEAR MAGNETIC RESONANCE SPECTROSCOPIC INVESTIGATION OF
THE MOLECULAR STRUCTURE AND AGGREGATION BEHAVIOR OF
ASPHALTENES

RUDRAKSHA DUTTA MAJUMDAR

Date of Defence: December 03, 2015

Dr. Paul Hazendonk Supervisor	Associate Professor	Ph.D.
Dr. Michael Gerken Supervisor	Professor	Ph.D.
Dr. Stacey Wetmore Thesis Examination Committee Member	Professor	Ph.D.
Dr. Peter Dibble Thesis Examination Committee Member	Associate Professor	Ph.D.
Dr. Locke Spencer Internal Examiner	Assistant Professor	Ph.D.
Dr. Gillian Goward External Examiner	Professor	Ph.D.
Dr. Hans-Joachim Wieden Chair, Thesis Examination Committee	Associate Professor	Ph.D.

DEDICATION

To my parents, Jaba and Joshomoy Dutta Majumdar for their sacrifices, and to all the enlightened minds that inspired, critiqued and challenged me to think differently on this academic journey.

ABSTRACT

The molecular and aggregate structure of asphaltenes derived from oil-sands bitumen, heavy black-oil and coal, and their aggregation behavior, have been studied comprehensively using solution- and solid-state nuclear magnetic resonance (NMR) spectroscopic techniques. It is shown using solution-state relaxation and 2D correlation methods, and cross-polarization-based solid-state techniques that the “island” model is the predominant architecture for asphaltenes derived from Athabasca oil-sands bitumen.

Asphaltenes derived from different petroleum and coal sources are compared, and it is shown that alkyl sidechains play a significant role in asphaltene aggregation. The average asphaltene molecule is shown to be larger than previously posited, likely possessing pendant aromatic rings. The very first experimental evidence for alkyl groups intercalated between asphaltene aromatic sheets is presented. Finally, ultrafast magic angle spinning solid-state NMR experiments were used to achieve unprecedented resolution in the solid-state ^1H NMR spectrum, allowing for the observation and relaxation measurements of otherwise obscure signals.

ACKNOWLEDGEMENTS

This academic endeavour would not have come to fruition without the assistance and kindness of several individuals. I would like to start by expressing my deepest gratitude to my supervisors Dr. Paul Hazendonk and Dr. Michael Gerken, without whose unwavering support none of the work presented herein would have been possible. I would also like to thank my supervisory committee members, Dr. Peter Dibble, Dr. Stacey Wetmore and Dr. Saurya Das, who have been nothing but supportive and insightful. I extend my gratitude to Dr. Gillian Goward of McMaster University and Dr. Locke Spencer for devoting their time to evaluate the thesis.

Two individuals without whom this work would have been exponentially more difficult are Tony Montana and Michael “Mike” Opyr. They are responsible for all of the hands-on knowledge and experience I have with the spectrometer. I would also like to acknowledge Dr. Oliver Mullins and Dr. Andrew Pomerantz of Schlumberger-Doll Research, USA for the valuable discussions and insight.

I would like to thank my cousin Deep Mazumdar, without whom I would not have started this journey in the first place. We shall soon be neighbors. I would be ungrateful if I did not thank the PubRats, who always made Friday evenings worth looking forward to. Cheers to you people.

Lastly, I would like to thank my parents Jaba and Joshomoy Dutta Majumdar, who have toiled every day of their lives to help me get where I am today. I do not express my gratitude often enough, but I am thankful.

TABLE OF CONTENTS

TITLE PAGE	i
THESIS EXAMINATION COMMITTEE MEMBERS	ii
DEDICATION	iii
ABSTRACT	iv
ACKNOWLEDGEMENTS	v
TABLE OF CONTENTS	vi
LIST OF TABLES	x
LIST OF FIGURES	xi
LIST OF ABBREVIATIONS	xvi
1. ASPHALTENES	1
1.1. Overview	1
1.2. Petroleum and Economics: The Current State of Affairs	4
1.3. Asphaltenes: Definition and Properties	5
1.4. Asphaltene Structure and Chemistry	8
1.4.1. Molecular Weight	8
1.4.2. Elemental composition	9
1.4.3. Molecular structure	9
1.4.4. Asphaltene aggregation	13
1.5. The Use of NMR Spectroscopy for Asphaltene Characterization	17
1.5.1. Solution-state NMR Spectroscopy	18
1.5.2. Solid-state NMR Spectroscopy	24
1.6. Thesis objectives	28
2. NUCLEAR MAGNETIC RESONANCE SPECTROSCOPY	30
2.1. Overview	30
2.2. NMR Spectroscopy Fundamentals	31
2.2.1. Nuclear Spin and Magnetism	31
2.2.2. Signal Generation, Relaxation and the NMR Experiment	35
2.2.3. Chemical Shielding and Chemical Shift	41
2.2.4. Nuclear Spin Interactions: J- and Dipolar Coupling	49
2.2.5. Magic-Angle Spinning	53
2.2.6. Decoupling	56
2.2.7. Product Operators	58
2.2.8. Coherence Transfer	64
2.2.9. Spin Echo	65
2.2.10. INEPT (Insensitive Nuclei Enhanced by Polarization Transfer)	67
2.2.11. Cross Polarization (CP)	69
2.2.12. Relaxation and Molecular Motion	72
2.2.13. Nuclear Overhauser Effect	76
2.3. Selected NMR Spectroscopic Experiments	79
2.3.1. One dimensional ^1H NMR Spectroscopy	79
2.3.2. One dimensional ^{13}C NMR Spectroscopy	80
2.3.3. ^{13}C NMR with inverse gated proton decoupling	82

2.3.4. T ₁ and T ₂ Relaxation Experiments.....	83
2.3.5. Heteronuclear Single Quantum Coherence Experiments.....	86
2.3.6. ¹ H Nuclear Overhauser Effect Spectroscopy (NOESY).....	90
2.3.7. ¹ H-to- ¹³ C Cross-Polarization under Magic Angle Spinning (CP-MAS) Experiments	94
2.3.8. CP Dipolar Dephasing	99
2.3.9. ¹ H Dipolar Filter	101
2.3.10. ¹³ C CP DIVAM and CP-Refocused DIVAM	102
2.3.11. ¹ H Back-to-Back (BABA) Recoupling Double Quantum Correlation under MAS (DQ-MAS)	106
3. VALIDATION OF THE YEN-MULLINS MODEL OF ATHABASCA OIL-SANDS ASPHALTENES USING SOLUTION-STATE ¹H NMR RELAXATION AND 2D HSQC SPECTROSCOPY	109
3.1 Overview	109
3.2. Experimental details.....	110
3.2.1. One-dimensional experiments.....	110
3.2.2. HSQC and relaxation experiments.....	110
3.3. Results and discussions.....	111
3.3.1. Calculation of structural parameters based on deconvolution analysis of NMR spectra	111
3.3.2. T ₂ and T ₁ relaxation measurements	119
3.3.3. HSQC NMR spectroscopy	123
3.3.4. Determination of aromatic core size and final structure	129
3.4. Conclusion	132
4. SOLID-STATE ¹H AND ¹³C NMR SPECTROSCOPY OF ATHABASCA OIL- SANDS ASPHALTENES: EVIDENCE FOR INTERLOCKING π-STACKED NANOAGGREGATES WITH INTERCALATED ALKYL SIDECHAINS	134
4.1. Overview	134
4.2. Experimental details.....	135
4.2.1. Asphaltene extraction.....	135
4.2.2. ¹³ C CP-MAS and DP-MAS	135
4.2.3. ¹³ C CP Dipolar dephasing	136
4.2.4. ¹³ C CP DIVAM.....	136
4.2.5. ¹ H Dipolar filter	136
4.3. Results and discussion	137
4.3.1. Validation of the peak fitting model	137
4.3.2. ¹ H- ¹³ C Cross Polarization (CP) dynamics	143
4.3.3. ¹³ C Direct Polarization and PAH size calculation	148
4.3.4. ¹ H- ¹³ C CP-Dipolar Dephasing	151
4.3.5. ¹ H- ¹³ C CP-DIVAM.....	153
4.3.6. Selecting the high-resolution signals in the ¹ H NMR spectrum using dipolar and T ₂ filters.....	154
4.4. Conclusion	161

5. COMPARISON OF ASPHALTENES DERIVED FROM BITUMEN, PETROLEUM AND COAL, USING 2D-PHASE-SENSITIVE HSQC SPECTROSCOPY	163
5.1. Overview	163
5.2. Experimental Details.....	164
5.2.1. Asphaltene samples.....	164
5.2.2. NMR spectroscopy parameters.....	164
5.3. Results and Discussion	165
5.4. Conclusions.....	179
6. COMPARISON OF PETROLEUM AND COAL DERIVED ASPHALTENE STRUCTURE USING SOLID-STATE NMR SPECTROSCOPY	181
6.1. Overview	181
6.2. Experimental section.....	181
6.2.1. Asphaltene samples.....	181
6.2.2. Solid-state NMR Spectroscopy.....	182
6.3. Results and Discussions.....	183
6.3.1. Spectral deconvolution.....	183
6.3.2. ^1H -to- ^{13}C CP Dynamics	187
6.3.3. ^{13}C Pre-CP Refocused DIVAM	202
6.4. Conclusions.....	208
7. RELATING STRUCTURE TO FUNCTION: CONTRASTING AGGREGATION BEHAVIOR OF PETROLEUM AND COAL DERIVED ASPHALTENES STUDIED USING ^1H T_2 RELAXATION AND 2D-NOESY.....	210
7.1. Overview	210
7.2. Experimental Details.....	211
7.2.1. Sample preparation	211
7.2.2. NMR spectroscopy parameters	211
7.3. Results and Discussions.....	212
7.3.1. Concentration dependence of ^1H T_2 relaxation behaviour.....	212
7.3.2. ^1H - ^1H Nuclear Overhauser Effect Spectroscopy (NOESY)	219
7.4. Conclusions.....	224
8. RECENT RESULTS, GENERAL DISCUSSIONS AND FUTURE DIRECTIONS	227
8.1. Overview	227
8.2. Experimental details.....	228
8.3. Results and Discussions.....	229
8.3.1. ^1H Dipolar Filter at 60 kHz MAS	229
8.3.2. ^1H T_2 Filter at 60 kHz MAS.....	232
8.3.3. ^1H Back-to-Back Recoupling DQ-MAS Homonuclear Correlation.....	235
8.4. Overall Conclusions, General Discussions	237
8.5. Future Directions	243
REFERENCES	248
APPENDIX 1	261
APPENDIX 2.....	263
APPENDIX 3.....	266
APPENDIX 4.....	268

APPENDIX 5270

LIST OF TABLES

Table 1.1. Brief chronological review of solution-state NMR spectroscopic techniques used for asphaltene characterization.

Table 1.2. Brief chronological review of solid-state NMR spectroscopic techniques used for asphaltene characterization.

Table 3.1. Chemical shift assignments for the fitted peaks of the ^{13}C NMR spectrum of AOSA.

Table 3.2. Chemical shift assignments for the fitted peaks of the ^1H NMR spectrum of AOSA.

Table 3.3. Distribution of different carbon species per 100 carbons and their corresponding protons calculated using the areas under the fitted peaks in the ^{13}C and ^1H NMR spectra.

Table 3.4. Average structural parameters for AOSA with distributions per 100 carbons and per PAH obtained using NMR spectroscopy and elemental analysis.

Table 3.5. Transverse (T_2) and longitudinal (T_1) relaxation times for the ^1H NMR peaks. The values in parentheses represent the percentage of protons having the corresponding T_2 .

Table 4.1. Chemical shift assignments and line widths ($\Delta\theta_{\frac{1}{2}}$) for the fitted peaks of solid-state CP-MAS (500 μs contact time) ^{13}C NMR spectra of AOSA, obtained at 8 kHz spinning speed. Also shown are the T_{CP} and $T_{1\rho\text{H}}$ values for each peak (except 150.29 and 174.42 ppm) obtained fitting the variable contact time CP experiment data to Eq. 2.43.

Table 4.2. Structural parameters calculated from the areas under the fitted peaks of the ^{13}C DP-MAS NMR spectrum at 8 kHz MAS and 20 s pre-scan delay.

Table 4.3. Chemical shift assignments, line widths ($\Delta\theta_{\frac{1}{2}}$) and transverse (T_2) relaxation constants for the fitted peaks of solid-state ^1H NMR spectrum at 8 kHz MAS, obtained with 414 μs dipolar filter and variable delay spin-echo filter.

Table 6.1. Elemental Analysis of UG8 petroleum and WY coal-derived asphaltenes.

Table 6.2. Description of the different carbon types numbered in Figure 6.2.

Table 6.3. CP dynamics parameters for the deconvolved ^{13}C CP-MAS peaks of UG8 P-asphaltenes.

Table 6.4. CP dynamics parameters for the deconvolved ^{13}C CP-MAS peaks of Wyoming CD-asphaltenes.

Table 6.5. Structural parameters for UG8 and WY asphaltenes calculated from the %C values obtained from Eq. 6.1.

Table 8.1. Assignments for the deconvolved peaks of the ^1H spectrum, along with their corresponding calculated T_2 values at 60 kHz MAS.

LIST OF FIGURES

- Figure 1.1.** Schematic diagram of a sampling tool which acquires crude oil samples and performs a spectral analysis on these samples for a chemical analysis in situ in the oil well.
- Figure 1.2.** Hypothetical a) Island molecule and b) Archipelago molecule.
- Figure 1.3.** Plot of the mole fraction of bridgehead carbons χ_b vs C, where C is the number of carbon atoms per aromatic cluster.
- Figure 1.4.** The “Yen-Mullins” model describing the hierarchical aggregation behavior of asphaltenes.
- Figure 1.5.** The “supramolecular assembly” model, composed of host and guest species in a representative asphaltene aggregate.
- Figure 2.1.** Distribution of spin magnetic moments in the a) absence and b) presence of an external magnetic field B_0 .
- Figure 2.2.** Precession of the nuclear magnetic moment μ about the static external magnetic field B_0 with frequency ω_0 .
- Figure 2.3.** Net longitudinal magnetization M_z resulting from the ensemble of spins precessing about B_0 .
- Figure 2.4.** Longitudinal magnetization (M_z) rotated to the transverse plane by an r.f. pulse and precession of the transverse magnetization $M_{x,y}$ at the Larmor frequency ω_0 .
- Figure 2.5.** Recovery of the longitudinal magnetization M_z to equilibrium under longitudinal T_1 relaxation, after the creation of transverse magnetization by a $\pi/2$ pulse.
- Figure 2.6.** Decay of the transverse magnetization $M_{x,y}$ under transverse T_2 relaxation during acquisition, after termination of the r.f. field.
- Figure 2.7.** a) The spiral trajectory of the transverse magnetization under T_2 relaxation; b) the overall helical trajectory of the magnetization, combining T_1 and T_2 relaxation; c) the resulting FID.
- Figure 2.8.** Digitization of the FID and subsequent generation of the NMR spectrum
- Figure 2.9.** A basic NMR pulse sequence diagram for a nucleus I, showing the building blocks.
- Figure 2.10.** An induced magnetic field B_{ind} , generated by diamagnetic current induced by the circulating electrons around the nucleus, in the presence of an external magnetic field B_0 .
- Figure 2.11.** The Principal Axes System (δ_{11} , δ_{22} , δ_{33}) of the chemical shift tensor, obtained by rotating the laboratory frame (x , y , z).
- Figure 2.12.** The effect of CSA on NMR spectra: a) Isotropic signal in solution-state NMR as a result of rapid motional averaging. b, c and d) Powder patterns observed at different values of the asymmetry parameter η
- Figure 2.13.** The ring current effect in aromatic rings. Nuclei on the periphery of the ring get deshielded, while those above or below the plane of the ring get shielded.
- Figure 2.14.** Splitting pattern of the ^1H NMR spectrum peaks of an ethyl group caused by the homonuclear J -coupling between the protons.
- Figure 2.15.** Depiction of the through-space dipolar coupling between two spins I and S, in the presence of an external magnetic field B_0 .
- Figure 2.16.** Homogeneous broadening of NMR signals by homonuclear dipolar coupling.
- Figure 2.17.** The unit cube representation of the magic angle (*left*) and sample rotation at the magic angle with a frequency ν_r (*right*).

Figure 2.18. a) Solid-state NMR spectrum obtained under static conditions; b) MAS NMR spectrum when the spinning speed is b) smaller and c) larger than the line broadening interaction.

Figure 2.19. Continuous wave (CW) decoupling.

Figure 2.20. An MAS NMR experiment on nucleus S with TPPM decoupling of nucleus I, where τ_r is the rotor period.

Figure 2.21. Rotation of operator I_z under a θ -pulse on the x -axis.

Figure 2.22. Representation of the rotation of any operator about the x , y or z axis.

Figure 2.23. In- and anti-phase signals.

Figure 2.24. Interconversion of in-phase and anti-phase magnetizations under J -coupling.

Figure 2.25. Coherence transfer from spin-I to spin-S. The $\pi/2$ pulses should be on an axis different than the coherence being transferred.

Figure 2.26. The spin-echo pulse sequence, showing the evolution of magnetization vectors.

Figure 2.27. Possible spin-echo scenarios when the refocusing π -pulse is applied to a) both spins, b) only spin-I and c) only spin-S.

Figure 2.28. The INEPT pulse sequence.

Figure 2.29. The I-to-S cross-polarization (CP) pulse sequence, using ramped-CP.

Figure 2.30. The spin-lock field B_1 causing precession about the x -axis at frequency $\omega_1 = \gamma B_1$.

Figure 2.31. Spectral density functions of the local field fluctuating a) rapidly and b) slowly.

Figure 2.32. Relaxation times plotted against correlation time τ_c . Short τ_c values represent fast molecular motion while longer values indicate slow motion.

Figure 2.33. Energy levels for a two-spin system **IS** showing the spin-states $\alpha\alpha$, $\alpha\beta$, $\beta\alpha$ and $\beta\beta$, and the transition probabilities W_0 , W_1 and W_2 . The spin-states are written with the first Greek letter representing spin-I and the second one representing spin-S.

Figure 2.34. Pulse sequence for ^{13}C NMR with inverse gated ^1H decoupling used for quantitative measurements.

Figure 2.35. Inversion recovery pulse-sequence for measurement of T_1 relaxation time constant.

Figure 2.36. Inversion recovery curve for T_1 measurement.

Figure 2.37. The decay of the signal intensity plotted against the delay period τ in a Hahn-echo T_2 relaxation experiment.

Figure 2.38. The CPMG pulse-sequence for measuring T_2 . The number of times the echo is repeated, n , should be an even integer.

Figure 2.39. The gradient-selected ^1H - ^{13}C HSQC pulse sequence used in Chapter 3.

Figure 2.40. The NOESY pulse sequence. (r.d. = recycle delay).

Figure 2.41. A schematic representation of a 2D-NOESY spectrum.

Figure 2.42. Schematic showing the variation of cross-peak and diagonal peak intensities with mixing time τ_m , for slow ($\omega\tau_c \gg 1$) and fast ($\omega\tau_c \ll 1$) molecular motion.

Figure 2.43. Cross-polarization build-up curves for moieties with strong (solid curve) and weak (dashed curve) effective heteronuclear dipolar coupling.

Figure 2.44. The variation of the ^1H spin-lattice relaxation time in the rotating frame ($T_{1\rho\text{H}}$) with respect to correlation time. The minima is determined by the ^1H spin-lock frequency $\omega_{1\text{H}}$.

Figure 2.45. The CP-dipolar dephasing pulse sequence.

Figure 2.46. The ^1H dipolar filter sequence.

Figure 2.47. The CP-DIVAM pulse sequence.

Figure 2.48. Illustration of the selection mechanism of the DIVAM sequence.

Figure 2.49. DIVAM nutation curves: Normalized signal intensity plotted against the excitation angle.

Figure 2.50. The CP refocused DIVAM sequence.

Figure 2.51. The BABA sequence with recoupling for $2n$ rotor periods (τ_r).

Figure 2.52. Schematic illustration of a Double Quantum MAS (DQMAS) correlation plot.

Figure 3.1. Solution-state a) $^{13}\text{C}\{^1\text{H}\}$ and b) ^1H NMR spectra of heptane-extracted AOSA in CDCl_3 , showing the deconvolved peaks.

Figure 3.2. Hypothetical asphaltene molecule showing the different carbon species identified by ^1H and ^{13}C NMR spectroscopy, as assigned in Tables 3.1 and 3.2.

Figure 3.3. Schematic showing the side view of an asphaltene nanoaggregate formed in solution by disordered aromatic stacking.

Figure 3.4. ^1H - ^{13}C HSQC NMR spectra of heptane extracted AOSA.

Figure 3.5. Figure demonstrating (a) modulation of the intensity of magnetization transfer by ^1H - ^{13}C J -coupling as a function of the INEPT transfer period (τ), (b) modulation of the short and long range correlations after magnetization transfer as a function of the acquisition period in the indirect (^{13}C) dimension.

Figure 3.6. ^1H - ^{13}C HSQC NMR spectra of heptane extracted AOSA. Acquired with ^{13}C SW=400 ppm, TD1=32 and 1700 scans. The 1 ms trim-pulse of the HSQC sequence was switched off for this experiment. The long-range correlations are more intense than the same experiment with the trim-pulse on, as shown in Fig. 3.4b.

Figure 3.7. Average structure of an asphaltene molecule constructed using parameters obtained from ^1H and ^{13}C NMR spectroscopy.

Figure 4.1. Solid-state ^1H - ^{13}C Cross Polarized (CP) MAS NMR spectrum of AOSA obtained at 8 kHz magic angle spinning rate with 500 μs contact time (middle), showing the deconvolved peaks (bottom) and the sum spectrum of the deconvolved peaks (top).

Figure 4.2. ^{13}C Direct Polarization (DP)-MAS spectrum of AOSA at 8 kHz spinning speed and 20.0 s recycle delay showing the fitted peaks which were used for quantitative analysis.

Figure 4.3. (a) ^1H - ^{13}C CP-MAS NMR spectra with variable contact time (10 to 600 μs) of AOSA. Signals appearing at short contact times are from carbons coupled strongly to neighbouring hydrogens. (b) ^1H - ^{13}C CP-MAS dipolar dephasing NMR spectra.

Figure 4.4. ^{13}C CP-MAS magnetization build-up curves of AOSA at 8 kHz spin rate: (a) aliphatic chain carbons, (b) alicyclic carbons and alkyl chain carbons ' α ' to aryl ring and (c) aromatic carbons.

Figure 4.5. Schematic (not to scale) showing the variation of $T_{1\rho\text{H}}$ with correlation time τ_c and at different motional regimes.

Figure 4.6. Hypothetical average structure of an asphaltene molecule based on the parameters obtained from ^{13}C DP-MAS NMR spectrum and EA, showing some of the important carbon types.

Figure 4.7. Decay of ^{13}C CP-MAS NMR signals plotted against the dephasing period in the dipolar dephasing experiments.

Figure 4.8. ^{13}C CP DIVAM nutation curves: the intensity of each peak is plotted against the excitation angle of the minipulses in the DIVAM sequence.

Figure 4.9. ^1H NMR spectra of AOSA: (top) Solid-state spectrum at 8 kHz MAS without any filtering, (middle) solution-state spectrum with deconvolved peaks (Chap. 3) and (bottom) solid-state spectrum at 8 kHz MAS after 414 μs dipolar filter and 125 μs Hahn-echo or T_2 relaxation filter showing the deconvolved peaks.

Figure 4.10. (a) Graphic illustrating the shielding effect of aromatic ring currents, which moves the aliphatic ^1H NMR signals upfield, as shown on Fig. 4.9. (b) Illustration of asphaltene nanoaggregates 1 and 2 interlocking. The broken lines off the aromatic rings are alicyclic groups. (c) A cluster of nanoaggregates where the aliphatic moieties on the inside are less mobile than the ones on the periphery due to interactions with neighbouring aliphatic chains.

Figure 5.1. The ph-HSQC spectrum of AOSA, with the aliphatic region expanded and the aromatic region in the inset.

Figure 5.2. The ph-HSQC spectrum of BG5 P-asphaltene, with the aliphatic region expanded and the aromatic region in the inset.

Figure 5.3. The ph-HSQC spectrum of UG8 P-asphaltene, with the aliphatic region expanded and the aromatic region in the inset.

Figure 5.4. The ph-HSQC spectrum of AD CD-asphaltene, with the aliphatic region expanded and the aromatic region in the inset.

Figure 5.5. The ph-HSQC spectrum of TH CD-asphaltene, with the aliphatic region expanded and the aromatic region in the inset.

Figure 5.6. The ph-HSQC spectrum of WY CD-asphaltene, with the aliphatic region expanded and the aromatic region in the inset.

Figure 5.7. HSQC slices taken at $\delta_{13\text{C}} = 14$ ppm.

Figure 5.8. HSQC slices taken at $\delta_{13\text{C}} = 19.7$ ppm.

Figure 5.9. HSQC slices taken at $\delta_{13\text{C}} = 22.7$ ppm.

Figure 5.10. HSQC slices taken at $\delta_{13\text{C}} = 30$ ppm.

Figure 5.11. HSQC slices taken at $\delta_{13\text{C}} = 32$ ppm.

Figure 5.12. HSQC slices taken at $\delta_{13\text{C}} = 37$ ppm.

Figure 5.13. HSQC slices taken at $\delta_{13\text{C}} = 121$ and 126.5 ppm.

Figure 6.1. ^{13}C CP-MAS NMR spectra of (top) UG8 petroleum asphaltene and (bottom) Wyoming coal asphaltene obtained under 8 kHz MAS, with 0.8 and 1.0 ms contact times respectively, showing the deconvolved peaks.

Figure 6.2. Hypothetical asphaltene molecule showing the different carbon types for which were assigned to the fitted peaks in the CP-MAS spectra.

Figure 6.3a. ^1H -to- ^{13}C cross-polarization build-up curves for the deconvolved aromatic peaks of the ^{13}C CP-MAS NMR spectra of UG8 and WY asphaltene.

Figure 6.3b. ^1H -to- ^{13}C cross-polarization build-up curves for the deconvolved aliphatic peaks of the ^{13}C CP-MAS NMR spectra of UG8 and WY asphaltene.

Figure 6.4. Not-to-scale illustration of the relative sizes of the aliphatic and aromatic ^1H spin-baths, with respect to the aromatic core, in UG8 and WY asphaltene.

Figure 6.5. Average structures of UG8 P-asphaltene and WY CD-asphaltene based on the calculated parameters and elemental analysis.

Figure 6.6a. Pre-CP refocused DIVAM nutation curves for the deconvolved aromatic peaks of the ^{13}C CP-MAS NMR spectra of UG8 and WY asphaltene.

Figure 6.6b. Pre-CP refocused DIVAM nutation curves for the deconvolved aliphatic peaks of the ^{13}C CP-MAS NMR spectra of UG8 and WY asphaltene.

Figure 7.1. The variation of the long and short components of T_2 relaxation time (left y-axis), and their respective percentages (right y-axis), with increasing concentration of UG8 and WY asphaltenes in CDCl_3 .

Figure 7.1. The variation of the long and short components of T_2 relaxation time (left y-axis), and their respective percentages (right y-axis), with increasing concentration of UG8 and WY asphaltenes in CDCl_3 .

Figure 7.2. Schematic describing the formation of nanoaggregates and clusters in UG8 and WY asphaltene solutions on increasing asphaltene concentration. Note the absence of clusters in WY.

Figure 7.3. Solution-state ^1H - ^1H NOESY spectra of UG8 (top) and WY (bottom) asphaltenes at a concentration of 15 g/L, obtained with a mixing time of 500 ms.

Figure 7.4. Schematic describing the inter- and intra-nanoaggregate interaction of alkyl sidechains that lead to clustering in UG8 asphaltenes.

Figure 8.1. Solid-state ^1H NMR spectra of UG8 asphaltenes obtained at MAS speeds of 8 kHz (red) and 60 kHz (blue).

Figure 8.2. The ^1H dipolar filtered NMR spectra at different filtering times obtained at 60 kHz MAS, compared to the unfiltered ^1H spectrum obtained at the same speed.

Figure 8.3. The ^1H NMR spectrum of UG8 asphaltenes at 60 kHz MAS, after 6.68 ms of T_2 filter, showing the deconvolved peaks and their sum.

Figure 8.4. ^1H DQ-MAS NMR spectrum of UG8 asphaltenes obtained at 60 kHz MAS using the BABA recoupling sequence. (ali. = aliphatic, aro. = aromatic).

Figure A1. Example fit for the CP build-up curve of the 128.81 ppm deconvolved solid-state ^{13}C NMR signal of AOSA using Eq. 2.43.

Figure A2. Examples of bi-exponential fits used in Chapter 4.

Figure A3. Non-linear regressive line-fitting of the cross-polarization build-up data of the 129.28 ppm ^{13}C signal (Chapter 6) using the non-monotonic $I-I^*-S$ CP model described by Eq. 2.44.

Figure A4. Non-linear regressive line-fitting of the cross-polarization build-up data of the 129.28 ppm ^{13}C signal (Chapter 6) using the classical $I-S$ CP model described by Eq. 2.43.

Figure A5. Plot showing the variation of ^1H T_1/T_2 ratio with correlation time at a ^1H Larmor frequency of 700 MHz.

LIST OF ABBREVIATIONS

(In alphabetical order)

ADC	Analog-To-Digital Converter
AFM	Atomic Force Microscopy
AOSA	Athabasca Oil-Sands Asphaltene
BABA	Back-to-Back
CCC	Critical Cluster Concentration
CD	Coal Derived
CNAC	Critical Nanoaggregate Concentration
COSY	Correlation Spectroscopy
CP	Cross-Polarization
CPMG	Carr-Purcell-Meiboom-Gill
CSA	Chemical Shift Anisotropy
CW	Continuous Wave
DC	Direct Current
DD	Dipolar Dephasing
DEPT	Distortionless Enhancement by Polarization Transfer
DF	Dipolar Filter
DFA	Downhole Fluid Analysis
DIVAM	Discrimination Induced by Variable Amplitude Minipulses
DOSY	Diffusion-Ordered Spectroscopy
DP	Direct Polarization
DQ	Double Quantum
EA	Elemental Analysis
EROI	Energy Return On Investment
FID	Free Induction Decay
FT	Fourier Transform
FWHH	Full Width at Half Height
GASPE	Gated Spin-Echo
GOR	Gas-to-Oil Ratio
GPC	Gel Permeation Chromatography
HETCOR	Heteronuclear Correlation
HSQC	Heteronuclear Single Quantum Coherence
ICR	Ion Cyclotron Resonance
INEPT	Insensitive Nuclei Enhanced by Polarization Transfer
L ² MS	Two-Step Laser Mass Spectrometry
LDSPI	Laser Desorption Single-Photon Ionization
MAS	Magic Angle Spinning
MRI	Magnetic Resonance Imaging
NMR	Nuclear Magnetic Resonance
NOE	Nuclear Overhauser Effect
NOESY	Nuclear Overhauser Effect Spectroscopy
OPEC	Organization of the Petroleum Exporting Countries
P	Petroleum
PAH	Polyaromatic Hydrocarbon

PAS	Principal Axes System
PI	Polarization Inversion
ppm	parts per million
PVDF	Poly(vinylidene fluoride)
RF or r.f.	Radio-Frequency
SANS	Small Angle Neutron Scattering
SARA	Saturates, Aromatics, Resins and Asphaltenes
SAXS	Small Angle X-ray Scattering
SEC	Size Exclusion Chromatography
SPE.....	Single Pulse Excitation
SQ	Single Quantum
SW.....	Spectral Width
TMS	Tetramethylsilane
TRFD	Time-Resolved Fluorescence Depolarization
VPO.....	Vapor Pressure Osmometry

CHAPTER 1

1. ASPHALTENES

1.1. Overview

Asphaltenes represent the heaviest and the most complex, polar, and structurally enigmatic fraction of petroleum.¹ The enigma stems from the fact that despite several decades of research, asphaltenes continue to plague the petroleum industry, particularly for heavy-oil recovery and processing. There are several different ways in which asphaltenes are problematic for oil production. One of them is the notorious tendency of asphaltene molecules to self-associate, forming large aggregates which precipitate out of the oil on slight change of pressure, temperature or composition, leading to blockage of well-bores, pipelines and sometimes entire reservoirs. This property also leads to coking of catalysts during processing. Asphaltenes, being the most polar fraction of petroleum, are also infamous for stabilizing water-in-oil emulsions during the production of crude oil,¹ which is extremely undesirable from a processing perspective and also for meeting the quality standards of the end product. These challenges drive up production costs and reduce the Energy Return on Energy Invested (EROI),² which eventually leads to increased emissions and detrimental effects on the environment.

These problems have become more pronounced in the modern era of petroleum, as we transition to increasingly difficult-to-extract and heavier hydrocarbon resources, such as bitumen, having exploited our abundance of easy-to-extract or light hydrocarbons to near-depletion. These new resources, often described as “heavy oils”, present new challenges

that the petroleum industry is often not prepared to solve. Traditionally, the petroleum industry has taken a phenomenological approach to solving problems, which is often grossly simplistic. Mullins¹ does an excellent job of describing this approach, why it was used and the associated pitfalls. These techniques have served the industry quite well in the era of easily extractable crude, but their efficacy has been challenged by the issues posed by the new petroleum resources. Heavy-oil and deep-sea explorations are extremely expensive and high-risk endeavours, both financially and environmentally. To justify the enormous costs involved, often in billions of dollars, accurate predictive modelling of reservoirs have become essential. Phenomenological approaches are usually not based on a detailed understanding of the molecular level structure and behavior of petroleum and its fractions, such as asphaltenes. Whereas for precise reservoir modelling using new techniques such as Downhole Fluid Analysis (DFA),^{3,4} as required for heavy-oil exploration, such an understanding is crucial.

As a general rule of thumb: the heavier the oil, the higher the asphaltene content. In other words, as the industry transitions to heavy oils, the problems associated with asphaltenes are expected to magnify proportionally. Reservoir model predictions need to be increasingly accurate to avoid multi-billion dollar mistakes. It calls for a far more detailed understanding of the molecular structure and behavior of asphaltenes than traditionally required. Over the years, numerous different analytical techniques have been employed to address asphaltene structure and aggregation.⁵⁻⁷ One such technique is nuclear magnetic resonance (NMR) spectroscopy, which has been widely used for asphaltene characterization, but not to its full potential. Solution-state NMR spectroscopy has been a standard technique for asphaltene characterization for a considerable length of time, but the

methodologies employed have been mostly rudimentary, leaving room for significant advancements and improvements. Even this much cannot be said for solid-state NMR spectroscopy, where the use of the technique in this field has been limited at best. For both of these techniques, there remains enormous scope to expand their capabilities for asphaltene characterization.

The motivation for this thesis is three-fold: i) to gain detailed insight into asphaltene structure, ii) to correlate structure with aggregation behavior and iii) to achieve these goals using advanced solution- and solid-state NMR spectroscopic methods. In this chapter, we shall first take an in depth look at asphaltenes: the ways in which they pose problems for the petroleum industry, how these problems are dealt with currently, what is known about the molecular structure and how the structure can be related to their behavior. It will be followed by a discussion on the role NMR spectroscopy has played in asphaltene characterization till date with a review of the literature.

In the subsequent chapters, I shall introduce fundamental NMR spectroscopic principles as they apply to this body of work, and eventually the results obtained in our laboratories. We shall also investigate structural and behavioral differences between petroleum asphaltenes and asphaltenes derived from coal liquids, which are economically less important, but shed light on the factors that drive asphaltene aggregation.

1.2. Petroleum and Economics: The Current State of Affairs

At the current time, the world has undergone a major shift in energy economics, when crude oil prices plummeted by over 50%, from a peak of \$115/barrel for Brent* crude in June 2014 to as low as \$50/barrel in January 2015. The current prices (as of December 2015) still remain low, fluctuating between \$40 and \$50, partly owing to the rapid growth of US shale oil and gas production and the OPEC's (Organization of the Petroleum Exporting Countries) decision, led by Saudi Arabia, to focus on market share rather than cap productions.

The low prices, fueled by surplus production, have had a negative economic impact on petroleum sectors which rely on high crude prices to sustain activities, such as heavy-oil and bitumen or even deep-sea operations. Extraction and processing of heavy-oils and bitumen is more energy intensive than traditional low-density light oils, and consequently come with significant financial risk. Low prices have forced operators to halt numerous operations and exploratory activities, cease new investments and terminate jobs. Countries such as Canada, specifically the province of Alberta, where as much as 98% of the crude reserves occur as oil-sands bitumen (Source: Canada's Energy Future, National Energy Board), have been affected the most. The high cost of bitumen extraction, normally offset by high prices of oil, makes it economically unsustainable, unless new, disruptive technological breakthroughs dramatically decrease the production cost or crude prices return to previous levels.

*Brent crude is a trading classification of sweet (low sulfur) and light (low density) crude oil used as a major benchmark to price two thirds of internationally traded crude oil supplies. It comprises a number of blends extracted from the North Sea.

On the other hand, the fact that the world's conventional crude oils are nearing depletion, makes it imperative for the petroleum industry to invest in the development of unconventional resources such as heavy-oils and bitumen and consequently find innovative solutions to the problems that come with it. One of the foremost challenges that plague the industry today is to find an efficient way to deal with asphaltenes. The first step in this endeavour would be to understand what asphaltenes are, chemically and physically.

1.3. Asphaltenes: Definition and Properties

Owing to the exceedingly complex nature of crude oils (mixture of 105-106 distinct chemical species),⁸ its components are often classified into four distinct groups based on their solubility. These 'solubility classes' are collectively called the SARA fractions: Saturates, Aromatics, Resins and Asphaltenes.⁹ The saturate fraction consists of nonpolar saturated hydrocarbons (linear, branched and cyclic), soluble in paraffinic solvents such as n-pentane, n-hexane or n-heptane. More polarizable aromatic molecules, consisting of one or more aromatic rings, constitute the aromatic fraction, also soluble in paraffins such as n-pentane, n-hexane or n-heptane and slightly polar solvents such as toluene and dichloromethane. Resins and asphaltenes both consist of molecules with polar substituents, but while asphaltenes are insoluble in an excess of heptane, resins are miscible in the same.

The operational definition of asphaltenes states it as the component of crude oil that precipitates out on addition of n-heptane or n-pentane in a 1:40 (crude:precipitant) volume ratio.¹⁰ They are the heaviest and most polar fraction of the SARA components and are soluble in solvents such as toluene and chloroform. Thus by definition, asphaltenes are a collection of numerous molecules with varying chemical structures rather than one single

component, all of which have one common factor, i.e. their solubility (or lack thereof). This fundamentally complex and uncertain nature of asphaltenes gives rise to the long-running debates about their true nature: What are their molecular weights? What are their structures? What drives their aggregation behavior? These and several other such questions still remain after several decades of asphaltene research and are often debated passionately among those studying it.

The principal problem with asphaltenes is that with changes in operating conditions such as temperature, pressure or composition during the different stages of crude-oil production, transportation and processing, they may get destabilized from solution and form deposits. The deposition of asphaltenes leads to blockage of well-bores, pipelines and fouling of refining and storage facilities.^{1,11} Asphaltenes can also assist in the hardening and deposition of other organic solids such as waxes and hydrates.¹ The polar character of asphaltenes helps stabilize water-in-oil emulsions¹ which require removal to meet product quality specifications. Thus, asphaltene related challenges have an enormous economic bearing on the petroleum industry at all stages of operation. They have been reported to cause complete blockage of wells very shortly after the start of production,¹² the remediation of which require cessation of all well activities.

Currently, a number of remedial techniques are employed by the industry for cleaning up organic deposits, including asphaltenes. These include treatment with solvents such as dimethyl disulfide ($\text{CH}_3\text{-S-S-CH}_3$),¹³ dispersants such as alkylphenols and alkylbenzenesulfonic acids¹⁴⁻¹⁷ and also mechanical removal methods such as ultrasonic treatment.^{12,18} However, prediction and prevention of asphaltene deposits are far more favourable options than remediation after deposits have already formed, especially since

the efficacy of the remedial treatments depend on the type of crude (e.g. light crude vs heavy crude) and are not always completely effective. Predictive tools such as DFA^{3,4} can model oil-reservoir connectivity and compartmentalization by interpreting the compositional gradient of reservoir fluids. DFA involves in-situ measurement of reservoir fluid properties such as density and viscosity, and collecting the fluids for laboratory assessment, using a sampling tool which is lowered into a freshly drilled hole in the reservoir.³ A schematic diagram of such a tool is presented in Fig. 1.1.

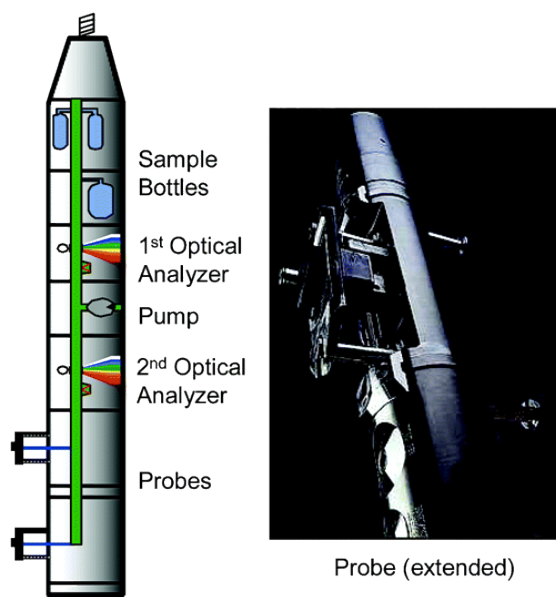


Figure 1.1. Schematic diagram of a sampling tool which acquires crude oil samples and performs a spectral analysis on these samples for a chemical analysis in situ in the oil well. This tool is used in the so-called “open hole” just after the well is drilled and prior to the placement of the casing in the well. A photograph of the “probe” or stout tube is shown, which is pressed firmly against the borehole wall to make hydraulic communication with permeable zones in the oil well to extract formation fluids. (Reproduced with permission from Mullins, O. C.; Rodgers, R. P.; Weinheber, P.; Klein, G. C.; Venkataramanan, L.; Andrews, A. B.; Marshall, A. G. *Energy & Fuels* **2006**, *20*, 2448. Copyright 2006 American Chemical Society)

It has been shown extensively in the laboratory and in oil-field studies that this modelling and prediction can be performed with greater accuracy using DFA-measured asphaltene

gradients. This is particularly true for low GOR (gas-to-oil ratio), heavy oils since only heavy-end gradients can be used for modelling, the GOR being homogeneous. But these measurements require a fundamental understanding of the factors that determine asphaltene aggregation and phase behavior, which in turn requires intricate knowledge of asphaltene structure.

1.4. Asphaltene Structure and Chemistry

1.4.1. Molecular Weight

The molecular weight of petroleum asphaltenes has been a topic of contention for several decades until very recently.^{6,19} The accurate determination of asphaltene molecular weight has always been complicated by firstly their polydispersity and second, most importantly, their tendency to form aggregates even in solvents where they are highly soluble.²⁰ Values reported in the literature often show discrepancies on the order of 10.^{21,22} Techniques such as vapor pressure osmometry (VPO) and size exclusion chromatography (SEC) report very high molecular weights on the order of 4000-10,000 u,²³⁻²⁵ whereas laser desorption and field ionization mass spectrometry have reported values around 400-800 u.^{26,27} The very high values can be attributed to the formation of nanoaggregates and clusters, while the smaller values are attributed to fragmentation. More recently, these issues have been largely settled by time-resolved fluorescence depolarization (TRFD),¹ two-step laser mass spectrometry (L²MS)^{28,29} and state-of-the-art Fourier transform ion cyclotron resonance (FT-ICR) techniques,¹ all of which put the molecular weight of asphaltenes between 500-1500 u¹⁹ which is largely accepted by the research community.

The molecular weight of asphaltenes derived from coal distillates, on the other hand, has been shown to be much less ambiguous, averaging around ~350 u.³⁰

1.4.2. Elemental composition

The elemental composition of asphaltenes is well-established but it depends on the source of the crude. They are hydrocarbons typically with a H/C ratio of 1.15 ± 0.5 , containing heteroatoms such as sulfur (0.3-10.3%), oxygen (0.3-4.9%) and nitrogen (0.6-3.3%) which occur as various polar functional groups such as sulfoxides, carboxylic acids and amides.^{31,32} Trace quantities of metals (ppm level) such as nickel, vanadium and iron are also found, which often occur as porphyrins.³³

Coal-derived asphaltenes have a much smaller H/C ratio (0.74-0.85) and a reduced sulfur content (0.09-0.13%), the remaining composition being approximately similar.³⁰ This will be an important fact to remember when comparing the two kinds of asphaltenes in later chapters.

1.4.3. Molecular structure

If anything has been the subject of more heated debate than the molecular weight of asphaltenes, it is their structure. Over the decades, several different average structures of asphaltenes have been proposed,^{21,34-43} all of which have one common theme, that asphaltenes are composed of fused polyaromatic hydrocarbon (PAH) cores, with pendant alkyl sidechains. The debate has been largely centred on how large these PAH cores are, how long the sidechains are and if the PAH cores are attached to each other via alkyl groups. More recently, extensive research has pared down the possible structure of asphaltenes to two fundamentally different models. One of them is the “island” or Yen-Mullins

model,^{7,21,39,42} which posits the asphaltene molecules as containing a single PAH with pendant aliphatic chains (Fig. 1.2a), and the other is the “archipelago” model,^{40,41,43} which proposes that several smaller PAH’s are bridged together by aliphatic linkages (Fig.1.2b).

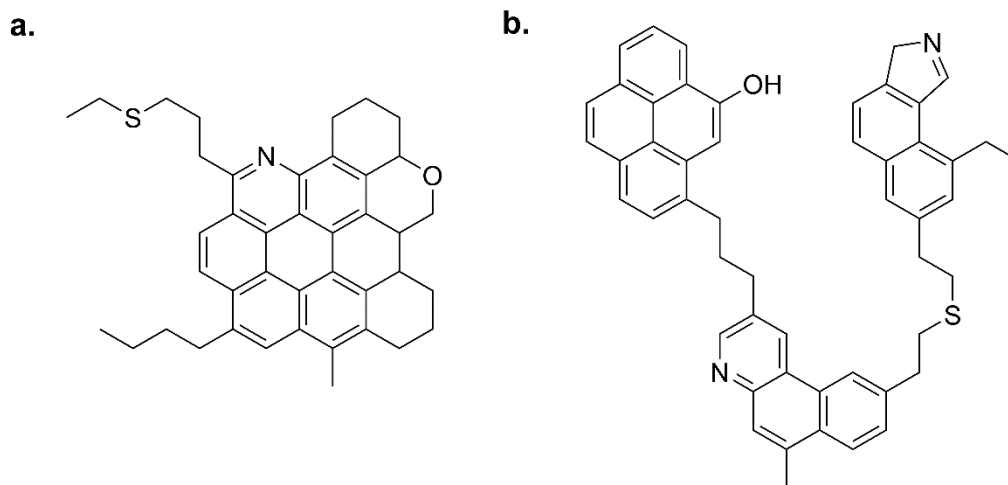


Figure 1.2. Hypothetical a) Island molecule and b) Archipelago molecule.

One of the central problems in asphaltene research is the determination of the predominant architecture between these two motifs. Most of the evidence in support of the archipelago model is based on destructive techniques such as thermal degradation, pyrolysis and oxidation,⁴³ which result in decomposition of the asphaltene molecules into small PAHs that are considered to be consistent with the model.⁴⁴ However, it has also been reported that model compounds mimicking the island model can also decompose into smaller aromatic molecules using the same techniques.⁴⁴ On the other hand, archipelago structures have been reported to form during thermal cracking of smaller model compounds,⁴⁵ which makes a strong case for the archipelago model.

The evidence for the island model comes from several different independent analytical techniques such as scanning tunneling microscopy,⁴⁶ high-resolution transmission electron microscopy,⁴⁷ electronic triplet-state spectroscopy⁴⁸ and time-resolved fluorescence depolarization.^{20,49–51} Mass spectrometric^{39,49,52} and diffusion studies^{21,22,50,53,54} also support this model. Mass spectrometry is known to suffer from aggregation and fragmentation effects, which leads to overestimation of molecular weights, suggesting archipelago architecture. However, recent mass spectrometric studies have shown that these effects can be minimized by using suitable ionization methods such as laser desorption single-photon ionization (LDSPI)⁵⁵ and laser desorption laser ionization (two-step laser or L²MS).^{28,56} These techniques use low-power lasers to desorb the substrate (asphaltenes), which prevents ionization within the desorption plume, thus precluding the formation of aggregates due to ion-induced interactions. In the next step soft-ionization methods are used which prevents fragmentation of the ions. The island model has also found support from solution state nuclear magnetic resonance (NMR) spectroscopic studies.³⁰ A very recent atomic force microscopy (AFM) study,⁵⁷ which can image single molecules, unambiguously shows island type molecules as the predominant architecture, although a few archipelago-type molecules were observed.

An important structural parameter, referred to as the aromatic condensation index (χ_b) is often used in literature to determine the number of aromatic rings in a single PAH core and how these rings are condensed. It was introduced by Solum *et al.*⁵⁸ in 1989 to help interpret nuclear magnetic resonance data in terms of structural features. Six-membered aromatic rings can condense to form PAHs in two distinct limiting geometries, linear (ortho-fused) and circular, and all possible combinations of them. Examples of linearly

condensed PAHs include anthracene, phenanthrene, tetracene and chrysene, while circularly condensed PAHs include pyrene, coronene and higher homologues. The carbons that are located at the junction of two or more aromatic rings are referred to as bridgehead carbons. The aromatic condensation index is defined as the mole fraction of the bridgehead carbons in a PAH, expressed in terms of the number of aromatic carbon atoms (C) in the PAH and the relationship depends on the type of condensation, given by equations 1.1 and 1.2.

$$\chi'_b = \frac{1}{2} - \frac{3}{C} \quad \text{Equation 1.1}$$

$$\chi''_b = 1 - \frac{\sqrt{6}}{\sqrt{C}} \quad \text{Equation 1.2}$$

where χ'_b and χ''_b corresponds to linear and circularly condensed PAHs, respectively. These parameters can be plotted against the number of aromatic carbon atoms (C) in the PAH for different model PAHs to obtain curves (Fig. 1.3) that make it possible to estimate the PAH motifs based on the χ'_b or χ''_b , that are calculated by dividing the fraction of bridgehead carbons by C, which are obtained from ^{13}C NMR spectroscopy. However, it is unlikely that a typical asphaltene molecule will conform to only one or the other of these motifs, but typical asphaltenes will be a combination of the two. Solum⁵⁸ used a hyperbolic tangent function to combine χ'_b and χ''_b , providing an empirical function for a generalized χ_b :

$$\chi_b = \frac{1 - \tanh\left(\frac{C-19.57}{4.15}\right)}{2} \chi'_b + \frac{1 + \tanh\left(\frac{C-19.57}{4.15}\right)}{2} \chi''_b \quad \text{Equation 1.3}$$

It can be seen in Fig. 1.3 that as χ_b becomes larger, the PAHs tend to be more circularly condensed. Using ^{13}C NMR spectroscopy, χ_b can be calculated and plotted on Fig. 1.3 to find the probable PAH size and motif.

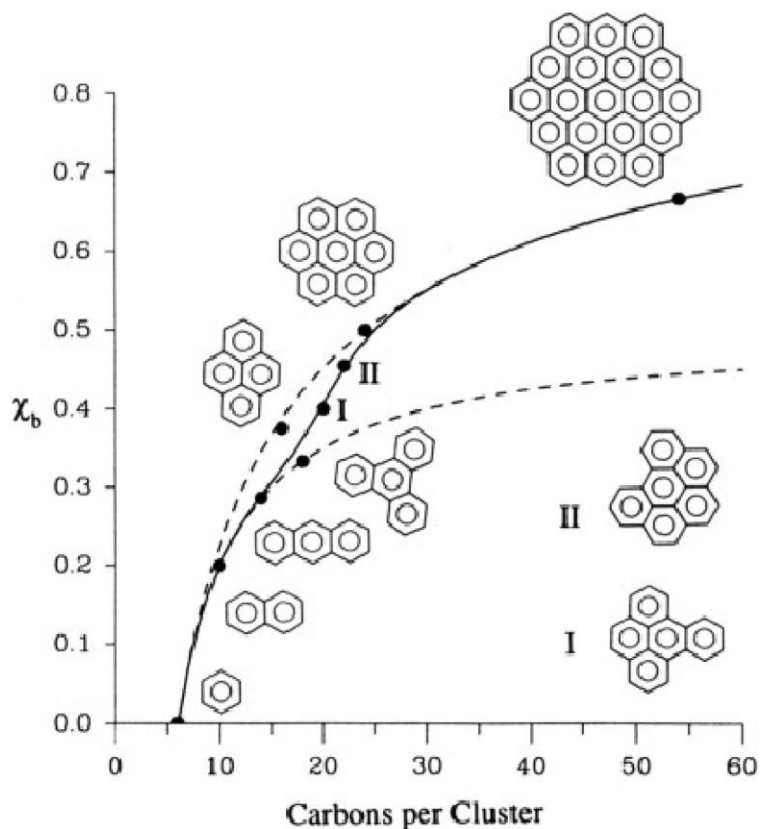


Figure 1.3. Plot of the mole fraction of bridgehead carbons χ_b vs C , where C is the number of carbon atoms per aromatic cluster. The solid curve is for the combined model, the upper dashed curve is for the circular condensation model, and the lower dashed curve is for the linear condensation model. (Reproduced with permission from Solum, M. S.; Pugmire, R. J.; Grant, D. M. *Energy Fuels* **1989**, 3, 187. Copyright 1989 American Chemical Society)

1.4.4. Asphaltene aggregation

Asphaltenes are viewed as nanoscale colloidal particles that remain suspended as particles or fully dissolved in the crude oil.⁵⁹⁻⁶² Since the very definition of asphaltenes is based on solubility, it is quite possible that asphaltenes can co-exist as both in a dissolved state and an aggregated solid state in the crude oil, which can depend on the type of oil and

conditions in the reservoir. The aggregation or self-association of asphaltenes are strongly solvent and concentration dependent^{24,31,63} and can also depend on the crude.⁶⁴ It can be viewed as a dynamic equilibrium between the dissolved individual molecules and the suspended aggregates, where increasing the asphaltene concentration increases the tendency to aggregate. A two stage aggregation model, based on the island model, has been proposed to describe the behavior and has been found to be very useful in DFA measurements.³ This is known as the “Yen-Mullins model”,⁴² often used interchangeably with “island model” and is illustrated in Fig. 1.4. According to this model, individual asphaltene molecules agglomerate through a balance of attractive and repulsive interactions. First, with increasing asphaltene concentration, the individual molecules aggregate via attractive π - π interactions of the aromatic cores, stacking upon each other to form what are referred to as nanoaggregates. After several molecules have aggregated in such fashion, the nanoaggregate projects primarily the alkyl sidechains to the outside.

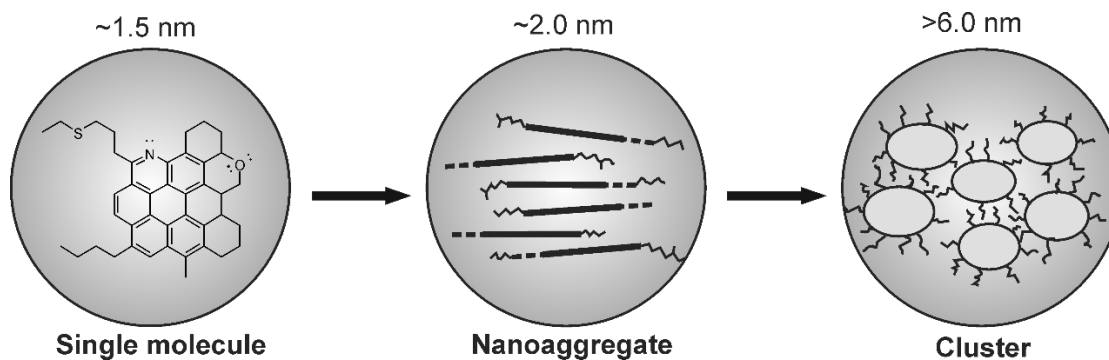


Figure 1.4. The “Yen-Mullins” model describing the hierarchical aggregation behavior of asphaltenes. The bold straight lines in the nanoaggregate represent the aromatic core, the dashed lines represent alicyclic groups and each oval in the cluster represents a nanoaggregate. The crooked lines represent alkyl chains.

The steric repulsion from the alkyl sidechains prevents further π - π interactions, thus halting further growth of the nanoaggregate (around ~ 2 nm in dimension) and remaining individual molecules form additional nanoaggregates. The lowest concentration at which the nanoaggregate growth stops is often referred to as the “critical nanoaggregate concentration” (CNAC)⁴² and below it asphaltene molecules are posited to form smaller multi-mers (dimers, trimers etc.). Centrifugation and DC conductivity studies of toluene-asphaltene solutions put the CNAC between 0.05-0.15 g/L, and the number of asphaltene molecules in a nanoaggregate are said to be < 10 based on small angle X-ray and neutron scattering (SAXS, SANS) experiments.^{7,61,65} The CNAC represents a range of concentrations rather than single point, and is not temperature dependent,⁷ which indicates that nanoaggregate formation is primarily entropy driven. The formation of nanoaggregates increases solvent entropy which becomes the driving force of aggregation.

Beyond the CNAC, a second aggregation step occurs where the nanoaggregates further group together to form ‘clusters’. Cluster formation has been shown to begin at a concentration of ~ 2.0 -5 g/L, called the ‘critical cluster concentration’ (CCC), but can be induced at lower concentrations upon addition of n-heptane.⁷ The full range of sizes of such clusters is uncertain, but they are bound by that of the nanoaggregates (~ 2 nm) and the smallest flocs (~ 300 nm) (flocs are the phase separated asphaltene clusters formed on sufficient destabilization of the solution). They are believed to be fractal in nature, with the smallest clusters around ~ 6 nm. They are less tightly packed than the nanoaggregates and can remain as a stable but delicate suspension in crude oil over geologic timescales.⁴²

The Yen-Mullins representation views the π - π stacking interactions as the primary driver of asphaltene aggregation. But this hypothesis has been challenged by yet another

model of asphaltene aggregation, which suggests that π - π stacking interactions are only one of the many contributing factors. This is the “supramolecular assembly” model (Fig. 1.5) proposed by Gray and co-workers,⁶⁶ which suggests that asphaltene aggregates are porous, formed by a combination of hydrogen bonding and acid-base interactions, metal coordination complexes, hydrophobic pockets formed by alkyl-cycloalkyl interactions and host-guest complexes. It suggests that a lot of the asphaltene properties can be fully explained only if this model is considered, such as aggregation, adhesion to surfaces, occlusion of soluble components, porosity and elasticity. However, subsequent evidence,³⁰ including recent AFM imaging study,⁵⁷ has shown that asphaltene PAHs are much larger, and less ‘archipelago’ type, than what this model proposes (Fig. 1.5).

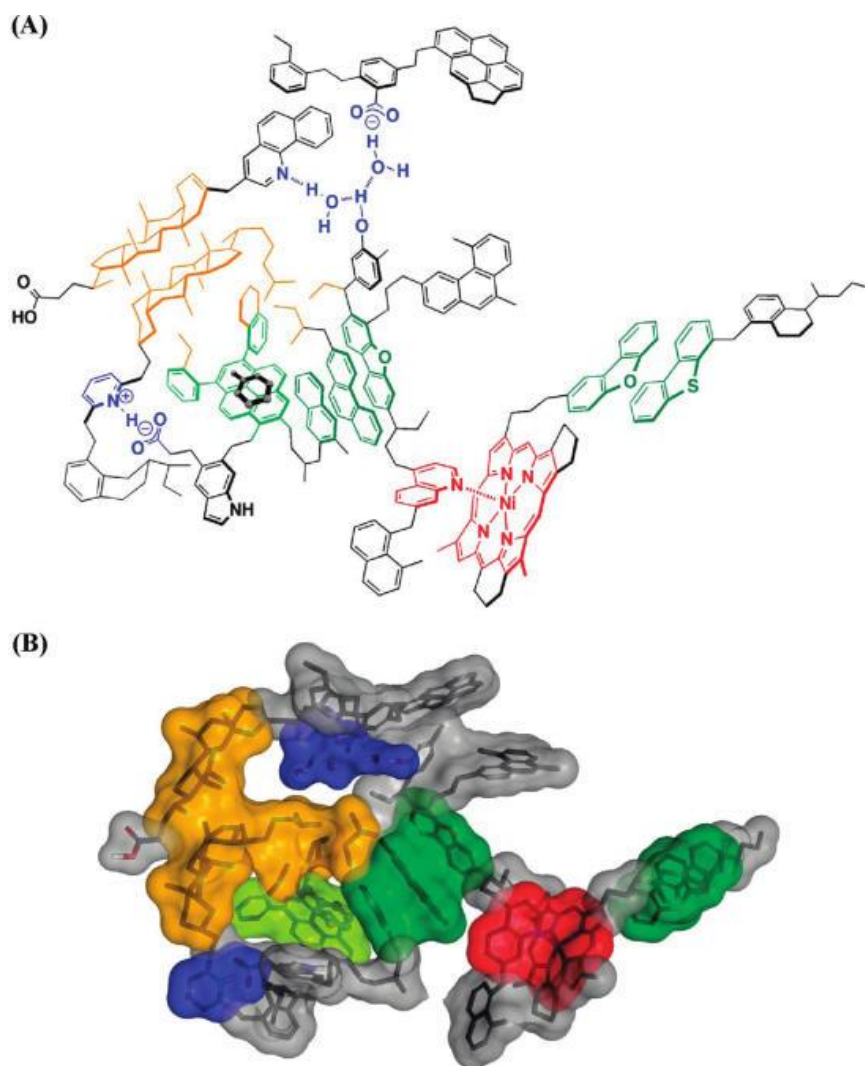


Figure 1.5. The “supramolecular assembly” model, composed of host and guest species in a representative asphaltene aggregate. Associations between molecules are color-coded in (A) the molecular depiction and (B) the space-filling version: acid-base interactions and hydrogen bonding (blue), metal coordination complex (red), a hydrophobic pocket (orange), π - π stacking (face-to-face dark green; within a clathrate containing toluene, light green). (Reproduced with permission from Gray, M. R.; Tykwinski, R. R.; Stryker, J. M.; Tan, X. *Energy Fuels* **2011**, 25, 3125. Copyright 2011 American Chemical Society)

1.5. The Use of NMR Spectroscopy for Asphaltene Characterization

In the discussion thus far, it has been established that there is a need for detailed knowledge of asphaltene structure. Besides fulfilling a fundamental curiosity, a comprehensive structural model for asphaltene will enable determination of the factors that drive asphaltene aggregation and provide the input parameters for predictive modelling of

reservoir fluids.^{3,4} Nuclear magnetic resonance (NMR) spectroscopy is a versatile, non-destructive and powerful analytical tool that has been crucial in the characterization of asphaltenes in the last few decades. There are several advantages that NMR spectroscopy offers over many other analytical techniques. Firstly, being non-destructive and non-invasive, it allows the study of intact asphaltenes, unlike mass spectrometric and thermal degradation techniques which can lead to fragmentation of the whole asphaltenes. NMR spectroscopy also offers an extremely wide array of different experiments with different objectives. Besides the standard one-dimensional experiments that allow the identification of different chemical groups, it is also possible to perform two-dimensional experiments which show connectivities between atoms and provide information about their spatial proximity. NMR-based relaxation measurements can provide information on molecular dynamics of a system, while diffusion-based experiments can probe the dimensions of a molecular species. NMR spectroscopy also allows quantification of the different chemical species. Another major advantage of NMR spectroscopy is the ability to investigate materials in all states, i.e. the solid state, liquid state, solution state and also in the gas phase if possible. This allows probing of various aspects of a particular material, even if it is not soluble in any solvent. Since asphaltenes are solids that remain dispersed or dissolved in the liquid phase, they are of interest as solids and in solution, which makes NMR spectroscopy an ideal tool to study these materials.

1.5.1. Solution-state NMR Spectroscopy

The solution-state ^1H NMR spectrum of a coal liquid asphaltene was first reported as early as 1959 by Friedel *et al.*⁶⁷ It was performed at 125 °C with CS_2 as solvent. Three distinct ^1H resonances could be readily identified and the presence of poly-aromatic

hydrocarbons (PAH) was postulated, demonstrating the usability of NMR spectroscopy for the purpose of asphaltene characterization. Proton NMR was also used by Gardner⁶⁸ in the same year to study a US mid-continent asphalt, using methods derived by Williams.⁶⁹ Soon after, Brown and Ladner demonstrated that important structural parameters for carbonaceous fuels, such as aromaticity (fraction of aromatic carbons, f_a), can be obtained using the hydrogen distribution determined from ¹H NMR spectroscopy.⁷⁰ They came up with what is often referred to as the Brown-Ladner equation^{70,71} (Eq. 1.4) for calculating aromaticity. On the basis of this equation, many other structural parameters such as the degree of aromatic ring substitution and the average size of the polyaromatic hydrocarbon (PAH) ring system can be calculated. It is written as:

$$f_a = \frac{\left[(C/H) - (H_\alpha/x) - \frac{(H_\gamma + H_\beta)}{y} \right]}{C/H} \quad \text{Equation 1.4}$$

where C/H is the carbon to hydrogen atomic ratio from elemental analysis; x is the average number of hydrogen atoms per alkyl group ‘ α ’ to an aromatic ring; y is the average number of hydrogen atoms per group in the remaining alkyl groups; and H_α , H_γ and H_β represent the normalized integrated intensities of the α , β and γ -alkyl hydrogen atoms, respectively. Yen and Erdman⁷² used a modified Brown-Ladner method to study a group of asphaltenes, and more studies were done by Friedel and Retcofsky.⁷³ Girdler⁷⁴ used NMR to compare asphaltenes from a number of different straight-run, precipitated and blown bitumen samples to study the chemical nature of bitumen. The Brown-Ladner method was again employed by Ramsey *et al.*⁷⁵ to study asphalts and one of the early highly resolved ¹H NMR spectra of asphaltenes was reported, which they used to calculate a number of structural parameters such as aromaticity, C/H ratio and average molecular weight. They compared

the aromaticities obtained using NMR spectroscopy to those obtained using other techniques to test the validity of the technique for asphaltene characterization. Yen⁷⁶ used ¹H NMR spectroscopy to show that mild thermal cracking can cleave alkyl chains and form aromatic structures from naphthenic ones. Semple⁷⁷ fractionated Cold lake heavy oil asphaltenes from Alberta by SEC and studied them using ¹H NMR spectroscopy. These early studies based on one-dimensional ¹H NMR spectroscopy laid the foundation for using more advanced NMR methodologies for asphaltene characterization and established the basic features of asphaltene structure, i.e., an aromatic core and alkyl sidechains. However, the Brown-Ladner equation (Eq. 1.4) which was used widely in this era required several assumptions and the results were often dependent on the assumed values for x and y . It was assumed that the average aliphatic carbon structure represented a $-\text{CH}_2$ group, making the assumed x and y values equal to 2. There were also issues with accurate integration of the H_α and $(H_\gamma + H_\beta)$ protons because of extensive overlap of the chemical shifts. Moreover, carbons without any attached protons are not represented in the ¹H spectrum, which can skew aromaticity calculations. These problems were only solved after the advent of high-resolution ¹³C NMR spectroscopy.

Some of the early work on the ¹H and ¹³C solution-state NMR spectroscopy of petroleum fractions was done by Knight⁷⁸ and Clutter.⁷⁹ One of the first detailed ¹³C NMR analyses of asphaltenes was performed by Ignasiak⁸⁰ and Dereppe.⁸¹ Dereppe⁸¹ set forth a large set of equations which could be used to calculate structural parameters using integrated spectral areas, such as the number of aromatic rings, number of substitutions on the aromatic rings, number of heteroatom substituents and the average length of the alkyl chains. A similar approach was used by Dickinson⁸² to study petroleum fractions including

asphaltenes. Sklenar *et al.*⁸³ tested three different decoupling methods to determine aromaticity by ¹³C NMR spectroscopy: broadband decoupling, gated decoupling and gated decoupling with relaxation reagent. They determined that the use of gated decoupling (see Chapter 2) and addition of a paramagnetic relaxation reagent enables the most quantitative measurements, a technique that is used to this day. Cookson⁸⁴ introduced spin-echo techniques to quantify C, CH, CH₂ and CH₃ groups in petroleum and coal liquids and similar techniques were employed by Cyr³⁴ to study Athabasca bitumen asphaltene and its gel permeation chromatography (GPC) fractions. One dimensional ¹³C NMR spectroscopic spectral editing techniques, such as gated spin-echo (GASPE) and DEPT,⁸⁵ were further utilized by a number of groups to study asphaltene structure.^{30,86-89} A brief review of solution-state NMR techniques used for asphaltene characterization is provided in Table 1.1.

It is evident from Table 1.1 that the majority of the efforts in solution-state NMR spectroscopy for asphaltene characterization have been focused on one-dimensional techniques such as ¹H, ¹³C and DEPT,⁸⁵ at least in the early days and up until the mid-90's. Owing to the large variations in carbon and proton environments within the asphaltene system, the signals are frequently misassigned, especially if solely one-dimensional methods were used. Two-dimensional (2D) NMR correlation techniques are well-known to enable more reliable assignments, but a survey of the literature revealed that 2D NMR spectroscopy has been used sparingly in asphaltene characterization. A few studies used ¹H diffusion-ordered spectroscopy (DOSY) experiments for analysis of aggregation behavior in asphaltenes and to determine the size of fused aromatic core and study aggregation behavior.^{54,64,90-93} Sarpal⁹⁴ used 2D-correlation spectroscopy (COSY) and heteronuclear

correlation (HETCOR) to characterize hydrocracked base stocks of petroleum, which are much lower in molecular weight, composed mostly of the paraffinic fractions and which are fundamentally distinct from asphaltenes as they are products of the cracking process. Moreover, recently it was demonstrated that thermal cracking produce archipelago-type structures.⁴⁵ Sarpal's findings⁹⁴ were subsequently used by Sheremata⁴³ to assign the ^1H and ^{13}C resonances of asphaltene NMR spectra. Similar 2D approaches were taken by Abu-Dagga⁹⁵ and Dosseh⁹⁶ to identify and characterize aromatic structures of crude oil components with low and intermediate boiling points, respectively.

Proton NMR solvent relaxation studies are frequently used to probe aggregation behavior of asphaltenes with increasing asphaltene concentration.⁹⁷⁻⁹⁹ A few studies rely on direct relaxation measurement on the asphaltene molecules themselves. Pekerar *et al.*¹⁰⁰ presented ^{13}C T_1 measurements in solution to investigate the mobilities of asphaltene molecules; however, T_1 values alone cannot provide a complete description of the mobility unless they are accompanied by T_2 measurements, as both are required to determine the regime of the motional time-scale. Östlund *et al.*⁶³ studied asphaltene flocculation with ^1H T_1 and T_2 measurements on the asphaltene molecules directly. This study used the 0.7 – 2.1 ppm range to represent the aliphatic region in the ^1H NMR spectrum, which inherently overlooks the role of the overlapping signals that can have markedly different relaxation behavior. Predictably, their analysis revealed two different T_2 relaxation times of 0.6 and 7.0 ms attributed to protons that are either close or far from the aromatic core, providing little insight into the molecular architecture. Lisitza⁵⁴ used the spin-echo technique (used to measure T_2) to study aggregation behavior of asphaltenes, but did not report T_2 values.

Table 1.1. Brief chronological review of solution-state NMR spectroscopic techniques used for asphaltene characterization.

Paper	^1H NMR	^{13}C NMR	GASPE/DEPT	Relaxation	NMR Diffusion	HSQC
Friedel '59 ⁶⁷						
Gardner '59 ⁶⁸						
Yen '62 ⁷²						
Girdler '65 ⁷⁴						
Ramsey '67 ⁷⁵						
Ignasiak '77 ⁸⁰						
Dereppe '78 ⁸¹						
Sklenar '80 ⁸³						
Cookson '83 ⁸⁴						
Yen '84 ⁷⁶						
Cyr '87 ³⁴						
Semple '90 ⁷⁷						
Storm '94 ³⁵						
Calemma '95 ⁸⁶						
Masuda '96 ¹⁰¹						
Christopher '96 ⁸⁷						
Pekerar '98 ¹⁰⁰				$^{13}\text{C } T_1$		
Desando '99 ¹⁰²		<i>also ^{19}F</i>				
Norinaga 2001 ¹⁰³						
Ostlund '02 ⁶³				$^1\text{H } T_2$		
Desando '02 ⁸⁸		<i>also ^{19}F, ^{29}Si</i>				
Ancheyta '02 ¹⁰⁴						
Evdokimov '03 ⁹⁸				$^1\text{H } T_2$		
Jestin '04 ⁹⁷				$^1\text{H } T_2$		
Evdokimov '06 ⁹⁹				$^1\text{H } T_2$		
Durand '08 ⁹⁰						
Durand '09 ⁹¹						
Lisitzia '09 ⁵⁴				$^1\text{H } T_2$		
Zielinski '10 ¹⁰⁵				<i>Low field ^1H T_1, T_2</i>		
Morgan '10 ¹⁰⁶						
Andrews '11 ³⁰						
Fossen '11 ⁸⁹						
Rane '12 ¹⁰⁷						
Majumdar '13*				$^1\text{H } T_1, T_2$		
Oliviera '14 ⁹²						
Vorapalawut '15 ⁹³				<i>Low field ^1H T_1, T_2</i>		

*see Chapter 3.

Low field NMR relaxometry has also been used to study asphaltene behavior in native crude oil.^{93,105} All these studies are important in their own right and provide insight into asphaltene behavior, but the relaxation behavior of specific chemical groups within the asphaltenes remains to be answered in a comprehensive manner.

1.5.2. Solid-state NMR Spectroscopy

While basic solution-state NMR spectroscopy has found widespread and continued use for asphaltene characterization, the use of solid-state NMR spectroscopy has been sporadic and insufficient at best. It is a result of the higher level of technical and conceptual difficulty in performing solid-state NMR experiments, which requires more spectroscopic expertise than routine solution-state NMR studies. In other words, solid-state NMR spectroscopy has been traditionally a lot less mainstream than its solution-state counterpart, despite its broad scope and the extensive array of applications that it offers. Solid-state NMR also offers several advantages over solution-state techniques. Generally, observables in NMR spectroscopy have an orientation dependence. In principle, detailed structural information can be gained via solid-state NMR spectroscopy because the orientation dependence of, for example, the chemical shift, can be measured, with little interference from chemical exchange and rapid motion. In solution, much of the valuable structural information is lost as a result of rapid isotropic motion and physical and chemical interactions between the system and the solvent. This is especially relevant for complex mixtures with hierarchical structural motifs, such as the asphaltenes with their monomer-nanoaggregate-cluster hierarchy. In contrast, solid-state NMR techniques are ideally suited for studying phase structures. The team of Murphy, Gerstein, Weinberg, and Yen published a series of solid-

state ^1H and ^{13}C NMR studies of coal-derived asphaltenes between 1981 and 1983^{108–110} using the dipolar dephasing technique.¹¹¹ These early experiments suffer from poor resolution, because of inefficient ^1H decoupling, owing to low magnetic field, low power and radio-frequency (r.f.) field inhomogeneity. Cyr *et al.*,³⁴ and Semple *et al.*⁷⁷ used ^{13}C cross-polarization magic angle spinning (CP-MAS, see Chapter 2) experiments to characterize bitumen- and heavy-oil-derived asphaltenes, respectively. They however, made the often repeated mistake of basing quantitative results on signal intensities from ^{13}C CP-MAS NMR spectra, especially of material that is expected to have extended networks of non-protonated aromatic carbons. Using integration values from a ^{13}C CP-MAS NMR spectrum to obtain quantitative information can be futile for asphaltenes because the proton-to-carbon CP efficiencies vary greatly between different carbons. These efficiencies depend upon the carbons' proximity to the protons in the system, which may result in the absence of certain carbon signals in the spectrum altogether. Cyr,³⁴ however, recognized this problem in their work but did not discuss it in detail. Further investigations using CP-MAS techniques were carried out by Storm *et al.*³⁵ and Pekarar *et al.*¹⁰⁰ on petroleum derived asphaltenes. They perform relaxation³⁵ and CP^{35,100} time measurements in the solid state, which appear fundamentally flawed because the measurements were performed only for the most intense signals, completely disregarding the underlying resonances in the broad background. These underlying resonances constitute a major fraction of the spectrum, as shown later on by Douda *et al.*,¹¹² Daaou *et al.*,^{113,114} and Bouhadda *et al.*¹¹⁵ using deconvolution (peak-fitting) analysis of the solid-state ^{13}C NMR spectrum, and under no circumstances should they be neglected. However, Storm³⁵ provides one of the earliest CP-dynamics studies, reporting cross-polarization time-constants (T_{CP}) and ^1H spin-lattice relaxation time in the rotating frame ($T_{1\rho\text{H}}$), which are

useful parameters required to understand molecular structure and dynamics. Doubt may be raised about the CP-dynamics model used by Storm to arrive at these values, which is different from the established models in solid-state NMR spectroscopy literature.¹¹⁶ Pekerar¹⁰⁰ also reported T_{CP} values but the CP-dynamics model used was not mentioned, neither was the CP-dynamics discussed in detail. The interpretation of the T_{CP} data was based only on segmental mobility arguments, which is not wrong, but is incomplete, as shall be demonstrated in the following chapter. A number of MAS studies^{112,114,117} ignore the aromatic spinning sidebands overlapping with the aliphatic signals, which can lead to errors in assignment and quantification. For example, in Douda *et al.*,¹¹² the aliphatic region of the ^{13}C NMR spectrum was deconvolved without accounting for the spinning sidebands of the aromatic region, which undoubtedly overlap with the aliphatic area at the 8 kHz MAS rate used, as demonstrated in Chapter 4. The same error was made by Daaou *et al.*¹¹⁴ at 14 kHz MAS. These studies provide a deconvolution model only for the aliphatic region, and simply integrate the aromatic area in the spectrum. Bouhadda¹¹⁵ reported a deconvolution analysis of the entire ^{13}C NMR spectrum, where they compared single-pulse excitation (SPE), cross-polarization and Hahn-echo sequences to determine the aromaticity of an Algerian crude. Not surprisingly, they found SPE to be the most accurate determinant of aromaticity. Hauser *et al.*¹¹⁸ reported a quantitative single-pulse excitation (SPE) MAS NMR spectrum of asphaltenes, along with a CP-polarization inversion (CP/PI) technique which was used for spectral editing. They studied the thermal stability of heavy-oil asphaltenes under pyrolysis and suggested that as the pyrolysis temperature increases, dealkylation or dehydrogenation is preferred over formation of larger polyaromatic rings. Other than these examples, the use of solid-state NMR spectroscopy for asphaltene

characterization has been limited. A brief review of most of the techniques employed thus far, along with the corresponding papers is provided in Table 1.2.

Table 1.2 highlights some of the gaps in the literature for solid-state NMR spectroscopic characterization of asphaltenes. While CP-MAS has been used extensively, a proper CP dynamics analysis has been lacking. The CP dynamics studies by Storm³⁵ and Pekerar¹⁰⁰ were preliminary in nature. Deconvolution of the broad ¹³C NMR spectrum is an important step in simplifying the problem, but efforts have been limited and often erratic.

Table 1.2. Brief chronological review of solid-state NMR spectroscopic techniques used for asphaltene characterization.

Paper	¹ H NMR	¹³ C NMR	Spectral editing	CP dynamics	Relaxation
Weinberg '81 ¹⁰⁸		CP-MAS	DD		
Murphy '82 ¹⁰⁹		CP-MAS			
Weinberg '83 ¹¹⁰		CP-MAS	DD		
Cyr '87 ³⁴		CP-MAS			
Semple '90 ⁷⁷		CP-MAS			
Storm '94 ³⁵		CP-MAS		$T_{CP}, T_{1\rho H}$	¹³ C T_1
Pekerar '98 ¹⁰⁰		CP-MAS		T_{CP}	
Siskin 2006 ¹¹⁷		CP-MAS			
Hauser '08 ¹¹⁸		SPE/ CP-MAS	CP/PI		
Douda '08 ¹¹²		SPE-MAS			
Daaou '09 ¹¹³		SPE-MAS			
Bouhadda '10 ¹¹⁵		SPE/ CP-MAS			
Daaou '12 ¹¹⁴		CP-MAS		T_{CP} <i>not reported</i>	
Majumdar '15*		SPE/ CP-MAS	DD, ¹ H DF, DIVAM	$T_{CP}, T_{1\rho H}$	¹ H T_2

*see Chapter 4.

Relaxation studies have also been limited, but the most conspicuous by its absence is a ¹H NMR study. This is not surprising given that the solid-state ¹H NMR spectrum is inherently

broad, owing to strong ^1H - ^1H homonuclear dipolar couplings that cannot be removed at moderate to high spinning speeds. Highly specialized pulse sequences, which are difficult to implement, are required to resolve such a spectrum and infer any useful information from it.

1.6. Thesis objectives

The above discussion on asphaltene structure and behavior, and the review of NMR techniques used for asphaltene characterization draws attention to the gaps in the literature and provides a starting point for this project. Questions about asphaltene structure still require unambiguous answers, such as the true size or range of sizes of the PAH core, the length of the alkyl chains and which is the dominating motif, island or archipelago. It also remains to be seen conclusively what structural features drive aggregation. In this thesis, asphaltenes derived from Athabasca oil-sands bitumen will be studied first, using a wide range of both solution- and solid-state NMR techniques, to establish some basic structural parameters. These methodologies shall then be extended to studying asphaltenes from different petroleum and coal sources and expanded upon further. Coal-derived and petroleum asphaltenes have been reported to have different structures, hence comparing them might hold key to answers about the structural features that drive aggregation. Finally, asphaltenes will be studied using ultrafast MAS techniques in the solid state at a very high magnetic field to explore the possibilities offered by modern and advanced NMR instrumentation. However, to understand the methodology used to perform these studies, a thorough knowledge of several basic and advanced NMR concepts is required. Therefore,

the next chapter in this thesis will introduce the reader to certain NMR fundamentals, and familiarize them with all the techniques (pulse sequences) employed in the later chapters.

CHAPTER 2

2. NUCLEAR MAGNETIC RESONANCE SPECTROSCOPY

2.1. Overview

Nuclear magnetic resonance (NMR) spectroscopy is one of the most powerful and versatile analytical tools available today for the characterization of materials in the liquid state, in solution or in solid state. Discovered independently by both Felix Bloch and coworkers, and Edward Mills Purcell and coworkers in 1946,^{119,120} the field of NMR spectroscopy has seen enormous developments since its inception, going from a niche topic of interest in physics, to perhaps the most widely used analytical technique in chemistry.¹²¹ Over the years, numerous techniques based on the NMR phenomenon have been developed, ranging from simple one-dimensional techniques, multidimensional correlation methods to specialized pulse sequences for determining specific structural parameters such as dipolar coupling and chemical shift anisotropy.^{122–124} Currently, besides the chemical discipline, NMR spectroscopy is used extensively in the field of biology as well, while its descendent magnetic resonance imaging (MRI) is one of the most important tools in neuroscience and medicine.

In this thesis, the application of NMR spectroscopy is focused on the characterization of asphaltenes using advanced methodology, both in solution and solid states. As such, the theoretical background will cover topics which are relevant to explaining these methodologies and some basic familiarity with NMR spectroscopy will be assumed. This chapter will first discuss certain fundamental and general concepts, followed by

descriptions of the specific pulse-sequences used for the studies included in this thesis, along with an explanation of the suitability of these techniques to investigate asphaltenes.

2.2. NMR Spectroscopy Fundamentals

The introduction to NMR spectroscopy fundamentals in this section is presented in a condensed fashion, adapted from the detailed discussions in books by Keeler,¹²⁵ Levitt¹²⁶ and Duer *et al.*¹²⁷ and a review article by Borisov *et al.*¹²⁸ The figures were generated by the author and were inspired by the diagrams in the books and the articles stated above.

2.2.1. Nuclear Spin and Magnetism

The components that make up an atomic nucleus, the nucleons, can be described in terms of certain intrinsic properties such as mass, charge and angular momentum. The last of these is referred to as the nuclear spin, characterized by two quantum numbers, **I** and **M**. The spin quantum number **I** represents the total angular momentum and could be a positive integer (0, 1, 2, ..., n) or half-integer ($\frac{1}{2}$, $\frac{3}{2}$, ..., $\frac{n}{2}$), determined by the number of protons and neutrons in the nucleus. The *z*-component of the angular momentum is given by the quantum number **M** and it can take on 2**I**+1 values from **-I** to **+I** in integer steps. For instance, a spin- $\frac{1}{2}$ nucleus has two possible values of **M**, $-\frac{1}{2}$ and $\frac{1}{2}$, while a spin-1 nucleus possesses three possible values **M**, -1, 0, and 1. The angular momentum or spin gives rise to the magnetic moment $\vec{\mu}$, which is expressed by Eq. 2.1:

$$\vec{\mu} = \gamma \hat{\mathbf{I}} \quad \text{Equation}$$

2.1 where γ is the magnetogyric ratio, the value of which is specific to each nucleus. The

energy of interaction between the magnetic moment $\vec{\mu}$ and an applied external magnetic field \vec{B}_0 is given by their product (Eq. 2.2):

$$E = -\vec{\mu} \cdot \vec{B}_0 \quad \text{Equation 2.2}$$

Since in a laboratory the magnetic field is vertical, it is defined along the z -axis and the energy of interaction can be written as a function of the z -component of magnetization (Eq. 2.3):

$$E = -\gamma \hat{I}_z B_0 \quad \text{Equation 2.3}$$

In the absence of \vec{B}_0 , the magnetic moments of each nucleus are randomly aligned or isotropically distributed making the net magnetic moment of the bulk system zero (Fig 2.1a) and the energy levels degenerate.

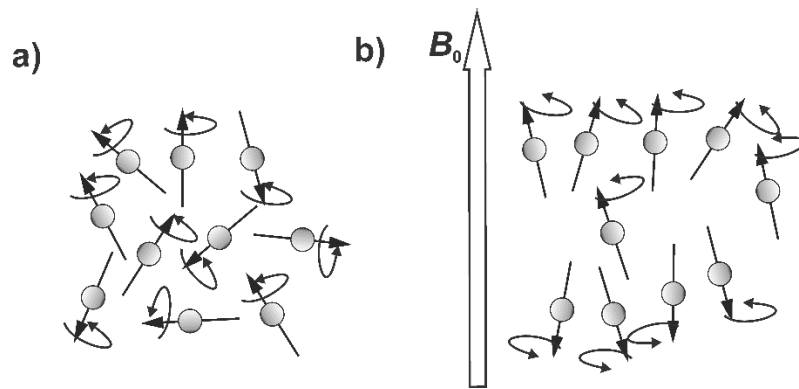


Figure 2.1. Distribution of spin magnetic moments in the a) absence and b) presence of an external magnetic field \vec{B}_0 .

The degeneracy is broken by the application of the \vec{B}_0 magnetic field, which is arbitrarily chosen to be along the z -axis, and the magnetic moments become aligned with it. As stated previously, for a spin- $1/2$ nucleus there are two possible states of the magnetic moment

vector: $+\frac{1}{2}$, which is aligned in the direction of \vec{B}_0 , called the ‘ α ’ state, and $-\frac{1}{2}$, which is aligned in the direction opposite \vec{B}_0 , called the ‘ β ’ state, (Fig. 2.1b), at an angle determined by the initial orientation of the vector prior to the application of the external field. The spins in the α -state have a lower energy level and thus have a higher probability of occurrence, according to the Boltzmann distribution (Eq. 2.4):

$$\frac{N_\beta}{N_\alpha} = \exp\left(-\frac{\Delta E}{kT}\right) \quad \text{Equation 2.4}$$

where N_α and N_β are the number of spins parallel and anti-parallel to \vec{B}_0 , ΔE is the difference between the two energy levels, k is the Boltzmann constant and T is the temperature in Kelvin. At room temperature, the difference in the population of up and down states is very small.

The magnetic moment $\vec{\mu}$, placed in an external magnetic field \vec{B}_0 experiences a torque given by:

$$\tau = \vec{\mu} \times \vec{B}_0 \quad \text{Equation 2.5}$$

The torque causes rotation of the nucleus about the axis of the applied magnetic field, referred to as precession, with an angular frequency ω_0 , as shown in Fig. 2.2:

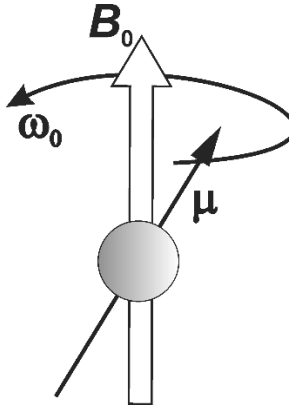


Figure 2.2. Precession of the nuclear magnetic moment μ about the static external magnetic field \vec{B}_0 with frequency ω_0 .

The frequency ω_0 is nucleus-specific and is known as the Larmor frequency, given by Eq. 2.6:

$$\omega_0 = -\gamma B_0 \quad \text{Equation 2.6}$$

Therefore, the Larmor frequency is dependent on the external magnetic field, and often in practice, the ω_0 of a proton is used to indicate the strength of the magnetic field.

At the macroscopic level in the presence of a magnetic field, a sample consists of an ensemble of spin magnetic moments precessing about the magnetic field at the Larmor frequency, with more spins aligned parallel (α) to the field than against (β) (Fig. 2.1b). This gives rise to a net longitudinal magnetization which is cylindrically symmetrical about the magnetic field, without any transverse components. In Fig. 2.3, this net magnetization is represented by the vector \vec{M}_z , which is parallel to the z -component of the magnetic field.

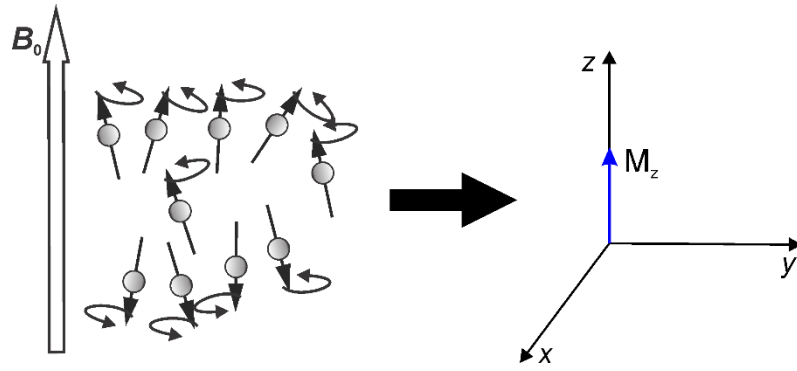


Figure 2.3. Net longitudinal magnetization \vec{M}_z resulting from the ensemble of spins precessing about B_0 .

For detection of this magnetization, it is transferred to the transverse plane. How and why this is done is explained in following section.

2.2.2. Signal Generation, Relaxation and the NMR Experiment

The longitudinal magnetization \vec{M}_z does not change with respect to time. However, for detection of the NMR signal, a time dependence of the magnetization is necessary, because only then can the signals from different chemical species be separated on a frequency scale. Time dependence can be achieved by transferring the longitudinal magnetization to the transverse (xy) plane. A strong radio frequency (r.f.) pulse on resonance with the Larmor frequency (ω_0), applied on any one of the transverse axes, causes all the spins, which were previously precessing at random phases (incoherently), to precess in phase with each other (coherently) and results in a net transverse magnetization precessing at the Larmor frequency, as illustrated in Fig. 2.4.

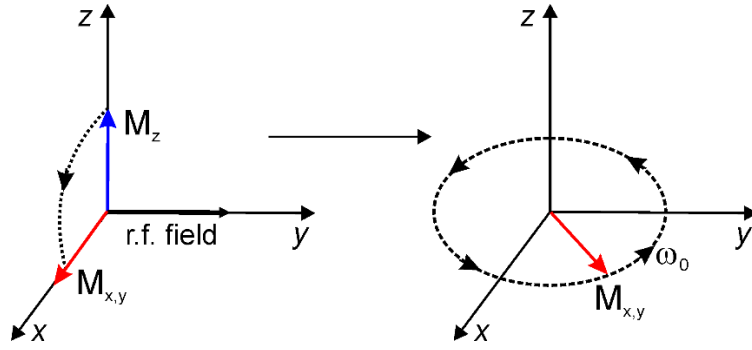


Figure 2.4. Longitudinal magnetization (M_z) rotated to the transverse plane by an r.f. pulse and precession of the transverse magnetization $M_{x,y}$ at the Larmor frequency ω_0 .

The r.f. pulse is generated by a coil with its winding axis in the xy plane. The precession of the transverse magnetization $\overrightarrow{M_{x,y}}$ causes oscillations in the magnetic field, which induces a current that can be detected by the same coil that was used to apply the r.f. pulse. Once the r.f. pulse is terminated, the transverse magnetization gradually returns back to the equilibrium state over time through a process called relaxation.

In a real sample, spins are not isolated but constantly interact with each other and their surroundings. They experience perturbations from random local time-dependent magnetic fields from neighboring spins and other electronic interactions, which leads them to relax back to an isotropic distribution at thermal equilibrium in the absence of an r.f. pulse. This occurs via two mechanisms viz. longitudinal or T_1 and transverse or T_2 relaxation.

Longitudinal relaxation, often referred to as spin-lattice relaxation although the terminology is outdated, is the process by which the longitudinal component of magnetization $\overrightarrow{M_z}$ returns to thermal equilibrium after the application of an r.f. pulse, illustrated by Fig. 2.5.

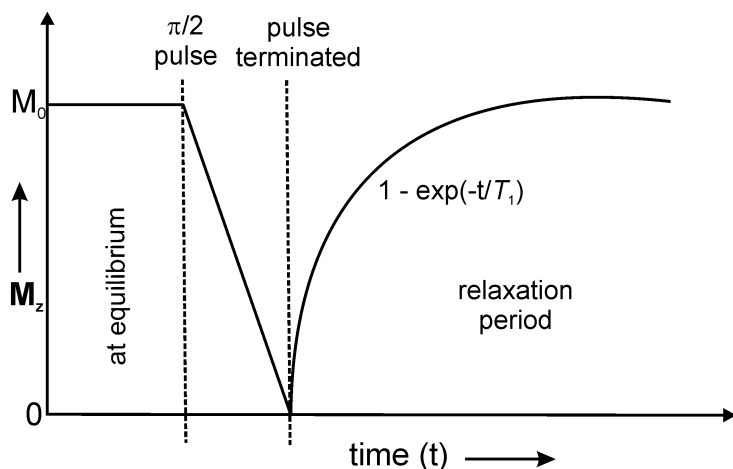


Figure 2.5. Recovery of the longitudinal magnetization M_z to equilibrium under longitudinal T_1 relaxation, after the creation of transverse magnetization by a $\pi/2$ pulse.

The return of M_z to thermal equilibrium is exponential in nature, given by Eq. 2.7:

$$M_z = M_0 \left[1 - \exp\left(-\frac{t}{T_1}\right) \right] \quad \text{Equation 2.7}$$

where M_0 is the equilibrium magnetization before the application of the r.f. pulse and T_1 is the longitudinal relaxation time constant. The time scale of T_1 is dependent upon factors such as the solvent viscosity, temperature, size, mobility and structure of the molecule, and it can range from milliseconds to days. In an NMR experiment, the time required to obtain a spectrum is directly related to the T_1 of the sample, since one needs to wait approximately $5-7 \times T_1$ between subsequent scans.

As discussed earlier (Fig. 2.4), the application of an r.f. pulse rotates the ensemble of spins, which create the longitudinal magnetization (M_z), into the transverse plane, resulting in a coherent or in-phase transverse magnetization ($M_{x,y}$). In other words, all the spins precess in-phase with each other about the z -axis as long as the r.f. field is on. As the r.f. field is turned off, small fluctuations in the local time-dependent magnetic fields cause the

individual spins in the ensemble to lose coherence over time, leading to loss of transverse magnetization, as illustrated by Fig. 2.6.

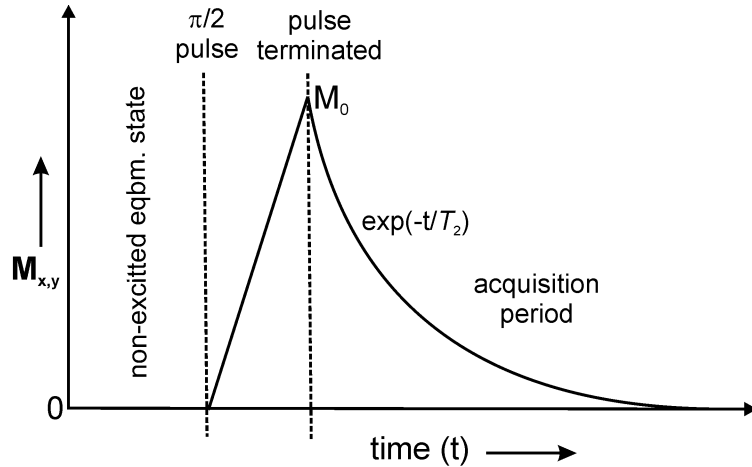


Figure 2.6. Decay of the transverse magnetization $M_{x,y}$ under transverse T_2 relaxation during acquisition, after termination of the r.f. field. (eqbm. = equilibrium).

Unlike longitudinal relaxation, the decay in transverse magnetization does not involve any energy exchange between the spins with the surrounding environment. The behavior is characterized by an exponential decay function given by Eq. 2.8:

$$M_{x,y} = M_0 \exp\left(-\frac{t}{T_2}\right) \quad \text{Equation 2.8}$$

where T_2 is the transverse relaxation time constant and M_0 is the initial intensity of the transverse magnetization.

It was mentioned earlier that the transverse magnetization rotating at the Larmor frequency creates an oscillating magnetic field, which in turn induces a current in the signal-detection coil. When the relaxation effects are taken into consideration, the trajectory of the rotating magnetization can be described by a gradually collapsing helix (Fig. 2.7b). While the transverse magnetization decays in a spiral trajectory on the transverse plane

(Fig. 2.7a) under T_2 relaxation, the longitudinal magnetization also recovers under T_1 relaxation, giving the helical trajectory. The induced current resulting from this oscillation is the source of the NMR signal and is referred to as the free induction decay or FID (Fig. 2.7c).

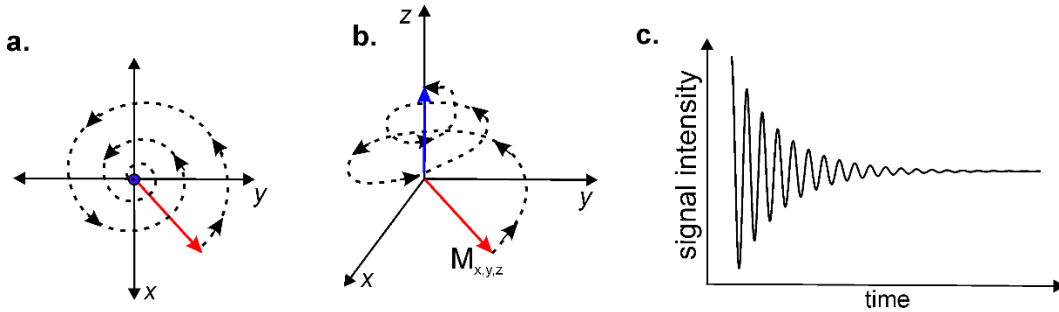


Figure 2.7. a) The spiral trajectory of the transverse magnetization under T_2 relaxation; b) the overall helical trajectory of the magnetization, combining T_1 and T_2 relaxation; c) the resulting FID.

The FID, or the signal (S) can be mathematically described by a complex function, given by Eq. 2.9:

$$S_t = S_0 \exp(i\omega_0 t) \exp\left(-\frac{t}{T_2}\right) \quad \text{Equation 2.9}$$

where S_t is the signal intensity at any time t and S_0 is the initial intensity. This is an example of a frequency encoded time domain signal, which means that it can be detected as a function of time, then digitized by an analog-to-digital converter (ADC) and subsequently converted into the frequency domain using a Fourier transform (FT). This provides the final NMR spectrum, a plot of the signal intensity as a function of frequency, which has a peak centered at the Larmor frequency (ω_0) with a full width at half height (FWHH) given by $1/\pi T_2$, as shown in Fig. 2.8.

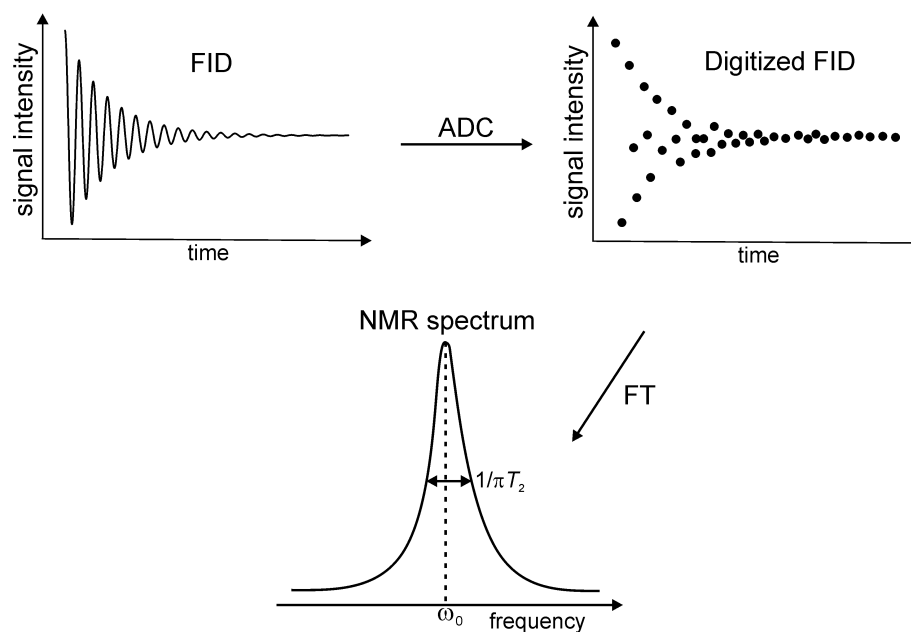


Figure 2.8. Digitization of the FID and subsequent generation of the NMR spectrum through Fourier Transform. The full width at half height is given by $1/\pi T_2$.

The order of events in an NMR experiment, such as pulses and delays, are conventionally illustrated with a pulse sequence timing diagram. A very basic NMR pulse sequence is shown in Fig. 2.9. It consists of an initial pre-pulse delay, also known as recycle or relaxation delay, followed by an excitation r.f. pulse, the length of which is given by the angle by which it rotates the longitudinal magnetization, terminating in the acquisition period where the FID is detected, with a pre-acquisition delay in between.

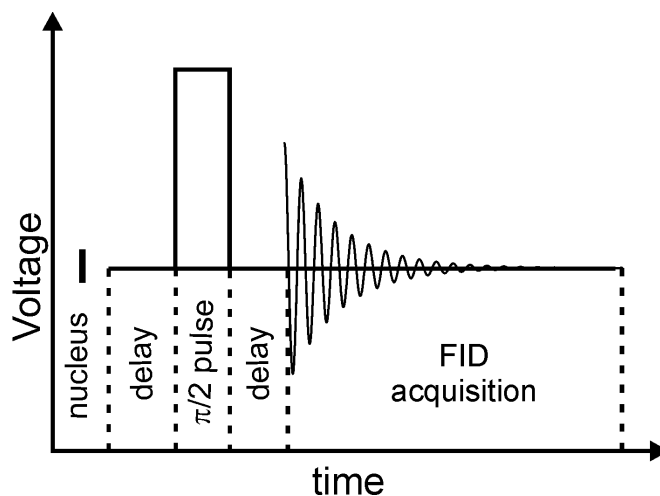


Figure 2.9. A basic NMR pulse sequence diagram for a nucleus I, showing the building blocks.

More advanced NMR spectroscopic experiments involve other elements such as decoupling schemes during acquisition, simultaneous r.f. pulses on multiple nuclei, combination of r.f. pulses of different lengths and polarization transfer from one nucleus to another. All these advanced sequences follow the same general scheme and will be discussed later on a case-by-case basis.

2.2.3. Chemical Shielding and Chemical Shift

In theory, an isolated spin-1/2 nucleus should give rise to a single peak centered at the Larmor frequency ω_0 after a Fourier transform of the FID. In practice, however, this is hardly ever the situation. A nucleus is surrounded by negatively charged electrons, which in the presence of a magnetic field start circulating to produce a current. This induced current can have two components to it, diamagnetic and paramagnetic, depending on the system. The diamagnetic and paramagnetic currents arise due to the circulation of electrons in their ground state and excited state, respectively. The paramagnetic term causes rapid relaxation of the FID and thus makes the study of paramagnetic materials very challenging.

Fortunately, the majority of NMR spectroscopic studies are performed on diamagnetic materials, including the studies included in this thesis, and hence from here onwards, only the diamagnetic component will be considered.

The diamagnetic current, induces a magnetic field which can either add or subtract from the \vec{B}_0 field experienced by the spin, as illustrated by Fig. 2.10.

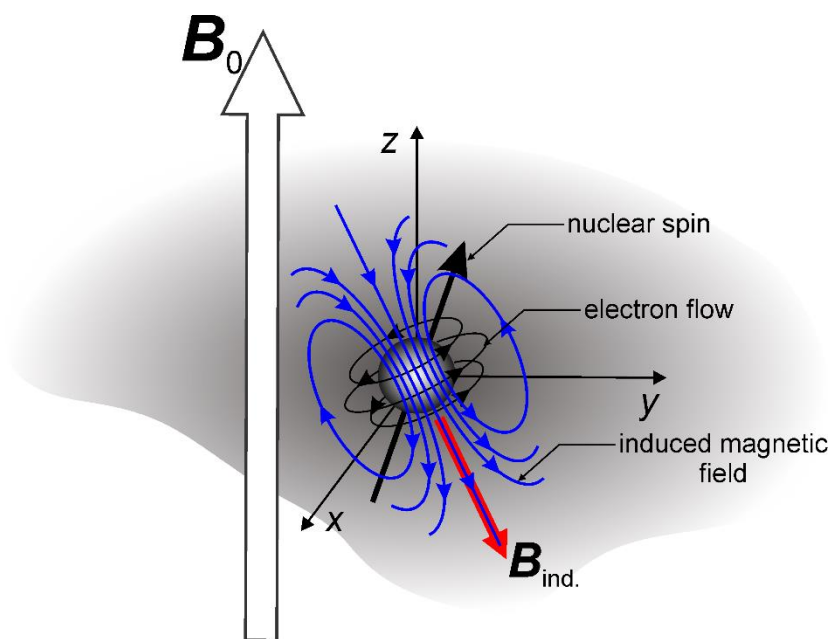


Figure 2.10. An induced magnetic field $\vec{B}_{ind.}$, generated by diamagnetic current induced by the circulating electrons around the nucleus, in the presence of an external magnetic field \vec{B}_0 .

This induced magnetic field, $\vec{B}_{ind.}$, is much weaker than the static field \vec{B}_0 ($\sim 10^{-4} \vec{B}_0$) but causes a small, observable shift in the Larmor frequency, which is commonly known as the ‘chemical shift’. The induced magnetization is related to the static field by the following relationship (Eq. 2.10):

$$\vec{B}_{\text{ind.}} = \hat{\sigma} \cdot \vec{B}_0 \quad \text{Equation 2.10}$$

where σ is referred to as the chemical shielding tensor. The induced field is dependent on the orientation of the molecule with respect to \vec{B}_0 , and the chemical shielding tensor provides that relationship. It is given by a 3×3 matrix of the following form:

$$\hat{\sigma} = \begin{pmatrix} \sigma_{xx} & \sigma_{xy} & \sigma_{xz} \\ \sigma_{yx} & \sigma_{yy} & \sigma_{yz} \\ \sigma_{zx} & \sigma_{zy} & \sigma_{zz} \end{pmatrix} \quad \text{Equation 2.11}$$

For a specific crystallite orientation, the resulting frequency due to B_{ind} can be obtained by incorporating the shielding tensor into Eq. 2.6:

$$\omega_i = -\gamma\sigma_i B_0 \quad \text{Equation 2.12.}$$

Since the spectral frequency scales with the static magnetic field, for consistency, it is not reported as a frequency value, but as parts per million (ppm) of the Larmor frequency. In practice, the frequency of a known standard compound, particular to the nucleus of interest, is used for reference (ω_{ref}), and the frequency difference is reported as the ‘chemical shift’ (δ_i), calculated as follows:

$$\delta_i = \frac{\omega_i - \omega_{\text{ref}}}{\omega_{\text{ref}}} \quad \text{Equation 2.13}$$

From an end-user perspective, chemical shift is the most important parameter obtained from NMR spectroscopy, because it provides a direct measure of the electronic environment of a chemical species. Different functional groups and chemical moieties resonate in their characteristic frequency (ppm) ranges which are well documented in literature and can be found in any standard textbook introducing NMR spectroscopy.¹²⁹

Similar to the chemical shielding, the chemical shift is also a tensor described by a 3×3 matrix:

$$\delta = \begin{pmatrix} \delta_{xx} & \delta_{xy} & \delta_{xz} \\ \delta_{yx} & \delta_{yy} & \delta_{yz} \\ \delta_{zx} & \delta_{zy} & \delta_{zz} \end{pmatrix} \quad \text{Equation 2.14}$$

This representation of the tensor is in the laboratory (LAB) frame, but for easier manipulation, it is often transformed to its own frame of reference, called the Principal Axes System (PAS), illustrated in Fig. 2.11.

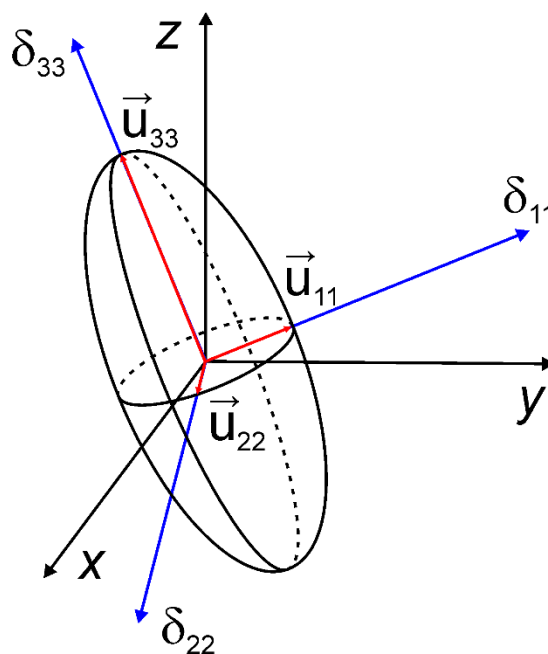


Figure 2.11. The Principal Axes System (δ_{11} , δ_{22} , δ_{33}) of the chemical shift tensor, obtained by rotating the laboratory frame (x , y , z).

The transformation to the PAS can be represented by the following rotation, which diagonalizes the chemical shift tensor:

$$\delta = \mathbf{u}^{-1} \cdot \delta_{\text{PAS}} \cdot \mathbf{u} \quad \text{Equation 2.15}$$

$$\text{where } \delta_{\text{PAS}} = \begin{pmatrix} \delta_{11} & 0 & 0 \\ 0 & \delta_{22} & 0 \\ 0 & 0 & \delta_{33} \end{pmatrix} \quad \text{Equation 2.16}$$

$$\text{and } \mathbf{u} = (\vec{u}_{11}, \vec{u}_{22}, \vec{u}_{33}) \quad \text{Equation 2.17}$$

The diagonal components of δ_{PAS} are called the principal components, representing the eigenvalues of the system, while the corresponding eigenvectors are given by \mathbf{u} , which represents the rotation that relates δ_{PAS} to the original LAB frame. The unit vectors of \mathbf{u} (u_{ii}) define the axes of the PAS frame (Fig. 2.11).

The isotropic chemical shift, i.e. the chemical shift observed when all three principal components of the PAS frame are equal, is obtained by taking their average:

$$\delta_{\text{iso}} = \frac{(\delta_{11} + \delta_{22} + \delta_{33})}{3} \quad \text{Equation 2.18}$$

This is usually the case in solution-state NMR spectroscopy, where rapid molecular motion averages the principal components and renders them equal. In solid-state NMR spectroscopy, all three principal components are usually unequal and the Larmor frequencies are orientation dependent. Thus, instead of a single isotropic chemical shift, a distribution of frequencies is obtained, which is characterized by additional parameters.

The Haeberlen convention for assigning the principal components of δ_{PAS} is chosen here, which is as follows:¹³⁰

- i. The δ_{33} is chosen such that it is farthest from δ_{iso} .
- ii. The δ_{22} is chosen such that it is closest to δ_{iso} , and the remaining principal component is assigned to δ_{11} .

$$\text{In brief: } |\delta_{33} - \delta_{\text{iso}}| \geq |\delta_{11} - \delta_{\text{iso}}| \geq |\delta_{22} - \delta_{\text{iso}}| \quad \text{Equation 2.19*}$$

Based on the above convention, a measure of the distribution of orientation dependent frequencies, called the chemical shift anisotropy (CSA), can be obtained, by finding the largest deviation from the isotropic value (Eq. 2.20):

$$\delta_{\text{aniso}} = \delta_{33} - \delta_{\text{iso}} \quad \text{Equation 2.20}$$

The shape of the distribution is characterized by the asymmetry parameter η , which is calculated as:

$$\eta = \frac{\delta_{22} - \delta_{11}}{\delta_{\text{aniso}}} \quad \text{Equation 2.21}$$

The CSA interaction manifests differently in solution- and solid-state NMR spectroscopy. Rapid molecular reorientation removes the CSA, and the spectrum consists of a single peak centered at δ_{iso} , as illustrated in Fig. 2.12a. However, in solid-state NMR spectroscopy, solid powder samples lack motional averaging, but usually contain multiple disparate crystallite orientations with respect to the magnetic field, making the chemical shielding tensor a function of orientation. In turn, it makes the precession frequency dependent on the spatial orientation, given by

$$\omega(\theta, \phi) = \left[\sigma_{\text{iso}} + \frac{\delta_{\text{zz}}}{2} \{ (3\cos^2\theta - 1) + \eta \cos 2\phi \sin^2\theta \} \right] \quad \text{Equation 2.22}$$

where θ and ϕ are the Euler rotation angles used to transform the shielding tensor from the LAB frame to the PAS frame. Each different orientation has a unique chemical shift, and

*Another convention often employed is the Hertzfeld-Berger convention, where instead of CSA, a quantity called ‘span’ is used to describe the width of the powder pattern, and ‘skew’ is used to describe the asymmetry parameter, and have slightly different expressions from their Haeberlen convention counterparts, although describing the same quantities.

this distribution leads to a ‘powder pattern’, as shown in Fig. 2.12b, c and d. The inflection points in the powder pattern correspond to the principal components (δ_{11} , δ_{22} and δ_{33}) of the δ_{PAS} in the PAS frame of reference, while the shape of the powder pattern is dependent on both the CSA and the asymmetry parameter η . The CSA determines the width of the frequency distribution, while the patterns corresponding to different η values are illustrated in Fig. 2.12b, c and d. The pattern in Fig. 2.12c represents a case of cylindrical symmetry in the tensor, where two of the principal components are equal. An example of this are methyl group protons which rotate rapidly about the $\text{CH}_3\text{-C}$ axis, leading to axial symmetry about the C-C bond. In brief, the symmetry of the tensor components is a combination of the electron density symmetry around the nucleus and the symmetry of any motion the system undergoes.

The isotropic chemical shift depends on the electronic environment of the nucleus of interest, and thus on the neighbouring groups. If the net effect of the neighboring groups is to remove some of the circulating electrons (refer to Fig. 2.10), the induced field is reduced, causing what is known as deshielding. The reduction of the opposing induced field by deshielding exposes the nuclei to the external field, which increases its resonance frequency to a higher ppm value. Deshielding can be caused by electron withdrawing groups such as carboxylic moieties, heteroatoms such as O, N and halogens and also by aromatic rings. The aromatic rings present a unique situation, where the circulating π -electrons create their own local field, causing shielding and deshielding for surrounding nuclei depending on their position relative to the ring. This is called the ring-current effect, illustrated in Fig. 2.13.

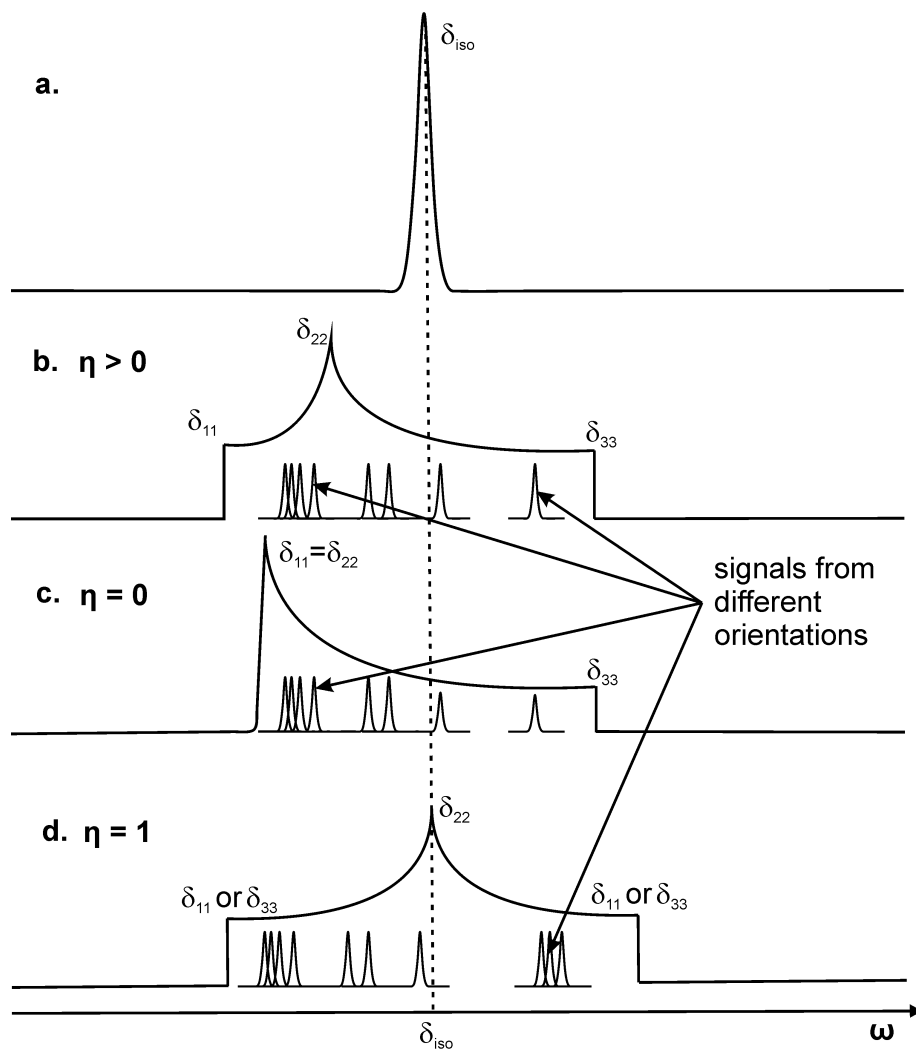


Figure 2.12. The effect of CSA on NMR spectra: a) Isotropic signal in solution-state NMR as a result of rapid motional averaging. b, c and d) Powder patterns observed at different values of the asymmetry parameter η .

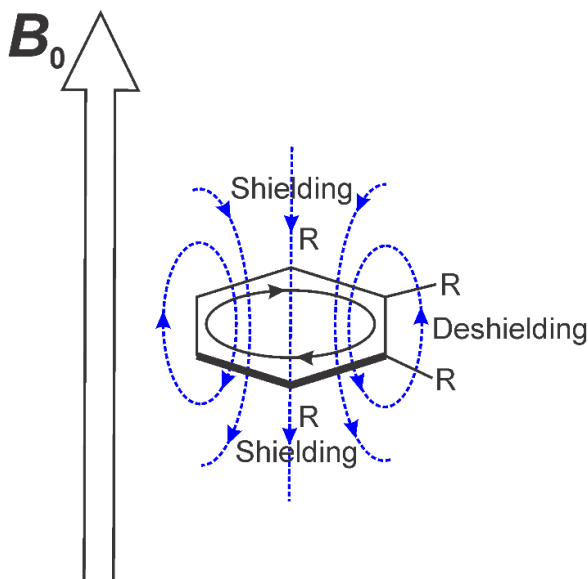


Figure 2.13. The ring current effect in aromatic rings. Nuclei on the periphery of the ring get deshielded, while those above or below the plane of the ring get shielded.

The ring-current induced by the external magnetic field further induces a local field which acts along the external field on the periphery of the rings and against it above and below the plane of the ring. Thus, any nuclei lying on the periphery of the ring, such as aromatic protons or any other substituent, will experience an effective field that is the sum of the external field and the induced field, or deshielding, thereby raising its resonant frequency or chemical shift. Conversely, nuclei lying above or below the planes of the ring will experience a reduced effective field, or be shielded, lowering their chemical shift. In certain cases, the shielding can be strong enough to substantially reduce chemical shifts beyond the otherwise characteristic chemical shift range. For ^1H , this can result in negative chemical shifts.

2.2.4. Nuclear Spin Interactions: *J*- and Dipolar Coupling

Thus far we have only considered interactions between the nucleus, its surrounding electrons and the static magnetic field. In all real circumstances, the nuclear spin also

interacts with neighbouring nuclei, through each other's local magnetic fields. This is referred to as spin-spin coupling and occurs between the same types (homonuclear) or between different types (heteronuclear) of nuclei. There are two ways in which these interactions can occur: directly between the spins or indirectly mediated through the electrons via chemical bonds. The latter is commonly referred to as through-bond or J -coupling, and involves the polarized electrons around one nucleus inducing a magnetic field at the other nucleus. This causes spins to be sensitive to neighboring spins that are within 1 to 3 bonds distance to it, resulting in multiplet peak structures, commonly seen in solution-state NMR spectra, often referred to as 'splittings'. These splittings are extremely useful in determining molecular structures, because a functional group giving a split signal contains information on the groups attached to it. A simple example would be the ^1H NMR spectrum of an ethyl group ($-\text{CH}_2-\text{CH}_3$), where the $-\text{CH}_2-$ signal is split into a quartet by the 3-bond $^1\text{H}-^1\text{H}$ homonuclear J -coupling ($^3J_{\text{HH}}$) from the $-\text{CH}_3$ group protons, while $-\text{CH}_3$ signal is split into a triplet by the same interaction, as illustrated in Fig. 2.14.

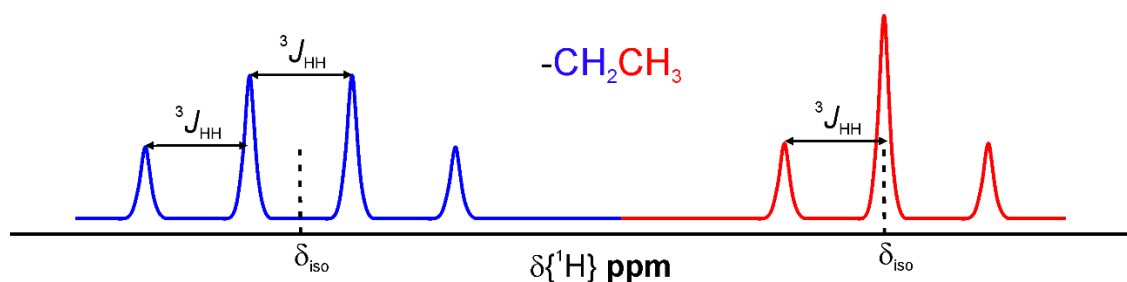


Figure 2.14. Splitting pattern of the ^1H NMR spectrum peaks of an ethyl group caused by the homonuclear J -coupling between the protons.

The splitting patterns due to J -coupling are observed in the spectra of most liquids and solutions, unless decoupling schemes are employed, which shall be discussed later. The J -coupling can also be observed in solid-state NMR spectroscopy, but it is dependent on

orientation, whereas only the isotropic value is observed in solution. It has a unit of frequency, usually reported in Hertz (Hz) and is independent of the strength of the static magnetic field.

The other kind of spin-spin interaction occurs directly between the magnetic dipole moments of nuclei through space, and is referred to as direct or through-space dipolar coupling. This is an orientation dependent interaction, illustrated by Fig. 2.15. It is characterized by the angle θ subtended by the internuclear vector joining the two nuclei, with the static field \vec{B}_0 , and by the dipolar coupling constant b .

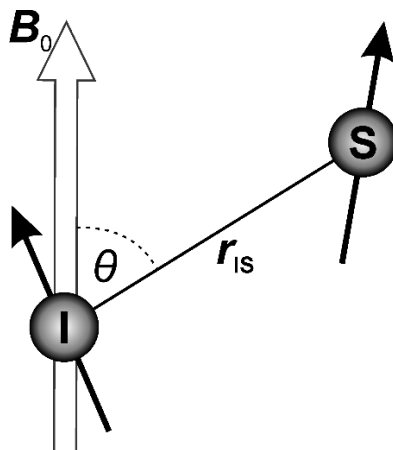


Figure 2.15. Depiction of the through-space dipolar coupling between two spins I and S, in the presence of an external magnetic field \vec{B}_0 .

Similar to the CSA tensor described in the previous section, the dipolar coupling tensor also has an orientation dependence (see Appendix 1 for details).^{131,132} Equation 2.23 provides the expression for dipolar coupling D :

$$D = \frac{1}{2} b (3 \cos^2 \theta - 1) \quad \text{Equation 2.23}$$

where

$$b = \frac{\mu_0}{4\pi} \frac{\hbar \gamma_I \gamma_S}{r_{IS}^3} \quad \text{Equation 2.24}$$

r_{IS} being the internuclear distance, γ_I and γ_S being the magnetogyric ratio of the I and S spins respectively, and μ_0 is the permittivity of free-space.

Since the dipolar coupling D is orientation dependent, it is also described by a tensor, but in this case the tensor is traceless, meaning that it has an isotropic value of zero. Therefore, under rapid molecular motion like in liquids, the dipolar coupling reduces to zero, and has no direct effect on the spectrum. However, due to lack of motion, solids can exhibit very strong dipolar coupling, from a few Hz to hundreds of kHz.

Similar to J -coupling, dipolar coupling can also be homo- or heteronuclear. Homonuclear coupling can cause severe homogeneous broadening of the spectrum which greatly reduces spectral resolution (Fig. 2.16). This kind of broadening is frequent in solid-state NMR spectroscopy and especially pronounced for abundant nuclei with large magnetogyric ratios, such as ^1H and ^{19}F , and the spectral lines can be as broad as tens to hundreds of kHz.

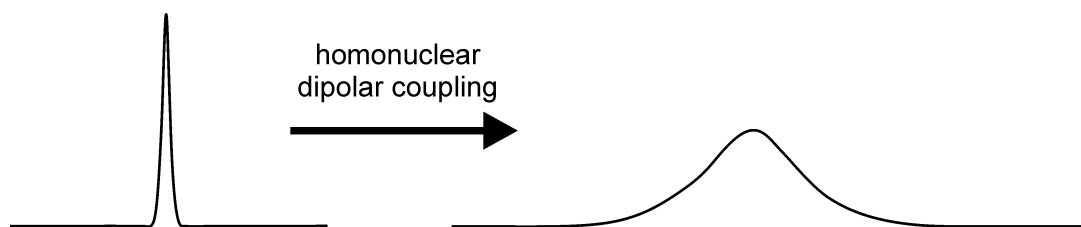


Figure 2.16. Homogeneous broadening of NMR signals by homonuclear dipolar coupling.

The spectra broadened in this manner lack sufficient resolution to provide structural information with any reasonable detail, hence simple solid-state ^1H NMR spectroscopy is generally not performed without any specialized pulse sequences which can improve the resolution. For a nucleus with low natural abundance and a small magnetogyric ratio, such as ^{13}C , homonuclear dipolar coupling interactions are rare and weak, thus not causing homogeneous line broadening. Hence, high-resolution ^{13}C NMR spectra can be obtained fairly easily in the solid state. Heteronuclear dipolar coupling interactions, on the other hand, do not cause such homogenous line broadening, and can be suppressed easily by decoupling sequences, which will be described later. Heteronuclear dipolar coupling does cause inhomogeneous broadening, but it can be removed by a technique called magic angle spinning (MAS).

A third type of interaction exists in the case of quadrupolar nuclei, where the spin is larger than $\frac{1}{2}$. In these cases, the charge distribution around the nucleus is no longer spherically symmetric, and it interacts with the surrounding electric field gradients. It can lead to rapid relaxation in solution state and complicated patterns in solids. Quadrupolar nuclei and related interactions, however, are beyond the scope of this thesis and will not be discussed further.

2.2.5. Magic-Angle Spinning

As discussed above, the strength of the dipolar coupling interaction is a function of the orientation of the internuclear coupling vector (Fig. 2.15) with respect to the external magnetic field \vec{B}_0 . The chemical shift anisotropy (CSA) is also dependent on its orientation with respect to \vec{B}_0 . The orientation dependence of both these interactions is given by a single term: $3\cos^2\theta-1$,¹²⁷ where θ is the angle describing the orientation (see Appendix 1

for details). Thus, if the angle θ for each crystallite is set such that the $3\cos^2\theta-1$ term reduces to zero, these interactions can be suppressed. This angle, referred to as the ‘magic angle’ (θ_m) is easily determined by Eq. 2.25:

$$\theta_m = \arccos \frac{1}{\sqrt{3}} \cong 54.74^\circ \quad \text{Equation 2.25}$$

The magic angle is the angle between the z -axis and the body diagonal of an unit cube, as shown in Fig.2.17. Rotating the sample about this diagonal will result in equal interchange between its x , y and z coordinates, which simulates isotropic motion and thereby averaging all the crystallite orientations to the magic angle. This is known as magic angle spinning (MAS) (Fig. 2.17, right) and is routinely used in solid-state NMR spectroscopy to average the orientation dependence of the nuclear interactions and thus reduce homogeneous and inhomogeneous broadening, improving spectral resolution.

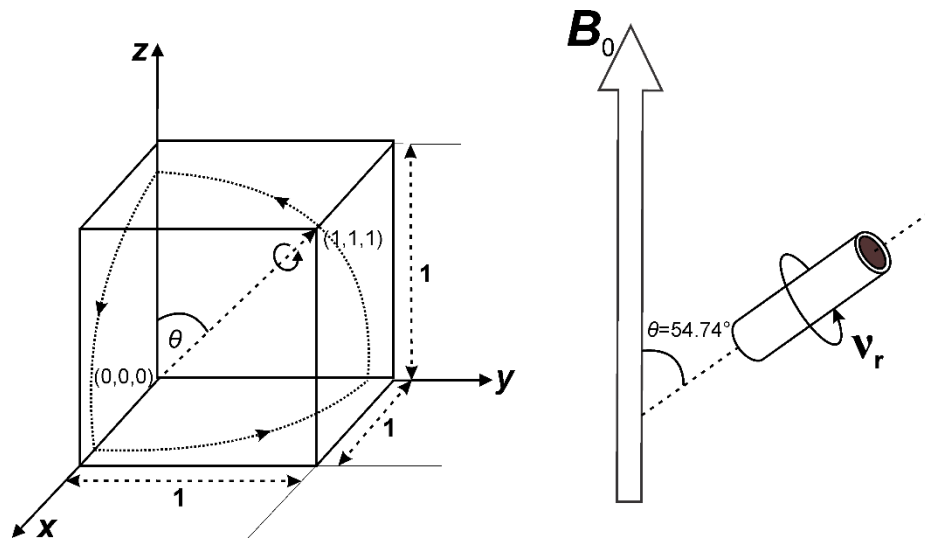


Figure 2.17. The unit cube representation of the magic angle (*left*) and sample rotation at the magic angle with a frequency ν_r (*right*).

The efficiency with which the broadening interactions can be suppressed is determined by the spinning speed ν_r . If the spinning speed is larger than the strength of the interaction,

complete suppression of these effects can be achieved. For interactions such as CSA and heteronuclear dipolar coupling in nuclei such as ^1H and ^{13}C , this suppression can be significant, since their frequencies often, but not always, fall below the highest spinning speeds achievable with modern instrumentation. In these cases, the powder pattern (Fig. 2.18a) is usually reduced to an isotropic peak (Fig. 2.18c). The highest spinning speed that a solid-state NMR spectroscopy rotor can attain depends on its size: the smaller the diameter is, the faster it can be spun. Often for reasons of sensitivity and sample volume, larger rotors are used, which limits the spinning speed, and complete suppression of these interactions is not possible.

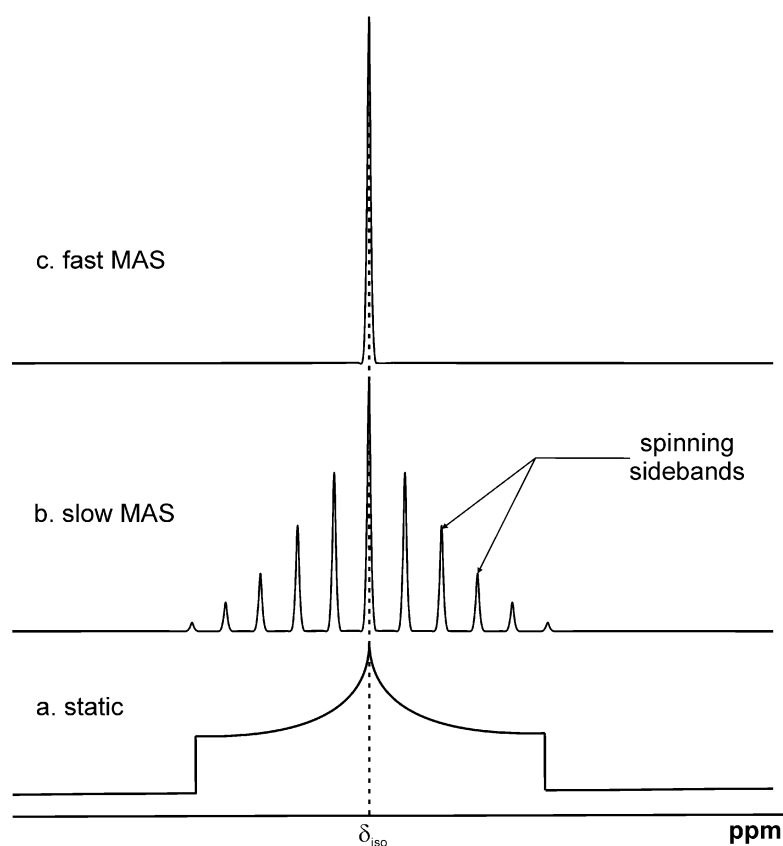


Figure 2.18. a) Solid-state NMR spectrum obtained under static conditions; b) MAS NMR spectrum when the spinning speed is b) smaller and c) larger than the line broadening interaction

In these cases, the spectrum shows a spinning sideband pattern (Fig. 2.18b), which resembles the static powder pattern, and can be directly related to the CSA tensor. The isotropic peak is not necessarily always the most intense peak, but it is the one which never changes its position for a specific chemical moiety, and can be determined by carrying out the experiment at different spinning speeds. Homonuclear dipolar coupling interactions, however, can get as large as hundreds of kHz and cannot be efficiently removed by the MAS speeds achievable with current equipment. Thus, often for nuclei such as ^1H and ^{19}F , high-resolution spectra can be elusive or riddled with sidebands. However, sidebands are not always a problem. Rather, they can be used to obtain important structural information, such as the CSA, and thus the end goal of an experiment determines if they are desirable or not.

2.2.6. Decoupling

Coupling interactions, both through-bond and through-space, can cause line splitting and broadening. Under certain circumstances, these interactions can be useful in determining the electronic environment of the nuclei or internuclear distances. However, they often need to be suppressed to improve spectral resolution. Besides MAS in the solid-state, another technique called decoupling is routinely used in both solution- and solid-state NMR spectroscopy. Although both homo- and heteronuclear decoupling can be performed, discussion will be limited to heteronuclear decoupling since it is more relevant to this thesis.

Heteronuclear decoupling, both in solution- and solid-state NMR spectroscopy, can improve spectral resolution. In liquids, it can simplify the spectrum by removing splittings caused by J -coupling, while in solids it can make the spectral linewidths narrower by

reducing broadening due to dipolar coupling. Several different pulse sequences exist which can achieve heteronuclear decoupling. The most basic type is called continuous wave (CW) decoupling, which consists of continuous r.f. irradiation on the nucleus being decoupled during acquisition (Fig. 2.19).

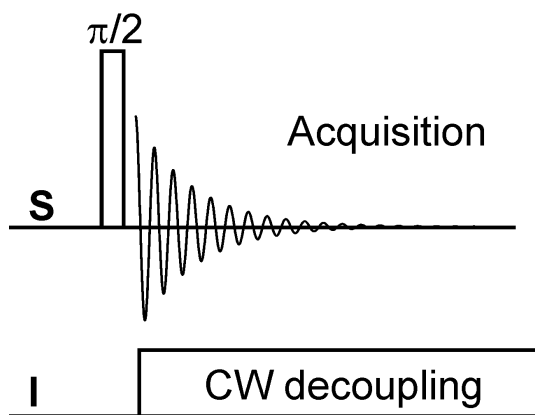


Figure 2.19. Continuous wave (CW) decoupling.

However, the strength of the r.f. field that can be used for CW decoupling is restricted by the fact that it has to remain on throughout the entire duration of acquisition, thus limiting the frequency range over which the decoupling is effective. This is usually not an issue when decoupling nuclei with a small chemical shift range, such as ^1H , but becomes a problem when decoupling nuclei with a large chemical shift range (large CSA) such as ^{19}F . For these nuclei, more specialized decoupling techniques are employed. One such widely used sequence is the Two Pulse Phase Modulated (TPPM) decoupling developed by Griffin and co-workers.¹³³ It is still a continuous decoupling method, but instead of one continuous pulse, it consists of a series of back-to-back r.f. pulses which are synchronized with the rotor period ($\tau_r = 1/\nu_r$), with alternating phases, illustrated in Fig. 2.20. The rotor-synchronized phase modulation ($\pm\Phi/2$) reduces the offset dependence of the decoupling

sequence, i.e. when the decoupling pulses are not on resonance with the signals being decoupled, improving its performance over CW decoupling. Other specialized decoupling techniques also exist, each with its own utility, but are beyond the scope of this thesis.

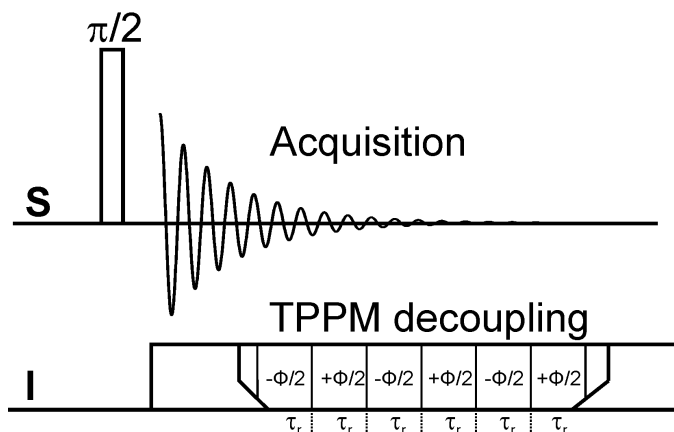


Figure 2.20. An MAS NMR experiment on nucleus S with TPPM decoupling of nucleus I, where τ_r is the rotor period.

2.2.7. Product Operators

A proper description of some of the concepts to be described in the following sections requires an understanding of how the magnetizations behave during the different events, i.e. the pulses and delays, in the course of an experiment. One of the simpler approaches of understanding this behavior is through the use of product operators. As described earlier, an external static magnetic causes an ensemble of spins to precess incoherently (without phase synchronization) about the field, with a slight bias towards the direction of field, resulting in a net vertical polarization of spins. This net longitudinal magnetization M_z (Fig. 2.3) can then be rotated to the transverse plane by an r.f. pulse, creating the transverse magnetizations M_x and M_y (Fig. 2.4) which coherently rotate about the magnetic field at the Larmor frequency (neglecting chemical shift effects). For a one-spin system, everything

about this spin-ensemble can be determined by a linear combination of the quantum mechanical operators I_x , I_y and I_z , as:

$$M_x(t) I_x + M_y(t) I_y + M_z(t) I_z \quad \text{Equation 2.26}$$

which represent the x -, y - and z -components of the spin angular momentum, respectively. Thus, at different points in time, the state of the spin system can be described by these operators, and will depend on the values of the coefficients $M_{x,y,z}(t)$.

Hamiltonians, which are operators that describe the energy states of a spin system, also affect how the spin system evolves in time during the course of a pulse sequence. The time evolution of spins are manipulated by altering the Hamiltonian, which takes on different forms under different cases, as described below:

For an x - or y -pulse on \mathbf{I} spin:

$$H_{p,x,y} = \omega_1 I_{x,y} \quad (\omega_1 \text{ being the frequency of the pulse}) \quad \text{Equation 2.27}$$

For free-precession (delay) of \mathbf{I} spin:

$$H_{\text{free}} = \Omega I_z \quad (\text{also called evolution under offset } \Omega) \quad \text{Equation 2.28}$$

Overall Hamiltonian for precession of a coupled two-spin system $\mathbf{I-S}$:

$$H = \Omega_I I_z + \Omega_S S_z + 2\pi J_{IS} I_z S_z \quad \text{Equation 2.29}$$

J_{IS} being the scalar coupling between the two spins. The effect these Hamiltonians have on the spin-system described in a simplified fashion the following section.

Rotation under r.f. pulses: The description of how the operators I_x , I_y and I_z evolve under r.f. pulses is simple. Their rotation about the axis on which the pulse is applied follows a

right-hand convention. If a pulse is applied to rotate one operator by an angle θ about a given axis, the general form of the rotation is given by:

$$\cos \theta \times \text{original operator} + \sin \theta \times \text{new operator} \quad \text{Equation 2.30}$$

This is best described by an example. If the pulse is applied along the x -axis, the operator I_z will rotate towards the $-y$ axis by an angle θ , as illustrated by Fig. 2.21 and Eq. 2.31:

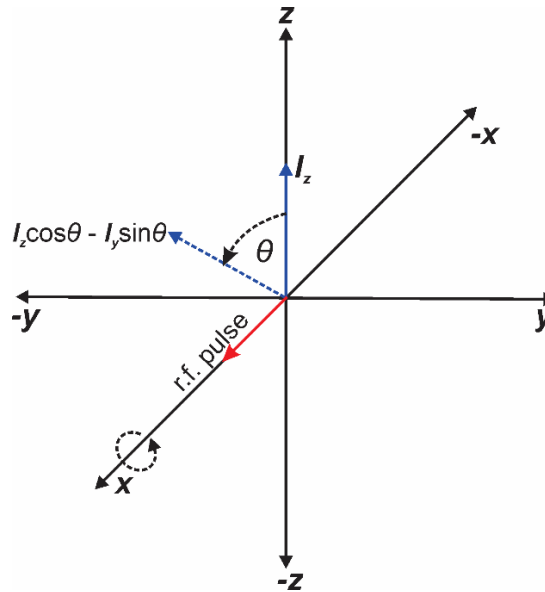


Figure 2.21. Rotation of operator I_z under a θ -pulse on the x -axis.

$$I_z \rightarrow I_z \cos \theta - I_y \sin \theta \quad \text{Equation 2.31}$$

Using this operator notation and right-hand convention, any rotation about any of the axes can be described in terms of the three operators. If $\theta = \pi/2$, it is evident that from Eq. 2.30 and Fig. 2.21 that the original operator reduces to zero and the new operator describes the entire magnetization. It is also worth noting that a pulse has no effect on an operator if it is applied on the same axis that the operator represents. For instance, an x -pulse will not cause

rotation of the I_x operator, but will rotate the other two. In general, $\theta = \omega_{\text{rf}} \times t_p$, where ω_{rf} is the frequency of the r.f. field and t_p is the duration of the pulse (pulse-width).

Free precession: In the absence of an r.f. field, the one-spin operators evolve under the effect of their chemical shift frequency offset (Ω) in exactly the same manner as they evolve under a pulse, except that in this case the $\theta = \Omega \times \tau$, where τ is the time over which the free precession takes place. The offset Ω is the apparent frequency of Larmor precession, given by the sum of the Larmor frequency and the transmitter frequency (frequency at which the r.f. pulse is applied). Thus, a very simplistic diagrammatic representation of the evolution of the single-spin operators, with or without an r.f. pulse, is possible and is presented in Fig. 2.22. A few examples are shown below:

Free-precession about the z-axis: $I_x \rightarrow I_x \cos \theta + I_y \sin \theta$ Equation 2.32

Effect of y-pulse on I_x : $I_x \rightarrow I_x \cos \theta - I_z \sin \theta$ Equation 2.33

Effect of $-x$ -pulse on I_y : $I_y \rightarrow I_y \cos \theta - I_z \sin \theta$ Equation 2.34

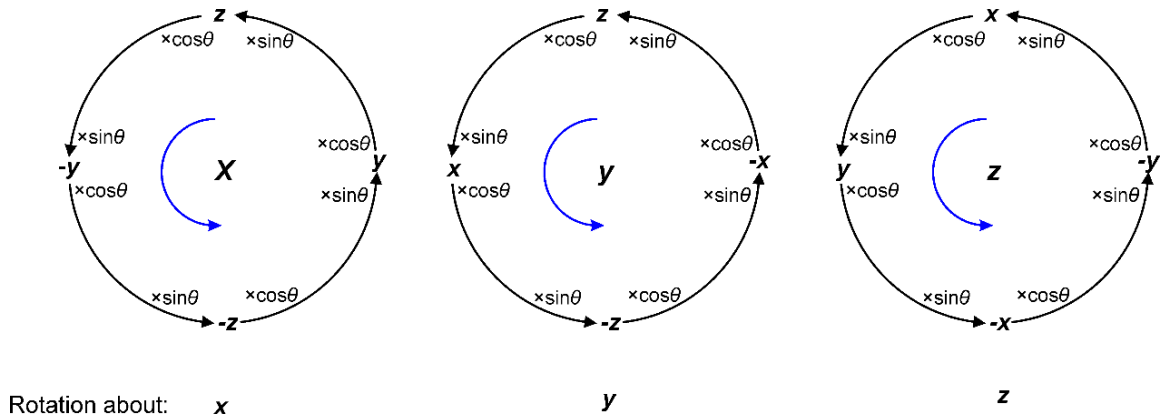


Figure 2.22. Representation of the rotation of any operator about the x, y or z axis. Following the arrow starting from the initial operator takes one to the final operator after rotation. Any state on the path of the arrow is given by multiplying the initial operator and final operator by $\cos \theta$ and $\sin \theta$, respectively and adding them.

Two-spin operators: The discussion thus far was limited to the one-spin case, but the effect of coupled spins have to be considered, which necessitates the construction of two-spin operators, by combining the one-spin operators of two different spin-systems **I** and **S**. The operators to be combined are as follows:

Spin-**I**: E_I, I_x, I_y, I_z

Spin-**S**: E_S, S_x, S_y, S_z

where E_I and E_S are the unit operators. The combination of the above operators provides a set of sixteen operators that can fully describe the two-spin system. For brevity, the contribution of the unitary operators can be omitted, without affecting the description, making a set of fifteen operators. These operators can be classified into different categories, as shown below:

z-magnetizations: I_z, S_z

‘in-phase’ *x* and *y* magnetizations: I_x, I_y, S_x, S_y (observable single quantum coherences)

‘anti-phase’ *x* and *y* magnetizations: $2I_xS_z, 2I_yS_z, 2I_zS_x, 2I_zS_y$ (observable)

multiple quantum coherences: $2I_xS_x, 2I_xS_y, 2I_yS_x, 2I_yS_y$ (unobservable multiple quantum coherences)

non-equilibrium population: $2I_zS_z$ (unobservable)

The factor of 2 in the operators combining the two spins is for normalization purposes. The only observable signals arise from the ‘in-phase’ phase and ‘anti-phase’ magnetizations. The terms ‘in-phase’ and ‘anti-phase’ arise from the appearance of the respective observed signals, where the coupling J_{IS} splits them into in-phase or anti-phase peaks, as shown in Fig. 2.23.

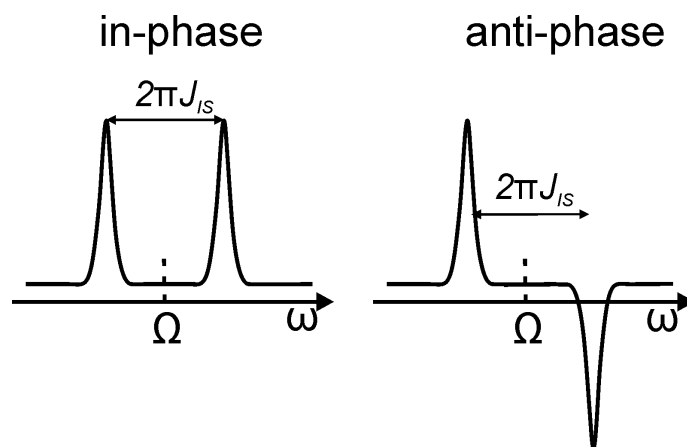


Figure 2.23. In- and anti-phase signals.

The evolution of these operators under the effect of chemical shift offset Ω occurs in exactly in the same manner as the one-spin operators, hence won't be elucidated further. The more important effect here is that of J -coupling. Only the in-phase and anti-phase transverse magnetizations evolve under J -coupling, while z -magnetizations and multiple quantum coherences stay unaffected. More importantly, in-phase and anti-phase magnetizations transform into each other through evolution under J -coupling, as described below:

$$I_x \rightarrow I_x \cos(\pi J_{IS}\tau) + 2 I_y S_z \sin(\pi J_{IS}\tau) \quad \text{Equation 2.35}$$

$$S_y \rightarrow S_y \cos(\pi J_{IS}\tau) - 2 I_z S_x \sin(\pi J_{IS}\tau) \quad \text{Equation 2.36}$$

$$2 I_y S_z \rightarrow 2 I_y S_z \cos(\pi J_{IS}\tau) - I_x \sin(\pi J_{IS}\tau) \quad \text{Equation 2.37}$$

$$2 I_z S_x \rightarrow 2 I_z S_x \cos(\pi J_{IS}\tau) + S_y \sin(\pi J_{IS}\tau) \quad \text{Equation 2.38}$$

Here, $I_y S_z$ is an anti-phase magnetization in spin **I** and $I_z S_x$ is an anti-phase magnetization in spin **S**. Thus, in-phase and anti-phase operators can be transformed into each if allowed to evolve for a period τ , the value of which is usually set according to the strength of the coupling J_{IS} . For complete conversion of one to the other, $\tau = 1/2J_{IS}$. A diagram similar to Fig. 2.22 can be constructed to illustrate this interconversion (Fig. 2.24).

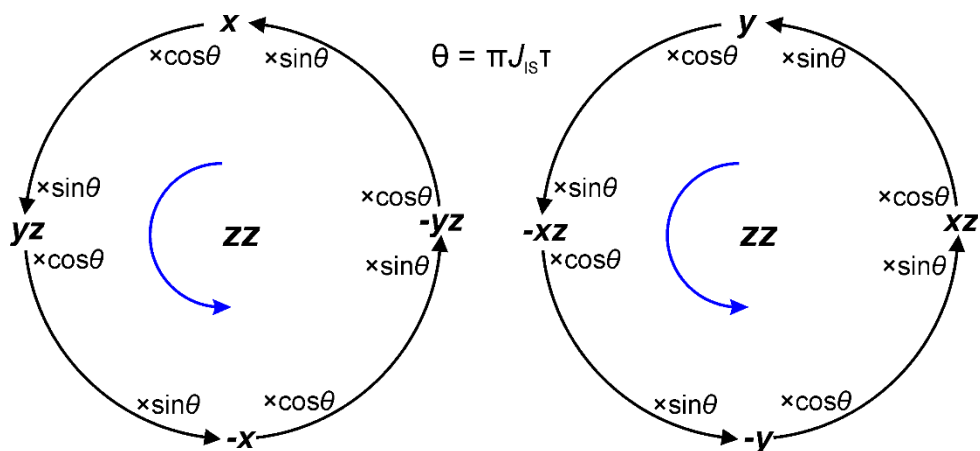


Figure 2.24. Interconversion of in-phase and anti-phase magnetizations under J -coupling. 'x' refers to I_x or S_x , 'yz' refers to I_yS_z or I_zS_y and so on. The same rules as Fig. 2.22 apply here.

2.2.8. Coherence Transfer

The interconversion of in- and anti-phase magnetization plays an extremely important role in a large number of NMR pulse sequences. It can be used to transfer coherence from an abundant spin **I** to rare spin **S** and vice versa, which is an essential step for experiments which require enhancement of the rare spin signal. Coherence transfer can be achieved by first generating an anti-phase magnetization on one spin, then applying simultaneous $\pi/2$ pulses with appropriate phase to both spins. The process is illustrated in Fig. 2.25, where an anti-phase magnetization on spin **I** is being transferred to an anti-phase magnetization on spin **S**.

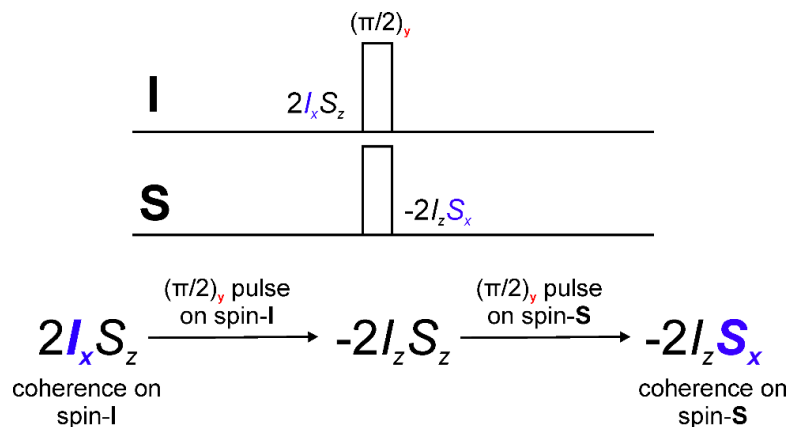


Figure 2.25. Coherence transfer from spin-I to spin-S. The $\pi/2$ pulses should be on an axis different than the coherence being transferred.

2.2.9. Spin Echo

In a large number of pulse-sequences, coherence transfer is used at tandem with another phenomenon called spin-echo. Spin echo is defined by the following sequence of events: delay— π -pulse—delay, the function of which is to ‘refocus’ or remove the effect of evolution of the transverse magnetization under the chemical shift offset. Figure 2.26 describes the mode of action of the spin-echo sequence for a one-spin system. In this sequence, the transverse magnetization allowed to evolve for a delay period $\tau/2$, during which it dephases via coherent (field inhomogeneity, isotropic chemical shielding) processes, illustrated in the figure by the fanning-out of magnetization vectors. The delay is followed by a refocusing π -pulse on the appropriate axis to which rotates the magnetization by 180° , reversing the sense of the dephasing caused by the coherent processes during the delay period, because the offset frequencies of the magnetization vectors remain the same.

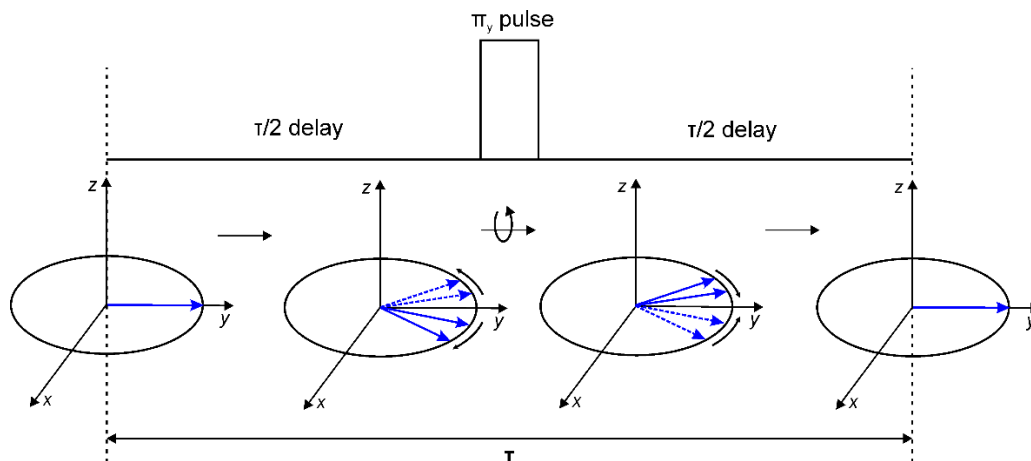


Figure 2.26. The spin-echo pulse sequence, showing the evolution of magnetization vectors.

In other words, the magnetization vectors which were rotating clockwise keep rotating in the same direction. Another $\tau/2$ period follows, during which the magnetizations, with their reversed sense of dephasing, ‘refocus’ and form an ‘echo’ at time τ . This $\tau/2$ — π -pulse— $\tau/2$ sequence thus effectively removes or refocuses any dephasing or loss of signal intensity due to chemical shielding or field inhomogeneity.

Although the offset is refocused by spin-echo, J -coupling is not refocused in a coupled spin system. Detailed calculations will not be shown here, but the overall effect of a ‘ $\tau/2$ — π -pulse— $\tau/2$ ’ spin echo on a homonuclear spin system is the same as letting the transverse magnetization evolve only under J -coupling for the entire τ -period, which is already discussed in Section 2.2.7 (Eq. 2.35-2.38, Fig. 2.24). In the case of a coupled heteronuclear **I-S** spin-system, three different situations can arise: i) spin-echo on both spins simultaneously, ii) spin-echo only on spin-**I** and iii) spin-echo only on spin-**S**. For brevity, the effect of spin-echo in these cases is illustrated in Fig. 2.27.

Spin-echo sequence		Effect	Initial state	End state
a.	I	Offset Ω_I refocused. Evolution under J_{IS} .	I_x	$-I_x c(\pi J_{IS}\tau) + 2I_y S_z s(\pi J_{IS}\tau)$
	S	Offset Ω_S refocused. Evolution under J_{IS} .	S_x	$-S_x c(\pi J_{IS}\tau) - 2S_y I_z s(\pi J_{IS}\tau)$
b.	I	Offset Ω_I refocused. J_{IS} -refocused.	I_x	$-I_x$
	S	Evolution under offset Ω_S . J_{IS} -refocused.	S_x	$S_x c(\Omega_S\tau) + S_y s(\Omega_S\tau)$
c.	I	Evolution under offset Ω_I . J_{IS} -refocused.	I_x	$I_x c(\Omega_I\tau) + I_y s(\Omega_I\tau)$
	S	Offset Ω_S refocused. J_{IS} -refocused.	S_x	$-S_x$

c = cosine, s = sine

Figure 2.27. Possible spin-echo scenarios when the refocusing π -pulse is applied to a) both spins, b) only spin-**I** and c) only spin-**S**. The refocusing pulse here is applied on the y -axis and the initial state of magnetization chosen to be along the x -axis for illustration purposes. In (a) the sequence has the same effect as in the homonuclear case, i.e. evolution only under J -coupling for a period τ , followed by a π -pulse on both spins. In (b) and (c), the overall effect is inversion of the spin on which the pulse is applied, while the other spin evolves only under the effect of its offset (free precession). The J -coupling is refocused on both spins.

2.2.10. INEPT (*Insensitive Nuclei Enhanced by Polarization Transfer*)

The spin-echo sequence can be seamlessly combined with the coherence transfer sequence to create the INEPT sequence, which is an ironic abbreviation because it is a very efficient way of enhancing the signals of insensitive, low- γ nuclei (such as ^{13}C) by transferring the equilibrium magnetization from high- γ nuclei (such as ^1H). This sequence can be used by itself, but it is often used as a part of more complicated sequences. The INEPT pulse-sequence is shown in Fig. 2.28.

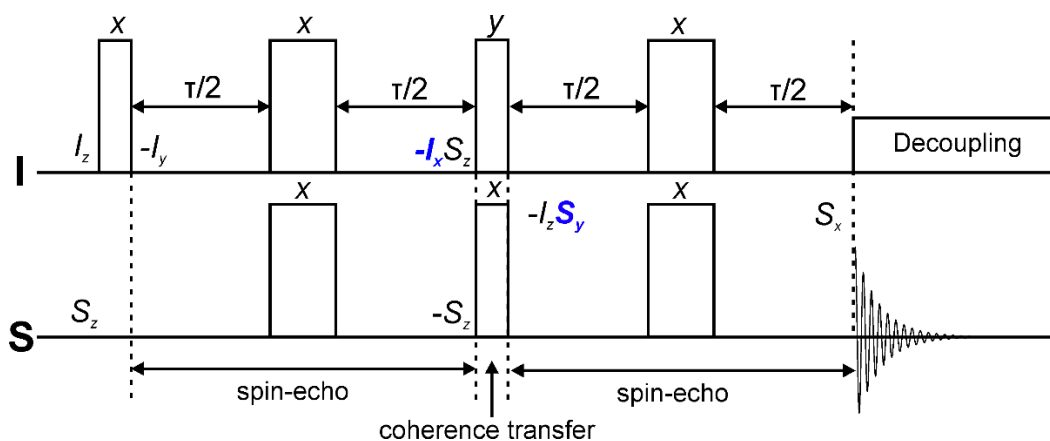


Figure 2.28. The INEPT pulse sequence. The transfer of polarization occurs at the $\pi/2$ pulses. The final spin echo period and the decoupling is optional, depending on how the sequence is used. The narrow pulses are $\pi/2$ and the wider ones are π . The phases of the applied pulses are denoted by the x and y above the pulses.

In brief, a transverse magnetization (I_y) is created on the high- γ spin (**I**), which evolves into an anti-phase magnetization on **I** ($I_x S_z$) after the first spin-echo period. This is where the $\pi/2$ -pulses for coherence transfer are applied and an anti-phase magnetization on **S** is created ($I_z S_y$), thus completing the transfer of polarization. This anti-phase term can be allowed to evolve further for another spin-echo period and become an in-phase term for detection. However, this last step is optional and often omitted when INEPT is used as a part of a larger sequence (such as 2D sequences) and the **S**-spin signal does not have to be observed right away. If it is required to be observed, the second spin –echo provides an in-phase multiplet on detection, which can be collapsed to one peak by decoupling the **I** spin. The INEPT sequence will be invoked later while explaining the HSQC sequence. It should be noted here that the discussions above do not include the effect of relaxation during the evolution periods.

2.2.11. Cross Polarization (CP)

In solid-state NMR spectroscopy, transfer of polarization from an abundant (e.g. ^1H) to a rare spin (e.g. ^{13}C) is routinely employed. The reason for doing this is two-fold: i) low abundance and low sensitivity of a nuclei makes the signal-to-noise ratio (S/N) inherently poor, which necessitates an extremely high number of scans per experiment to obtain useful signal; ii) the relaxation times of low abundance nuclei are usually very long due to the lack of strong homonuclear dipolar coupling interactions, mandating inconveniently long delays between subsequent scans (relaxation delay), which can be up to several hours. These issues can be circumvented by using a technique called cross-polarization (CP), which can be thought of as a different means to the same end as that of the solution-state INEPT experiment. In CP experiments, the polarization transfer is achieved by using the heteronuclear dipolar coupling between the two nuclei, instead of J -coupling as in INEPT. Cross-polarization can reduce the time requirement for an experiment and enhance the dilute nucleus signal manifold, and is regarded as one of the most important techniques in solid-state NMR spectroscopy.

The pulse-sequence for CP is illustrated in Fig. 2.29. After the initial excitation pulse on the abundant spin-**I**, the transfer of polarization occurs during the spin-lock period, which requires explanation. A spin-lock is a low-power pulse applied along the axis of the transverse magnetization, which, if of sufficient power, causes the transverse magnetization to remain along the corresponding axis (hence ‘spin-lock’) and precess about the same axis according to the frequency of the applied locking pulse (ω_1). To make the explanation less complicated, a ‘rotating-frame’ formalism is often used to describe spin-lock. The rotating frame is a frame of reference where the coordinate system is considered as rotating at the frequency of the transverse magnetizations, but in the opposite sense, which makes the

applied transverse spin-lock field (\vec{B}_1) appear static. Assuming the contact pulse to be on resonance, the \vec{B}_0 field is no longer effective, and \vec{B}_1 field acts as the polarizing static field. It makes the spins align either along (spin-up) or against (spin-down) the \vec{B}_1 field, similar to the α and β states in the lab frame. The difference in energy between the two spin states is given by the rotating-frame precession frequency (ω_1) of the respective spins. Therefore, the precession of the spins is no longer governed by the static field \vec{B}_0 , but the locking field \vec{B}_1 , as illustrated in Fig. 2.30.

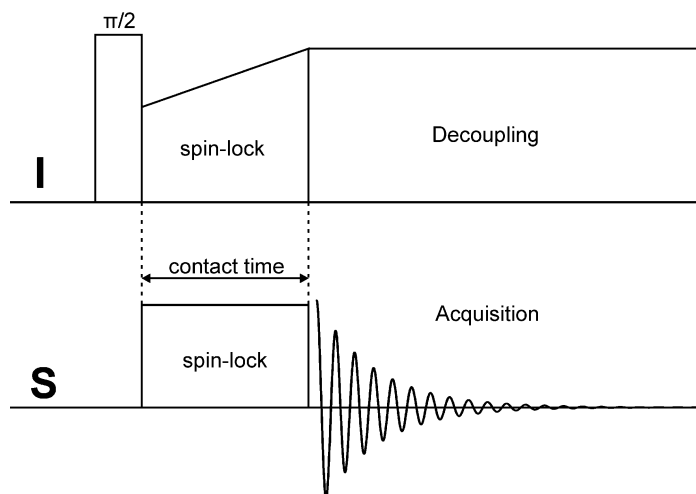


Figure 2.29. The I-to-S cross-polarization (CP) pulse sequence, using ramped-CP.

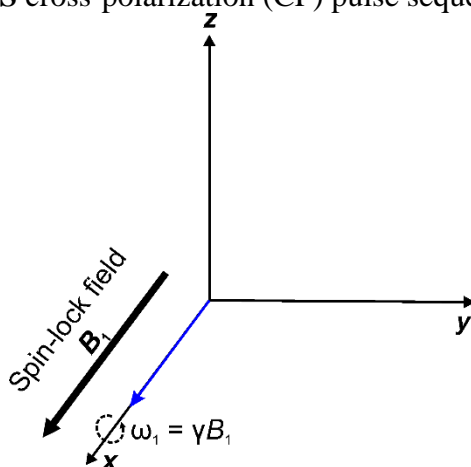


Figure 2.30. The spin-lock field B_1 causing precession about the x -axis at frequency $\omega_1 = \gamma B_1$.

Thus, if a spin-lock is applied simultaneously on both nuclei, the r.f. power of the locking fields can be adjusted to make the precession frequency of both nuclei equal, given by Eq. 2.39:

$$\omega_{1,I} = \gamma_I B_{1,I} + \gamma_S B_{1,S} = \omega_{1,S} \quad \text{Equation. 2.39}$$

This is known as the Hartmann-Hahn matching condition and is a basic requirement for CP to occur. When the Hartmann-Hahn condition is met, it equalizes the energy gaps between the respective rotating-frame up- and down-spin-states of the **I** and **S** spins (Eq.2.39). The dipolar coupling between two spins cannot alter the net energy (or net magnetization) of the spin-system when the spins are quantized on the transverse plane, perpendicular to the z -axis.¹²⁷ Thus the dipolar coupling has to act in such a way that the energy and the angular momentum of the spin-system is conserved. So at the Hartmann-Hahn match, for instance, any transition requiring energy on one spin has to be compensated by an energy releasing transition on the other spin. Thus a redistribution of energy states between the **I** and **S** spins is facilitated via dipolar coupling, without altering the net magnetization of the system. The nature of this redistribution depends on the initial distribution of magnetization in the rotating frame. The initial magnitude of the **I** spin in the rotating frame is the same as the equilibrium state in the laboratory frame, since it was created by a $\pi/2$ pulse on the longitudinal magnetization parallel to static magnetic field \vec{B}_0 . The spin-lock field \vec{B}_{1I} being much weaker than \vec{B}_0 , cannot sustain an equal amount of magnetization, which then reduces via spin-up to spin-down transitions which require energy. Therefore, these transitions are compensated by energy releasing spin-down- to spin-up transitions in spin **S**, ultimately leading to a much larger magnetization on **S** than the initial state. Since this thesis will only

include CP between ^1H and ^{13}C , the spins **I** and **S** will be replaced by ^1H and ^{13}C , respectively, in subsequent discussions.

The contact pulse on ^1H in Fig. 2.29 represents a ramped-CP. The Hartmann-Hahn matching condition can often be very sensitive, and minor missettings in locking powers or instrumental instability can lead to loss of the CP signal. Using a ramped contact pulse reduces this sensitivity by spreading out the matching condition over different power levels.

2.2.12. Relaxation and Molecular Motion

The concepts of longitudinal (T_1) and transverse (T_2) relaxation were introduced briefly in section 2.2.2, but since relaxation analysis forms an important part of this thesis, they require a more detailed discussion.

As discussed briefly in section 2.2.2, relaxation arises from fluctuating local magnetic fields (B_i) at the nucleus, which are caused by thermal motion of the molecules. Consider two nuclear spins within the same molecule which interact with each other through dipolar coupling. As the molecule randomly reorients or tumbles, the magnitude and direction of the local magnetic field exerted by one spin on the other also fluctuates, since the dipolar coupling is dependent on orientation. The CSA is another orientation-dependent source of local magnetic fields, which is affected by motion in the same manner. Thus relaxation processes are inherently connected to molecular motion, and understanding this relationship is key to obtaining invaluable information from relaxation experiments, as shall be seen in Chapters 3, 4, 7 and 8 of this thesis.

Autocorrelation function and correlation time: The fluctuating magnetic field B_t averages to zero over a sufficiently long period of time due to its random nature. Thus, its magnitude is generally considered in terms of its mean square value, defined by Eq, 2.40:

$$\langle B_t^2(t) \rangle \neq 0 \quad \text{Equation 2.40}$$

The time dependence of B_t , or how rapidly the local field fluctuates, can be defined using an autocorrelation function, $\mathbb{G}(\tau)$, given by:

$$\mathbb{G}(\tau) = \langle B_t(t)B_t(t+\tau) \rangle \approx \langle B_t^2(t) \rangle \exp\left(-\frac{|\tau|}{\tau_c}\right) \quad \text{Equation 2.41}$$

where B_t and $B_t(t+\tau)$ are the local field values separated by a time τ . The parameter τ_c is called the correlation time and it provides a measure of the rate of fluctuation: it is small for rapid fluctuations and large for slower fluctuations. The Fourier Transform of the autocorrelation function is a quantity called the spectral density, given by:

$$J(\omega) = \frac{\tau_c}{1+\omega^2\tau_c^2} \quad \text{Equation 2.42}$$

If the local field fluctuates rapidly, the short τ_c makes the spectral density function broad, as shown in Fig. 2.31a, while for slow fluctuations the spectral density function is narrow (Fig. 2.31b).

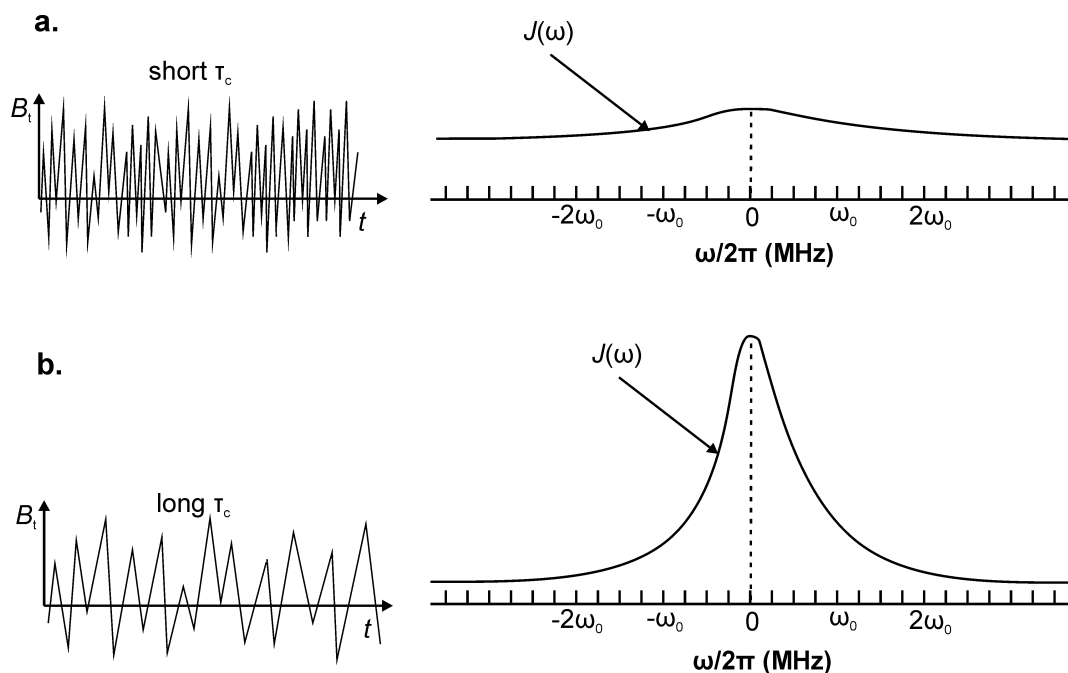


Figure 2.31. Spectral density functions of the local field fluctuating a) rapidly and b) slowly.

For a nucleus such as ^1H , which has a small CSA, a strictly dipolar-coupling induced relaxation mechanism can be assumed. Based on this assumption, the relaxation rates, $1/T_1$ and $1/T_2$, can be written as functions of the spectral density, given by Eq. 2.43 and 2.44.¹²⁶

$$\frac{1}{T_1} = \frac{3}{10} b^2 \{J(\omega_0) + 4J(2\omega_0)\} \quad \text{Equation 2.43}$$

$$\frac{1}{T_2} = \frac{3}{20} b^2 \{3J(0) + 5J(\omega_0) + 2J(2\omega_0)\} \quad \text{Equation 2.44}$$

Here, $J(0)$, $J(\omega_0)$ and $J(2\omega_0)$ are the spectral densities at frequencies 0, ω_0 (Larmor frequency) and $2\omega_0$. Since the spectral density is a function of the correlation time τ_c , T_1 and T_2 can be plotted against τ_c to determine how the relaxation rates are related to motion, as illustrated in Fig. 2.32.

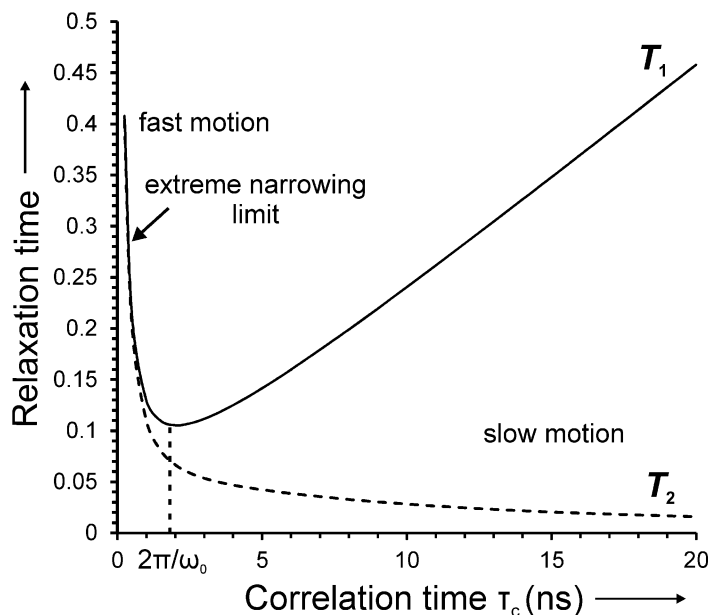


Figure 2.32. Relaxation times plotted against correlation time τ_c . Short τ_c values represent fast molecular motion while longer values indicate slow motion.

The correlation time represents the rate of fluctuation of the local magnetic fields, which in turn depends on the rate of molecular motion. Thus short and long correlation times correspond to fast motion and slow motions, respectively. At very short correlation times, where random isotropic motion dominates, such as small molecules in non-viscous liquids, T_1 and T_2 are of the same order and this is known as the extreme narrowing limit. The T_1/T_2 ratio in this range is ~ 1 . As the molecular motion slows down, due to increasing molecular size, viscosity or other inhibiting interactions, T_1 and T_2 both decrease until T_1 reaches a minimum. The minimum occurs near a correlation time corresponding to the Larmor frequency ω_0 , given by $2\pi/\omega_0$, beyond which the T_1/T_2 ratio increases rapidly. Also, since Larmor frequency is magnetic field dependent, this minimum also depends on the external magnetic field, moving to smaller τ_c values with higher field, closer to the extreme narrowing limit. Thus, performing experiments at higher magnetic fields usually leads to

narrower peaks, improving spectral resolution. On the other hand, relaxation due to CSA would have an opposite effect.

Therefore, if T_1 and T_2 are measured, they can provide information about the molecular dynamics of a system. If the T_1/T_2 ratio is close to unity, the system is mobile, and increasingly rigid as the ratio becomes larger. Measuring T_2 by itself can also provide similar information, since it decreases exponentially with increasing τ_c . However, measuring T_1 by itself is not as fruitful, since two τ_c values can be possible for a single T_1 . Since molecular motion is affected by temperature and concentration, relaxation times are also dependent on these two parameters. Therefore, measuring relaxation times at different concentrations and temperatures can provide important information about the structure and dynamics of a system. The experiments that are used to measure relaxation times are discussed in section 2.3.

2.2.13. Nuclear Overhauser Effect

The Nuclear Overhauser Effect or NOE is a particular form of relaxation phenomenon, closely related to dipolar coupling. In brief, it is defined as the change in intensity of one resonance when another resonance coupled to it is saturated by an r.f pulse. If appreciable NOE is detected between a pair of spins, it indicates a relatively short spatial distance between them ($< 5 \text{ \AA}$). The NOE is independent of the bonding structure of the molecules, and relies on spatial proximities and hence is a powerful tool for characterizing molecular conformations.

The NOE arises from population changes via a form of longitudinal relaxation, called cross-relaxation, facilitated by dipole-dipole coupling (not J -coupling). To understand cross-relaxation, recall that longitudinal relaxation involves exchange of energy between

the nuclear spin-states and the lattice, which represents the different energy levels of the system as a whole. If the population of the high-energy state of a specific spin-transition is higher than the population of the equilibrium state, it will try to restore equilibrium by flipping individual nuclei from their high-energy (spin-down, β) state to low-energy (spin-up, α) state. The energy released by this transition is absorbed by the lattice by increasing the molecular motion of the molecule concerned. The reverse phenomenon occurs when the high-energy state population is lower than the equilibrium population, causing spin-flips in the opposite sense, facilitated by energy released by the lattice through slowing down of molecular motion. For these relaxation processes to occur, the molecular motion must cause fluctuations in the local magnetic field at a frequency corresponding to the energy of the spin-flip. In the instance of dipole-dipole relaxation, the local fluctuating field originates from the magnetic dipoles of neighbouring spins, and therefore creates the possibility of both spins flipping simultaneously, where the lattice absorbs or provides the corresponding energy. When such a synchronized relaxation occurs, it is called a dipole-dipole cross-relaxation.

In the simplest case of a two-spin system **IS**, all the possible nuclear spin transitions are shown in Fig. 2.33, assuming a homonuclear system, which makes the energy difference between the $\alpha\beta$ and $\beta\alpha$ states very small. Suppose that an r.f pulse is used to saturate the **S** spin, i.e. the populations of the $\alpha\alpha$ and $\alpha\beta$ states are equalized, as well the populations of the $\beta\alpha$ and $\beta\beta$ states, through $\alpha \rightarrow \beta$ transitions. This creates a larger population of spins in the high-energy state than what it would be at equilibrium, and therefore, the **S** spin will relax through an excess of high-to-low energy transitions ($\beta \rightarrow \alpha$) to return to equilibrium.

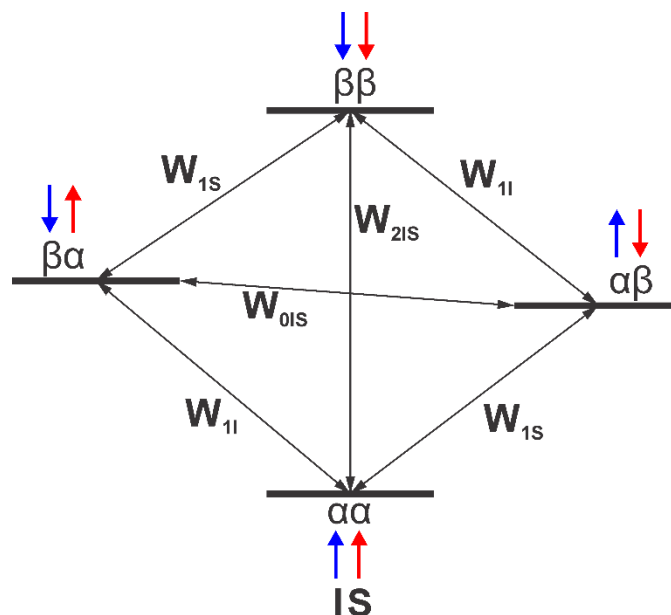


Figure 2.33. Energy levels for a two-spin system **IS** showing the spin-states $\alpha\alpha$, $\alpha\beta$, $\beta\alpha$ and $\beta\beta$, and the transition probabilities W_0 , W_1 and W_2 . The spin-states are written with the first Greek letter representing spin-**I** and the second one representing spin-**S**.

These downward (in energy) spin flips in **S** do not have any impact on the **I** spins if the W_{1S} transitions dominate. For cross-relaxation, where the transition of one spin affects the other, there are two probable transition probabilities, W_{0IS} and W_{2IS} . In the transition characterized by W_2 , both spins flip in the same sense, and to occur, it requires fluctuations in the local field, caused by molecular motion, that correspond to the sum of the frequencies (or energies) of the individual transitions, $\omega_I + \omega_S$. Similarly, in the transition characterized by W_0 , both spins flip, but in the opposite sense, and require local field fluctuations at the difference in frequency between the individual transitions, $\omega_I - \omega_S$. Thus, when the **S** spin flips from a high to low energy state as mentioned above, if there is fluctuating field frequency is sufficient for W_{2IS} transitions, it will also cause the **I** spins to flip in the same sense, thereby increasing the population difference in **I**. Conversely, if the fluctuating field frequency is sufficient for W_{0IS} transitions and not W_{2IS} transitions, the **I** spins flip in the

opposite sense from low to high energy state, reducing its population difference. The population difference between spins in the low (\uparrow) and high (\downarrow) energy states represents the intensity of magnetization. Thus, when the molecular motion is fast, causing high-frequency local field fluctuations, W_2 transitions dominate, causing a net positive NOE enhancement in the intensity of the **I** spin. Similarly, when the fluctuations are small, W_0 dominates and the NOE enhancement is negative, resulting in decrease in the signal intensity. If the number of W_2 and W_0 transitions are equal, no net NOE enhancement occurs since the opposing effects cancel each other.

Therefore in summary, NOE enhancements occur when two nuclei interact with each other through dipolar coupling, and one of them is saturated by an r.f pulse. Whether the enhancement is positive or negative depends on the molecular motion. For small molecules undergoing fast motion, the correlation time $\tau_c \ll 1/\omega$, where ω is the transition frequency, and the NOE enhancement is positive. Conversely, for slow tumbling molecules, $\tau_c \gg 1/\omega$ and the NOE enhancement is negative, resulting in decreased intensity. While it is possible to perform one-dimensional NOE experiments to study molecular conformation, the two-dimensional variant called NOESY (Nuclear Overhauser Effect Spectroscopy) is more convenient and will be used in this thesis. It is described in a later section of this chapter.

2.3. Selected NMR Spectroscopic Experiments

2.3.1. One dimensional ^1H NMR Spectroscopy

^1H or proton NMR spectroscopy is the simplest, and consequently the most widely used solution-state NMR technique for structural analysis of a wide range of chemicals and materials. It is a quick and easy experiment that can be performed in a few minutes and

requires very basic knowledge of NMR methodology on the users' part. A ^1H NMR spectrum covers a small chemical shift range, typically 0-20 ppm, where it provides information on the different types of ^1H containing moieties, which resonate at characteristic chemical shifts. The chemical shifts reflect the chemical environment of the moieties. ^1H NMR spectra also show splitting patterns caused by scalar J -coupling between the ^1H nuclei (J_{HH}) which assist in establishing connectivity among the nuclei and signal assignment. Also, the signals in a ^1H NMR spectrum are proportional to the number of hydrogen nuclei in the sample, provided the experimental parameters are set-up correctly. Hence it can also be used to obtain quantitative information. In highly complex molecules with numerous magnetically inequivalent protons in a large number of chemical environments, such as asphaltenes, the small dispersion in proton chemical shift makes their ^1H spectrum highly crowded with many overlapping signals, leading to heterogeneous broadening. Because of the broad nature of these ^1H spectra, J -coupling information is lost and interpretation of the spectrum becomes difficult. In these cases, one has to resort to deconvolution analysis to make spectral assignments. A drawback of ^1H NMR is that for hydrocarbons, if there are any carbons which do not have attached protons (quaternary carbons), their presence cannot be detected via ^1H NMR spectroscopy alone. Only ^{13}C NMR can detect these carbons.

2.3.2. One dimensional ^{13}C NMR Spectroscopy

Besides ^1H NMR spectroscopy, one dimensional solution-state ^{13}C NMR spectroscopy is the other preferred analytical tool for organic chemists and for characterizing any soluble carbon containing material in general. It is usually more information rich than ^1H NMR

because of the much larger chemical shift dispersion of carbon, i.e. the different carbon moieties are generally better separated on the chemical shift scale, which makes it easier to discern the different chemical environments. However, obtaining a ^{13}C spectrum takes significantly longer because of the low natural abundance of carbon-13 (1.1%) and its low sensitivity (1.59% of ^1H). For example, for the same amount of sample, if it takes only a ten to fifteen minutes to obtain a ^1H spectrum with a good signal to noise ratio (S/N), it can take up to several hours to obtain a ^{13}C spectrum with the same S/N. As a consequence of low natural abundance, splitting due to J -coupling between carbons (J_{CC}) is not generally observed, because the probability of two ^{13}C nuclei occurring adjacent to each other is incredibly low. Moreover, it also makes the T_1 relaxation time of carbon very long, necessitating long recycle delays. Heteronuclear J -coupling between ^1H and ^{13}C (J_{CH}) can however be observed which can complicate the spectrum, unless the ^1H spins are decoupled. A basic pulse-acquire ^{13}C NMR experiment is usually not quantitative because of the nuclear Overhauser effect (NOE) which can enhance the signal from certain carbons while diminishing others. For quantitative solution-state ^{13}C NMR spectroscopy, inverse gated ^1H decoupling is required.¹³⁴

In solid-state NMR spectroscopy, a pulse-acquire type experiment on carbon, with ^1H decoupling, is often called a directly polarized (DP) or single pulse excitation (SPE) experiment. This also requires very long recycle delays, and is only used when quantitative information is required. A technique called cross-polarization (CP), discussed earlier, is usually preferred in the solid state, which reduces experimental time requirements to a large extent.

2.3.3. ^{13}C NMR with inverse gated proton decoupling

Figure 2.34 shows the pulse sequence for a one dimensional ^{13}C NMR experiment with inverse gated decoupling:

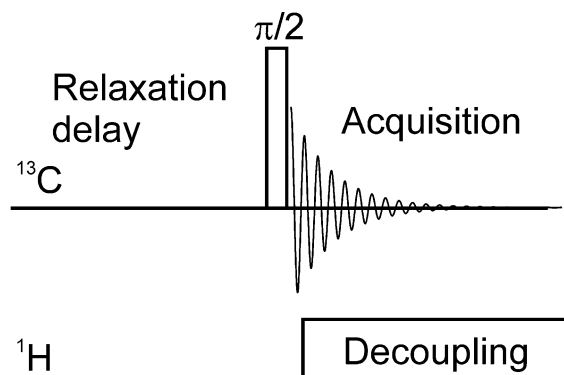


Figure 2.34. Pulse sequence for ^{13}C NMR with inverse gated ^1H decoupling used for quantitative measurements.

In this sequence, the proton decoupling is turned off during the relaxation delay and turned on only during acquisition, as opposed to decoupling being on during the entire sequence. If the decoupling is on during the relaxation delay period, the irradiation of the ^1H nuclei causes enhancement of the carbon signals through NOE and the signal intensities no longer remain proportional to the number of carbons. Turning off the decoupling during this period prevents the enhancement and provides a quantitative ^{13}C NMR spectrum. The solution-state ^{13}C NMR spectra shown in this thesis have been obtained using this sequence, unless stated otherwise.

2.3.4. T_1 and T_2 Relaxation Experiments

Relaxation experiments are very useful and important tools in the NMR armoury, used to investigate molecular dynamics. They provide essential insight into the different mobility regimes within a material. The details of the origins the T_1 and T_2 relaxation mechanisms and what they signify have been covered in detail in the NMR Fundamentals section, hence the discussion here will be restricted to a strictly experimental paradigm.

Spin-lattice or T_1 relaxation: T_1 is a measure of the time taken by the longitudinal magnetization (M_z) to return back to thermal equilibrium after the application of an r.f. pulse. It can be measured both in the solution- and solid-state by the “*Inversion-recovery*” experiment as shown in Fig. 2.35. It involves the application of a π “inversion” pulse which inverts the longitudinal z -magnetization M_z to $-M_z$, followed by a variable delay period τ , which allows the magnetization to recover through spin-lattice relaxation. The sequence is terminated by a $\pi/2$ pulse which rotates the recovered longitudinal z -magnetization to the transverse xy -plane for observation. The delay period is gradually incremented from a very short τ , where the observed signals will be completely inverted or negative, to very long τ values (typically $5-7 \times$ expected T_1) where the signals have fully recovered to their maximum positive value.

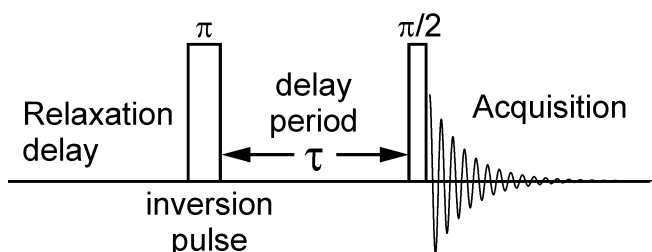


Figure 2.35. Inversion recovery pulse-sequence for measurement of T_1 relaxation time constant.

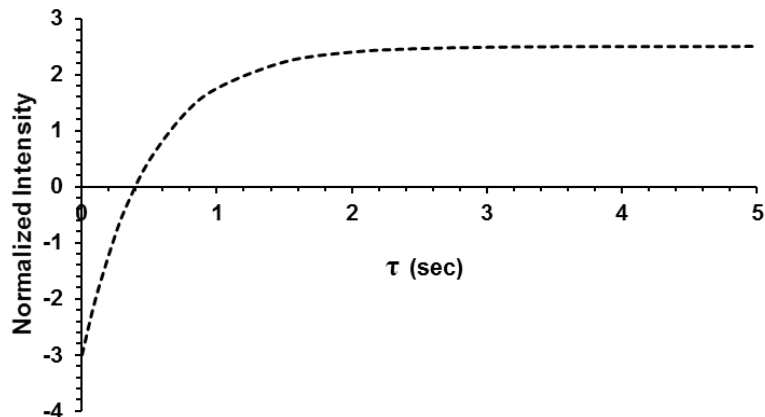


Figure 2.36. Inversion recovery curve for T_1 measurement.

A typical T_1 inversion recovery curve is shown in Figure 2.36. The T_1 can be calculated by fitting this experimental data-curve to Eq. 2.45:

$$M_z(\tau) = M_\infty + (M_0 - M_\infty) \exp\left(-\frac{\tau}{T_1}\right) \quad \text{Equation 2.45}$$

where M_0 is the intensity of the inverted magnetization at $\tau = 0$ and M_∞ is the magnetization at equilibrium.

Spin-spin or T_2 relaxation: The constant T_2 is a measure of the time taken by the transverse magnetization (M_x , M_y) to lose coherence after the pulse applied to create them is turned off. T_2 is usually measured by variations on a pulse sequence called Hahn-echo or spin-echo, which has been discussed in detail in the NMR Fundamentals section. This $\tau/2$ — π -pulse— $\tau/2$ sequence effectively removes or refocuses any dephasing or loss of signal intensity due to chemical shielding or field inhomogeneity, but loss of signal caused by the natural T_2 relaxation process cannot be refocused because it is random in nature. Longer the delay period, greater will be the loss due to transverse relaxation. Hence, a series of spectra at gradually increasing values of τ are recorded and the decay in signal intensity is

plotted as a function of τ (Fig. 2.37). The T_2 can be extracted by fitting it to an exponential function given by Eq. 2.46:

$$M(\tau) = M_0 \exp\left(-\frac{\tau}{T_2}\right) \quad \text{Equation 2.46}$$

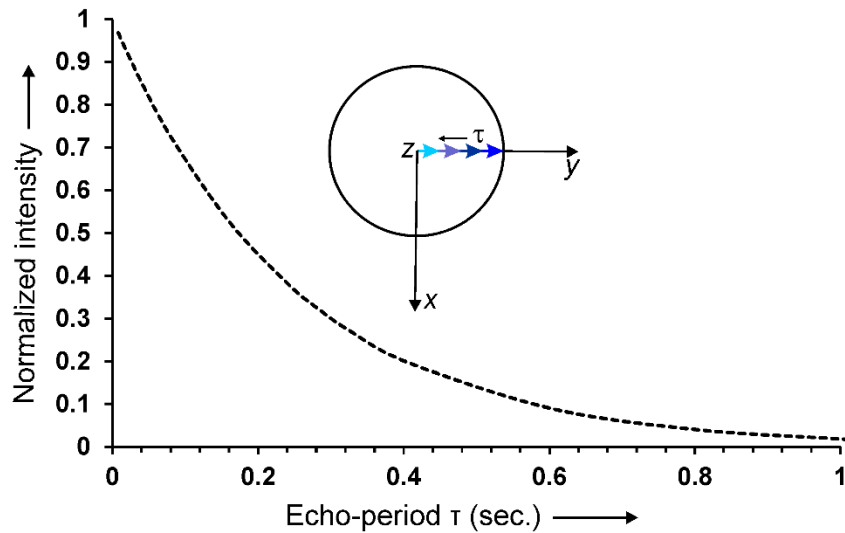


Figure 2.37. The decay of the signal intensity plotted against the delay period τ in a Hahn-echo T_2 relaxation experiment.

More often than not, the decay of the Hahn-echo signal intensity does not follow a mono-exponential decay. In most of these cases, as shall be shown in later chapters, the decay can be fitted with a bi-exponential function containing a short and a long T_2 .

The CPMG sequence: The Hahn-echo experiment just described is inherently sensitive to any refocusing π -pulse imperfections, i.e. when the pulse is not exactly on resonance or not exactly 180° and also inhomogeneity in the magnetic field. These can lead to phase distortions and also loss of signal intensity due to inhomogeneity-induced diffusion. These effects can be minimized by using a modification of the Hahn-echo sequence, called the

Carr-Purcell-Meiboom-Gill (CPMG) echo train.¹³⁵ In this experiment, instead of gradually incrementing the value of τ , it is kept constant at a small value, but the $\tau/2$ — π -pulse— $\tau/2$ ‘echo’ sequence is repeated n times, thereby indirectly incrementing the echo period, as illustrated in Fig. 2.38. The n is always an even integer, to avoid phase distortions and a spectrum is collected for each $n = 2, 4, 6, \dots, n$ ($2n \times \tau/2 > 5-7 \times \text{expected } T_2$) and the exponential decay is plotted and fitted in the same manner as the Hahn-echo sequence to obtain T_2 .

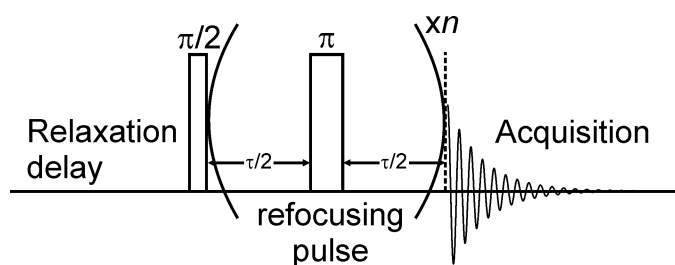


Figure 2.38. The CPMG pulse-sequence for measuring T_2 . The number of times the echo is repeated, n , should be an even integer.

All the solution-state T_2 relaxation measurements in this thesis will employ the CPMG sequence, while solid-state T_2 experiments will be performed using the Hahn-echo sequence because of minimized sample diffusion in solids.

2.3.5. Heteronuclear Single Quantum Coherence Experiments

(Reproduced in part with permission from Dutta Majumdar, R.; Gerken, M.; Mikula, R.; Hazendonk, P. *Energy Fuels* **2013**, *27*, 6528. Copyright 2013 American Chemical Society)

The HSQC (Heteronuclear Single Quantum Coherence) pulse sequence (Fig. 2.39) is an inverse detected (observed via the ^1H nucleus) two-dimensional heteronuclear correlation experiment, where the resulting spectrum has ^1H chemical shifts in one dimension and

chemical shifts of a magnetically active hetero-nucleus such as ^{13}C or ^{15}N in the second dimension (^{13}C in this case). Correlation peaks observed on the 2D-plot therefore have both ^1H and ^{13}C chemical shift values, representing protons and carbons which are connected by a single bond.¹³⁶ A typical two-dimensional experiment constitutes three stages: excitation, evolution or mixing and detection, and is collected as a series of one-dimensional experiments at different evolution periods. HSQC is an inverse detected 2D pulse sequence (Fig. 2.39), i.e. the final detection is done using the ^1H nucleus. In the excitation period of HSQC, the ^1H nucleus is excited and the resulting magnetization is transferred to the ^{13}C nucleus via an INEPT sequence, discussed in the NMR Fundamentals section, after which it is allowed to evolve under ^{13}C chemical shift for a period t_1 , sampling which furnishes the indirect ^{13}C dimension in the final 2D spectrum. The magnetization is again transferred back to the ^1H nucleus via a reverse INEPT sequence for the final detection period t_2 , which provides the direct ^1H dimension. The INEPT transfer consists of a 90° pulse on ^1H , followed by a spin echo period, during which the in-phase ^1H magnetization (I_y) transforms only under the heteronuclear J -coupling into an anti-phase magnetization on ^1H ($I_x S_z$) (see ‘NMR Fundamentals’ section for explanation of *spin-echo*, *in-* and *anti-phase magnetizations*). Subsequently, simultaneous $\pi/2$ -pulses on both channels converts this into an anti-phase term on ^{13}C ($I_x S_z \rightarrow I_z S_y$). The sinusoidal relationship of this transferred magnetization with time is given by $\sin(2\pi J\tau)$, where τ is half the spin-echo period, and is set equal to $1/4J$ for complete conversion of the ^1H magnetization to ^{13}C magnetization.

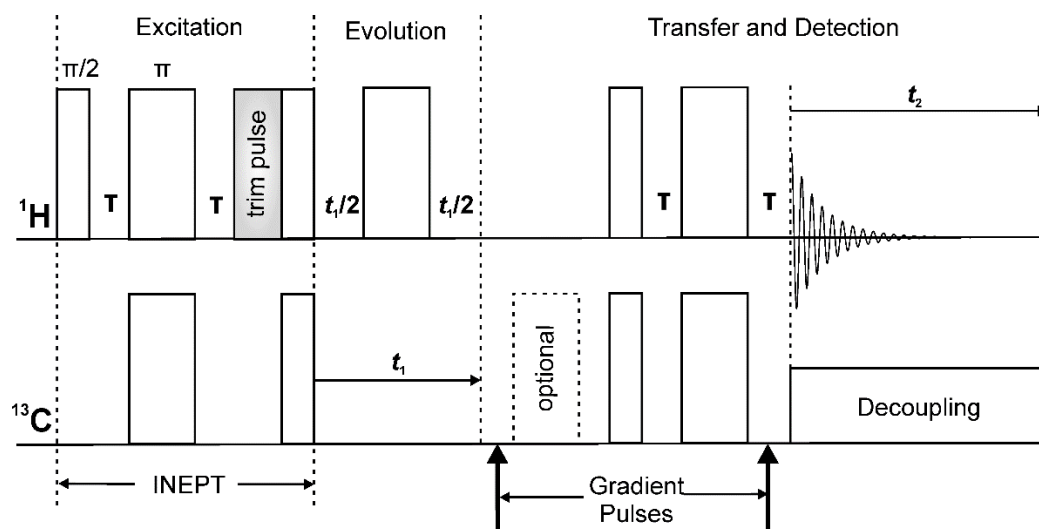


Figure 2.39. The gradient-selected ^1H - ^{13}C HSQC pulse sequence used in Chapter 3. The gradient pulses (vertical arrows), with the optional 180° pulse (shown with broken lines) on ^{13}C , only select a coherence pathway and do not discriminate between multiple and single quantum coherences. An optional 1 ms trim-pulse in ^1H (shaded), used during the excitation (INEPT transfer) period to suppress long-range coherences, was turned off for one of the long-range HSQC experiments. The value of τ is set as $\frac{1}{4J}$ s, where J is the heteronuclear scalar coupling between ^1H and ^{13}C ; t_1 represents the acquisition time in the indirect dimension, while t_2 represents that in the direct dimension. The delay times are not to scale.

It is followed by a period of evolution (t_1) of the magnetization only under the ^{13}C chemical shift (see NMR Fundamentals), which is then transferred back to the ^1H spins by simultaneous $\pi/2$ -pulses on both channels. Another spin-echo period follows, which allows the anti-phase terms to evolve into observable in-phase terms, followed by detection under broadband ^{13}C decoupling. Since in a standard HSQC sequence only the single bond correlations are desired in the final spectrum, typically a ^1H - ^{13}C one bond J -coupling value of 145 Hz is used in most spectrometers for regular molecules, which corresponds to $\tau = 1.72$ ms. The important point to note here is that it is the ^1H magnetizations that are observed in the end. Hence, the strength of the signal is entirely dependent on what fractions of these magnetizations survive for detection at the end of the sequence, which is predicated

on the spin-spin relaxation time (T_2) of the ^1H signals. For a standard HSQC sequence, with $J = 145$ Hz, the total period of evolution is given by $(4\tau + t_1) = (6.88 + t_1)$ ms (neglecting pulse durations). Hence any ^1H signal which does not have a T_2 considerably longer than this period will have very little contribution to the final spectrum. This total evolution period can be reduced by increasing the value of J ($\tau = 1/4J$) or by changing t_1 . The t_1 period represents the acquisition time in the indirect dimension of the spectrum (i.e. ^{13}C). Its value in the spectrometer is set according to the relation $t_1 = TD1/(2*SW)$, where $TD1$ is the number of transients or FID's (free induction decay) recorded in the indirect dimension and SW is the spectral width sampled in the indirect dimension. Hence by reducing the $TD1$ and increasing the SW , the t_1 period can be greatly reduced. For complex systems such as asphaltenes, rapid relaxation limits the time window over which correlations can be built-up, impeding the intensity of the correlations observed. Reducing the t_1 by means mentioned above can solve this problem. Although such a measure would result in a loss of digital resolution ($1/t_1$), it would make it possible to observe signals which are otherwise unobservable, besides allowing for more scans to improve the signal to noise ratio significantly. In Chapter 4, it will be demonstrated how by changing the excitation and evolution periods, single-bond correlations, as well as correlations over multiple bonds can be observed.

Another variation of the HSQC sequence will be used in this thesis, which allows distinction between different $-\text{CH}_n$ moieties. This sequence operates in the same manner as that of the standard HSQC sequence described above, but with a spin-echo period between the evolution period and the final reverse INEPT period, which allows for multiplicity editing based on C-H J -coupling. Essentially, this additional selection step makes the $-\text{CH}_2$ signals opposite in phase to the $-\text{CH}_3$ and $-\text{CH}$ signals in the 2D spectrum.

This HSQC variation is extremely useful in resolving overlapping signals of different multiplicities for complex material, and helps confirm assignments made using one-dimensional spectra and non-selective HSQC described earlier.

2.3.6. ^1H Nuclear Overhauser Effect Spectroscopy (NOESY)

The Nuclear Overhauser effect or NOE was introduced in in section 2.2.13. The NOESY experiment is a two-dimensional homonuclear correlation technique that uses the NOE phenomenon to investigate molecular conformation and spatial proximities of different moieties. The NOESY pulse sequence is shown in Fig. 2.40.

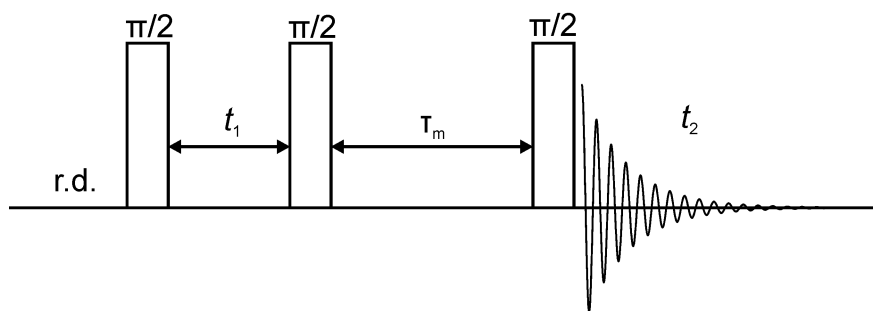


Figure 2.40. The NOESY pulse sequence. (r.d. = recycle delay).

It consists of three $\pi/2$ pulses, separated by two periods of delay, the first of which (t_1) is for furnishing the indirect dimension and the second one is the mixing period τ_m to allow NOE to occur. The mode of operation of the sequence can be explained by considering a system of two isolated protons **I** and **S**, which are not J -coupled to each other. Absence of J -coupling is a valid assumption because in NOESY the protons that are observed are usually removed from each other by several bonds and NOE occurs through dipolar coupling. The first pulse (assuming it to be on the x -axis) transfers the longitudinal

magnetization I_z (and S_z) to the transverse plane ($I_z \rightarrow -I_y$), following which the transverse magnetization evolves under its chemical shift offset as: $-I_y \rightarrow -I_y \cos \omega_I t_1 + I_x \sin \omega_I t_1$. A second x -pulse rotates these magnetizations on to the xz -plane, where they have both longitudinal and transverse components. Therefore, to eliminate any transverse components, this second pulse is phase-cycled (i.e. suitably applied on the other axes in a specific sequence) such that only the longitudinal component I_z remains, labeled by its corresponding frequency as $I_z \cos \omega_I t_1$. The same fate follows the S_z magnetization, which at the end of period t_1 , is frequency labeled as $S_z \cos \omega_S t_1$. Therefore, sampling the t_1 period and subsequent Fourier transform provides the indirect frequency dimension. The next segment in the sequence is called the mixing period, τ_m , during which NOE occurs. At the beginning of this period both the spins have non-equilibrium magnetizations, $I_z \cos \omega_I t_1$ and $S_z \cos \omega_S t_1$, which leads them to cross-relax each other, causing NOE enhancement. Thus at the end of the mixing period, each spin acquires a fraction of the magnetization of the other, given as $(a_I I_z \cos \omega_I t_1 + a_{IS} S_z \cos \omega_S t_1)$ for spin **I** and $(a_S S_z \cos \omega_S t_1 + a_{SI} I_z \cos \omega_I t_1)$ for spin **S**. The coefficients a_{ij} represent the intensity of the magnetizations and depends on the cross-relaxation rate and the mixing time. The final $\pi/2$ -pulse converts these longitudinal magnetizations for observation. In the expressions for the magnetizations at the end of the mixing period, the first terms give rise to the diagonal peaks in the NOESY spectrum (auto-correlation peaks), while the second terms give rise to the cross-peaks. Figure 2.41 shows a schematic diagram for a typical 2D-NOESY spectrum. A horizontal line drawn from the cross-peaks to the diagonal peaks gives the pair of protons that cross relax each other. The intensity and phase of the cross peaks depend on the rate of cross relaxation and the mixing time. These factors in turn depend on the rate of molecular

motion, given by the correlation time τ_c . For a transition frequency ω , which depends on the effective Larmor frequency of the nuclei involved, if the molecular motion is fast enough such that $\omega\tau_c \ll 1$, the cross-peaks are usually of opposite phase to that of the diagonal peaks. Conversely, for slow-tumbling molecules, if $\omega\tau_c \gg 1$, the cross-peaks will be of the same phase as that of the diagonal peaks.

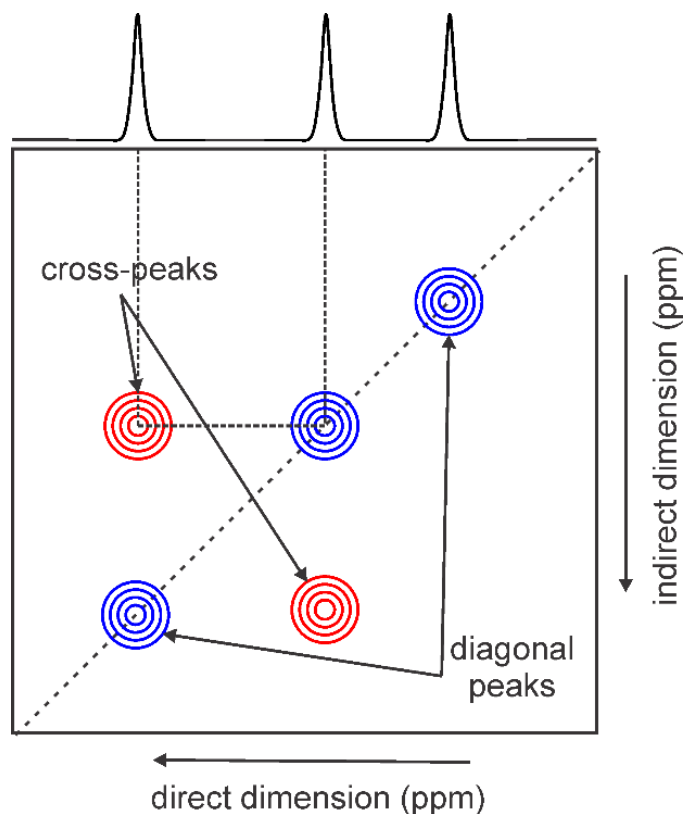


Figure 2.41. A schematic representation of a 2D-NOESY spectrum. The signals of the protons that cross-relax each other give rise to the cross-peaks, which may be of the same or opposite phase with respect to the diagonal peaks, depending on the rate of molecular motion.

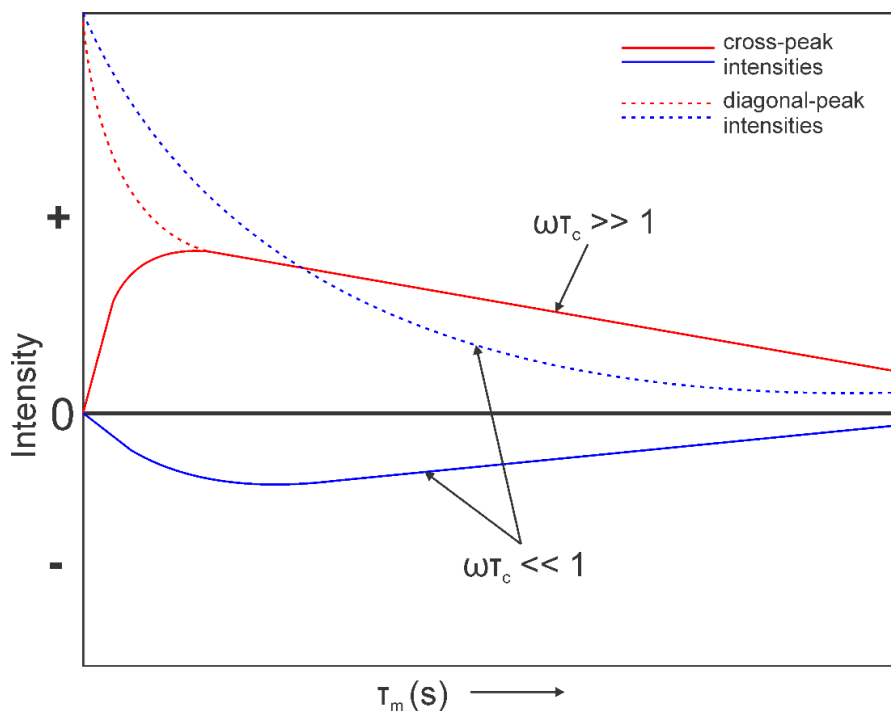


Figure 2.42. Schematic showing the variation of cross-peak and diagonal peak intensities with mixing time τ_m , for slow ($\omega\tau_c \gg 1$) and fast ($\omega\tau_c \ll 1$) molecular motion.

The schematic in Fig. 2.42 shows how the intensity of the cross-peaks and diagonal peaks vary on changing the mixing time. For rapidly tumbling molecules, the negative intensity cross-peaks build-up slowly with increasing mixing time, and then decay slowly due to relaxation, while for rigid, slow-tumbling molecules, the positive cross peaks build up rapidly, followed by a slow decay. The diagonal peaks decay with increasing mixing time, but at different rates depending on the molecular mobility. Thus, the relative phases of the cross-peaks and diagonal peaks are indicators of the motional regime of the molecular species. Positive cross-peaks can also arise from protons that are undergoing chemical exchange with each other but that is beyond the scope of this thesis.

2.3.7. ^1H -to- ^{13}C Cross-Polarization under Magic Angle Spinning (CP-MAS)

Experiments

The concept of cross-polarization (CP) was introduced in the section 2.2.11. All CP experiments in this thesis involve polarization transfer from ^1H to ^{13}C , and are performed under magic angle spinning to improve resolution. A DP experiment on ^{13}C in the solid-state is extremely time consuming, for reasons stated in section 2.2.11. In CP experiments, the time requirements are reduced drastically, because the relaxation delay between scans is based on the ^1H T_1 relaxation, which is much smaller compared to that of ^{13}C , due to strong homonuclear dipolar coupling. Moreover, the ^1H nucleus is four times as sensitive as ^{13}C ($\gamma_{\text{H}}:\gamma_{\text{C}} = 4 : 1$), making the number of scans required for a good signal-to-noise ratio much less. Typically, CP experiments are carried out by first adjusting r.f. pulse powers to establish the Hartmann-Hahn matching condition. Then the CP experiment, shown in Fig. 2.28, is performed at a several different contact times which are gradually incremented from a few microseconds to a few milliseconds. The contact time at which most, if not all, of the signals achieve maximum intensity is used to perform all other CP-based experiments, which will be discussed subsequently. The magnetization build-up, when plotted against contact time, generates the CP build-up curves, as shown in Fig. 2.43. The rate of magnetization build-up depends on the effective strength of heteronuclear dipolar coupling between the carbon in question and its neighbouring protons. The strength of the dipolar coupling is affected by the spatial proximity of the nuclei (^{13}C and ^1H) to each other and by the mobility of the groups involved in the polarization transfer.

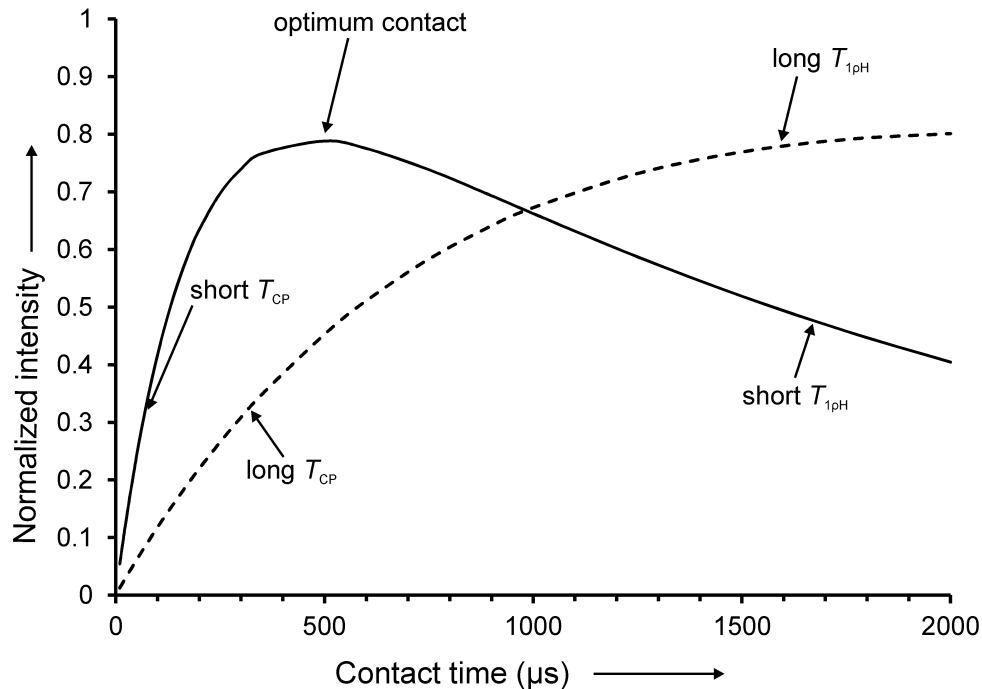


Figure 2.43. Cross-polarization build-up curves for moieties with strong (solid curve) and weak (dashed curve) effective heteronuclear dipolar coupling.

For groups where the effective C-H dipolar coupling is strong, magnetization builds up rapidly and reaches a maximum, beyond which relaxation takes over (*vide infra*) and the signal begins to decay. If the effective coupling is weak, the magnetization builds up slowly, and may take a very long time to reach its maximum value, which also depends on the rate of relaxation. Therefore, if different moieties in a sample have different effective dipolar coupling, it is impossible to obtain a single optimum contact time, which provides signals that reflect a quantitative distribution of these moieties. Hence, it is not advisable to use a single CP-spectrum for quantitative analysis.

Cross-Polarization Models: The build-up of the ^1H to ^{13}C CP magnetization and eventual decay is traditionally described by the two-spin thermodynamic *I-S* model, described by the following equation:¹¹⁶

$$I_t = I_0 \times \lambda^{-1} \times \left(1 - \exp\left(-\frac{\lambda t}{T_{\text{CP}}}\right)\right) \times \exp\left(-\frac{t}{T_{1\rho\text{H}}}\right) \quad \text{Equation 2.47}$$

where I_t is the experimental intensity of the cross-polarized ^{13}C magnetization at a contact time t , I_0 is the equilibrium carbon magnetization and $\lambda = 1 - \frac{T_{\text{CP}}}{T_{1\rho\text{H}}}$. The parameter T_{CP} is the cross-polarization transfer time constant that governs the build-up portion of the CP dynamics curves while the decay part of the curves is governed by $T_{1\rho\text{H}}$ or the rotating-frame spin-lattice relaxation time constant of ^1H (discussed later). In this model the inherent assumption is that the ^1H spin-diffusion through the system occurs fast enough so that all the carbons spins (*S*) are polarized by a single proton spin-bath (*I*).¹¹⁶ All other factors being equal, a shorter ^1H - ^{13}C distance means a stronger dipolar interaction, which facilitates faster magnetization build-up and hence shorter T_{CP} values. The shortest T_{CP} values are usually seen for carbons which have directly attached protons, except highly mobile moieties such as $-\text{CH}_3$ where the dipolar coupling is averaged. T_{CP} can get exceptionally long for carbons which do not have directly attached protons, such as quaternary and carboxylic carbons.

Another cross-polarization model, described by Equation 2.47, allows for two different proton-spin-baths.¹³⁸

$$I_t = I_0 \times \left(1 - \frac{1}{2} \exp\left(-\frac{t}{T_{\text{CP1}}}\right) - \frac{1}{2} \exp\left(-\frac{3t}{2T_{\text{CP2}}}\right) \times \cos\left(\frac{bt}{2}\right)\right) \times \exp\left(-\frac{t}{T_{1\rho\text{H}}}\right) \quad \text{Equation 2.48}$$

All the terms in Eq.2.48 have the same meaning as Eq. 2.47. T_{CP1} and T_{CP2} are the cross-polarization time constants associated with two different ^1H spin-baths (*vide infra*), $b = \frac{\gamma_{\text{H}}\gamma_{\text{C}}\hbar}{2r_{\text{C-H}}^3} \times (3\cos^2\theta - 1)$ is the ^{13}C - ^1H dipolar coupling parameter (in radians/s) which contains the ^1H and ^{13}C gyromagnetic ratios (γ_{H} , γ_{C}), ^1H - ^{13}C distance $r_{\text{C-H}}$ and the chemical shift anisotropy term ($3\cos^2\theta - 1$).

Equation 2.48 represents the I - I^* - S model where two different sized proton spin baths are assumed. The first is the smaller spin bath I^* which is directly coupled to the carbon (S) spin bath of comparable magnitude via dipolar coupling b , and the I^* - S pair exchange magnetization in an oscillatory manner, governed by the $\cos(bt/2)$ term of Eq. 2.48. The larger spin-bath is denoted by I , representing the bulk of the protons at a larger distance from the carbons, which damp the oscillatory exchange through spin-diffusion.¹¹⁶ In other words, T_{CP1} represents the CP mechanism where fast magnetization transfer (short T_{CP1}) occurs between contiguous protons and carbons, with strong dipolar coupling. For quaternary or carboxylic carbons, the dipolar coupling is weaker due to no attached protons, leading to slower CP transfer (long T_{CP1}). The initial magnetization transfer at short contact periods (t) occurs through this mechanism. As the contact period is incremented, a slower CP mechanism, characterized by T_{CP2} , takes over. It is facilitated through energy exchange with the whole ^1H spin-system via proton spin-diffusion, which in turn is predicated on segmental motion within the molecules.^{137,138} Larger segmental motion interferes with spin-diffusion and weakens the effective dipolar coupling, which leads to longer T_{CP2} values. This spin-diffusion mechanism also becomes a lot less effective at “fast” MAS speeds. “Fast” MAS can be defined as speeds which are much faster than the natural ^1H linewidth and can narrow the ^1H signals. Most CP experiments in this thesis were carried

out at 8 kHz MAS, which is small compared to the very broad ^1H solid-state NMR signal of asphaltenes (Chapter 4), thus the spin-diffusion mechanism of polarization transfer can be safely assumed to be effective.

The parameter $T_{1\rho\text{H}}$ represents the relaxation of the ^1H magnetization in the rotating frame, i.e. the relaxation that occurs during the spin-lock period. Therefore, unlike T_1 and T_2 relaxation, the time scale of $T_{1\rho\text{H}}$ is governed by the frequency of the locking pulse, instead of the Larmor frequency. If the $T_{1\rho\text{H}}$ is very short, the onset of decay of the CP signal occurs early, which inhibits further build-up of magnetization. Therefore, a necessary condition for cross-polarization to occur and for these models to apply is given by:

$$T_{1\rho\text{H}} > T_{\text{CP}} \quad \text{Eq. 2.49}$$

The $T_{1\rho\text{H}}$ is also related to molecular motion and can be plotted against the correlation time, as shown in Fig. 2.44. It varies in the same manner as T_1 relaxation, but with the minima determined by the ^1H spin-lock frequency $\omega_{1\text{H}}$. The spin-lock frequency, usually in kHz, is orders of magnitude smaller than the Larmor frequency, which is in MHz. Therefore, the timescale of motion that $T_{1\rho\text{H}}$ operates on is much larger than that of T_1 and T_2 .

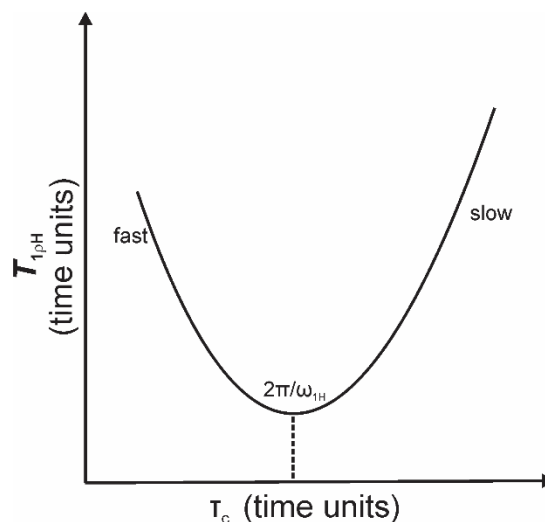


Figure 2.44. The variation of the ^1H spin-lattice relaxation time in the rotating frame ($T_{1\rho H}$) with respect to correlation time. The minima is determined by the ^1H spin-lock frequency ω_{1H} .

2.3.8. CP Dipolar Dephasing

The dipolar dephasing (DD) experiment is a standard technique to suppress protonated carbon signals introduced by Opella and Frey in 1979.¹¹¹ It is a modification of the standard ^1H - ^{13}C CP sequence, with the ^1H decoupling switched off for a variable period, called the dephasing delay (τ_{DD}) after the contact pulse, and switched on again during acquisition, as shown in Fig. 2.45. During τ_{DD} any signal originating from species that are strongly dipolar coupled to protons will decay much more rapidly than those arising from species weakly dipolar coupled to protons. Once MAS removes the orientation dependence, the dipolar coupling interaction between the ^{13}C and ^1H spins is proportional to the dipole-dipole coupling constant b .

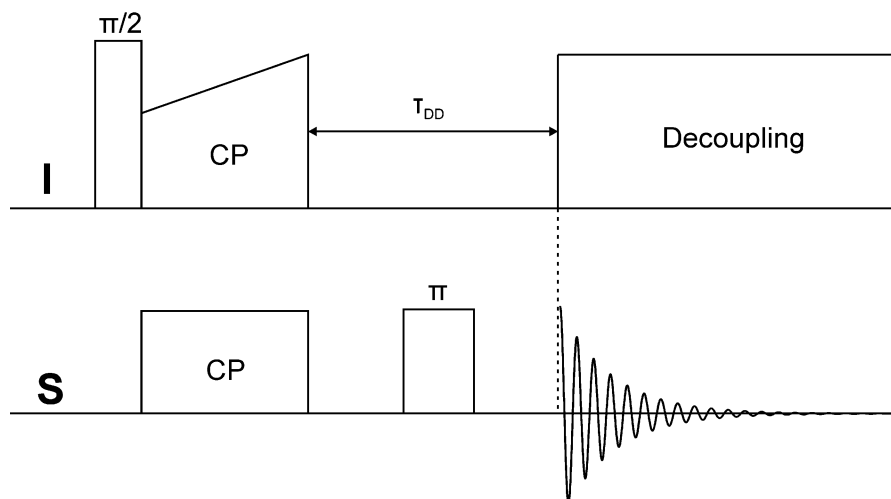


Figure 2.45. The CP-dipolar dephasing pulse sequence.

The effective dipolar coupling (D) is given by the dipole-dipole coupling constant b averaged by the rotational and librational motion of the molecules as:

$$D = \eta b \quad \text{Equation 2.50}$$

where η is the scaling factor, which is a function of the rate and the geometrical parameters that govern the motion. The scaling factor is 0 for rapid isotropic motion and tends to 1 for slow processes. Hence for rigid moieties, the motional averaging is minimum ($\eta \rightarrow 1$) and the coupling is strongly dependent on the internuclear distance. For more mobile groups, the coupling is less sensitive to internuclear distance as it is reduced considerably by motion ($\eta \rightarrow 0$), which is especially true for mobile $-\text{CH}_3$ groups. Usually for slow MAS rates (3 – 6 kHz), dephasing delays of 30 – 50 μs are sufficient to suppress most $-\text{CH}$ and CH_2 signals that have restricted mobility, as the heteronuclear dipolar couplings are still large. Higher spinning speeds reduce the heteronuclear dipolar couplings, thus longer dephasing delays are required. To avoid phase distortions due to chemical shift evolution, when using longer delays, a refocusing 180° pulse is applied to ^{13}C in the centre of the dephasing period.

Besides for spectral editing, this experiment is used to determine the degree of molecular motion, as fast motion greatly reduces dipolar couplings. The decay of the ^{13}C signal over a series of increasing dephasing periods reflects the effective strength of heteronuclear dipolar coupling experienced by the carbon to the nearby protons.

2.3.9. ^1H Dipolar Filter

The dipolar filter (DF) pulse sequence,¹³⁹ shown in Fig. 2.46 is a well-known domain selective technique based on refocusing the homonuclear dipolar coupling interactions and chemical shift anisotropy interactions.

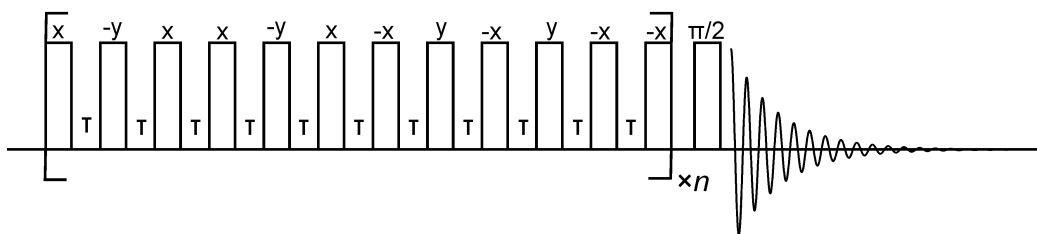


Figure 2.46. The ^1H dipolar filter sequence.

It consists of a train of twelve 90° pulses separated by a variable interpulse delay, followed by a final pulse for observation. The total evolution period is given by: $12n \times (\text{interpulse delay} + 90^\circ \text{ pulse length})$, n being the number of times the pulse-train is looped. The total evolution period determines the effective refocusing timescale and the effective coupling strength that is refocused. For a given interpulse delay, the weak dipolar coupling interactions are refocused more efficiently than the stronger interactions, consequently removing the magnetizations from the rigid domains, leading to selection based on average dipolar coupling strength. The dipolar filtered signal can also be transferred to ^{13}C via CP, if observation through ^{13}C is desired.

2.3.10. ^{13}C CP DIVAM and CP-Refocused DIVAM

The DIVAM (Discrimination Induced by Variable Amplitude Minipulses) pulse sequence was originally designed as a domain selective technique for fluoropolymers.^{140–143} Using this sequence, signals from mobile, disordered domains or rigid, ordered domains can be selected by exploiting differences in their T_2 relaxation rates and dipolar coupling strength. Previously it was used to study hydrogen containing fluoropolymers such as poly(vinylidene fluoride) (PVDF), and polyphosphazenes,^{128,144,145} but not to study complex naturally occurring substances such as asphaltenes. The sequence is shown in Fig. 2.47.

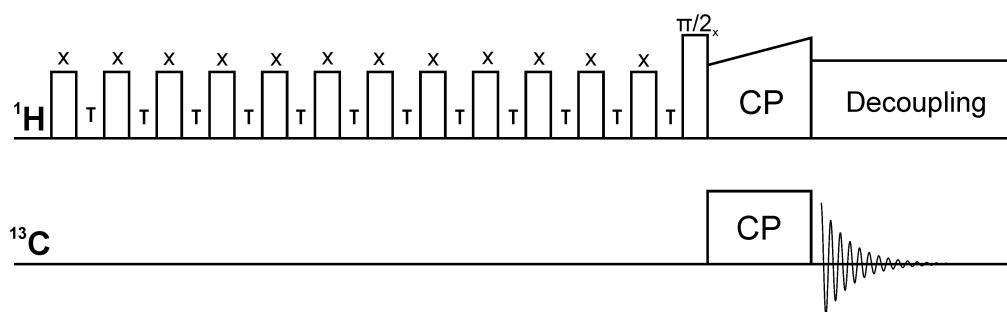


Figure 2.47. The CP-DIVAM pulse sequence.

It is similar to the dipolar filter sequence discussed earlier, but the flip-angle of the pulses in the pulse-train, referred to as the excitation angle, is not constant at $\pi/2$ and their phases are the same. The excitation angle is varied from 0° to 90° in small steps in separate experiments, by changing the pulse r.f. power while keeping the pulse duration constant. Also, while dipolar filter can only select for signals from mobile domains, DIVAM can select for both mobile and rigid domain signals. A simplistic selection mechanism of the DIVAM sequence is illustrated in Fig. 2.48.

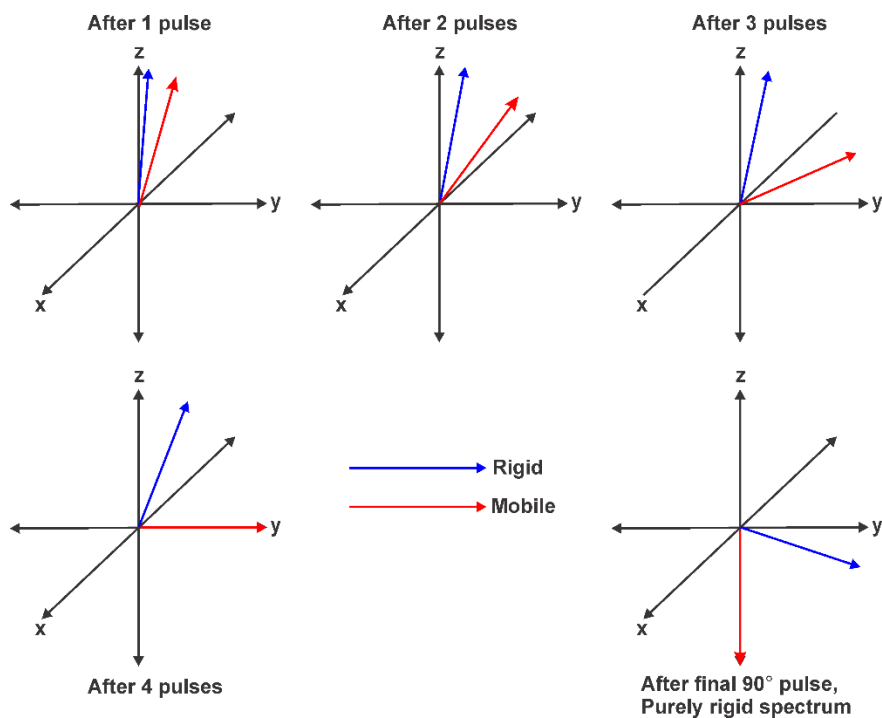


Figure 2.48. Illustration of the selection mechanism of the DIVAM sequence.

The selection of the signals can be thought of as occurring on the basis of transverse relaxation time differences between the rigid and mobile domains. Each DIVAM-train pulse rotates the longitudinal component of each magnetization vector, one from a rigid and one from a mobile domain, slightly into the transverse plane. During the inter-pulse delay period, the transverse component of each signal decays at a different rate: the rigid component has a shorter T_2 and hence decays faster, while the mobile component, with a longer T_2 , decays slower. This results in a difference in the net angle of rotation from the z -axis between the two vectors. After each subsequent pulse and delay cycle, this difference in phase accumulates, and at a certain excitation angle, one of the components is transferred completely to the transverse plane. The mobile component is the first one to meet this fate, and upon application of the final $\pi/2$ pulse, it is transferred to the vertical axis rendering its intensity as null, while the other component is cross-polarized to the ^{13}C nucleus for

observation. This null condition occurs at smaller excitation angles for the signals from more mobile domains, and at larger excitation angles, the signals become negative, null again, positive and so on, creating an oscillatory behaviour in the signal intensity when plotted versus the excitation angles, called a ‘nutaton’ profile. The signals from the more rigid signals attain the null condition at much larger angles, if at all, and therefore, by careful selection of the excitation angle, the signals from components with different mobilities can be separated and selectively observed. The nutation profiles obtained by plotting the signal intensities against the excitation angles are also indicative of the mobilities of the different chemical moieties. The nutation profile of the more mobile groups have their null- or zero-crossing at a much smaller excitation angle and show more pronounced oscillations in intensity, compared to the more rigid groups, where the oscillations are damped. Typical examples of nutation curves are shown in Fig. 2.49.

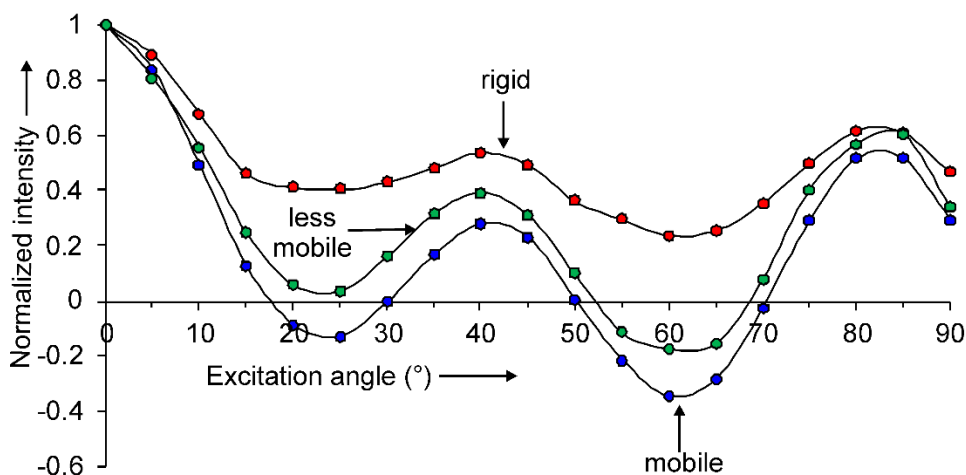


Figure 2.49. DIVAM nutation curves: Normalized signal intensity plotted against the excitation angle.

The refocused DIVAM sequence is similar to the DIVAM sequence, but with added refocusing π -pulses between the minipulses, and an appropriate phase cycle, to remove

coherent dephasing due to heteronuclear coupling and chemical shift evolution. It reduces the phase distortions and offset dependence associated with non-refocused DIVAM, and allows the selection to be governed by T_2 rather than T_2^* .¹⁴⁶ The CP refocused DIVAM sequence is illustrated in Fig. 2.50.

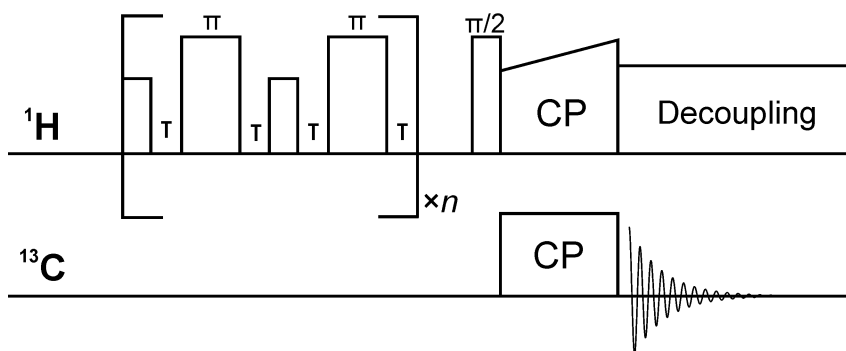


Figure 2.50. The CP refocused DIVAM sequence.

It consists of a repeatable loop of four pulses on the ^1H channel: $2 \times$ low-amplitude ($\leq 90^\circ$) r.f. pulses, $2 \times$ refocusing pulses, separated by interpulse delays of fixed duration. This is followed by a standard ^1H to ^{13}C CP sequence, where the ^1H magnetization remaining after the refocused DIVAM filter is transferred to ^{13}C . It operates according to the same selection mechanism as the non-refocused DIVAM sequence discussed previously, only the refocusing pulses removing the dephasing under coupling interactions and chemical shift evolution. The phase cycling ensures that the final magnetization accumulates in the transverse plane in a manner similar to the DIVAM sequence, and nutation profiles can be obtained in the same way.

In both variations of the DIVAM experiment, although the final observation is done on ^{13}C , since the filtering is performed on the ^1H nucleus, in essence the nutation curves

represent the mobilities of the protons from which the CP is occurring. This will be an important fact to remember while we discuss the nutation curves in later chapters.

2.3.11. ^1H Back-to-Back (BABA) Recoupling Double Quantum Correlation under MAS (DQ-MAS)

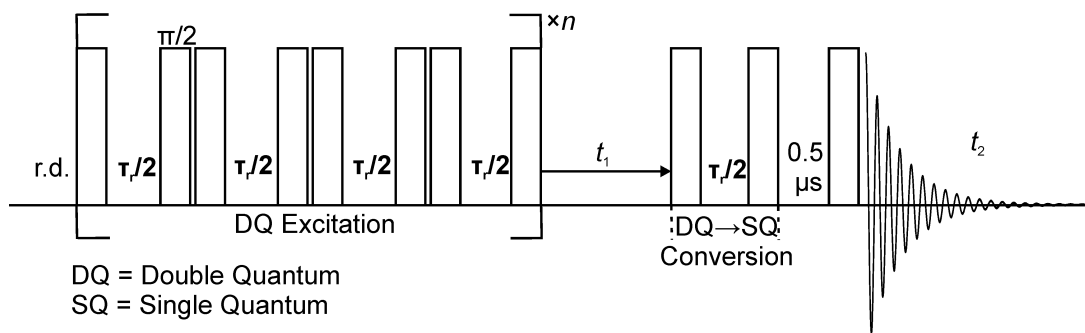


Figure 2.51. The BABA sequence with recoupling for $2n$ rotor periods (τ_r).

The dipolar coupling that is averaged out by MAS can be reintroduced by using recoupling sequences. This reintroduction is necessary in certain cases for the purpose of establishing connectivities within the molecule or to measure internuclear distances. This is particularly true under fast MAS conditions, where the averaging of dipolar coupling is more effective. Recoupling sequences can be used for both homonuclear and heteronuclear cases, but only the homonuclear ^1H - ^1H recoupling is relevant to this thesis.

In the case of ^1H , which has strong homonuclear dipolar coupling, double quantum (DQ) coherences ($I_x S_y$, $I_y S_x$) can be created, which arise from the nuclei that are coupled to each other. Since DQ coherences cannot be detected directly, they have to be converted to single quantum (SQ) coherences (I_x , I_y , S_x , S_y) for observation. A commonly used pulse sequence

for creating DQ coherences is the Back-to-back (BABA)¹⁴⁷ recoupling sequence. The name is derived from the back-to-back $\pi/2$ pulses that are used to excite the homonuclear DQ coherences. The pairs of back-to-back $\pi/2$ pulses are rotor synchronized, such that there is half a rotor period ($\tau_r/2$) between each pair. A rotor period is the inverse of the MAS frequency ω_r . Multiple such pairs of pulses can be used in a BABA sequence, depending on the time, called the mixing time, for which recoupling is desired. Figure 2.51 shows the BABA sequence where recoupling, or DQ excitation, is allowed for at least two rotor periods. This mixing period can be extended if required by looping the block of pulses by integer multiples. Once the DQ coherences are created, they are allowed to evolve for a period t_1 , which is incremented in steps that are integer multiples of the rotor period. Fourier transform of this period provides the indirect dimension of the final 2D plot. Since DQ coherences cannot be detected directly, the final observation is done by converting them to SQ coherences using another pair rotor synchronised $\pi/2$ pulses and a final detection pulse, which provides the direct dimension for the 2D plot. A schematic of a typical DQ-SQ correlation plot is shown in Fig. 2.52. The SQ dimension contains the normal one-dimensional spectrum with signals at their characteristic chemical shifts, while the DQ dimension has chemical shifts that are double that of the SQ dimension. If dipolar coupling exists between two nuclei, say with SQ chemical shifts of δ_1 and δ_3 , it will give rise to two cross peaks at $(\delta_1, \delta_1 + \delta_3)$ and $(\delta_3, \delta_1 + \delta_3)$, the first term being the SQ chemical shift of one of the nuclei and the second term being the sum of the SQ shifts in the DQ dimension.

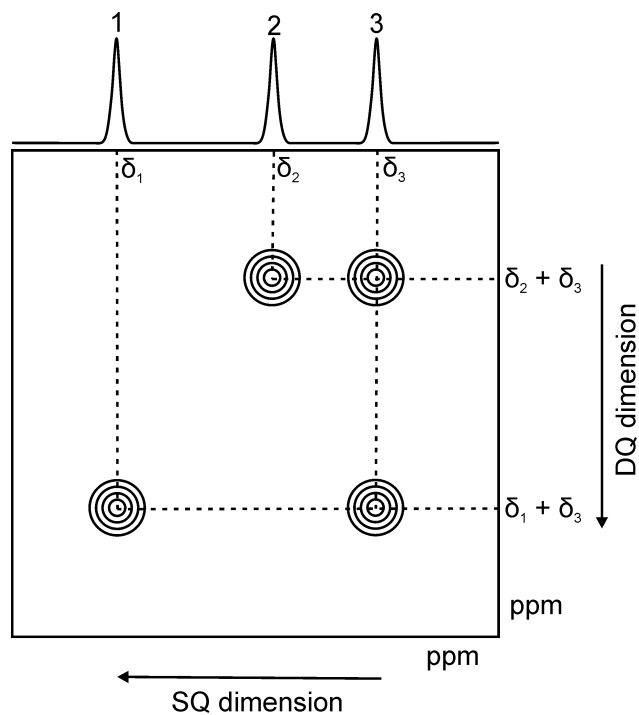


Figure 2.52. Schematic illustration of a Double Quantum MAS (DQMAS) correlation plot.

A correlation peak between two signals indicates spatial proximity of the corresponding nuclei that interact with each other via dipolar coupling. To choose the optimum mixing time, the experiment is often initially performed in one dimension at different mixing times, without incrementing the t_1 evolution period. The intensity is plotted against the mixing time to construct a build-up curve, where the maximum intensity is chosen as the optimum mixing period.

The subsequent chapters will demonstrate how the NMR spectroscopic techniques described in this chapter can be utilized to investigate the structure of asphaltenes from various sources. These techniques by no means cover all the possible NMR spectroscopic methodology that can be employed for the stated purpose, but provide an extensive groundwork upon which further improvements can be made.

CHAPTER 3

3. VALIDATION OF THE YEN-MULLINS MODEL OF ATHABASCA OIL-SANDS ASPHALTENES USING SOLUTION-STATE ^1H NMR RELAXATION AND 2D HSQC SPECTROSCOPY

(Reproduced in part with permission from Dutta Majumdar, R.; Gerken, M.; Mikula, R.; Hazendonk, P. *Energy Fuels* **2013**, *27*, 6528. Copyright 2013 American Chemical Society. First author performed all experiments and corresponding analysis.)

3.1 Overview

This chapter presents the first major study performed for this thesis on asphaltenes derived from Athabasca oil-sands bitumen using solution-state NMR spectroscopy. Solution-state NMR spectroscopy has been essential in developing the current structural motifs for asphaltenes and thus features prominently in the asphaltene literature.^{30,34,35,38,77,81,86–88,102} A detailed review of how the technique has been used for asphaltene characterization is provided in Chapter 1 of this thesis. Here we provide an in-depth ^1H T_1 and T_2 relaxation analysis accompanied by a reexamination of the ^1H and ^{13}C NMR spectral assignments aided by HSQC methods. Relaxation at specific sites in asphaltene molecules will depend strongly on the size of the aromatic core and the arrangement of these molecules in solution. Both of these aspects are markedly different for the two proposed models, island and archipelago and therefore are expected to be instrumental in distinguishing between them. Both ^1H and ^{13}C NMR spectroscopy, coupled with deconvolution analysis of the spectra, have been used to obtain detailed quantitative information, which allowed the calculation of several important structural parameters.

3.2. Experimental details

3.2.1. One-dimensional experiments

The sample for 1D ^1H and ^{13}C NMR spectroscopy was prepared by dissolving 91 mg asphaltene powder in ca. 1 ml deuterated chloroform (CDCl_3). Chromium acetylacetonate [$\text{Cr}(\text{acac})_3$] (40 mg) was added as a paramagnetic relaxation agent to shorten the carbon longitudinal relaxation times (T_1). All NMR spectra were obtained using a Bruker Avance II 300.13 MHz NMR spectrometer, equipped with a two-channel BBFO 5-mm solutions probe. Experiments were carried out at ambient temperature. The ^{13}C NMR spectrum was collected by using a 30° excitation angle, with inverse-gated proton decoupling during acquisition with a recycle delay of 21 s as 6500 scans. A recycle delay of 1 s was used for the ^1H NMR experiment.

3.2.2. HSQC and relaxation experiments

The sample for the initial HSQC experiment to observe short-range correlations (henceforth to be referred to as s-HSQC) was prepared by dissolving 80 mg of the asphaltene in 1 ml toluene- d_8 . The experiment was carried out at 60°C and no relaxation agent was added. An elevated temperature was used as room temperature did not provide the desired resolution for some of the correlations. The sample for the HSQC experiment to observe long-range correlations (henceforth to be referred to as l-HSQC) and the ^1H T_1 and T_2 measurements was prepared by dissolving 60 mg of asphaltene in approximately 1 ml of CDCl_3 , without any relaxation agent. A standard Carr-Purcell-Meiboom-Gill (CPMG)¹³⁵ sequence was used for the T_2 experiments and T_1 were determined via standard inversion recovery methods. For the s-HSQC experiment the sweep widths in both dimensions were optimized to contain just the observable signals (10 ppm for ^1H , 150 ppm

for ^{13}C). The number transients used in the indirect dimension ($TD1$) was 128 where 256 scans were recorded for each. A 1-ms trim-pulse was used in the INEPT period to remove long range couplings. In the 1-HSQC experiments, the ^{13}C sweep width (SW) was changed to 400 ppm (30 kHz) and the number of transients in the indirect dimension was reduced to 32 where 1700 scans were recorded for each. The 1-ms trim pulse was retained for one of the 1-HSQC experiments while it was turned off for the other by setting its duration to 0 ms. The ^{13}C dimension FIDs in both HSQC spectra were zero filled and forward linear predicted to 1024 points to improve the digital resolution.

All chemical shifts were internally referenced with respect to tetramethylsilane (TMS). The deconvolution analysis was done using the MestRenova[®] software (version 6.0.2). Lorentzian lineshapes were maintained and the chemical shifts and the line-widths were adjusted to establish a consistent model where the peak heights were allowed to be optimized by the software until minimum residual error was achieved. The presence of overlapping peaks at 22.8 and 37.3 ppm were confirmed by HSQC.

3.3. Results and discussions

3.3.1. Calculation of structural parameters based on deconvolution analysis of NMR spectra

Elemental analysis of Athabasca oil-sands asphaltene (AOSA) provided the relative distribution of the major elements as following: 78.41% C, 8.47% H, 1.12% N, 8% S and 2% O, which agree closely with reported values.^{34,43,102} Figure 3.1a shows the deconvolved ^{13}C NMR spectrum of AOSA acquired under inverse-gated proton decoupling.

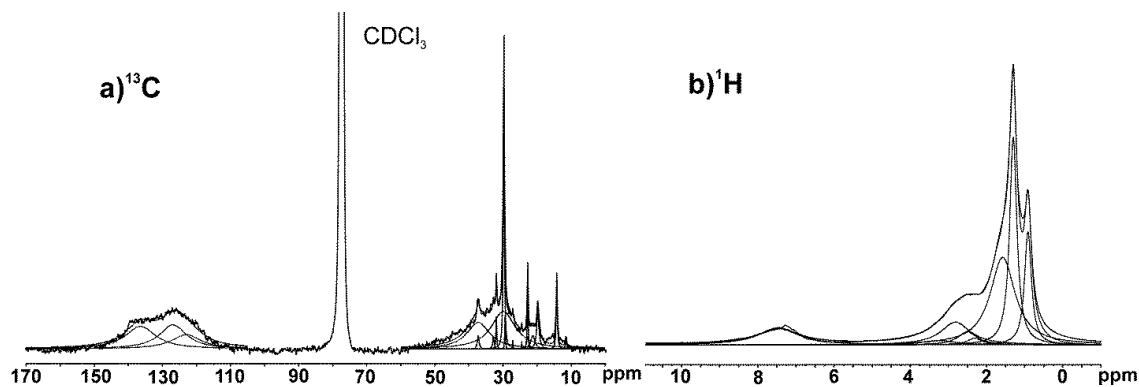


Figure 3.1. Solution-state a) $^{13}\text{C}\{^1\text{H}\}$ and b) ^1H NMR spectra of heptane-extracted AOSA in CDCl_3 , showing the deconvolved peaks. The ^{13}C NMR experiment was carried out with inverse-gated ^1H decoupling to obtain a quantitative spectrum. Detailed assignments for all the deconvolved peaks in the ^{13}C and ^1H spectra are provided in Tables 3.1 and 3.2 respectively.

Detailed assignment for each signal are shown in Table 3.1, where a corresponding model is shown in Figure 3.2 indicating the various carbon sites prescribed by the spectral assignments. The relative contribution from each carbon species were obtained from the peak areas. These distributions were used to compute the number of protons per 100 carbons with the help of Eq. 3.1,

$$\text{H per 100 C} = (3 \times \% \text{CH}_3) + (2 \times \% \text{CH}_2) + \% \text{CH}, \quad \text{Equation 3.1}$$

where $\% \text{CH}_3$, $\% \text{CH}_2$ and $\% \text{CH}$ are the percentages of methyl, methylene and methine (including aromatic $=\text{C}-\text{H}$) carbons present, respectively.

Table 3.1. Chemical shift assignments for the fitted peaks of the ^{13}C NMR spectrum of AOSA.

$\delta\{^{13}\text{C}\}$ (ppm)	Assignment	$\delta\{^{13}\text{C}\}$ (ppm)	Assignment
11.5, 14.2	Terminal (t-) CH_3 on aliphatic chain, at least 3 carbons long.	32.0	CH_2 ' β ' to t- CH_3 or aromatic ring.
19.8	Branched CH_3 , ' β ' or more from end of chain.	32.8	Aliphatic CH.
21.3	CH_3 substituent on aromatic ring.	37.3 ^a	CH_2 or CH ' α ' to aromatic ring, CH_2 ' α ' to branched point in chain.
22.8 ^a	Terminal isobutyl CH_3 . CH_2 ' α ' to t- CH_3 .	122.9	Triple bridgehead quaternary aromatic C.
24.5	Alicyclic CH_2 ' β ' to aromatic ring.	127.0	Aromatic protonated C (CH).
27.2, 29.4, 29.7	Aliphatic chain CH_2 's more than ' α ' or ' β ' to aromatic ring.	136.4	Double bridgehead and substituted quaternary aromatic C.
29.9	Alicyclic CH_2 .		

^a The signals at 22.8 and 37.3 ppm contain contributions from more than one carbon environment as shown by the overlapping fitted peaks in Fig. 3.1a and evidenced by the HSQC spectrum of Fig. 3.4a. The different species of carbons described are illustrated in Fig. 3.2

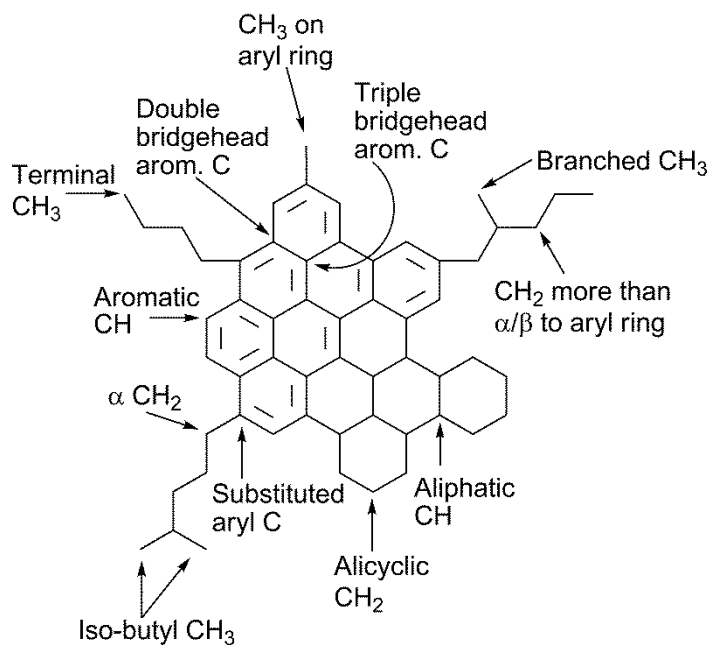


Figure 3.2. Hypothetical asphaltene molecule showing the different carbon species identified by ^1H and ^{13}C NMR spectroscopy, as assigned in Tables 3.1 and 3.2.

Table 3.2. Chemical shift assignments for the fitted peaks of the ^1H NMR spectrum of AOSA.

$\delta\{^1\text{H}\}$ (ppm)	Assignment	$\delta\{^1\text{H}\}$ (ppm)	Assignment
0.9	CH_3 not attached to aromatic rings.	2.8	Aliphatic chain/cyclic CH_2 'α' or 'β' to aromatics
1.3	Aliphatic chain CH_2 .	3.3	CH_2 , CH 'α' to aromatic rings under steric strain.*
1.6	Alicyclic CH_2 .	7.5	Aromatic CH.
2.3, 2.5	CH_3 attached to aromatic rings.		

*See Artok *et al.* (1999)³⁸

To validate the deconvolution model, the calculated H/C ratio (1.33) was compared to the H/C ratio obtained from elemental analysis (1.30). This 97.7% agreement between their H/C ratios suggests that the peak-fitting model and the assignments of the ^{13}C resonances are accurate. Had the peaks been misassigned, the distribution of the various carbon species would have been markedly different and furthermore have predicted the number of protons to deviate as well. For instance, if the number of CH_3 carbons had been overestimated, it would have led to an increase in the overall number of protons and hence an overestimate of the H/C ratio. The corresponding deconvolution analysis and subsequent calculations were carried out on the ^1H NMR spectrum (Fig. 3.1b and Table 3.2). In this case, the percentage of each species of proton was multiplied by the experimental H/C ratio of 1.3, to enable comparison with the corresponding values obtained from the ^{13}C NMR deconvolution analysis. The number of carbons corresponding to each type of proton was also calculated. Since the number of quaternary aromatic carbons cannot be calculated directly from ^1H NMR spectrum, it was obtained by subtracting from 100 the total number of carbons calculated, assuming that there are 100 carbons for every 130 protons (H/C=1.3).

The number of protons and carbons obtained from both the ^{13}C and ^1H NMR spectra are compared in Table 3.3. The values obtained independently from the two spectra show remarkably good agreement in most cases, proving the self-consistency in the deconvolution models. On average, there are 5-6 CH_3 groups per 100 carbons ($C_{3\text{H,al}}$) that are not directly attached to aromatic carbons. Of these, about 2 are branched CH_3 (Fig. 3.2, $\delta\{^{13}\text{C}\} = 19.8$ ppm) and the remaining 3-4 are terminal CH_3 , implying 3-4 non-bridging aliphatic chains (more than 1 carbon long) per 100 carbons. The number of methyl groups attached to aromatic carbon ($C_{3\text{H,ar}}$) is approximately 2 per 100 carbons. Hence, the number of aromatic carbons substituted by non-bridging aliphatic chains is 5 or 6 per 100 carbons. The number of quaternary aromatic carbons ($C_{\text{quat,ar}}$) calculated from ^{13}C NMR spectroscopy is approximately 28, of which 10-11 are triple bridgehead aromatic carbons (junction of three aromatic rings, C_{tb} , $\delta\{^{13}\text{C}\} = 122.9$ ppm). This implies 17-18 quaternary aromatic carbons comprising both substituted (C_{sub}) and double bridgehead aromatic (C_{db}) carbons (since $C_{\text{quat,ar}} = C_{\text{tb}} + C_{\text{db}} + C_{\text{sub}}$), both of which appear in the $\delta\{^{13}\text{C}\} = 136.4$ ppm range.

Table 3.3. Distribution of different carbon species per 100 carbons and their corresponding protons calculated using the areas under the fitted peaks in the ^{13}C and ^1H NMR spectra.

Functionality	From ^{13}C NMR		From ^1H NMR	
	No. of C	No. of H	No. of C	No. of H
All CH_3 not attached to aryl carbon.	4.9 ± 0.1	14.7 ± 0.2	5.3 ± 0.0	15.9 ± 0.0
CH_3 attached to aryl carbon.	1.4 ± 0.1	4.2 ± 0.4	2.5 ± 0.0	7.4 ± 0.0
Aliphatic chain CH_2	25.2 ± 0.0	50.4 ± 0.1	23.9 ± 0.0	47.7 ± 0.0
Alicyclic CH_2	23.2 ± 0.0	46.4 ± 0.1	22.5 ± 0.0	45.0 ± 0.0
Aromatic CH	$16.7^{\text{a}}/13.7^{\text{b}} \pm 0.0$	$16.7^{\text{a}}/13.7^{\text{b}} \pm 0.0$	14.0 ± 0.0	14.0 ± 0.0
Quaternary aromatic C	$28.3^{\text{a}}/31.3^{\text{b}} \pm 0.0$	---	$31.8 \pm 0.0^{\text{c}}$	---

^a Before reassignment of 3 aromatic CH to quaternary carbons.

^b After reassignment.

^c Calculated by difference.

Relative errors were calculated with a 3σ corresponding to 99.7% confidence level, obtained from the residual error (χ^2) in the deconvolution analysis.

Substituted aromatic carbons, (excluding those with attached CH₃) were estimated to be 15 per 100 C by calculating the number of aliphatic carbons ‘ α ’ to aromatic rings ($\delta\{^{13}\text{C}\} = 37.3$ ppm). This leads to approximately three C_{db} carbons, which is disproportionately low compared to C_{tb} (≈ 10), since a $C_{\text{db}}/C_{\text{tb}}$ ratio which is even close to $\frac{3}{10}$ is only possible in a highly pericondensed PAH with more than 36 aromatic rings. This apparent discrepancy is removed by re-assigning three of the $C_{\text{H,ar}}$ groups from the ^{13}C NMR data as C_{db} , making $C_{\text{H,ar}}$ and $C_{\text{quat,ar}}$ obtained from both ^{13}C and ^1H NMR spectroscopy eventually equal (Table 3.3). This re-assignment was done since many of the C_{db} often appear in the $\delta\{^{13}\text{C}\} = 128$ -129 ppm region (e.g. coronene, benzo(e)pyrene), lying in the range of $C_{\text{H,ar}}$. Later it will be discussed that asphaltenes are dominated by pericondensed aromatic cores such as coronene and benzo(e)pyrene which supports this reassignment. Moreover, it turns out that the number of protonated aromatic carbons ($C_{\text{H,ar}}$) obtained from ^{13}C and ^1H NMR spectra differed by three before re-assignment. The double bridgehead aromatic carbons are now approximately 6 per 100 carbons and $C_{\text{H,ar}}$ is 14. The H/C ratio was recalculated as 1.29, which is in better agreement with the elemental analysis at 1.30 than the previously calculated ratio of 1.33. Furthermore, the signal at $\delta\{^{13}\text{C}\} = 37.3$ ppm used to determine C_{sub} is significantly broadened to a linewidth of 608 Hz, implying that aliphatic carbons other than those ‘ α ’ to aromatic rings contribute to it. Hence the value of C_{sub} becomes less than 15, and that of C_{db} ends up being more than 6.

The aromaticity (% aromatic carbon) of the system is 45%, calculated from ^{13}C NMR spectroscopy. It can be broken down as $C_{\text{H,ar}} + C_{\text{quat,ar}}$. Since $C_{\text{H,ar}}$ is 14, $C_{\text{quat,ar}}$ comes out to be 31. With C_{tb} being 10 (Table 3.4), C_{db} and C_{sub} are adjusted so that $C_{\text{db}} + C_{\text{sub}}$ is always 21 ($C_{\text{quat,ar}} = C_{\text{tb}} + C_{\text{db}} + C_{\text{sub}}$), with $C_{\text{db}} \geq 6$ and $C_{\text{sub}} \leq 15$. The number of aromatic carbons

which are substituted by non-bridging aliphatic chains or CH₃ groups is 5 or 6 as discussed previously, setting the lower limit for C_{sub} to 5-6, which is representative of the “island” architecture⁷ with no bridging chains. Since the number of aliphatic chain CH₂ groups ($C_{2\text{H,al}}$) is about 24-25 per 100 carbon (Table 3.3), and in case of the island model the number of non-linking aliphatic chains being 3-4 (not including $C_{3\text{H,ar}}$), the average chain length (L) was calculated to be 6-8. This length is in close agreement with chain lengths reported by Cyr *et al.*³⁴ and Christopher *et al.*⁸⁷ and lies midway of those reported by Andrews *et al.*,³⁰ which show 3-carbon chains on average and a small fraction of 9-carbon chains.

It should be noted that this model does not take into account alicyclic substitutions or bridging aliphatic chains, the inclusion of which would result in the prediction of a higher C_{sub} and lower L . If only the bridging aliphatic chains are considered, each chain corresponding to 2 C_{sub} 's and $6 \leq C_{\text{sub}} \leq 15$, there cannot be more than 4 aliphatic linkages per 100 carbons, making $C_{\text{sub}} \approx 13-14$, when alicyclic rings substituted on aromatic rings are neglected. This structure would give $L \approx 3$. As discussed subsequently, relaxation measurements and the 1-HSQC experiment indicate close association of the alicyclic rings with the aromatic core, thereby reducing the number of possible linking chains. As a large fraction of the carbons are alicyclic (Table 3.3), the number of aliphatic linkages is most likely to be less than 4 per 100 carbons.

Table 3.4. Average structural parameters for AOSA with distributions per 100 carbons and per PAH obtained using NMR spectroscopy and elemental analysis.

Structural parameter	Value for AOSA
Carbon aromaticity (%)	45
Carbon aliphaticity (%)	55
Aromatic rings per PAH	6-7
Clusters per 100 C	2
Aromatic CH per 100 C ($C_{H,ar}$)	14
Aromatic CH per PAH	7
Triple bridgehead carbons per 100 C (C_{tb})	10-11
Triple bridgehead carbons per PAH	5-5.5
Substituted aromatic + double bridgehead aromatic carbon per 100 C ($C_{sub} + C_{db}$)	21
Substituted aromatic + double bridgehead aromatic carbon per PAH	10.5
Total aromatic carbons per PAH	22.5
Free aliphatic chains more than one carbon long per 100 C	3-4
Free aliphatic chains more than one carbon long per PAH	1.5-2
Methyl groups substituted on aromatic ring per 100 C ($C_{3H,ar}$)	2
Methyl groups substituted on aromatic ring per PAH	1
Carbons per aliphatic chain (L)	3-8
Alicyclic carbons per 100 C	23
Alicyclic carbons per PAH	11.5
Nitrogen atoms per 100 C	1.22
Nitrogen atoms per PAH	0.61
Sulfur atoms per 100 C	3.8
Sulfur atoms per PAH	1.9
Oxygen atoms per 100 C	1.9
Oxygen atoms per PAH	0.9
Average molar mass of PAH	719.37 g/mol
Average molar mass per 100 C	1438.74 g/mol

3.3.2. T_2 and T_1 relaxation measurements

The transverse relaxation time constants (T_2) for the peaks in the ^1H NMR spectrum of AOSA are listed in Table 3.5.

Table 3.5. Transverse (T_2) and longitudinal (T_1) relaxation times for the ^1H NMR peaks. The values in parentheses represent the percentage of protons having the corresponding T_2 .

$\delta\{^1\text{H}\}$ (ppm)	Assignment	T_2 (ms)	T_1 (s)
0.9	CH_3 not attached to aromatic rings.	33.3 (11.6%), 84.7 (88.4%)	0.73, 2.50
1.3	Aliphatic chain CH_2 .	31.8 (9.7%), 59.5 (90.3%)	0.59, 1.50
1.6	Alicyclic CH_2 .	24.9 (21.5%), 86.9 (78.5%)	0.35, 5.00
2.5	CH_3 attached to aromatic rings.	64.9	0.55, 7.10
2.8	Aliphatic chain/cyclic CH_2 'α' or 'β' to aromatics.	24.4	0.42, 7.70
7.5	Aromatic CH.	30.9 (15.6%), 75.2 (84.4%)	0.69, 2.90

Simply speaking, short T_2 's reflect a rigid molecular structure, while long T_2 's indicate higher mobility. Each of the signals at $\delta\{^1\text{H}\} = 0.9, 1.3, 1.6$ and 7.5 ppm exhibit bi-exponential transverse relaxation behavior, with one long and one short T_2 component, indicating that these protons exist in sites with disparate mobilities. The aliphatic chain CH_3 signals at 0.9 ppm are expected to be mobile, with a T_2 of 84.7 ms. The shorter T_2 of 33.3 ms would thus arise from CH_3 groups with some restriction in their motion, which would be steric in origin when explained in terms of the Yen-Mullins model.^{7,42} This model proposes that island-type asphaltene molecules form nanoaggregates (<10 aggregation number) via disordered aromatic stacking at concentrations higher than the critical

nanoaggregate concentration (CNAC) which is 0.05-0.10 g/L in toluene. At concentrations higher than 2-5 g/L (critical cluster concentration, CCC),⁷ these nanoaggregates form clusters, bringing many of the peripheral aliphatic chains in close proximity (see Figure 1 in reference 7). The sample used in the T_2 measurements had a concentration of 60 g/L, much higher than the CCC, hence clusters are formed. The aliphatic CH_3 groups which are located on the inside, or bulk, of the cluster will therefore exhibit restricted motion and hence have a shortened T_2 . The CH_3 groups on the periphery of the cluster will be much less restricted in their mobility, hence possessing longer T_2 's. A similar argument applies for the chain CH_2 groups at $\delta\{^1\text{H}\} = 1.3$ ppm, with T_2 values of 59.5 and 31.8 ms. The peripheral CH_2 groups with 59.5 ms T_2 are less mobile than the peripheral CH_3 groups, indicating short aliphatic chain lengths, since CH_2 groups longer chains would have higher mobility.

The long and short T_2 of the alicyclic proton at $\delta\{^1\text{H}\} = 1.6$ ppm is explained in terms of the aforementioned disordered aromatic stacking. If the alicyclic rings are condensed with the aromatic core, they can have two possible conformations with respect to the stacked nanoaggregate, one where they lie inside the stacked core and one where they are on the periphery, as illustrated in Fig. 3.3. Those on the inside will have significantly reduced mobility compared to those on the periphery, hence will have much shorter T_2 's of 24.9 ms, in comparison to the more mobile ones at 86.9 ms. The CH_3 groups attached to aromatic rings have T_2 's at 59.8 ms comparable to the peripheral CH_2 groups at 59.5 ms, indicating that both the moieties lie in the same motional regime. The $\delta\{^1\text{H}\} = 2.8$ ppm signal assigned to CH_2 groups α to aromatic rings has 23.4 ms T_2 , which is very close to that of the rigid alicyclic protons, suggesting that most of these methylene groups are alicyclic in nature, lying inside the stacked core as described previously.

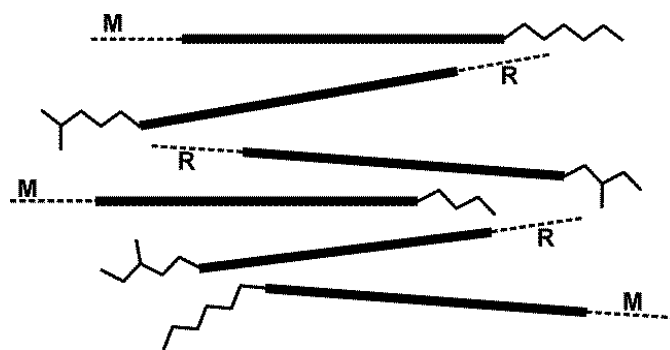


Figure 3.3. Schematic showing the side view of an asphaltene nanoaggregate formed in solution by disordered aromatic stacking. The thick lines represent the aromatic core while the thinner dashed lines represent the condensed alicyclic rings. The alicyclics labeled ‘**R**’ (Rigid) lie within the stacked core and highly rigid with a 24.9 ms T_2 . The ones labeled ‘**M**’ (Mobile) lie on the periphery of the nanoaggregate and have much higher mobility with a T_2 of 86.9 ms.

Short T_2 's (30.9 ms) for the presumably rigid aromatic protons are expected, but to explain the longer T_2 at 75.2 ms, a better appreciation of the relationship between T_2 , T_1 and correlation time (τ_c) is required. In brief, correlation times, τ_c , are a measure of the timescale of motion of molecules and are loosely defined as the time required for a molecule to change its orientation over a given angle. When the frequency of reorientational motion (given by $1/\tau_c$) exceeds the Larmor frequency (ω_0), it is said to be in the fast motion regime where the correlation time, $\tau_c < \frac{1}{\omega_0}$, is considered to be short. Conversely, when the frequency of reorientational motion is significantly slower than ω_0 , it's considered to be in the slow motion regime where $\tau_c > \frac{1}{\omega_0}$ (refer to the Relaxation section in Chapter 2 for details). The trends in T_1 and T_2 are similar in the fast motion regime where they gradually decrease with increasing τ_c ,¹⁴⁸ however they diverge upon entering the slow motion regime, where T_1 gradually increases while T_2 decreases asymptotically. Hence

when the T_1 is orders of magnitude larger than T_2 , the slow-motion regime applies, which was found to be the case for asphaltenes (Table 3.5). The longer T_2 and shorter T_1 values in Table 3.5 represent sites that are less rigid than their shorter and longer counterparts, respectively. The aromatic protons with 75.2 ms T_2 and 0.69 s T_1 therefore belong to the nanoaggregates which are on the periphery of the clusters, making them relatively less rigid than the aromatic protons belonging to nanoaggregates at the center of the clusters, with 30.9 ms T_2 and 2.90 s T_1 . Moreover, the T_1/T_2 ratio provides an estimate of timescale of motion. Considering a purely dipolar relaxation model and neglecting chemical shift anisotropy contributions, at very short τ_c (0.001 – 1.0 ns), *i.e.* when the reorientational motion is very fast (small molecules in low-viscosity liquids), T_1/T_2 approaches unity, and in the case of ^1H , the Larmor timescale is 3.3 ns, where T_1/T_2 approaches 2. The T_1/T_2 ratios calculated for asphaltenes range between 4 and 200, which correspond to correlation times between 6 and 52 ns, which are two to three orders of magnitude slower than small molecules. This shows that rather than being simple isolated units, asphaltene molecules behave as clusters which imposes a high degree of restriction on their reorientational motion, which is supportive of the island model.

Estimates of the relative percentages of the rigid and mobile components of each signal were made by using the bi-exponential behavior of T_2 decay curves and are listed within parentheses in Table 3.5. These percentages are indicative of the geometry and size of the nanoaggregates and their clusters. The low percentage of rigid aliphatic methyl and methylene groups (11.6 and 9.7%, respectively) indicates that majority of the aliphatic chains remain on the periphery of the clusters. This in turn implies that the clusters are made up of a small number of nanoaggregates, which is consistent with 15.6% (~1 in 6) of the nanoaggregates making up the interior of the clusters. Therefore the number of

nanoaggregates per cluster can be predicted as 6 to 7, where the peripheral nanoaggregates have a higher mobility than the internal ones. Furthermore, a relatively higher percentage of rigid alicyclic groups (21.5%) compared to rigid chain aliphatics (9-12%) is indicative of the cyclic groups being more closely associated with the aromatic core.

3.3.3. HSQC NMR spectroscopy

The mode of operation of the HSQC experiment and the related concepts have been explained in detail in Chapter 2. Normally, the excitation period in the sequence is optimized to observe single-bond correlations in small molecules, but for a complex system such as asphaltenes, rapid relaxation limits the time window over which correlations can be built-up, impeding the intensity of the correlations observed. For the current study, the sequence was optimized by changing the excitation and evolution periods, to observe single-bond correlations (to be referred to as s-HSQC), as well as long-range correlations over multiple bonds (to be referred to as l-HSQC), as described below.

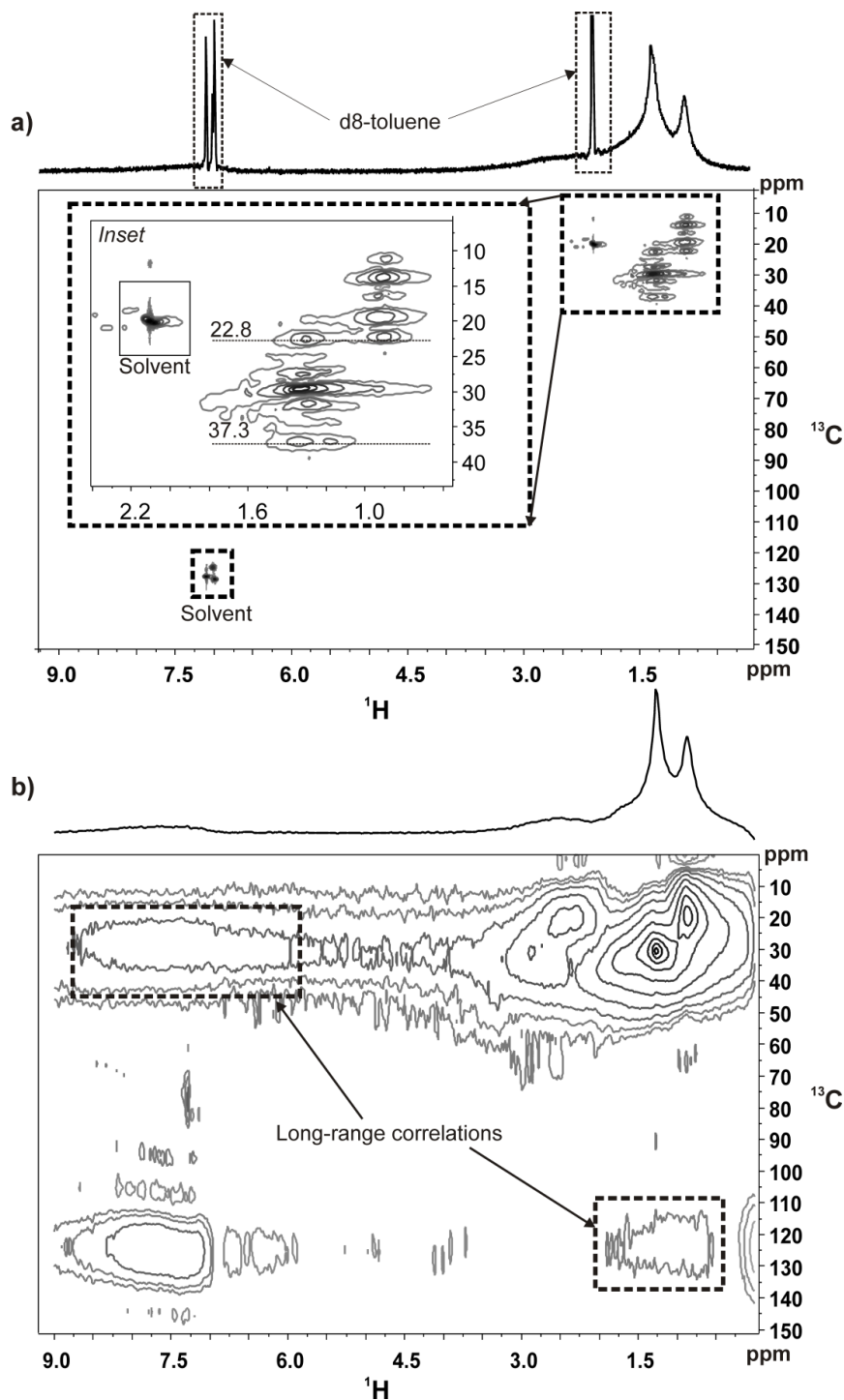


Figure 3.4. ^1H - ^{13}C HSQC NMR spectra of heptane extracted AOSA. Acquired with (a) ^{13}C SW=150 ppm, TD1=128 and 256 scans, (b) ^{13}C SW=400 ppm, TD1=32 and 1700 scans. The 1 -ms trim pulse was on for both. Experiment (a) was done at 60 °C in d_8 -toluene while (b) was done at r.t. in CDCl_3 . (a) *Inset*: Magnification of the aliphatic region, showing the signals (22.8 and 37.3 ppm ^{13}C dimension) which contain overlapping peaks in the 1D ^{13}C NMR spectrum. Aliphatic-aromatic long-range correlations are highlighted (dashed boxes) in (b).

The ^1H - ^{13}C s-HSQC spectrum is shown in Fig. 3.4a, with an expansion of the aliphatic region in the inset. Well-resolved aliphatic (CH_3 , CH_2 , CH) ^1H -to- ^{13}C single-bond correlations were observed. The correlations arising from the toluene- d_8 are marked as solvent. Unfortunately these solvent signals overlap with some of the asphaltene correlations in both the aliphatic and aromatic region, which were well-resolved in CDCl_3 where the correlations are clearly visible in the 1-HSQC (Fig. 3.4b). No correlations between aromatics and aliphatics are seen, hence, any useful information derived from these connectivities between the aromatic core and the aliphatics is lost. Nonetheless, these correlations proved to be invaluable in carrying out the deconvolution analysis, validating the model, as it distinguished overlapping signals such as those at $\delta\{^{13}\text{C}\} = 22.8$ and 37.3 ppm. The signal at $\delta\{^{13}\text{C}\} = 22.8$ ppm contains contributions from two carbon types: terminal isobutyl CH_3 and CH_2 that are α to terminal CH_3 . The signals at $\delta\{^{13}\text{C}\} = 37.3$ ppm consists of rigid CH_2 groups α to aromatic rings and the comparatively mobile CH_2 groups α to branched points in a chain. The correlations also helped to validate these assignments since the ^1H and ^{13}C chemical shifts of any particular moiety could be verified. Assignments in literature were based solely on the 1D ^{13}C NMR spectrum^{38,43} and were verified via their ^1H chemical shifts. The broadness of the strongest correlation at $\delta\{^{13}\text{C}\} = 29$ ppm indicates that this aliphatic CH_2 signal consists of a rigid (broad) and a mobile (narrow) component, which was subsequently used in the deconvolution analysis.

The absence of aromatic-aliphatic correlations in Fig. 3.4a, however, does not imply that such connectivities are absent in the asphaltene molecules. Any aromatic-aliphatic heteronuclear correlation results from multiple-bond, 2J or 3J C-H couplings. The intensity of the magnetization transferred from ^1H to ^{13}C in the INEPT transfer segment of the HSQC sequence is modulated as $\sin(2\pi J\tau)$,¹³⁶ where J is the heteronuclear scalar-coupling

constant in Hz and 2τ is the total transfer period. Hence the ^1H - ^{13}C single-bond correlations with stronger J coupling (typically 145 Hz) build up magnetization much faster than the weakly coupled (0-60 Hz) multiple (2-3) bond correlations, as illustrated in Fig. 3.5a. For the typical J value, $\tau = 1/4J$ gives the maximum transfer efficiency. In a routine HSQC experiment, as in the s-HSQC, $\tau = 1.72$ ms is used, corresponding to $J = 145$ Hz, because only single-bond correlations are desired. At this short value of τ , the multiple-bond correlations are much weaker, as evident from Fig. 3.5a.

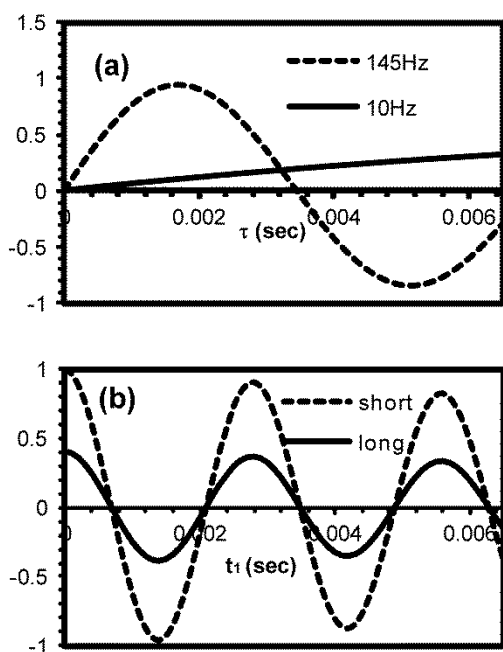


Figure 3.5. Figure demonstrating (a) modulation of the intensity of magnetization transfer by ^1H - ^{13}C J -coupling as a function of the INEPT transfer period (τ), (b) modulation of the short and long range correlations after magnetization transfer as a function of the acquisition period in the indirect (^{13}C) dimension. The short and long range correlations correspond to 145 Hz and 10 Hz J -coupling respectively of (a).

Moreover, a 1-ms trim-pulse on ^1H during the INEPT transfer is implemented to remove long-range effects. The INEPT period is followed by a period of evolution t_1 where the coherences are labeled by their corresponding ^{13}C chemical shift, providing the ^{13}C

dimension in the spectrum. The intensity of magnetization in this period is modulated as $\cos(\Omega_C t_1)$, where Ω_C is the carbon chemical shift offset in Hz and transverse (T_2) relaxation is also in effect which leads to gradual decay as illustrated in Fig. 3.5b. Gradient pulses are used at this stage to generate a spectrum with absorption mode line shapes by proper coherence pathway selection.¹⁴⁹ It is clear from Fig. 3.5b that if t_1 is sufficiently long, the long-range correlations are hardly detectable, while the short range ones still have appreciable intensity. Also, the shorter the T_2 of a signal is, the faster it will decay. Hence, to observe the long-range correlations, the t_1 needs to be shortened such that the long range correlations can be observed at or close to their maximum intensity. This can be done by reducing $TD1$ (number of increments in the indirect dimension) and increasing SW (^{13}C sweep width) since $t_1 = TD1/(2*SW)$. However, the effect of the aforementioned 1-ms trim-pulse should not be overlooked. If it is efficient, then it should ideally remove all long-range coupling effects, and no aromatic-aliphatic correlations should be observable. To test this, two separate 1-HSQC experiments were carried out, one with (Fig. 3.4b) and one without the trim pulse (Fig. 3.6). The t_1 of 6 ms used for the s-HSQC experiment was reduced to 0.5 ms for 1-HSQC, which reduces the digital resolution due to a smaller $TD1$ but a much higher number of scans were recorded to increase the signal-to-noise ratio. Now, the total evolution period ($4\tau + \text{trim-pulse} + t_1$, not considering the gradient pulses) for the 1-HSQC sequences with and without the trim pulse are 8.38 and 7.38 ms, respectively, which are much lower than the T_2 values reported earlier (shortest $T_2 = 24.4$ ms). The same for the s-HSQC sequence with the trim-pulse was 13.9 ms. Using these modified parameters, it was observed that both the 1-HSQC sequences, with and without the trim-pulse, give very similar spectra, both showing long-range aromatic-aliphatic correlations. The trim-pulse omitted 1-HSQC spectrum shows slightly more intense long-

range correlations than the one where the trim pulse was retained (Fig. 3.4b), showing that the trim-pulse does filter out some of the long-range heteronuclear couplings, but not efficiently enough.

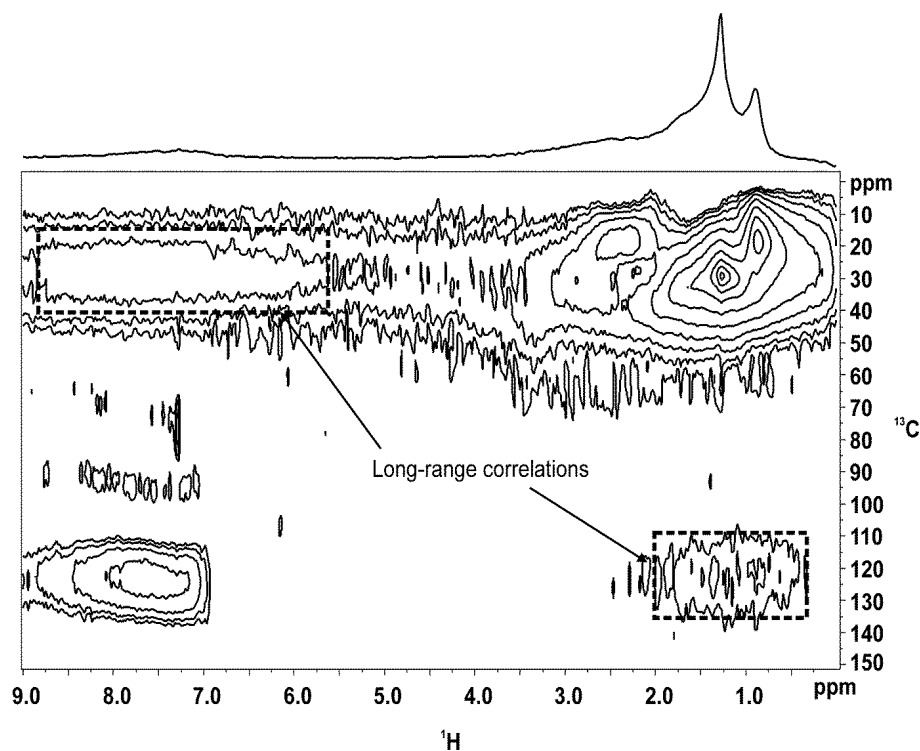


Figure 3.6. ^1H - ^{13}C HSQC NMR spectra of heptane extracted AOSA. Acquired with ^{13}C SW=400 ppm, TD1=32 and 1700 scans. The 1 ms trim-pulse of the HSQC sequence was switched off for this experiment. The long-range correlations are more intense than the same experiment with the trim-pulse on, as shown in Fig. 3.4b.

These correlations are not observed in the s-HSQC experiment due to its longer evolution period, where the long-range signals are dephased. The evolution period t_1 is longer because of higher number of increments and a shorter sweep-width. Thus, rather than the trim-pulse, it is largely the acquisition time in the indirect dimension that determines which signals survive the sequence to be detected.

The above discussion shows that the effective long-range (2J , 3J) C-H couplings between the aromatic core and aliphatic substituents are significantly stronger than what is

found in regular, well defined molecules.¹⁵⁰ It is already established that all segments of asphaltene molecules lie in the slow motion regime, among which some segments are structurally more rigid than others. The structural rigidity inhibiting the motional averaging of heteronuclear dipolar couplings and ¹H spin-diffusion between proximal segments of the molecules make the effective coupling stronger than standard long-range scalar couplings, the effect being more pronounced for the more rigid segments. It results in better magnetization transfer during the INEPT period of the HSQC sequence. It is reasonable to postulate that alicyclic rings condensed with the aromatic core would be structurally more rigid than chain aliphatics. Also, as shown earlier using T_2 relaxation, majority of the rigid aliphatics proximal to the aromatic core are the alicyclic rings. Thus the long-range aromatic-aliphatic correlations observed in the 1-HSQC spectrum are mostly due to the rigid alicyclic segments of the asphaltene molecules, which are condensed with the aromatic core.

3.3.4. Determination of aromatic core size and final structure

The model proposed here closely resembles the island model, with aromatic rings with condensed with alicyclic rings. The aromatic cores are substituted by pendant aliphatic chains that are 3-6 carbons long. A small number of linked archipelago type structures may be present and cannot be ruled out completely as they have been shown to be present in previous studies.^{41,64} The number of linking aliphatic chains, however, are not expected to be as high as the structures proposed by Sheremata *et al.*⁴³ which was later refined by Boek *et al.*¹⁵¹ in support of the island model. The size of the aromatic core can be determined by using a protocol developed by Solum *et al.*,⁵⁸ which was later used by Andrews *et al.*³⁰ They plot the mole fraction of bridgehead aromatic carbons χ_b (ratio of bridgehead carbons

to the aromaticity) versus the number of carbons per PAH, using equation number 18 in reference 60; χ_b can be easily calculated using the NMR data and its value can be used to obtain the number of carbons per PAH from the plot. As established earlier, in our case $C_{tb} \approx 10$ and $6 \leq C_{db} \leq 15$, putting the total bridgehead carbon value between 16 and 25. The aromaticity being 45, we get $0.36 \leq \chi_b \leq 0.56$, which corresponds to 16-30 aromatic carbons per PAH, *i.e.*, between 4 and 9 aromatic rings per PAH with pericondensed structures dominating and no purely catacondensed structures present (refer to figure 6 in ref. 58). Hence the average PAH size is 6.5, *i.e.*, 6-7 aromatic rings and the number of PAH's per 100 carbons is 1.9. For the sake of calculation, the average number of PAH's per 100 carbons can be rounded to two and all the corresponding structural parameters have been listed in Table 3.4. Each PAH of 6-7 pericondensed rings have two to three aliphatic chain substitutions, including CH_3 groups substituted on aryl rings. The average length of the aliphatic chains can vary between 3 and 8, subject to the presence of bridging chains. If bridging structures are present, the average chain length will be on the shorter side. Based on elemental analysis results, there appears to be approximately 1 N, 2 S and 1 O atom per PAH. This PAH size of ~ 7 rings is consistent with several other older and more recent studies using a variety of techniques such as scanning tunneling microscopy,⁴⁶ high-resolution transmission electron microscopy,⁴⁷ electronic triplet-state spectroscopy⁴⁸ and time-resolved fluorescence depolarization.^{20,49-51} All of these studies support the island molecular architecture. Moreover, as discussed previously, the relaxation behavior of the asphaltenes can be explained in light of the Yen-Mullins model. The average molecular mass of a PAH based on all these parameters was calculated to be approximately 720 g/mol. It lies in the molecular weight range of 500-1000 g/mol as reported by most mass

spectroscopic^{49,52,55} and diffusion studies.^{21,22,50,53,54} Mass spectrometry is known to suffer from aggregation and fragmentation effects, which often leads to overestimation of molecular weights, suggesting archipelago architecture. However, recent mass spectrometric studies have shown that these effects can be minimized by using suitable ionization methods such as laser desorption single-photon ionization (LDSPI)⁵⁵ and laser desorption laser ionization (two-step laser or L²MS).^{28,56} Results from these studies strongly support the island model and the average molecular weight calculated in this work falls in the range reported by these studies. A final average structure of an aromatic cluster is constructed in Fig. 3.7 using the parameters mentioned in Table 3.4 with a molecular formula of C₄₈H₅₁NOS₂ and a molecular weight of 722.05 g/mol. It cannot be said with certainty from this study that how many of such structures form the nanoaggregates, but it was determined from the relaxation measurements that 6-7 nanoaggregates constitute a cluster.

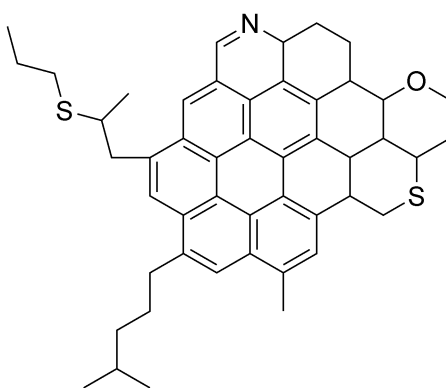


Figure 3.7. Average structure of an asphaltene molecule constructed using parameters obtained from ¹H and ¹³C NMR spectroscopy. Molecular formula: C₄₈H₅₁NOS₂.
Molecular weight: 722.05 g/mol.

3.4. Conclusion

The solution-state ^1H and ^{13}C NMR spectra of heptane-extracted Athabasca oil-sands asphaltenes have been resolved into their respective component peaks by using deconvolution analysis. The peak areas of the various carbon species were obtained from both spectra independently and were found to agree closely. The overlapping peaks in the spectra were revealed with help of the HSQC NMR experiment. The validity of the peak-fitting model was further verified by comparing the H/C ratio obtained from the NMR spectra to that obtained from elemental analysis. Various structural parameters such as size of aromatic clusters, number of substitutions per cluster and average aliphatic chain length were determined. It was found that each polyaromatic cluster is composed of 6-7 aromatic rings, which agrees with the number of rings predicted by the Yen-Mullins model.^{7,42} The ^1H T_1 and T_2 relaxation parameters of all the moieties were determined, and using the T_1/T_2 ratios it was shown that the asphaltene nanoaggregates and clusters exhibit highly restricted reorientational motion which is two to three orders of magnitude slower compared to simpler molecules. The bi-exponential relaxation behavior of most of the signals revealed that the same moieties can lie in different domains of mobility, which was explained in terms of the Yen-Mullins model and the percentages lying in the separate domains were also calculated. It was shown that the nanoaggregate clusters are small in size, consisting of 6 to 7 nanoaggregates per cluster on average. By modification of the HSQC experimental parameters, it was shown that the alicyclic rings are closely associated with the aromatic core and strong long-range heteronuclear couplings exist between them. This study adds to the evidence for the island model as the predominant asphaltene architecture and confirms

several structural features proposed by the Yen-Mullins model, using NMR spectroscopy exclusively. However, to get an even better understanding of the dynamics of the asphaltene molecules, nanoaggregates and clusters, relaxation measurements different asphaltene concentrations are required, along with further use of 2D correlation NMR spectroscopic methods, which shall be dealt with in future studies.

CHAPTER 4

4. SOLID-STATE ^1H AND ^{13}C NMR SPECTROSCOPY OF ATHABASCA OIL-SANDS ASPHALTENES: EVIDENCE FOR INTERLOCKING π -STACKED NANOAGGREGATES WITH INTERCALATED ALKYL SIDECHAINS

(Reproduced in part with permission from Dutta Majumdar, R.; Gerken, M.; Hazendonk, P. *Energy Fuels* **2015**, *29*, 2790. Copyright 2015 American Chemical Society)

4.1. Overview

In this chapter, we discuss new ways of approaching the asphaltene structure problem using solid-state NMR spectroscopy of Athabasca oil-sands asphaltenes (AOSA). Employing pulse sequences that are often used for characterization of polymers, we were able to distinguish between signals from rigid and mobile environments in the asphaltene molecules, and gain insight on the structural motif of the PAHs (peri- or cata-condensed) that predominate in asphaltenes. The nature of the condensation of the aromatic rings indicates the type of molecular architecture. Also, we were able to select for the well-resolved signals underlying the otherwise broad solid-state ^1H NMR spectrum of the asphaltenes. The chemical shifts, along with an in-depth T_2 relaxation analysis of these signals, reveal valuable information regarding the interactions between the pendant aliphatics and the aromatic core, asphaltene aggregation, and its driving factors.

4.2. Experimental details

4.2.1. Asphaltene extraction

Bitumen samples from the Athabasca oil-sands were obtained from Natural Resources Canada, CanmetENERGY Laboratory at Devon, Alberta. The asphaltenes were extracted from the bitumen using a protocol similar to Bouhadda *et al.*¹¹⁵ by stirring in *n*-heptane for 2 h at 60 °C and continued stirring at room temperature for 12 h. The resulting solution was suction filtered and the insoluble part containing the asphaltenes was dissolved in toluene at 50 °C and subsequently filtered. The filtrate was dried under an air-stream resulting in a black flaky solid, which was ground to a fine powder and dried under dynamic vacuum for several days to remove residual toluene. Trapped resin molecules may be present but as shall be discussed later in section 4.1, their amount is negligible. Moreover, consistency with a previous solution-state NMR study (Chapter 3) performed on the same sample, was necessary to draw comparisons.

4.2.2. ¹³C CP-MAS and DP-MAS

All experiments were performed using an 11.74 T Varian Unity Inova solid-state NMR spectrometer (500 MHz ¹H and 125 MHz ¹³C frequencies), equipped with four RF (radio frequency) channels. A 4.0-mm magic-angle spinning quadruple resonance probehead with a 52 µl rotor was used at a spinning speed of 8 kHz. The ¹H and ¹³C 90° pulse widths were 4.5 and 2 µs, respectively, with a recycle delay of 2 s and a contact time of 500 µs for all CP experiments, except for the variable contact time study. The ¹H spin-lock field was 55.6 kHz. For the DP ¹³C NMR experiment, a recycle delay of 20 s was used. Broadband ¹H decoupling was used for all carbon NMR experiments.

4.2.3. ¹³C CP Dipolar dephasing

The dephasing period was varied from 20 to 120 s at intervals of 20 s with all other parameters the same as the CP-MAS experiment.

4.2.4. ¹³C CP DIVAM

A non-rotor synchronized CP-DIVAM sequence consisting of twelve 4.5 μs pulses with an interpulse delay of 2.5 μs was used. Normally for direct DIVAM experiments the delay is chosen based on the rotor period, but a ¹H-¹³C CP-DIVAM experiment is mainly a T_2 driven process and hence not very sensitive to rotor synchronization. A series of measurements were carried out with the excitation angles arrayed in 2.5° steps from 0° to 65° by varying the radio-frequency pulse power and the peak intensities were plotted against the excitation angles.

4.2.5. ¹H Dipolar filter

An interpulse delay of 30 μs was chosen with $n = 1$, since this combination provided the optimum filtering conditions required to observe the unfiltered signals. The 90° pulse length was 4.5 μs, and the train of pulses for dipolar filtering was followed by a spin-echo period (delay-180°-delay), which was varied to obtain the transverse relaxation time constants (T_2). T_2 values reflect the mobility or rigidity of the different moieties and its use has been discussed in details Chapter 3.

4.3. Results and discussion

4.3.1. Validation of the peak fitting model

The solid-state ^{13}C NMR spectrum of AOSA is complex, with highly overlapping unresolved signals of varying widths and thus a deconvolution (peak fitting) model is essential to study in detail different parts of the asphaltene system. Since deconvolutions of non-resolved lines in a spectrum are not unique, the chemical shifts obtained from the better-resolved solution-state ^{13}C NMR spectrum of AOSA are taken as a starting point. It is safe to assume that the ^{13}C chemical shifts in the solid state are similar to those in the solution-state spectrum, since ^{13}C chemical shifts are less solvent dependent than those of ^1H , although a few differences can be expected. In a previous solution-state NMR study (Chapter 3) we showed in detail where the different carbon moieties resonate on the ^{13}C NMR spectrum. Using this information, along with the nature of CP ^{13}C signal build-up and dipolar dephasing behavior, the solid-state ^{13}C CP- and DP- MAS NMR spectra obtained at 8 kHz spinning speed were deconvolved into constituent peaks. The DP spectrum was used to determine the exact peak positions since it is more representative of the different species of carbon compared to the corresponding CP spectrum that are known to be non-quantitative. The peak-fitting model for the CP spectrum is shown in Fig. 4.1, with the corresponding assignments in Table 4.1. For reference, the corresponding DP spectrum is shown in Fig. 4.2.

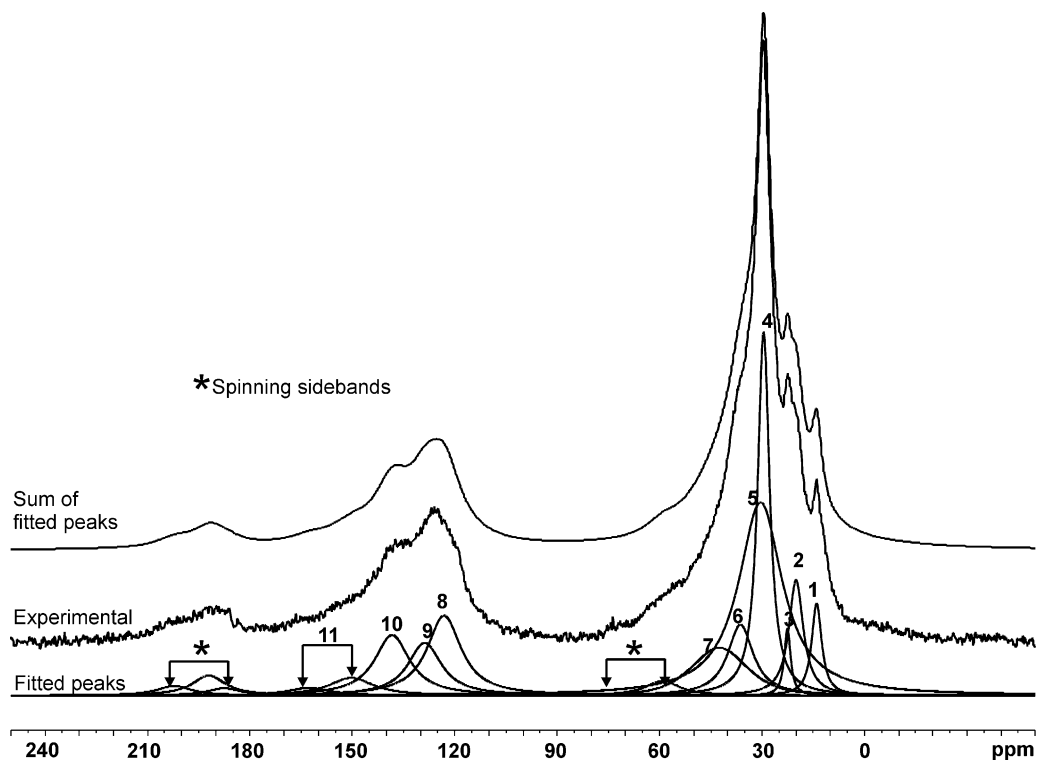


Figure 4.1. Solid-state ^1H - ^{13}C Cross Polarized (CP) MAS NMR spectrum of AOSA obtained at 8 kHz magic angle spinning rate with 500 μs contact time (middle), showing the deconvolved peaks (bottom) and the sum spectrum of the deconvolved peaks (top). The peaks marked with asterisks (*) represent spinning sidebands. The numbers on the deconvolved peaks of the bottom spectrum correspond to the assignments in Table 4.1.

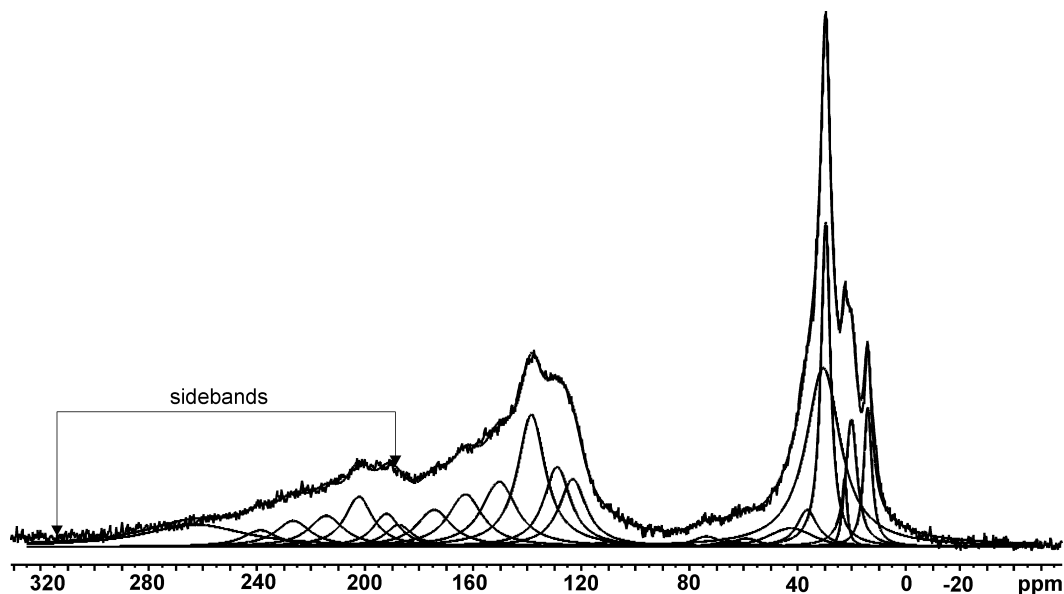


Figure 4.2. ^{13}C Direct Polarization (DP)-MAS spectrum of AOSA at 8 kHz spinning speed and 20.0 s recycle delay showing the fitted peaks which were used for quantitative analysis. The DP deconvolution had to account for higher order sidebands which were not observed in the corresponding CP spectrum.

Table 4.1. Chemical shift assignments and line widths ($\Delta\theta_{\frac{1}{2}}$) for the fitted peaks of solid-state CP-MAS (500 μ s contact time) ^{13}C NMR spectra of AOSA, obtained at 8 kHz spinning speed. Also shown are the T_{CP} and $T_{1\rho\text{H}}$ values for each peak (except 150.29 and 174.42 ppm) obtained fitting the variable contact time CP experiment data to Eq. 2.47.

Peak(s) #	$\delta\{^{13}\text{C}\}$ (ppm)	$\Delta\theta_{\frac{1}{2}}$ (Hz)	Assignment	CP dynamics	
				T_{CP} (ms)	$T_{1\rho\text{H}}$ (ms)
1	14.00	448	terminal aliphatic chain CH_3	0.18	50.88
2	20.03	638	branched CH_3 or CH_3 directly attached to aromatic ring	0.09	25.00
3	22.57	280	terminal isobutyl CH_3 and/or chain CH_2 'α' to terminal CH_3	0.08	15.62
4	29.54	525	aliphatic chain CH_2 more than 'α' or 'β' to aromatic ring	0.05	11.39
5	30.45	1938	alicyclic CH_2/CH more than 'α' to aromatic rings	0.02	4.33
6	36.31	1134	chain CH_2/CH 'α' to aromatic rings	0.15	2.80
7	42.53 [†]	2419	alicyclic CH_2/CH 'α' to aromatic rings	0.05	4.13
8	123.13 [‡]	1520	aromatic CH (+triple-bridgehead quaternary aromatic C)	0.02, (0.23)	0.18, (75.00)
9	128.81	1500	triple-bridgehead quaternary aromatic C	0.23	64.64
10	138.37	1560	double-bridgehead + substituted quaternary aromatic C	0.42	75.00
11	150.29, 162.78, 174.42	1949	aromatic carbons α to heteroatoms (O, N), carboxylic acids (R-COOH) and carboxylic acid esters (R-COOR')	<i>a</i>	<i>a</i>

^a Could not be calculated due to low signal intensity in the variable contact time CP experiments. [†]50% Gaussian peak. All other peaks deconvolved peaks are 100% Lorentzian. [‡]Two different aromatic carbon species with different T_{CP} and $T_{1\rho\text{H}}$. (See Appendix 2 for example and fitting errors).

The validity of the peak fitting and the assignments can be checked by using the variable contact time array of ^{13}C CP-MAS NMR spectra (Fig. 4.3a) and the nature of signal decay with increasing dephasing time in the dipolar dephasing (DD) experiment (Fig. 4.3b).

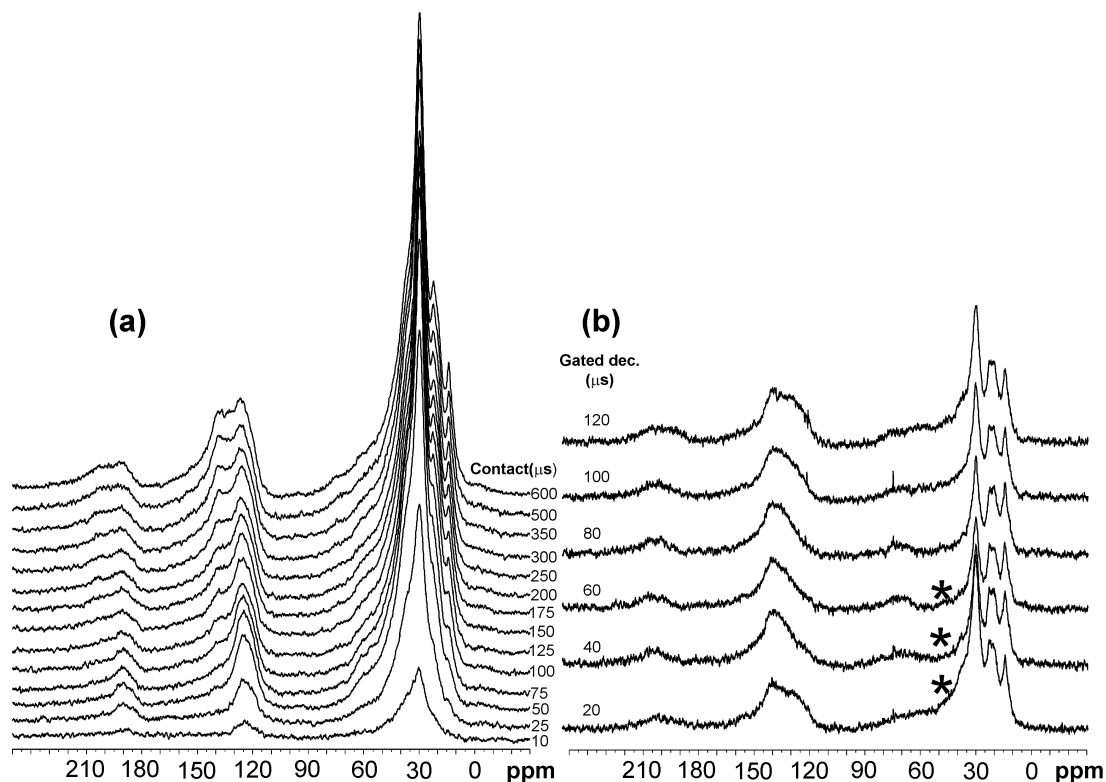


Figure 4.3. (a) ^1H - ^{13}C CP-MAS NMR spectra with variable contact time (10 to 600 μs) of AOSA. Signals appearing at short contact times are from carbons coupled strongly to neighbouring hydrogens. (b) ^1H - ^{13}C CP-MAS dipolar dephasing NMR spectra. The gated decoupling period was varied from 20-120 μs . Signals decay up to 80 μs but reappear again when the dephasing period approaches the rotor period of 125 μs , due to the refocusing of the heteronuclear dipolar coupling. All experiments were performed at 8 kHz spinning rate. *Refer to text in Section 4.3.1.

Aromatic $-\text{CH}$ carbons (C_{arH}) and triple-bridgehead quaternary carbons (C_{tb}) resonate in the 110 – 129.5 ppm region. From the variable contact time spectra, it can be seen that at very short contact times of 10, 25 and 50 μs , the only signals that appear arise from carbon moieties that are strongly coupled to nearby or attached protons. It was also observed that a part of the same region dephases rapidly in the dipolar dephasing experiments, while a

part of it shows no dephasing. Accordingly, the 110 – 129.5 ppm region was deconvolved into two peaks, one showing rapid CP build-up at $\delta_{13\text{C}} = 123.13$ ppm (peak 8, Fig. 4.1), assigned to aromatic –CH carbons and another at $\delta_{13\text{C}} = 128.81$ ppm (peak 9, Fig. 4.1), assigned to triple-bridgehead quaternary aromatic carbons based on its slow CP build-up and no dephasing. The signals at $\delta_{13\text{C}} = 14.00$, 20.03 and 22.57 ppm (peaks 1, 2 and 3, Fig. 4.1) are assigned based on previous solution-state NMR work (Chapter 3). As in the aforementioned solution-state study, the 30.00 ppm region is deconvolved into a broad ($\delta_{13\text{C}} = 30.45$ ppm, peak 5, Fig. 4.1) and a narrow ($\delta_{13\text{C}} = 29.54$ ppm, peak 4, Fig. 4.1) component, which correspond to alicyclic –CH₂/–CH and chain –CH₂ groups, respectively. This was verified by fitting the 30.00 ppm region in the dipolar dephasing series with a single peak ($\delta_{13\text{C}} = 29.54$ ppm). In the unfiltered spectrum, the fit was satisfactory, but for the longer dephasing periods, the signal narrowed, causing the peak at $\delta_{13\text{C}} = 29.54$ ppm to be too broad for the corresponding signal. This disparity was resolved by changing the model by decreasing the linewidth of the $\delta_{13\text{C}} = 29.54$ ppm peak and including an additional broad peak at $\delta_{13\text{C}} = 30.45$ ppm. The broad shoulder downfield of 30.00 ppm (marked by * in Fig. 4.3b) in the unfiltered spectrum decays completely after 40 μs in Fig. 4.3b, indicating the presence of strongly coupled species in the region and fitted with peaks at $\delta_{13\text{C}} = 36.31$ ppm and $\delta_{13\text{C}} = 42.53$ ppm (peaks 6 and 7, Fig. 4.1). These can be attributed to chain and cyclic aliphatic –CH or –CH₂ moieties ‘ α ’ to the aromatic core. The peak at $\delta_{13\text{C}} = 138.37$ ppm was assigned to double-bridgehead (C_{db}) and substituted (C_{sub}) quaternary aromatic carbons. It does not decay significantly with increasing dephasing period, which means they are remote from the protons. The aromatic carbons usually have large chemical shift anisotropies (CSA) of *ca.* ~ 50 kHz (~ 100 ppm at the current field strength) due to their rigidity and hence 8 kHz spinning is not expected to suppress all the sidebands. Accordingly

the bands from $\delta_{13\text{C}} = 50 - 75$ ppm and $\delta_{13\text{C}} = 187 - 203$ ppm are assigned as spinning sidebands attributed to the centre bands at $\delta_{13\text{C}} = 123.13, 128.81$ and 138.37 ppm. To ensure a proper fit, three additional peaks at $\delta_{13\text{C}} = 150.29, 162.78$ and 174.42 ppm (peaks grouped as no. 11, Fig. 4.1) were required, which were not encountered previously in the solution-state spectrum (Chapter 3). The region of $\delta_{13\text{C}} = 150-175$ ppm typically includes aromatic carbons α to electronegative heteroatoms (O, N), and carboxylic acids (R-COOH) and carboxylic acid esters (R-COOR'), thus a small number of these functionalities are likely to be present. For the purpose of this work, especially for the CP based experiments, these signals will not be looked at closely other than for quantitative purposes (in the DP spectrum) since i) they constitute only a very small fraction of the overall CP spectrum and ii) their signal-to-noise ratio is too low to arrive at any substantive conclusions and requires separate investigation. These signals are significantly more prominent in the DP spectrum, which also required inclusion of sidebands for these signals and also higher frequency sidebands for the aromatic signals. Some of the important types of carbon, which shall be discussed below, are shown in Fig. 4.6.

From the fitted peaks in DP spectrum, the H/C ratio was calculated to be 1.2, which is reasonably close to the H/C ratio 1.3 calculated from elemental analysis (78.41% C, 8.47% H, 1.12% N, 8% S and 2.0% O), showing that the deconvolution model is reliable. The elemental analysis of the AOSA sample used in this work, also reported in Chapter 3, was found to agree closely with literature values.^{34,43,102} This indicates that even if trapped resins are present in the sample, the amount is negligible.

4.3.2. ^1H - ^{13}C Cross Polarization (CP) dynamics

Figure 4.4 shows the build-up of cross-polarized magnetization of the various carbon signals with increasing contact time. Figure 4.4a shows just the aliphatic signals except those that are 'α' to the aromatic core. Figure 4.4b shows the alicyclic signals along with the aliphatics which are 'α' to the aromatic core, and 4.4c shows the aromatic carbon signals. These CP curves clearly indicate there is no single contact time that ensures the maximal magnetization transfer for all the carbons. Hence, quantitative analysis of a ^{13}C CP-MAS spectrum of asphaltenes will be inaccurate.

Cross-polarization transfer time constant T_{CP} : The rate of build-up depends on the effective strength of heteronuclear dipolar coupling between the carbon in question and its neighbouring protons. Magnetization build-up is characterized by the cross-polarization transfer time constant T_{CP} ,¹²⁷ which is short for fast, and long for slow build-up. The decay of this magnetization with increasing contact time is characterized by the rotating-frame spin-lattice relaxation time constant of ^1H or $T_{1\rho\text{H}}$. The intensity of the cross-polarized magnetization $I(t)$ at a contact time t is given by Eq. 2.46 in Chapter 2. Using Eq. 2.46, the T_{CP} and $T_{1\rho\text{H}}$ values were determined by minimising the sum of least squares between the experimental and calculated data and then optimizing for the best fit by non-linear regression (see Appendix 3 for fitting quality). Table 4.1 lists the calculated T_{CP} values. The non-methyl aliphatic chain carbons at $\delta_{13\text{C}} = 22.57, 29.54$ and 36.31 ppm show rapid magnetization build-up with $T_{\text{CP}} = 0.08, 0.05$ and 0.15 ms respectively, while that of the terminal $-\text{CH}_3$ carbons ($\delta_{13\text{C}} = 14.00$ ppm) is slower with $T_{\text{CP}} = 0.18$ ms, since the ^1H - ^{13}C dipolar-coupling is diminished by the large degree of motional freedom. The signal from

CH₃ attached to aromatic ring ($\delta_{13C} = 20.03$ ppm) has a $T_{CP} = 0.09$ ms, slightly shorter than the terminal CH₃, as its motion is restricted due to the aromatic ring.

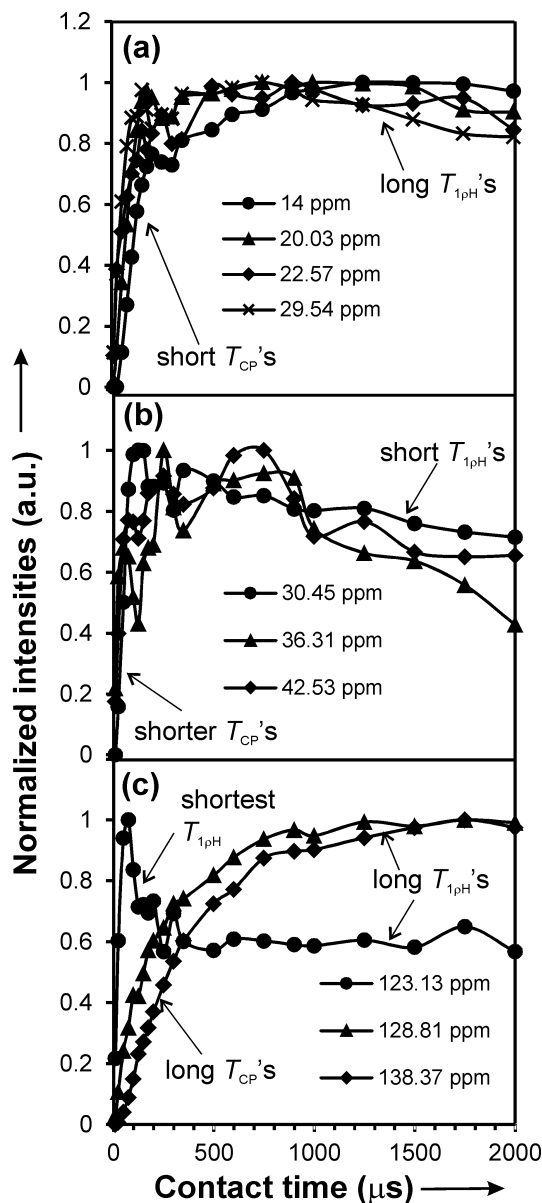


Figure 4.4. ¹³C CP-MAS magnetization build-up curves of AOSA at 8 kHz spin rate: (a) aliphatic chain carbons, (b) alicyclic carbons and alkyl chain carbons ‘α’ to aryl ring and (c) aromatic carbons. The areas under the deconvolved peaks are plotted against the corresponding contact times. The 123.13 ppm signal contains contributions from both C_{arH} and C_{tb} , which explains the odd behavior of the decay part of the curve. Refer to Table 4.1 for chemical shift assignments.

The alicyclic CH₂/CH carbons at $\delta_{13\text{C}} = 30.45$ and 42.53 ppm also show a rapid build-up, with $T_{\text{CP}} = 0.02$ and 0.05 ms respectively, resulting from lower degree of motional freedom imposed by the nearby aromatic core.

Among the aromatics, the C_{arH} ($\delta_{13\text{C}} = 123.13$ ppm) show fast magnetization build-up, which is consistent with the rigidity of the aromatic core. However, it was observed that the decay part of the curve clearly contains contributions from a different species of carbon. This region of a carbon spectrum is often attributed to both C_{arH} and C_{tb} , hence the second contribution to this signals is not surprising. Hence this build-up curve was fitted using the weighted average of two simulated curves: one with a short T_{CP} and $T_{1\rho\text{H}}$ representing C_{arH} and another with longer T_{CP} and $T_{1\rho\text{H}}$ representing C_{tb} . The parameters for the C_{tb} contribution were kept the same as those of the originally assigned C_{tb} signal at $\delta_{13\text{C}} = 128.81$ ppm (shown later) and the C_{arH} parameters were adjusted for the best fit. The T_{CP} for C_{arH} was calculated in this way to be 0.02 ms and this weighted fitting also enabled the calculation of the net contribution of C_{tb} to the signal assigned to C_{arH} . It was found that $\sim 35\%$ of the $\delta_{13\text{C}} = 123.13$ ppm signal is C_{tb} , an observation which will be useful in the quantitative interpretation of the DP spectrum shown later. The quaternary aromatic carbons ($\delta_{13\text{C}} = 128.81, 137.38$ ppm), on the other hand, have the slowest magnetization build-up with $T_{\text{CP}} = 0.23$ and 0.42 ms, an order of magnitude longer than that of C_{arH} . The longer T_{CP} illustrates that most of the quaternary bridgehead and substituted aromatic carbons are more remote from the protons on the edge of the core compared to the protonated aromatic carbons, consequently very weakly coupled to them.

¹H rotating-frame spin-lattice relaxation time constant $T_{1\rho\text{H}}$: The decay of the carbon magnetization transferred from proton with contact time is governed by the rotating-frame

spin-lattice relaxation time constant of ^1H or $T_{1\rho\text{H}}$. When plotted with correlation time τ_c , $T_{1\rho\text{H}}$ (Fig. 4.5) exhibits a curve with maximal values at the extremes and has a minimum at $\tau_c = 1/\nu_{1\text{H}}$, where $\nu_{1\text{H}}$ is the frequency corresponding to the spin-locking field.

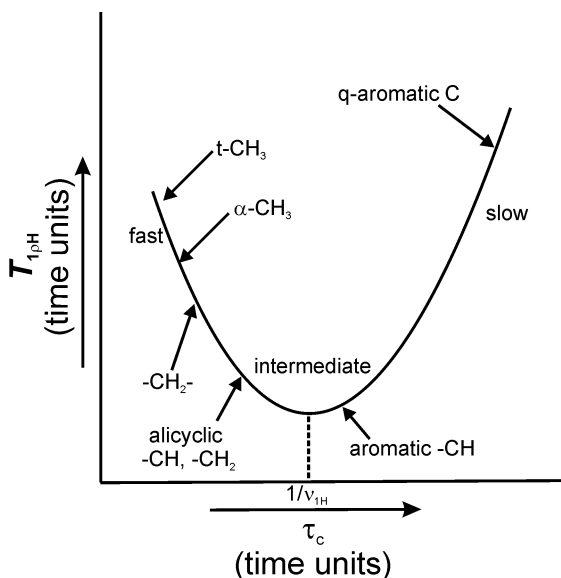


Figure 4.5. Schematic (not to scale) showing the variation of $T_{1\rho\text{H}}$ with correlation time τ_c and at different motional regimes. The $T_{1\rho\text{H}}$ minimum occurs at $\tau_c = 1/\nu_{1\text{H}}$, where $\nu_{1\text{H}}$ is the frequency of the spin-locking field during cross-polarization. (q-aromatic C = quaternary aromatic carbons including substituted C).

The correlation time is small for fast and long for slow motional processes. Thus large values of $T_{1\rho\text{H}}$ (slow magnetization decay) arise for very fast and very slow motion, while smaller values (faster magnetization decay) occurring near the minimum correspond to motion on the timescale of $1/\nu_{1\text{H}}$.

Figure 4.5 shows the different motional regimes (slow, intermediate, fast) and how they relate to the $T_{1\rho\text{H}}$ calculated fitting the CP build-up curves, which are listed in Table 4.1. The long $T_{1\rho\text{H}} = 50.88$ ms of the terminal methyl groups ($\delta_{13\text{C}} = 14.00$ ppm) indicate their high mobility while the -CH_3 groups attached to the aryl ring ($\delta_{13\text{C}} = 20.03$ ppm) are slightly less mobile with $T_{1\rho\text{H}} = 25.00$ ms. The other chain -CH_2 groups at $\delta_{13\text{C}} = 22.57$ and

29.54 ppm, which are not close to the aromatic core are also slightly less mobile with $T_{1\rho\text{H}} = 15.62$ and 11.39 ms respectively. The $-\text{CH}_2/\text{CH}$ groups α to aryl rings ($\delta_{13\text{C}} = 36.31$ ppm) have a short $T_{1\rho\text{H}} = 2.80$ ms, indicative of their rigidity, and it is in the same regime with the alicyclic groups ($\delta_{13\text{C}} = 30.45$ and 42.53 ppm) which have $T_{1\rho\text{H}} = 4.33$ and 4.13 ms respectively. The quaternary carbons, bridgeheads and substituted alike ($\delta_{13\text{C}} = 128.81$ and 138.37 ppm), exhibit very long $T_{1\rho\text{H}} = 64.64$ and 75.00 ms respectively, indicating their highly rigid nature. The aromatic $-\text{CH}$ groups ($\delta_{13\text{C}} = 123.13$ ppm) have a very short $T_{1\rho\text{H}} = 0.18$ ms which indicates that they are much less rigid than the quaternary groups and more rigid than the aliphatic chain groups.

$T_{1\rho\text{H}}$ values clearly reveal a distribution of mobilities in the structural features of the asphaltene system: i) the highly mobile terminal $-\text{CH}_3$ groups, ii) the slightly less mobile aliphatic chain $-\text{CH}_2$ remote from the aromatic rings, iii) the slightly more rigid alicyclic groups, alkyl chain groups which are directly attached to the core, aromatic $-\text{CH}$ groups and iv) the highly rigid quaternary aromatic groups. The mobility in the aliphatics clearly increases with decreasing proximity to the aromatic core, except the $\alpha\text{-CH}_3$ (attached to the aromatic core), which have additional motional freedom. The aromatic environments are very rigid, at least in part due to aggregation. There was no evidence for mobile aromatic environments, ruling out the possibility of pendant aromatic centres attached to the main aromatic core.

As mentioned previously, quantitative ^{13}C NMR spectroscopy using CP is not feasible for asphaltenes. In contrast, it has been shown that for certain PAHs, such as 7-methylbenzo[α]pyrene and 9-anthracenemethanol, it is possible to get quantitative spectra under fast spinning conditions (~ 40 kHz) if the contact times and recycle delays are

considerably long. (Mao 2012) But in the case of asphaltenes, at sufficiently long contact times to provide quantitative estimates of quaternary carbons, the signals from most other carbons will have decayed considerably under $T_{1\rho H}$. This is a strong indicator that the asphaltene PAHs are considerably larger and more circularly condensed than the above two examples of PAHs. Despite not being quantitative in nature, when possible CP based experiments are preferred as they dramatically increase sensitivity, and thus significantly reduce experimental time when compared with DP experiments. For instance, the recycle delay used for CP experiments here is 2.0 seconds, whereas that for DP is 20.0 seconds. Hence for a conservative 2:1 enhancement in sensitivity using CP, the time required will be 40 times less than the DP experiment.

4.3.3. ^{13}C Direct Polarization and PAH size calculation

As established in the discussions above, the ^{13}C CP-MAS NMR spectrum is not suitable for any quantitative calculations on asphaltenes. Hence we rely on the ^{13}C directly polarized or DP NMR spectrum for quantitative information. Table 4.2 lists some of the structural parameters calculated from the DP ^{13}C spectrum. The nature of the polyaromatic ring system is the most decisive factor in determining the structural model of asphaltenes and hence we mainly focus on this aspect. The size or the degree of condensation of a PAH is often assessed by calculating a quantity sometimes referred to as the ‘aromatic condensation index’, represented by χ_b , and it is the ratio of bridgehead carbons to the aromaticity.^{30,58,152} As shown in Table 4.2, the aromaticity calculated from the DP spectrum was ~ 0.50 (C_{ar}/C_{total}) which is close the aromaticity value obtained in Chapter 3.

Table 4.2. Structural parameters calculated from the areas under the fitted peaks of the ^{13}C DP-MAS NMR spectrum at 8 kHz MAS and 20 s pre-scan delay.^a

Structural parameter	Value for AOSA
% aromaticity	49.8 (\pm 0.07)
% aliphaticity (incl. alicyclic)	50.2 (\pm 0.02)
$^1\text{H}/^{13}\text{C}$ ratio	1.2
aromatic -CH (% C_{arH})	6.0-9.2 (\pm 0.04)
substituted quaternary aromatic C (% C_{sub})	9.9 (\pm 0.04)
double-bridgehead quaternary aromatic C (% C_{db})	8.5 (\pm 0.01)
triple-bridgehead quaternary aromatic C (% C_{tb})	10.6-13.9 (\pm 0.04)
aromatic carbons α to heteroatoms	11.6 (\pm 0.04)
aromatic condensation index (χ_{b})	0.38-0.45
no. of condensed aromatic rings	5-7
avg. aliphatic chain length	4
alicyclic C (% C_{alic})	19.6 (\pm 0.02)

^a Relative errors were calculated with a 3σ corresponding to 99.7% confidence level, obtained from the residual error (χ^2) in the deconvolution analysis.

The fraction of bridgehead aromatic carbons was calculated by first separately determining the double-bridgehead (C_{db}) and triple-bridgehead (C_{tb}) fractions. The C_{db}

signals remain mixed with the C_{sub} (ipso-carbons) at $\delta_{13\text{C}} = 138.37$ ppm, hence determination of the latter is necessary first. This was achieved by calculating the fraction of aliphatic carbons ' α ' to the aromatic core ($\delta_{13\text{C}} = 20.03, 36.31$ and 42.53 ppm) and subtracting it from the total $C_{\text{db}} + C_{\text{sub}}$ signal. As discussed earlier, to calculate C_{tb} , both the area under the $\delta_{13\text{C}} = 128.81$ ppm peak and up to 35% of the area under the $\delta_{13\text{C}} = 123.13$ ppm peak have to be considered. Hence upper and lower limits can be set to the C_{tb} fraction by assuming 35% or 0% contribution to the 123.13 ppm signal. Similarly, limits to the C_{arH} ($\delta_{13\text{C}} = 123.13$ ppm) can also be set. The final calculated values are listed in Table 4.2. The aromatic condensation index or χ_b obtained using these values was in the range 0.38-0.45, which corresponds to peri-condensed PAHs with 5-7 aromatic rings, with 20-25 aromatic carbons per PAH (see Fig. 6, Solum 89). Large peri-condensed PAHs like these are characteristic of the island model and corroborate our findings from the CP dynamics study shown earlier. It should be kept in mind that when doing these calculations, the areas under the spinning sidebands are also considered. Ignoring these would lead to erroneous values. The average number of carbons on an aliphatic chain was also calculated by simply dividing the chain $-\text{CH}_2/\text{CH}$ fraction by the terminal $-\text{CH}_3$ fraction. A final hypothetical average structure of a single asphaltene based on these calculations and elemental analysis is shown in Fig. 4.6.

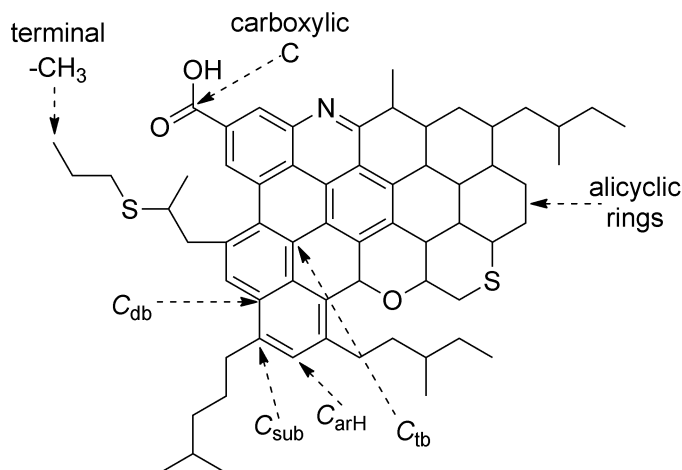


Figure 4.6. Hypothetical average structure of an asphaltene molecule based on the parameters obtained from ^{13}C DP-MAS NMR spectrum and EA, showing some of the important carbon types. Molecular formula: $\text{C}_{63}\text{H}_{77}\text{NO}_3\text{S}_2$, Mol. Wt.: 960.42 g/mol.

4.3.4. ^1H - ^{13}C CP-Dipolar Dephasing

Figure 4.7 shows the decay of ^{13}C CP-MAS NMR signals with increasing dephasing period in the dipolar dephasing experiment. The ^{13}C signals with high CP efficiency are expected to dephase fastest, as they have the largest ^1H - ^{13}C dipolar coupling (D_{CH}). The alicyclic CH_2/CH carbons ($\delta_{13\text{C}} = 30.45$ and 42.53 ppm) dephase rapidly, indicating that these groups experience strong D_{CH} resulting from their conformational rigidity compared to the free alkyl chains. The aliphatic chain carbons, $-\text{CH}_2$ and CH groups ($\delta_{13\text{C}} = 22.57$, 29.54 and 36.31 ppm) all dephase at diminishing rates reflecting their proximity to the aromatic core. The signals from chain CH_2/CH groups ‘ α ’ to aromatic rings ($\delta_{13\text{C}} = 36.31$ ppm) dephase the fastest, followed by those from the aliphatic chain CH_2 groups beyond the ‘ β ’ position with respect to the aromatic ring ($\delta_{13\text{C}} = 29.54$ ppm), terminal isobutyl CH_3 groups and/or chain CH_2 groups ‘ α ’ to terminal methyl ($\delta_{13\text{C}} = 22.57$ ppm).

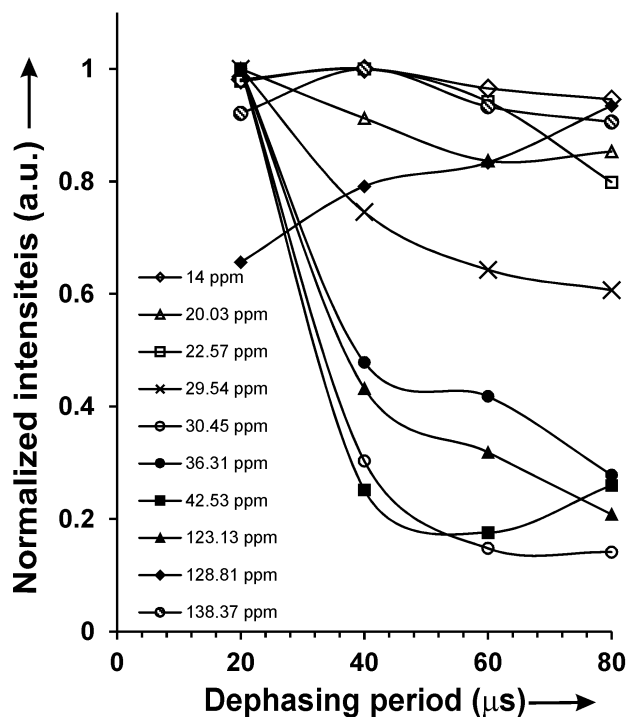


Figure 4.7. Decay of ^{13}C CP-MAS NMR signals plotted against the dephasing period in the dipolar dephasing experiments. Signals from moieties with stronger effective dipolar coupling to neighbouring hydrogens decay more rapidly. For the quaternary aromatic carbons, the unfocused chemical shift anisotropies (CSA) dominate, and interfere with the dipolar dephasing, causing the anomalous behavior. For other carbons the dipolar coupling interaction dominates over CSA.

The terminal CH_3 groups ($\delta_{13\text{C}} = 14.00$ ppm) experience diminished D_{CH} because of enhanced motional averaging resulting from higher degree of conformational freedom, which is clearly indicated by the lack of dephasing. The signals from the CH_3 groups attached to the aromatic core ($\delta_{13\text{C}} = 20.03$ ppm) show more pronounced dephasing, their motion being sterically restricted by their position. Among the aromatic signals, the C_{arH} ($\delta_{13\text{C}} = 123.13$ ppm) dephase significantly as the rigidity of the aromatic core prevents motional averaging of the C-H dipolar coupling. The quaternary carbon signals behave somewhat differently. The $\text{C}_{\text{db}}+\text{C}_{\text{sub}}$ signal ($\delta_{13\text{C}} = 138.37$ ppm) oscillates slightly but does

not dephase significantly. The lack of significant dephasing indicates that any proximal hydrogen must be remote, resulting in weak dipolar coupling. As a result, the chemical shift anisotropy or CSA interaction dominates the spin dynamics, and thus are responsible for the oscillations observed, as this sequence is not rotor synchronized. This effect is most pronounced for the C_{tb} ($\delta_{13C} = 128.81$ ppm) signal, where the C-H dipolar coupling is weakest. This is congruent with the findings from the CP dynamics study and also with the following results from the DIVAM experiments, which show that these carbons are positioned deep within a large PAH.

4.3.5. 1H - ^{13}C CP-DIVAM

Figure 4.8 shows the ^{13}C CP-DIVAM nutation curves for some of the deconvolved signals where the normalized areas are plotted as a function of excitation angle. Only the curves of the signals which have an appreciable signal to noise ratio are shown. Based on the nutation behaviour, the signals can be grouped into two categories: i) groups which attain zero intensity or cross zero at excitation angles below 30° ($\delta_{13C} = 14.0, 20.03, 29.69$ ppm) and ii) those which cross zero intensity at or above 30° ($\delta_{13C} = 30.45, 123.13, 128.81$ and 138.37 ppm). The former group represents the relatively more mobile domains with smaller D_{HH} and longer T_2 -s, compared to the latter, with larger D_{HH} and shorter T_2 -s, representing the rigid domains. In this context, the alicyclic carbons ($\delta_{13C} = 30.45$ ppm) are of particular interest, as they also show nutation behavior similar to the aromatic carbons. This suggests that, contrary to some archipelago models,^{117,153} the alicyclic structures are directly attached to the aromatic core, rather than being linked via aliphatic chains. The same observation was made using solution-state 2D HSQC techniques in Chapter 3.

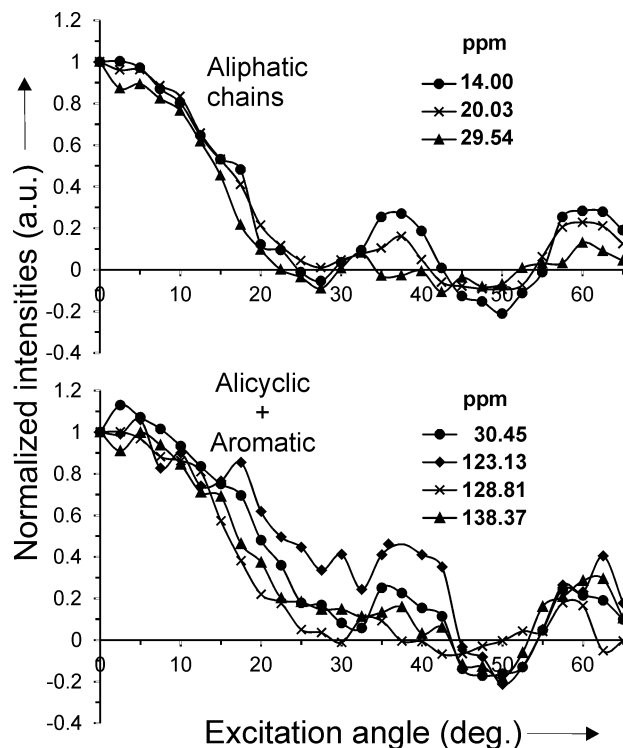


Figure 4.8. ^{13}C CP DIVAM nutation curves: the intensity of each peak is plotted against the excitation angle of the minipulses in the DIVAM sequence. Signals, which attain zero intensity at smaller excitation angles, arise from groups with higher mobility, while a delayed zero crossing implies higher rigidity.

4.3.6. Selecting the high-resolution signals in the ^1H NMR spectrum using dipolar and T_2 filters

The solid-state ^1H NMR spectrum of AOSA (Fig 4.9, top spectrum) at 8 kHz MAS consists of featureless broad signals at the aliphatic and aromatic regions, whereas the solution-state ^1H spectrum (Fig. 4.9, middle spectrum) suggests at least three distinct components in the aliphatic region. The inherent broadness is due to strong ^1H - ^1H homonuclear dipolar coupling, which cannot be suppressed efficiently by spinning the sample even at much higher speeds. A closer look at the ^1H MAS NMR spectrum shows some low intensity inflections resulting from small underlying high-resolution signals. To select for the narrow signals, the dipolar filter (DF) sequence was employed, which is a

technique used to filter out broad components via the large homonuclear dipolar coupling. The resulting DF spectrum (not shown) consists almost entirely of narrow peaks. Three sharp signals in the aliphatic region were observed, however, a broad baseline remained, making peak fitting difficult. The broad baseline was removed by the addition of a spin-echo filter, using $\tau = 125 \mu\text{s}$ (one rotor period), i.e. a T_2 filter immediately following the DF filtering sequence.

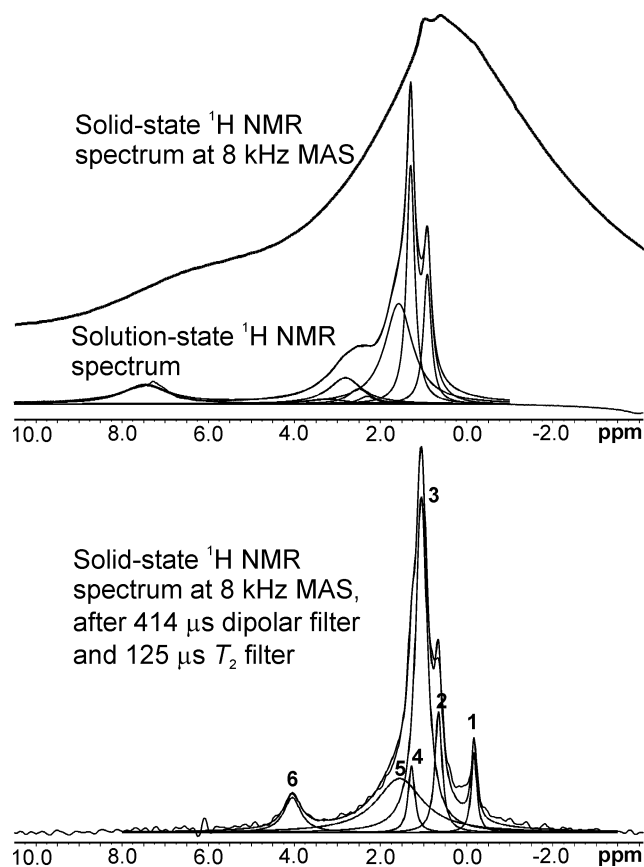


Figure 4.9. ^1H NMR spectra of AOSA: (top) Solid-state spectrum at 8 kHz MAS without any filtering, (middle) solution-state spectrum with deconvoluted peaks (Chap. 3) and (bottom) solid-state spectrum at 8 kHz MAS after 414 μs dipolar filter and 125 μs Hahn-echo or T_2 relaxation filter showing the deconvoluted peaks. The aromatic signals have been filtered out in the bottom spectrum. The numbers on the deconvoluted peaks of the bottom spectrum correspond to the assignments in Table 4.3.

The resulting spectrum, shown in Fig. 4.9 (bottom spectrum), reveals additional signals that were conspicuously absent in the solution-state ^1H NMR spectrum. The most striking among these was a peak at $\delta_{1\text{H}} = -0.18$ ppm, (peak 1, Fig. 4.9), which, to the best of our knowledge, has never been reported. Another interesting signal is a slightly broader peak at $\delta_{1\text{H}} = 4.04$ ppm (peak 6, Fig. 4.9). Also note that the chemical shifts of the remaining signals were shifted slightly to lower frequencies compared to their solution-state counterparts. A shoulder was also observed at a frequency slightly higher than the $\delta_{1\text{H}} = 1.06$ ppm peak, indicating underlying signals. Of particular significance is that no sharp aromatic proton signals were observed. The results of the deconvolution analysis performed on the DF spectrum are listed in Table 4.3.

The negative chemical shift at $\delta_{1\text{H}} = -0.18$ ppm is a direct evidence for π -stacking in AOSA. Negative chemical shifts result from the ring-current effect. Depending on the position of a moiety relative to the aromatic rings, it will either be shielded or de-shielded from the external magnetic field by the ring currents generated in the aromatic π -system. The effect is illustrated in Fig. 4.10a.

Table 4.3. Chemical shift assignments, line widths ($\Delta\theta_{\frac{1}{2}}$) and transverse (T_2) relaxation constants for the fitted peaks of solid-state ^1H NMR spectrum at 8 kHz MAS, obtained with 414 μs dipolar filter and variable delay spin-echo filter.*

Peak #	$\delta\{^1\text{H}\}$ (ppm)	$\Delta\theta_{\frac{1}{2}}$ (Hz)	Assignment	T_2 (ms)
1	-0.18	76	-CH ₃ intercalated deep within the SC of its own NA or adjacent NA if on a long chain	0.11 (74.5%)
			-CH ₃ intercalated to a lesser extent within the SC of adjacent NA	24.25 (26.5%)
2	0.65	99	-CH ₃ on the cluster interior, ali. -CH ₂ intercalated within the SC	0.09 (70.0%)
			-CH ₃ on the cluster periphery	5.83 (30.0%)
3	1.06	167	ali. CH ₂ on the cluster interior, -CH ₃ attached to aro. ring	0.40 (21.1%)
			ali. CH ₂ on the cluster periphery	4.74 (78.9%)
4	1.29	90	ali. CH ₂ 'α' to aro. core	3.33
5	1.56	653	alic. CH ₂ not 'α' to aro. core	0.58
6	4.04	242	alic. CH/CH ₂ 'α' to aro. core	1.11

*aro. = aromatic, ali. = aliphatic, alic. = alicyclic, NA = nanoaggregate, SC = shielding cone. The values in parentheses represent the percentage of unfiltered signal having the corresponding T_2 . All the deconvolved peaks are Lorentzian.

A nucleus in the shielding cone of an aromatic system (as shown in Fig. 4.10b) will have a decreased chemical shift. Thus for signals with small $\delta_{1\text{H}}$, it is quite possible for the chemical shifts (terminal -CH₃) to become negative. Examples of this effect have been reported in literature, where the effect of ring-currents contribute to upfield shifts of up to 1-2 ppm for protons.¹⁵⁴

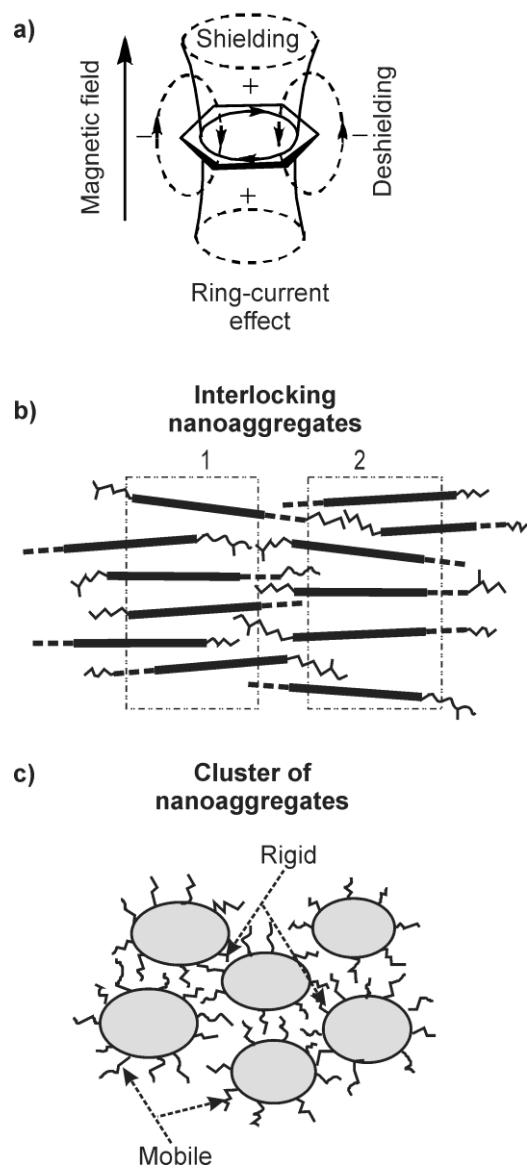


Figure 4.10. (a) Graphic illustrating the shielding effect of aromatic ring currents, which moves the aliphatic ^1H NMR signals upfield, as shown on Fig. 4.9. (b) Illustration of asphaltene nanoaggregates 1 and 2 interlocking. The broken lines off the aromatic rings are alicyclic groups. (c) A cluster of nanoaggregates where the aliphatic moieties on the inside are less mobile than the ones on the periphery due to interactions with neighbouring aliphatic chains.

Molecular dynamics (MD) calculations have predicted that asphaltenes exhibit aromatic stacking. Pacheco-Sanchez *et al.*^{155,156} described three types of stack orientations: face-to-face (π - π interactions), edge-on or T-shaped (π - σ interactions) and offset π -stacked (σ - σ).

These studies note that some of the distances between two seemingly stacked aromatic sheets often do not add up to the total height of an aggregate, and the difference was attributed to the presence of intercalated aliphatic chains interfering with the stacking interaction, increasing the π - π distance. Jian *et al.*¹⁵⁷ recently demonstrated through MD simulations of model compounds in water that long aliphatic chains can promote aggregation through aliphatic-aromatic interactions. The negative chemical shift observed in the solid-state ^1H NMR spectrum supports these hypotheses. The signal provides the direct evidence by NMR that aliphatic chains indeed occupy the region between aromatic sheets.

The transverse relaxation times (T_2) for the ^1H resonances were measured using the Hahn-echo sequence, following an initial dipolar filtering period of 414 μs [= 12 \times (30 +4.5) μs]. The T_2 values are listed in Table 4.3. On fitting the relaxation data, bi-exponential relaxation was observed for the aliphatic chain signals at $\delta_{1\text{H}} = -0.18, 0.65$ and 1.06 ppm, where the long and short T_2 's correspond to mobile and rigid environments (see Appendix 3 for proof of bi-exponential behavior). The relationship between relaxation times and mobility has been discussed in detail in Chapter 3. Recall that the $\delta_{1\text{H}} = -0.18$ ppm peak arises from the terminal $-\text{CH}_3$ groups intercalated between aromatic sheets. Among these, we attribute the shorter T_2 of 0.11 ms to the terminal $-\text{CH}_3$ protons deep inside the shielding cone, their motion sterically hindered by π -stacking. The alkyl chains could be either part of the same nanoaggregate that is shielding the methyl groups, or they could be long chains from adjacent nanoaggregates (Fig. 4.10b). The longer T_2 of 24.25 ms is assigned to the more mobile CH_3 protons which are intercalated between the aromatic sheets to a lesser extent, their motion less restricted by the stacking (Fig. 4.10b). These methyl groups most

likely belong to alkyl chains from adjacent nanoaggregates. The $\delta_{1H} = 0.65$ ppm signal can be ascribed to non-intercalated $-CH_3$ groups and also to intercalated $-CH_2$ groups which have been shifted to a lower frequency by the ring-current effect. The fraction with the short $T_2 = 0.09$ ms comprises the rigid intercalated $-CH_2$ s and the $-CH_3$ s in the cluster interiors, their motion sterically hindered by alkyl chains from adjacent nanoaggregates (Fig. 4.10c). The mobile fraction with $T_2 = 5.83$ ms are $-CH_3$ groups lying on the periphery of the cluster (Fig. 4.10c). Similarly, the $\delta_{1H} = 1.06$ ppm signals are assigned to $-CH_2$ moieties on the interior ($T_2 = 0.4$ ms) and on the periphery ($T_2 = 4.74$ ms) of the clusters. De-shielded $-CH_3$ groups attached to the aromatic core can also contribute to the rigid fraction of the 1.06 ppm signal. The $\delta_{1H} = 1.29$ ppm signal with a single, short T_2 of 3.3 ms are attributed to CH_2 groups 'α' (directly attached) to the rigid aromatic core. The signal at $\delta_{1H} = 1.56$ ppm is assigned to alicyclic $-CH_2$ protons with a short $T_2 = 0.58$ ms, while the $\delta_{1H} = 4.04$ ppm signal is assigned to de-shielded CH/CH_2 groups 'α' to the aryl ring with a short $T_2 = 1.11$ ms, indicating their rigid nature. This is consistent with our earlier observation that alicyclic groups are condensed with the aromatic core. The $\delta_{1H} = 4.04$ ppm signal is at a higher frequency than its corresponding solution-state NMR signal, indicating these groups are de-shielded by the ring-current effect and hence lie immediately outside the shielding cone.

Recent MD studies have suggested that the aliphatic chains do not interfere with π - π stacking when asphaltenes are dissolved in toluene.¹⁵⁸ However, we show here that in the solid state, alkyl chains occupy the region between aromatic sheets, hence interfering with π - π stacking, but likely promoting stacking via π - σ interactions. This implies that on addition of a solvent such as toluene, π - σ interactions become weaker and aggregation is

driven mainly by π - π stacking which could be due to the fact that toluene undergoes π - π stacking with the asphaltenes.¹⁵⁸ This could explain why negative ^1H chemical shifts from intercalated alkyl groups are not observed in the solution-state NMR spectrum, if they were not broadened due to chemical exchange. At this juncture, it is difficult to speculate if these up-field signals would be observable in crude oil without further investigation. Advanced two-dimensional NMR techniques might be required to isolate them from an inevitably overcrowded spectrum and this shall remain an impetus for the authors to further their research.

4.4. Conclusion

The solid-state ^{13}C CP- and DP-MAS NMR spectra of heptane-extracted AOSA were resolved into their component signals using deconvolution analysis. The peak-fitting model was validated using the variable contact time ^1H - ^{13}C CP and DD experiments, along with quantitative validation using the ^{13}C DP experiment. The $T_{1\rho\text{H}}$ values calculated from the variable contact time results reveal that the mobility of alkyl groups increase with decreasing proximity to the aromatic core. It also shows that all of the aromatic groups are highly rigid, and no evidence for mobile aromatic rings was found, ruling out the possibility of pendant aromatic rings attached to the main aromatic core. The significantly slow magnetization build-up (long T_{CP} values) of the bridgehead aromatic carbons is indicative of large PAH systems. This observation is confirmed by calculating the aromatic condensation index (χ_b) which puts the number of condensed rings in a PAH between 5 and 7. The DD curves also compliment the CP dynamics results because the signals with high

CP efficiency (fast build-up) dephase faster in the DD experiments. The bridgehead aromatic carbons show very little dephasing despite their rigid environment and CSA dominates over C-H dipolar coupling, indicating their remoteness from the aromatic protons. The CP-DIVAM nutation curves helped differentiate between the mobile and rigid components, clearly showing that the alicyclic groups have similar rigidity to the aromatic core, with which they are condensed.

Using the dipolar and T_2 filter sequences, we were able to select the well-resolved, sharp signals underlying the broad ^1H NMR spectrum for the first time, to the best of our knowledge. The negative chemical shift at $\delta_{1\text{H}} = -0.18$ ppm provides strong experimental evidence that aliphatic groups occupy the region between stacked aromatic sheets in the solid state and likely interfere with the π - π stacking between asphaltene units, thus promoting stacking via π - σ interactions. The biexponential T_2 relaxation behavior of the intercalated protons suggests that they also contain $-\text{CH}_3$ groups belonging to long alkyl chains from adjacent nanoaggregates. This, along with the biexponential behavior of the other alkyl chain groups, suggests clustering of the nanoaggregates, where they form interlocking structures. All of these observations are consistent with the island or Yen-Mullins model of asphaltenes⁷ and provide compelling evidence that the nanoaggregate-cluster structure exists in a solvent-free environment.

CHAPTER 5

5. COMPARISON OF ASPHALTENES DERIVED FROM BITUMEN, PETROLEUM AND COAL, USING 2D-PHASE-SENSITIVE HSQC SPECTROSCOPY

5.1. Overview

Correlating the structure of asphaltenes to their aggregation behavior first requires understanding which structural features contribute to aggregation and which hinder it. To determine this, it is necessary to examine how aggregation behavior changes on varying the structural parameters of asphaltenes. It is known that asphaltenes derived from coal distillates are structurally distinct from those derived from petroleum.³⁰ Coal derived asphaltenes are posited to be less complex than their petroleum counterparts, owing to the manner in which they are processed from liquefied coal residues by distillation, which leads to cracking of the alkane chains.³⁰ It is also the prevailing notion that coal-derived asphaltenes are of lower mass and smaller size than petroleum asphaltenes, making them less complex and easier to study.²⁰ Therefore, if the structures of these asphaltenes are compared and then their aggregation behavior is studied, valuable insight into the factors driving aggregation may be obtained. In this chapter, asphaltenes derived from six different sources, one bitumen, two petroleum and three coals, will be studied using a solution-state two-dimensional ^1H - ^{13}C correlation experiment, called the phase-sensitive heteronuclear single quantum coherence (ph-HSQC). This is a variation of the HSQC sequence used in Chapter 3, with the added advantage of being able to distinguish between $-\text{CH}$, $-\text{CH}_2$ and $-\text{CH}_3$ groups. The observations and discussion in this chapter will be mostly qualitative,

since this is a comparative study, and will highlight some of the basic differences between the structures of petroleum- and coal-derived asphaltenes.

5.2. Experimental Details

5.2.1. Asphaltene samples

The Athabasca oil-sands bitumen derived asphaltene is the same one used in Chapters 3 and 4, and will be referred to as AOSA. All the other samples were obtained from Schlumberger-Doll Research, Cambridge, Massachusetts, USA. Of the three different coal-derived (CD) asphaltenes, two were from Indonesia, Tanito Harum (TH) and Adaro (AD), and one was from the USA, Wyoming (WY). The two petroleum (P) asphaltene samples are codenamed UG8 and BG5, of which UG8 is a Kuwaiti black-oil and BG5 is a Middle Eastern oil. The extraction methodology of the P- and CD-asphaltenes has been discussed in detail in literature.³⁰

All samples were prepared in CDCl₃ at a concentration of 30 g/L, which is well above the critical cluster concentration⁷ and the asphaltenes can be expected to occur in their aggregated states.

5.2.2. NMR spectroscopy parameters

All experiments were performed using a 16.4 T Bruker Avance III HD NMR spectrometer, operating at 700 MHz ¹H Larmor frequency, in 5 mm outer diameter NMR tubes. The number of increments obtained in the indirect dimension (TD1) was 256, and 64 scans were recorded for each increment. A recycle delay of 2.5 s was used for all samples. The indirect dimension was zero-filled to 1024 points to improve digital

resolution, and exponential line broadenings of 10 and 25 Hz were applied to the direct and indirect dimensions, respectively. All experiments were performed at room temperature.

5.3. Results and Discussion

The phase-sensitive HSQC spectra of all six samples are shown in Figures 5.1 through 5.6. The cross-peaks in red and yellow are positive, where the higher intensities have a more yellowish appearance, and represent $-\text{CH}_3$ and $-\text{CH}$ moieties. The green and blue cross-peaks are negative, blue being more negative and represent $-\text{CH}_2$ moieties. At first glance, it is evident that all P-asphaltenes (BG5, UG8) and the bitumen derived asphaltene (AOSA) have similar HSQC spectra, while those of the CD-asphaltenes are similar to each other, but significantly different from the P-asphaltenes. In the AOSA and the P-asphaltenes, the $-\text{CH}_3$ signals do not overlap with $-\text{CH}_2$ signals in the ^1H dimension, all appearing around 0.8 ppm. They show separation in the ^{13}C dimension, corresponding to the methyl groups in different positions: the terminal $-\text{CH}_3$ (~14 ppm), branch $-\text{CH}_3$ (~20 ppm) and terminal isobutyl $-\text{CH}_3$ (~22 ppm) (See Chapter 3 for visualization of these moieties). However, in the CD-asphaltenes there is definite overlap in the ^1H dimension between methyl and methylene signals, with positive cross peaks appearing around 1.2 ppm and at low ^{13}C chemical shifts. The higher ^1H chemical shift of these methyl groups indicates that they are closer to the aromatic core, in chains that are not more 2 carbons long, evidencing the presence of shorter aliphatic chains in CD-asphaltenes. The positive cross peaks in the 2.0 – 2.4 ppm range in the ^1H dimension can be attributed to $-\text{CH}_3$ groups directly attached to aryl rings or aliphatic $-\text{CH}$ moieties.

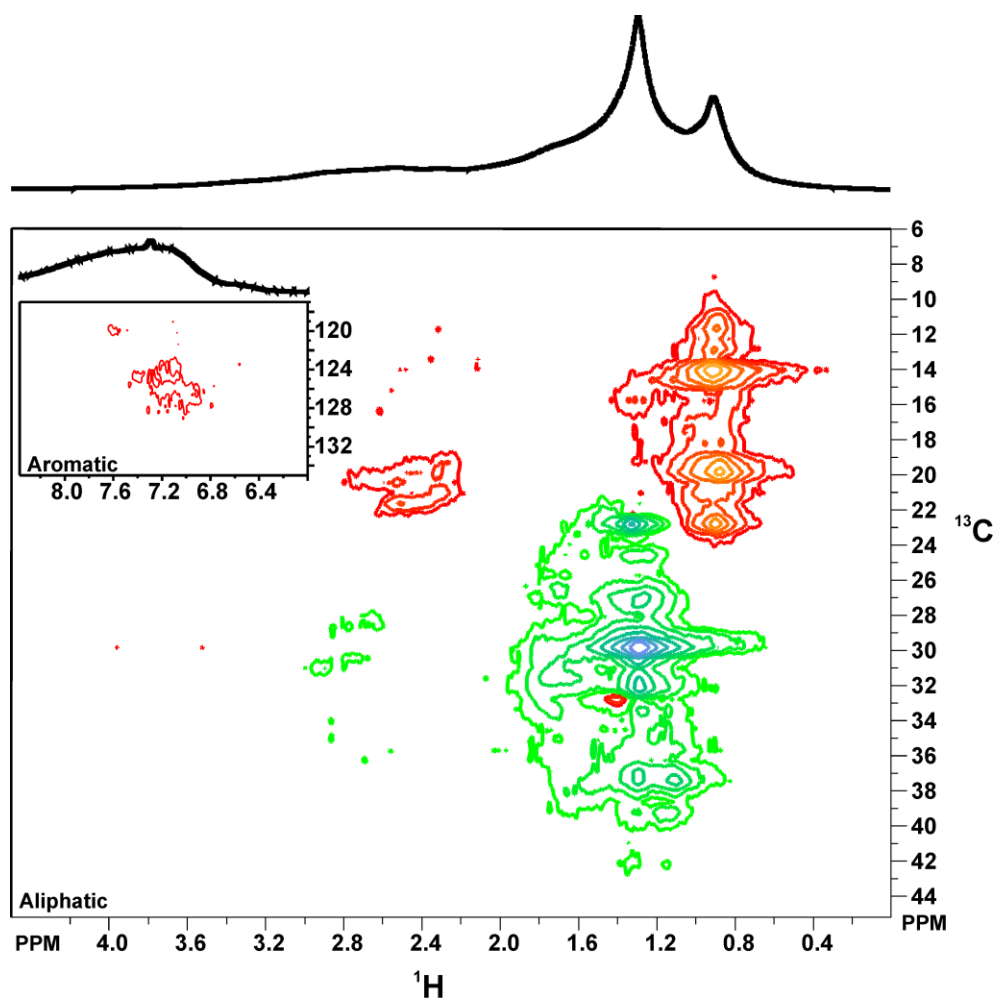


Figure 5.1. The ph-HSQC spectrum of AOSA, with the aliphatic region expanded and the aromatic region in the inset. The red and yellow cross-peaks are positive, yellow being at a higher intensity, while the green and blue cross-peaks are negative, blue being at a greater negative intensity.

The aliphatic cross-peaks in the CD-asphaltenes are generally narrow and discrete, whereas those in AOSA and P-asphaltenes are wide. This indicates that AOSA and P-asphaltenes have a greater distribution of types of chain groups compared to the CD-asphaltenes. It points to a mixture of chains of different lengths, long and short, in P-asphaltenes, whereas CD-asphaltenes are likely to have less variation in aliphatic chain length, most of them being short, as will be shown quantitatively in the subsequent chapter.

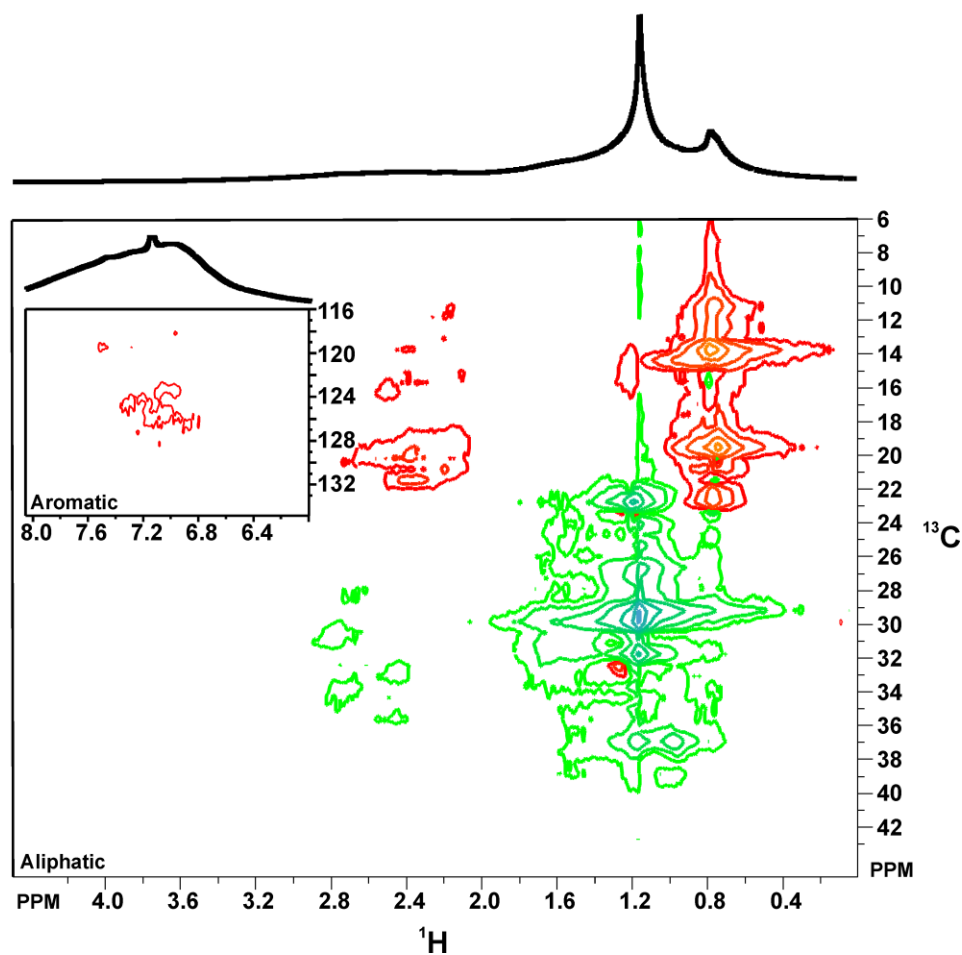


Figure 5.2. The ph-HSQC spectrum of **BG5** P-asphaltene, with the aliphatic region expanded and the aromatic region in the inset.

An additional explanation for the general broadness of the $-\text{CH}_2$ cross-peaks in P-asphaltenes is the presence of alicyclic groups condensed with the aromatic core, which makes them rigid and hence result in broader signals. These alicyclic groups seem less abundant in CD-asphaltenes.

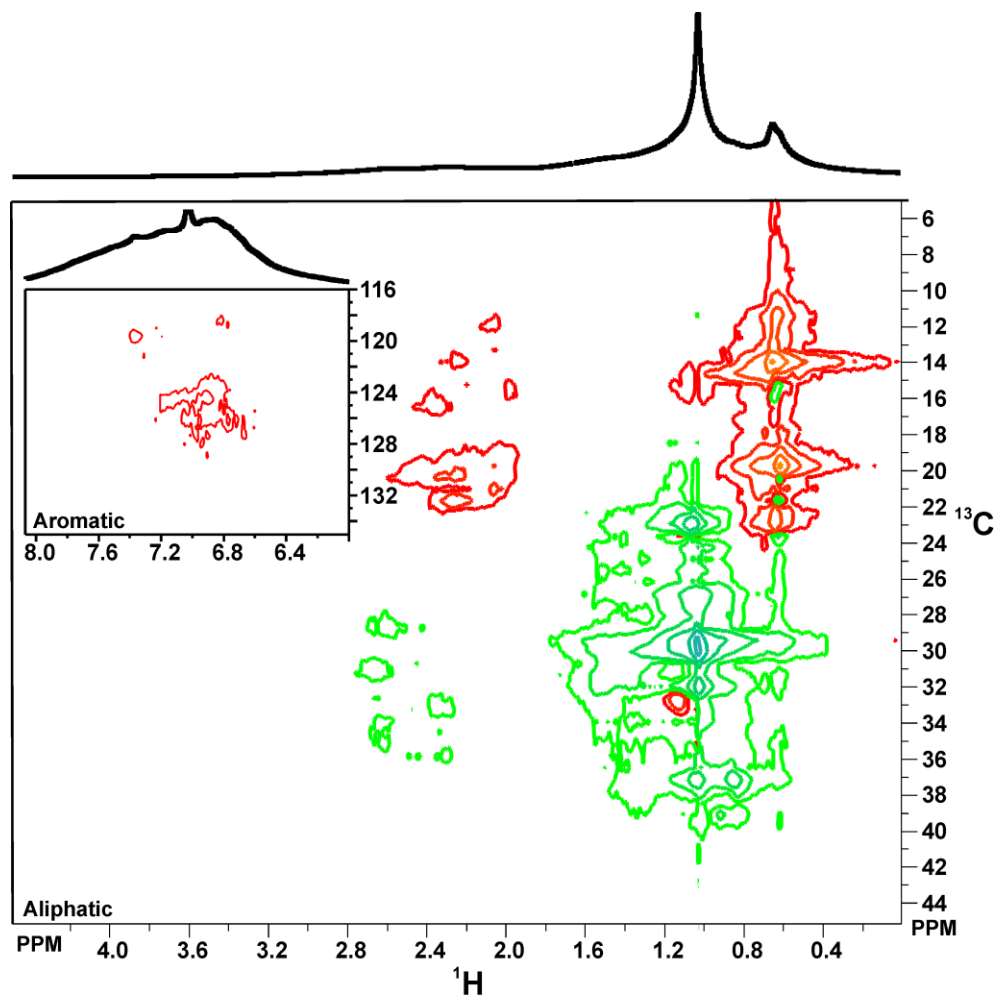


Figure 5.3. The ph-HSQC spectrum of UG8 P-asphaltene, with the aliphatic region expanded and the aromatic region in the inset.

The CD-asphaltenes have an abundance of strong negative cross-peaks at ^1H chemical shifts higher than ~ 1.2 ppm, which are significantly weaker and scarce in the AOSA and P-asphaltenes. Based on the chemical shifts in both dimensions, these signals are generally attributed $-\text{CH}_2$ groups that are closer to the aromatic ring than those around ~ 1.2 ppm. The abundance of these signals in CD-asphaltenes indicates that a large fraction of the chain $-\text{CH}_2$ groups are located close, i.e. α or β to the aromatic ring, whereas in P-asphaltenes and AOSA, the majority of the $-\text{CH}_2$ groups resonate around ~ 1.2 ppm. This is yet another observation that hints to CD-asphaltenes having very short aliphatic chains without much

variation in the length, while P-asphaltenes and AOSA have longer chains, with the majority of $-\text{CH}_2$ moieties being more than α or β from the aromatic rings.

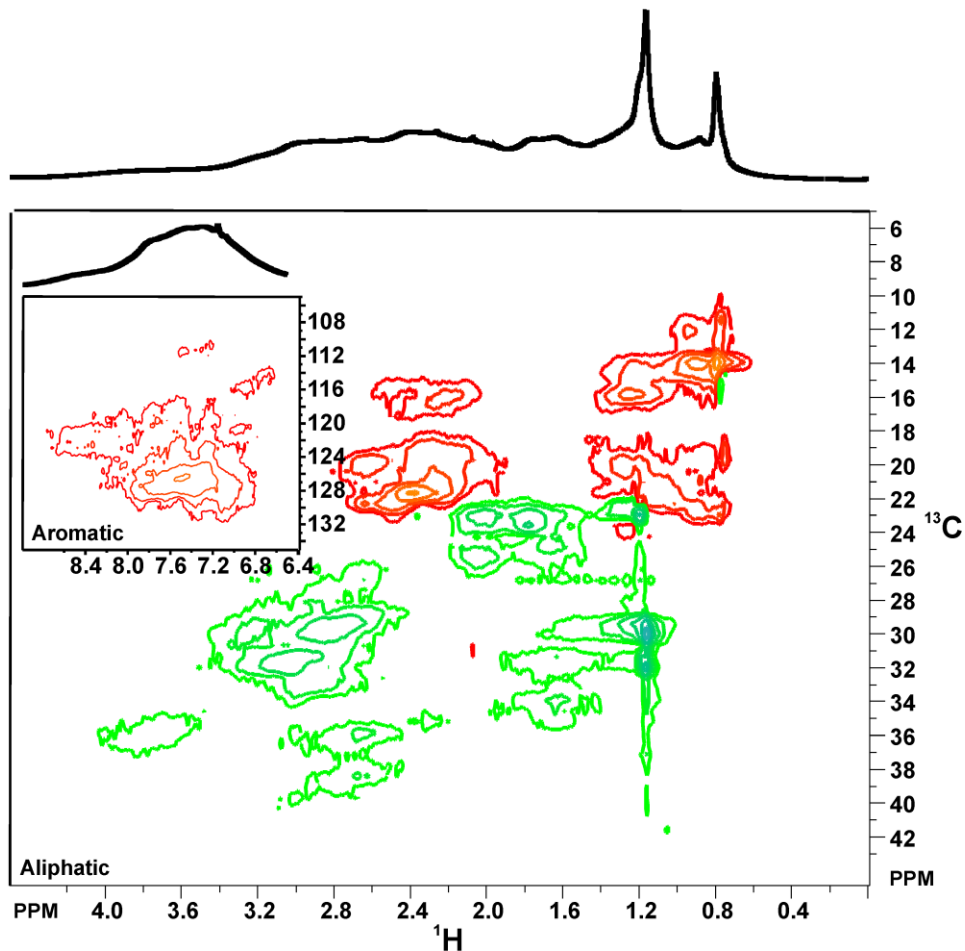


Figure 5.4 The ph-HSQC spectrum of AD CD-asphaltene, with the aliphatic region expanded and the aromatic region in the inset.

The cross-peaks from the $-\text{CH}_2$ groups close to aromatic rings also appear broader, which is consistent with them being more rigid compared to groups further down the chain (~ 1.2 ppm cross-peaks). These signals can also arise from alicyclic $-\text{CH}_2$ groups, suggesting that the majority of the alicyclic groups are naphthenic in nature, directly attached to the aromatic core, and do not extend out further. Alicyclic groups that are further out, distant

from the aromatic core, will have a smaller ^1H chemical shift, like in the P-asphaltenes and AOSA.

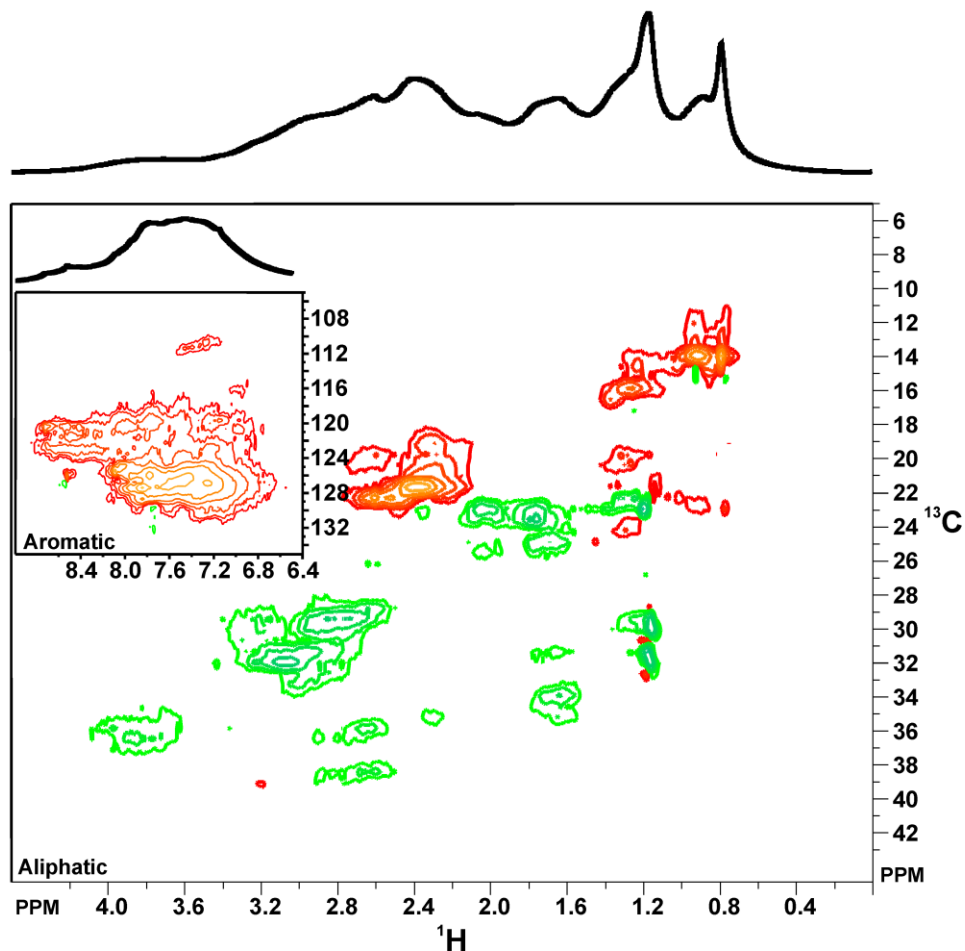


Figure 5.5. The ph-HSQC spectrum of TH CD-asphaltene, with the aliphatic region expanded and the aromatic region in the inset.

The most significant difference between these two classes of asphaltenes (grouping AOSA and P-asphaltenes under the same class), however, is in the aromatic region. The aromatic cross peaks in CD-asphaltenes are significantly more intense, implying the presence of a far greater fraction of aromatic $-\text{CH}$ moieties. A greater number of aromatic $-\text{CH}$ groups occurs when the number of substitutions is smaller. Moreover, the chemical shift range over which these correlations occur is much larger for CD-asphaltenes, which

represent the many different possible chemical environments for this group. This is strong evidence that P-asphaltenes are more heavily substituted, thereby reducing the fraction of aromatic protons.

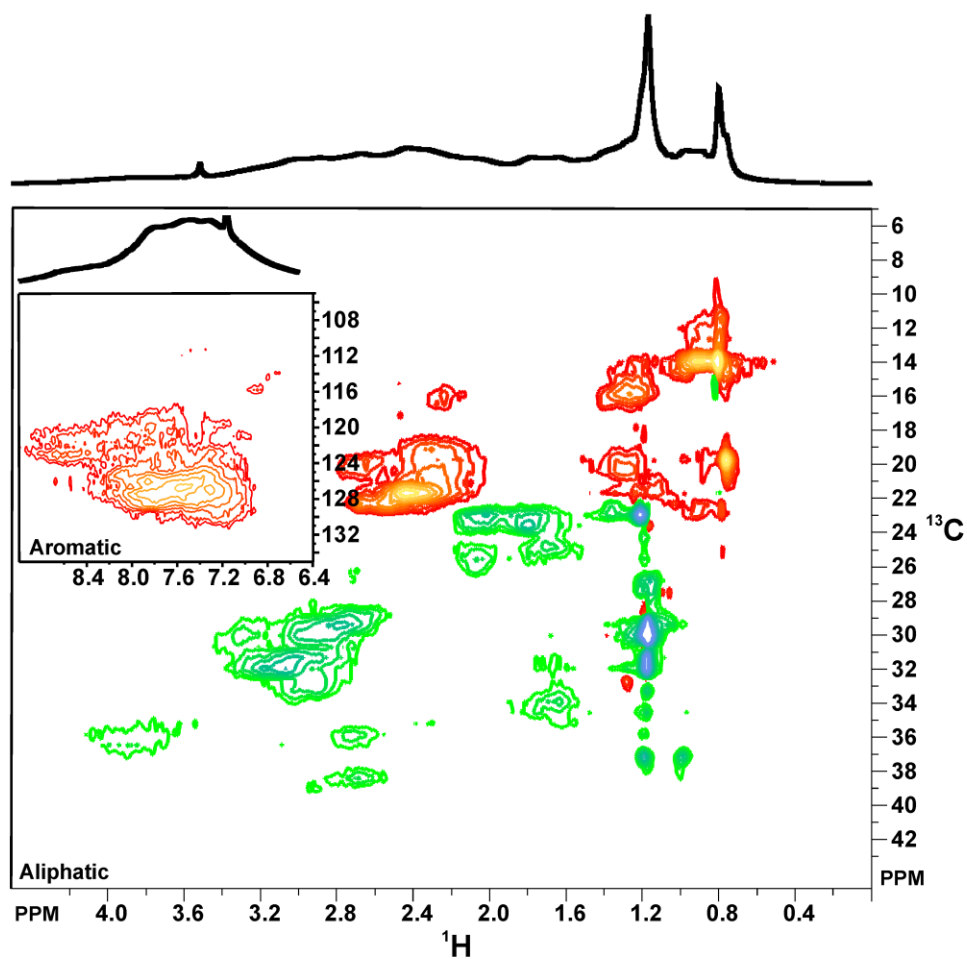


Figure 5.6. The ph-HSQC spectrum of WY CD-asphaltene, with the aliphatic region expanded and the aromatic region in the inset.

Further insight into structural differences can be gained by examining the horizontal slices extracted from the ph-HSQC spectra, taken at selected carbon chemical shifts.

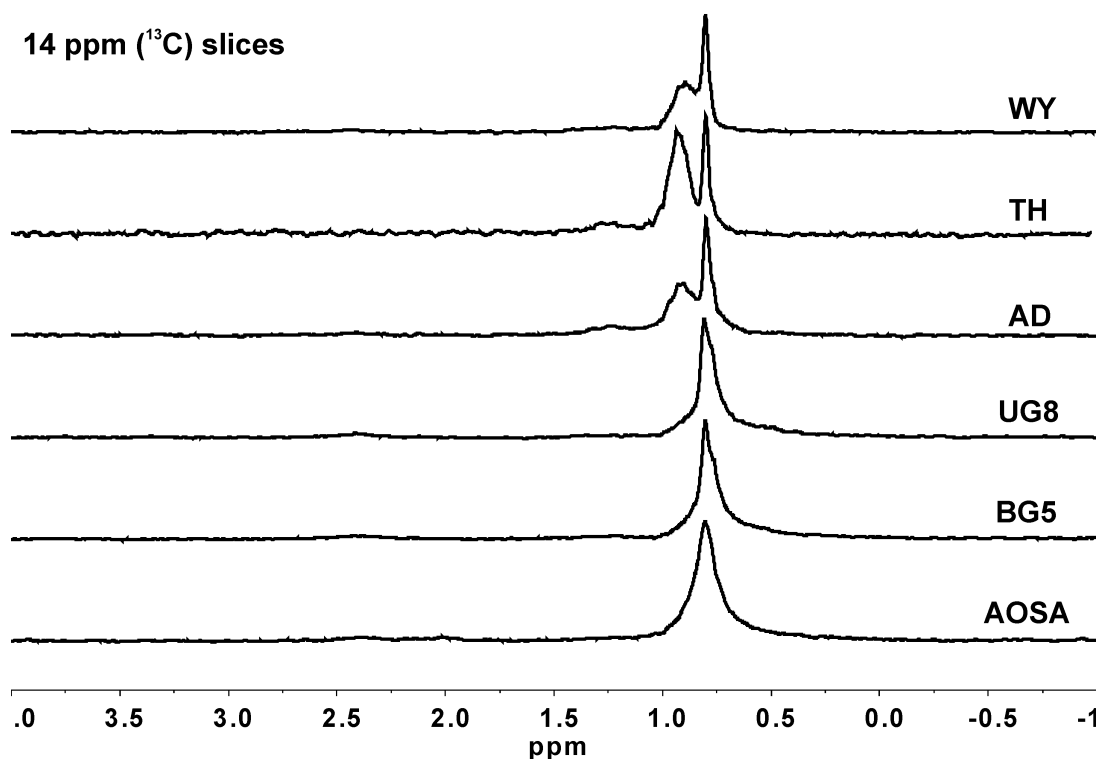


Figure 5.7. HSQC slices taken at $\delta_{13\text{C}} = 14$ ppm.

The horizontal slice taken at 14 ppm ¹³C chemical shift is shown in Fig. 5.7, which represents terminal methyl groups. The AOSA and P-asphaltenes show a single, slightly broadened peak around 0.8 ppm, while the corresponding peak in CD-asphaltenes is narrower, along with an additional broader peak at a slightly higher chemical shift (~0.9 ppm). The peaks at the higher chemical shift likely correspond to -CH₃ groups which are close to the aromatic ring, belonging to very short chains. The proportion of these shorter chains in TH seems higher, evinced by a more intense signal. While these signals might be present in the AOSA and P-asphaltenes as well, the broadness of the peaks might render them undetectable. The broader nature of the AOSA and P-asphaltene signals is a common a feature that can be observed through all the slices and will be explained in subsequent discussions.

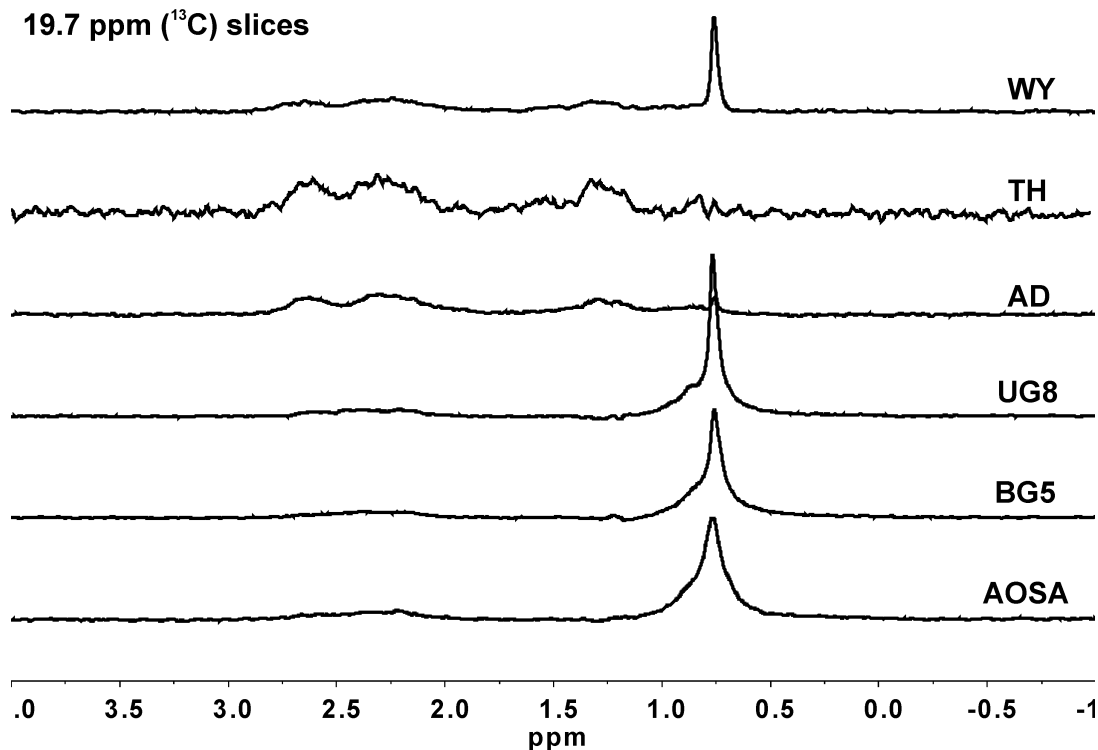


Figure 5.8. HSQC slices taken at $\delta_{13\text{C}} = 19.7$ ppm.

Slices were also taken at 19.7 ppm ^{13}C chemical shift (Fig. 5.8), which correspond to branched $-\text{CH}_3$ moieties ($\delta_{1\text{H}} \sim 0.8$ ppm) and those directly attached or close to aromatic rings (broad, low intensity peaks between 1-3 ppm). Branched $-\text{CH}_3$ groups appear to be absent in both TH and AD, while all the CD asphaltenes appear to have a greater abundance of short aliphatic chains, compared to the other class, reinforcing the previous observation. The slices extracted at 22.7 ppm (Fig. 5.9) reveal the $-\text{CH}_2$ and $-\text{CH}_3$ signals that otherwise overlap in a 1D ^{13}C NMR spectrum. The CD-asphaltenes show the $-\text{CH}_2$ signals downfield of ~ 1.2 ppm, which were discussed earlier, and assigned to methylene groups close to the aromatic core (also in Figs. 5.10, 5.11). The signals of AOSA and P-asphaltenes once again appear broader than the corresponding CD-asphaltene signals.

22.7 ppm (^{13}C) slices

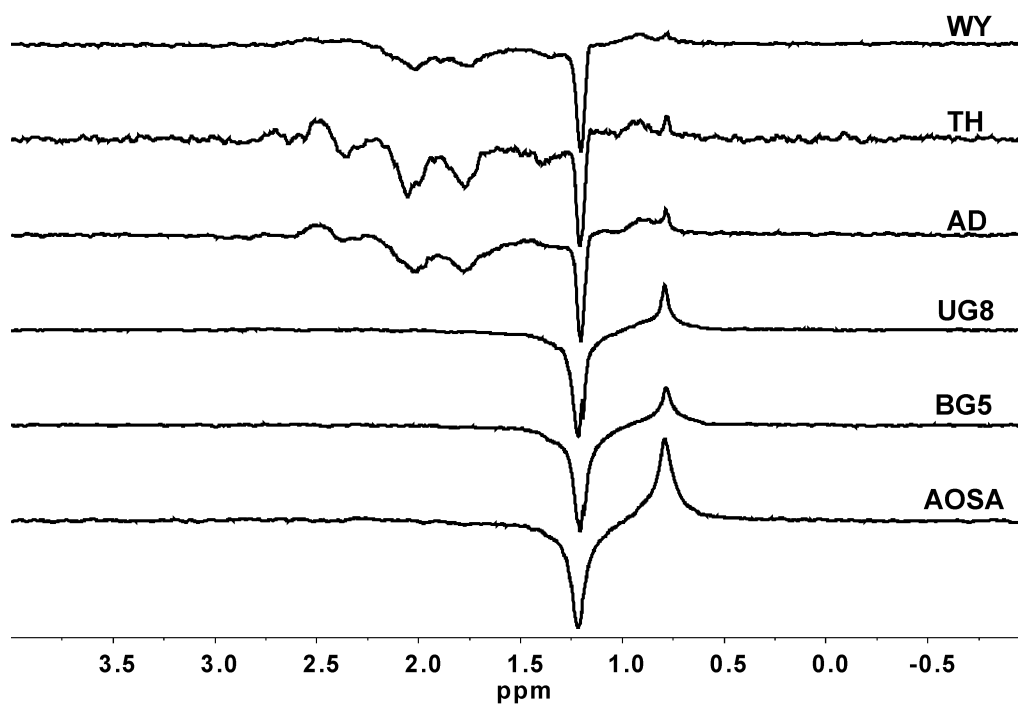


Figure 5.9. HSQC slices taken at $\delta_{13\text{C}} = 22.7$ ppm.

30 ppm (^{13}C) slices

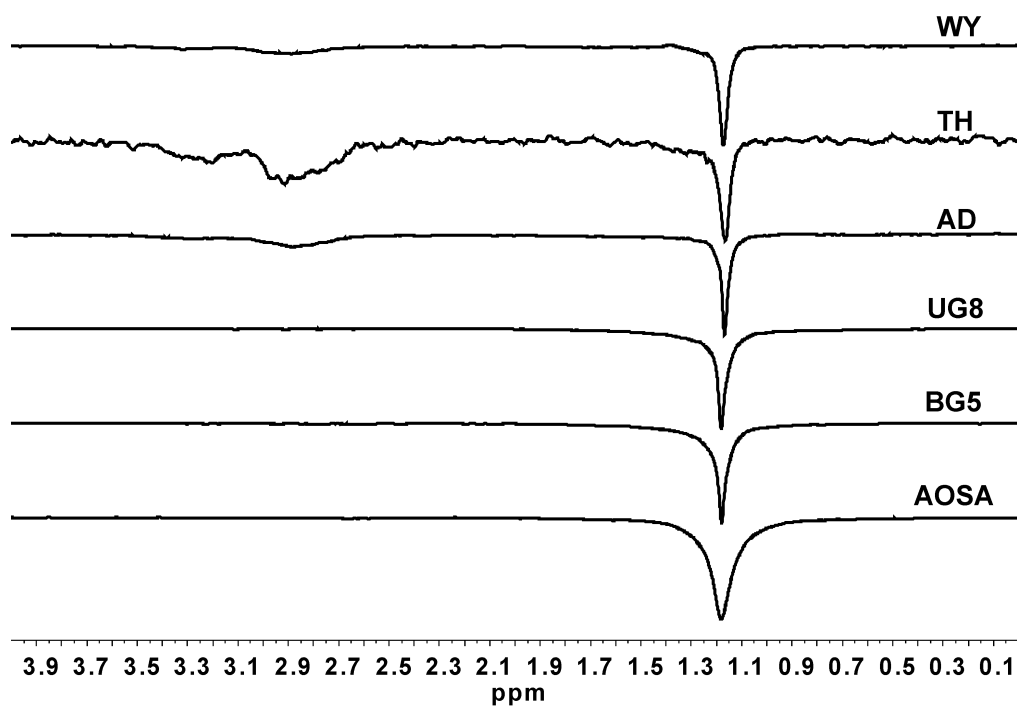


Figure 5.10. HSQC slices taken at $\delta_{13\text{C}} = 30$ ppm.

The signals of the 30 ppm slices (Fig. 5.10) represent the $-\text{CH}_2$ moieties that are γ or more removed from the aromatic rings. The AOSA signal appears to be the broadest, which could be due to the rigid alicyclic groups. A similar situation arises in the 32 ppm slice as well (Fig. 5.11), where the P-asphaltenes and AOSA also show a broad low-lying, broad signal in the 1.3-1.8 ppm range, assigned to rigid alicyclic groups. It is the strongest for AOSA, suggesting that AOSA have the largest alicyclic fraction among all the asphaltenes.

The 37 ppm slice (Fig. 5.12) can be assigned to $-\text{CH}_2$ groups α to a branched point in the chain ($\delta_{1\text{H}} \sim 1$ ppm) or the aromatic ring ($\delta_{1\text{H}} \sim 1.2$ ppm). Recall that TH and AD did not have signals from branched $-\text{CH}_3$ groups (Fig. 5.8), which explains the absence of the signal from an adjacent $-\text{CH}_2$ group in Fig. 5.12. The signal at ~ 1.2 ppm is also missing for TH, but inspection of all other slices at the different ^{13}C chemical shifts reveals that TH has majority of its $-\text{CH}_2$ groups resonating at higher ^1H chemical shifts. This suggests that TH has the shortest aliphatic chains, not more than 2-3 carbons long, most of them being close to the aromatic ring.

The slices extracted from the aromatic region (Fig. 5.13 and 5.14) show that the signals from the CD-asphaltenes are more intense and much better resolved, especially those at the higher ^{13}C chemical shift of 126.5 ppm. Also, the CD-asphaltene signals occur at a higher ^1H chemical shift. The reason for the AOSA and P-asphaltene aromatic signals having poor resolution, and also being broader than corresponding CD-asphaltene signals in general, is likely the concentration at which the experiments were performed, 30 g/L. At this concentration, the asphaltenes exist in an aggregated state. The larger the aggregates, the more restricted the motion. As explained while discussing relaxation, rigid molecules have

a shorter T_2 . In HSQC, the signals that survive the entire length of the sequence until the acquisition period without dephasing significantly, provide the most intense cross peaks.

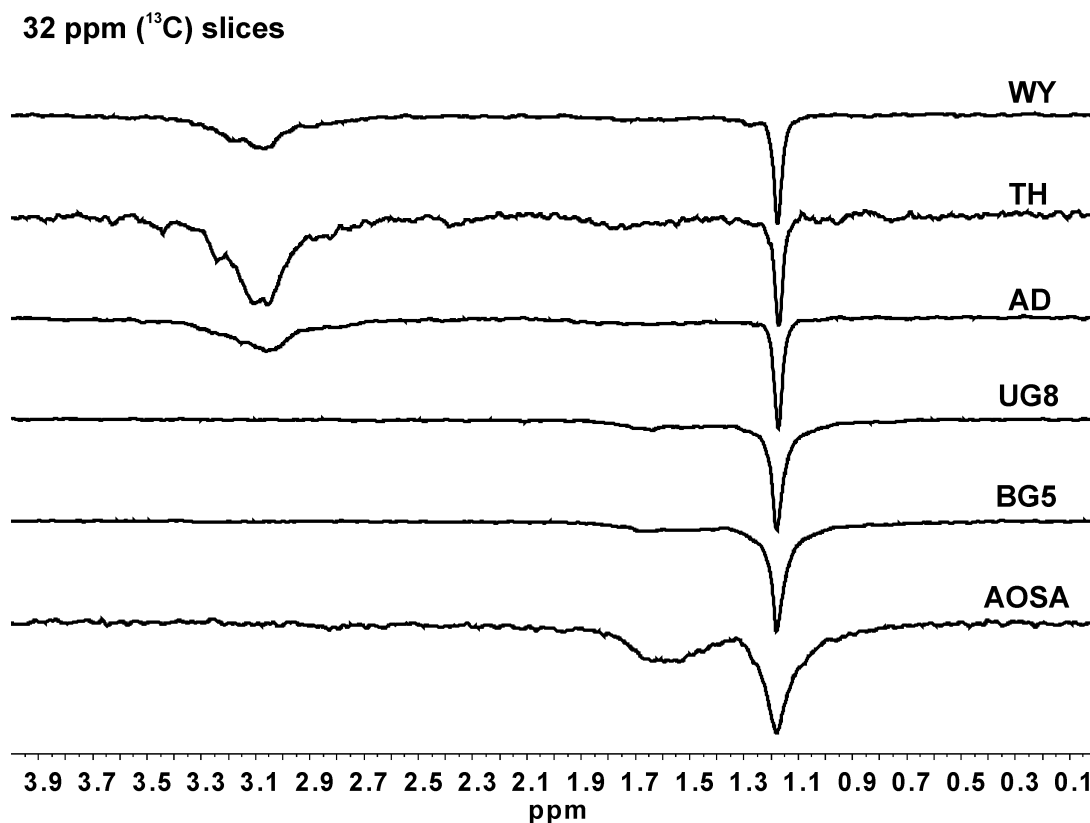


Figure 5.11. HSQC slices taken at $\delta_{13\text{C}} = 32$ ppm.

Signals from rigid components can have a very short T_2 , which leads to rapid decay of the intensity during the duration of the pulse sequence, resulting in weak cross-peaks. Also, a shorter T_2 means broader linewidth ($= 1/\pi T_2$). Therefore, at the current concentrations, the AOSA and P-asphaltenes occur as aggregates that are larger and more rigid in nature, compared to the CD-asphaltenes.

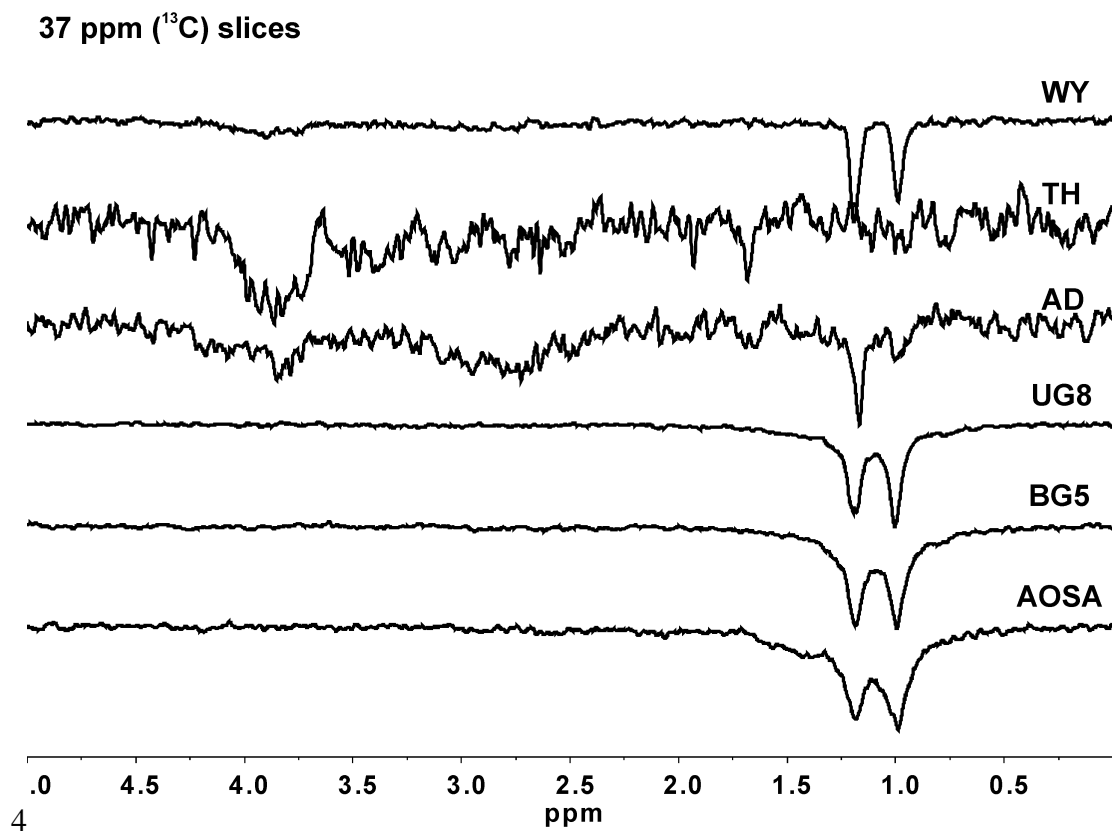


Figure 5.12. HSQC slices taken at $\delta_{13\text{C}} = 37$ ppm.

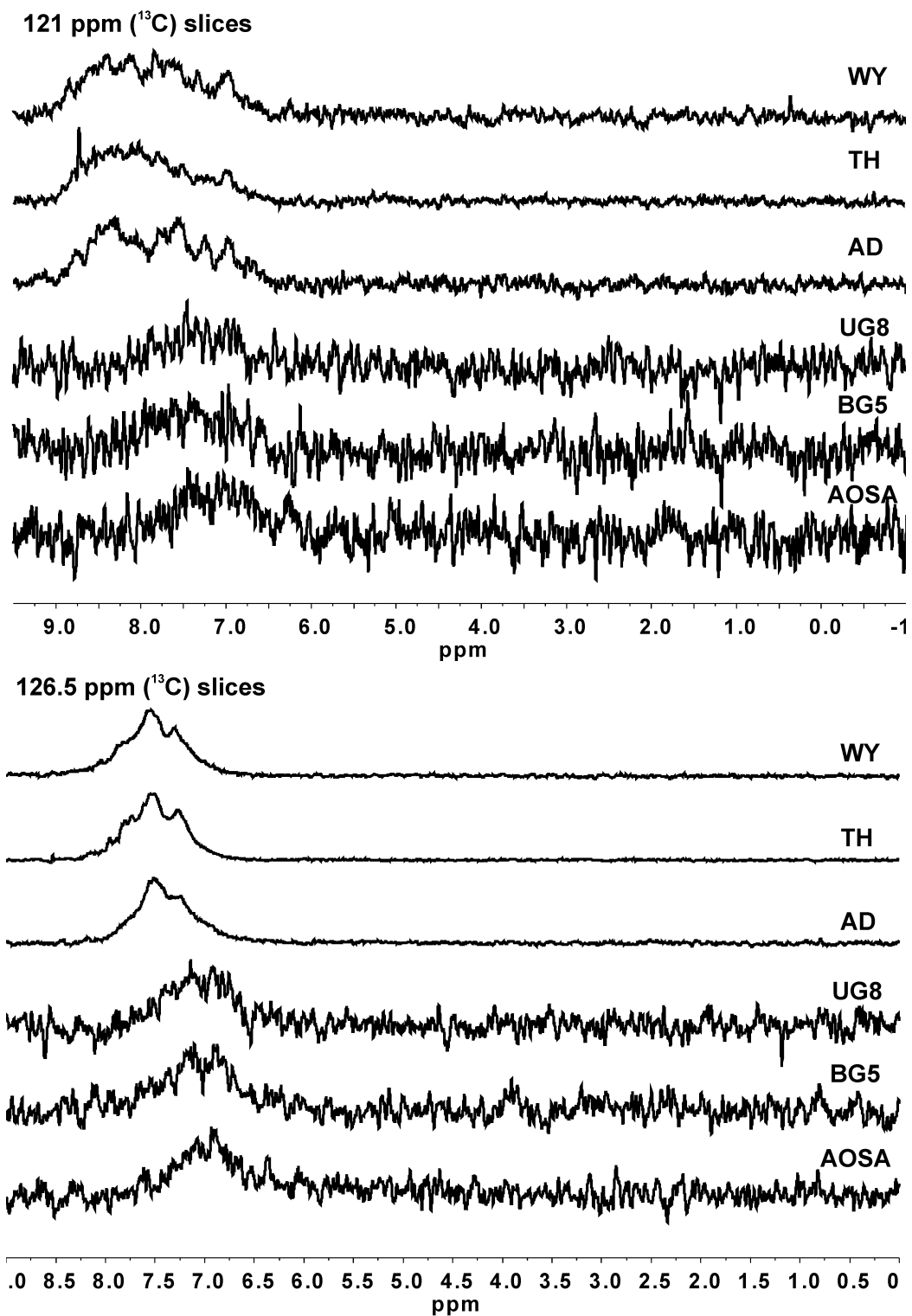


Figure 5.13. HSQC slices taken at $\delta_{^{13}\text{C}} = 121$ and 126.5 ppm.

5.4. Conclusions

This chapter sets out to compare asphaltene samples from six different sources using solution-state NMR spectroscopy, and highlights key structural differences between petroleum and coal-derived asphaltenes, the AOSA being considered as a P-asphaltene. It was shown that multiplicity edited HSQC can be effectively used to make assignments that are more accurate than one-dimensional methods and enables the identification of the finer differences between the spectra of P- and CD-asphaltenes. The CD-asphaltenes appear to have predominantly short aliphatic sidechains, whereas P-asphaltenes possess a distribution of long and short chains, consistent with a previous report.³⁰ A more extended network of alicyclic groups is present in P-asphaltenes, since a large fraction appears to be distant from the aromatic core. The alicyclic groups in coal asphaltene appear to be mostly naphthenic in nature, directly attached to the core. The P-asphaltene aromatic cores are also substituted to a greater extent, evinced by the low intensity of the C-H correlations in the aromatic region. The TH CD-asphaltenes have the shortest chains, while branched $-\text{CH}_3$ groups seem to be absent from both TH and AD asphaltenes. The weakness of the aromatic correlations and the overall greater broadness of the P-asphaltene signals suggest that at the concentrations at which these experiments were performed, they form larger and more rigid aggregates or clusters compared to the CD-asphaltenes. However, further investigation is required to verify this observation.

The qualitative differences between the two classes of asphaltenes observed here in the solution phase require quantitative validation. Since it is shown that all the P-asphaltenes have very similar characteristics regardless of the source, and that most of the CD-asphaltenes have a generally similar motif, it should suffice to quantitatively investigate

one of each class. In the following chapter, the UG8 and WY asphaltenes will be studied using solid-state NMR spectroscopy, where the effect of concentration is eliminated. Solid-state NMR spectroscopy also offers more detailed structural information, since the effect of orientation-dependent interactions is not lost due to random isotropic motion as in solution.

CHAPTER 6

6. COMPARISON OF PETROLEUM AND COAL DERIVED ASPHALTENE STRUCTURE USING SOLID-STATE NMR SPECTROSCOPY

6.1. Overview

As stated in the previous chapter, coal-derived (CD) and petroleum (P) asphaltenes are structurally different and some of these differences were highlighted. One type of P- and one of CD-asphaltene are investigated further using solid-state NMR spectroscopic techniques. Cross-polarization dynamics is used quantitatively to derive average asphaltene structures and also to set limits to the size of the aromatic core. Refocused CP-DIVAM enables differentiation between rigid and mobile domains, highlighting key differences between the two types of asphaltene. A more refined, alternative approach to CP dynamics, and how it should be used for complex substances such as asphaltene, is presented here and is compared to the one presented in Chapter 4. Several preconceptions about asphaltene size and structure will be challenged and refined, while reinforcing certain observations made in previous chapters.

6.2. Experimental section

6.2.1. Asphaltene samples

The petroleum asphaltene sample used was UG8, while the coal derived asphaltene sample was WY, which are two of the asphaltene previously used in Chapter 5. The elemental compositions of UG8 petroleum (P) and WY coal-derived (CD) asphaltene (Table 6.1) were obtained from collaborators at Schlumberger-Doll Research, USA, who

provided the samples, and published previously by Andrews *et al.*³⁰ The principal differences are the dramatically higher sulfur content and a higher H:C atomic ratio of the UG8 P-asphaltenes.

Table 6.1. Elemental Analysis of UG8 petroleum and WY coal-derived asphaltenes.

	Wt %, dry					
	C	H	N	S	O	H:C atomic ratio
UG8 Petroleum asphaltene	81.07	7.11	1.02	8.94	1.6 (measured)	1.05
Wyoming (WY) Coal-derived asphaltene	89.41	6.04	1.43	0.13	2.99 (by difference)	0.81

6.2.2. Solid-state NMR Spectroscopy

All experiments were performed on an 11.74 T Bruker Avance III HD dedicated solid-state NMR spectrometer (499.85 MHz ¹H and 125.67 MHz ¹³C frequencies) equipped with four RF channels, using a 4.0 mm MAS quadruple resonance probehead with a 53 μ L rotor, at a spinning rate of 8 kHz. A recycle delay of 2.0 s was used for all experiments and a 3.0 μ s 90° pulse-width was used for both ¹H and ¹³C. Other than the variable contact time experiments (CP dynamics study), all other CP experiments were performed with a contact time of 0.8 ms for UG8 P-asphaltenes and 1.0 ms for WY CD-asphaltenes. 2048 scans were recorded for each variable contact time experiment and a 50 Hz exponential line broadening was used to improve resolution. The ¹H spin-lock field for all CP experiments was 55.6 kHz. Broadband ¹H decoupling was used for all experiments.

The pre-CP refocused DIVAM filtering sequence consists of a repeatable block of four pulses on the ¹H channel: 2 \times low-amplitude ($\leq 90^\circ$) r.f. pulses, 2 \times refocusing π -pulses, separated by interpulse delays of fixed duration which was automatically calculated by

rotor-synchronization to 8.0 kHz. The block was repeated 4 times for each experiment and the pulse powers used corresponded to a 3.0 μs 90° pulse on ^1H . Following the filtering sequence the magnetization was cross-polarized to ^{13}C using the exact same conditions as the CP experiments. A series of 19 measurements were carried out by increasing the excitation angle of the low-amplitude ‘minipulses’ in 5° steps from 0° to 90°, with 1024 scans at each step, and the peak areas were plotted against the excitation angles.

All spectral processing, deconvolution and analysis were done using the MestreNova software (version 9.0.1). The CP dynamics parameters were obtained by fitting the experimental curves (Figs. 6.3a and b) with the non-monotonic CP dynamics equation (Eq. 2.44, Chapter 2) on the statistical software Minitab 17, using a Levenberg- non-linear regression algorithm. The standard errors for the parameters were calculated by the software with a 95% confidence interval.

6.3. Results and Discussions

6.3.1. Spectral deconvolution

Figure 6.1 shows the deconvolution models for the ^{13}C CP NMR spectra of UG8 and WY asphaltenes obtained under 8 kHz MAS. The starting point of constructing the models was the fitting model used previously in Chapter 4 (Fig. 4.1). Since these samples are different from the one used in Chapter 4, all the chemical shifts and linewidths had to be adjusted to provide the optimum fit. Peaks were added at chemical shifts where shoulders or features were observed. For example, in the UG8 NMR spectrum (Fig. 6.1), the peak at 31.98 ppm was added to account for the obvious shoulder (i.e. not an artefact) present on the most intense aliphatic signal around ~30 ppm. Whether an obscure spectral feature is a

real signal or an artefact was determined by checking if it is consistent between the spectra at different contact times. The spinning sidebands were placed such that they are separated from the corresponding centerband by an integer multiple of around ~ 64 ppm ($= 8$ kHz/125.67 MHz), and their linewidths were kept the same as the centerband. A total of 25 and 26 peaks were fitted to the UG8 and WY spectra, respectively, including the spinning sidebands, which were 10 in UG8 and 15 in WY. The deconvolution models, along with details of the fitting parameters such as linewidths and Lorentzian/Gaussian (L/G) lineshape ratios, have been provided in Appendix 4. A pictorial depiction of the different types of carbons assigned is provided in Fig. 6.2 along with their description in Table 6.2, while the assignments for each fitted isotropic peak can be found in Tables 6.3 (UG8) and 6.4 (WY). Not much information can be gathered from comparing a single spectrum of each kind of asphaltene, other than the obvious conclusion that WY coal-derived (CD) asphaltenes have a larger aromatic fraction and smaller aliphatic fraction. It would also be unwise to perform quantitative analyses on these two spectra since CP spectra of complex polyaromatic hydrocarbon (PAH) systems are inherently non-quantitative. To obtain more meaningful and quantitative information, the build-up of ^{13}C magnetization over increasing contact time, i.e. the CP dynamics, were studied. The CP dynamics curves are shown in Figs. 6.3a and 6.3b, and the following section discusses them in detail.

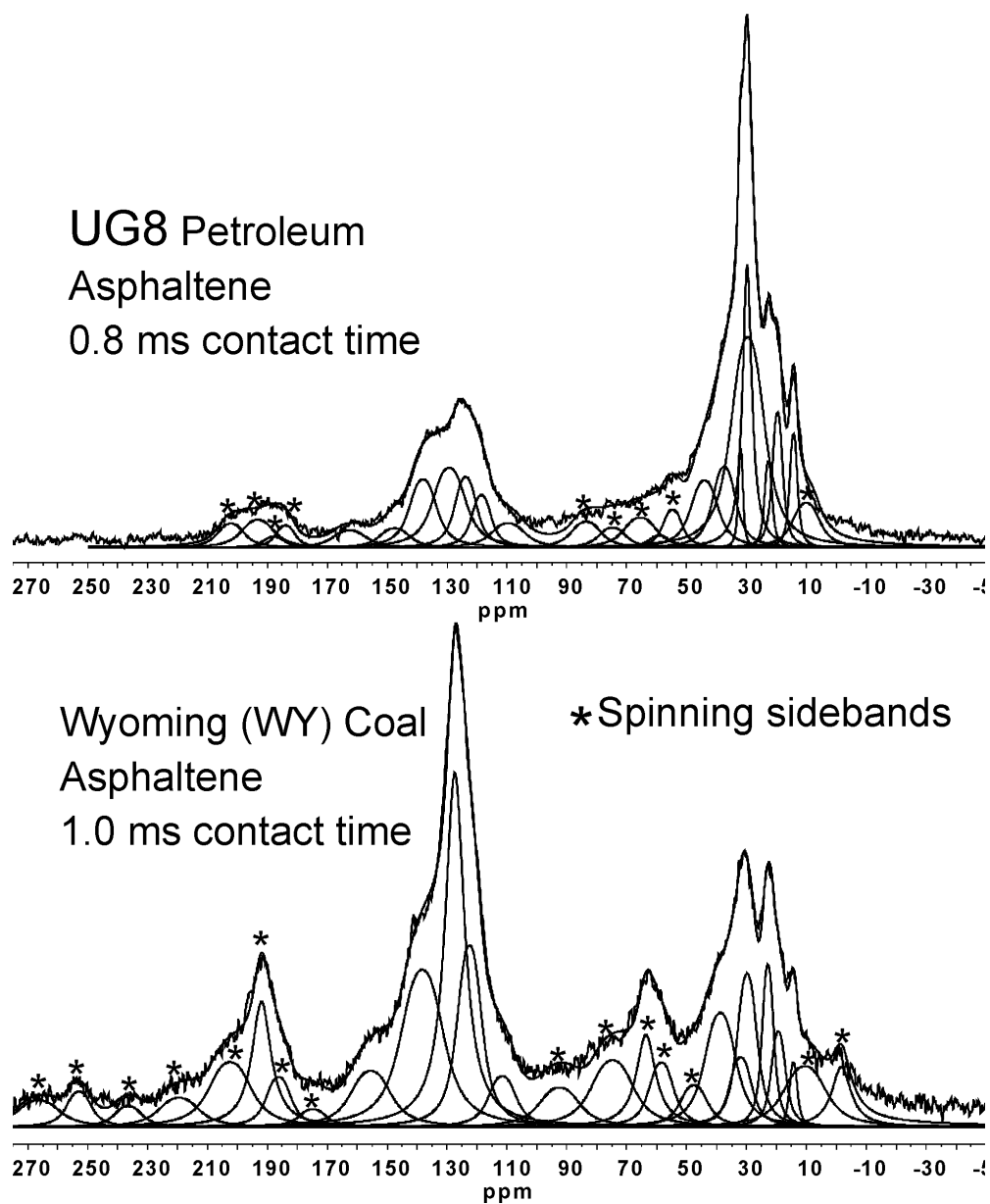


Figure 6.1. ^{13}C CP-MAS NMR spectra of (top) UG8 petroleum asphaltenes and (bottom) Wyoming coal asphaltenes obtained under 8 kHz MAS, with 0.8 and 1.0 ms contact times respectively, showing the deconvoluted peaks.

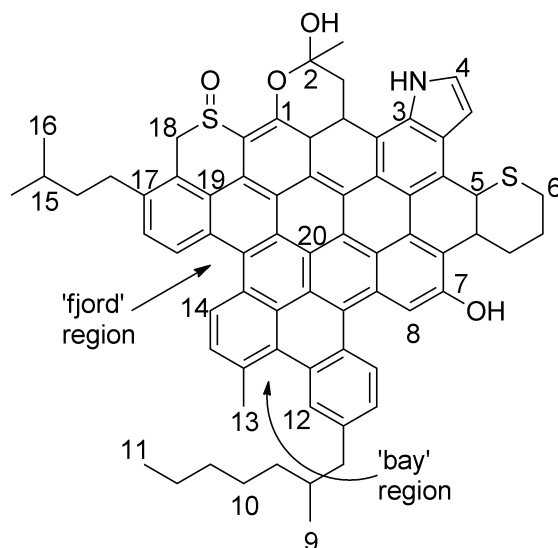


Figure 6.2. Hypothetical asphaltene molecule showing the different carbon types for which were assigned to the fitted peaks in the CP-MAS spectra. The types of carbons corresponding to each number on the figure are listed in Table 6.2.

Table 6.2. Description of the different carbon types numbered in Figure 6.2.

Carbon # in Figure 6.2	Type of carbon	Carbon # in Figure 6.2	Type of carbon
1	$C_{\text{sub-O-C}}^{\text{a}}$	11	terminal $-\text{CH}_3$
2	anomeric O-C-O	12	'bay' type $C_{\text{H,ar}}^{\text{a}}$
3	$C_{\text{sub-N}}^{\text{a}}$	13	CH_3 -aryl
4	$C_{\text{H,ar}}$ 'α' to $C_{\text{sub-N}}^{\text{a}}$	14	'fjord' type $C_{\text{H,ar}}^{\text{a}}$
5	Cyclic CH	15	Aliphatic $-\text{CH}$
6	$-\text{CH}_2\text{-S-R/cyclic } -\text{CH}_2$	16	isobutyl $-\text{CH}_3$
7	$C_{\text{sub-O-H}}^{\text{a}}$	17	$C_{\text{sub-R}}^{\text{a}}$
8	$C_{\text{H,ar}}$ 'α' to $C_{\text{sub-O}}^{\text{a}}$	18	cyclic $-\text{C-S=O}$
9	branched $-\text{CH}_3$	19	C_{db}^{a}
10	ali. $^{\text{a}}$ $-\text{CH}_2$ not 'α' to ar. or to term. Methyl group	20	C_{tb}^{a}

^a $C_{\text{H,ar}}$ = aromatic $-\text{CH}$; C_{sub} = substituted/ipso aromatic C; C_{db} = double bridgehead aromatic C; C_{tb} = triple bridgehead aromatic C. ali. = aliphatic.

6.3.2. ^1H -to- ^{13}C CP Dynamics

The curve fitting for the variable contact time data was initially done using both Eq. 2.47 and Eq. 2.48, but on comparison Eq. 2.48 was found to provide a better fit, especially in cases where the build-up portion of the curves show two distinct components (See Appendix 4). Hence, Eq. 2.48 will be used to study the CP dynamics in this chapter.

The inverse of the T_{CP} time constants, i.e., the CP rates (R_1 for T_{CP1} , R_2 for T_{CP2}), provide a measure of the scaling of the theoretical single bond C-H dipolar coupling (D_{CH}), which reflects the distance of the carbon nuclei of interest to the ^1H spin-bath and its segmental mobility. It provides a more intuitive and direct measure of the effective dipolar coupling and spin-diffusion. A typical D_{CH} for a C-H spin pair with an internuclear distance of 1.10 Å, in the absence of any motional averaging, is 22.7 kHz. If the cross-polarization rate is comparable to this value of D_{CH} , it implies directly bonded C-H pairs with no or little motional averaging. Significantly scaling smaller CP rates could result from increased distance between the carbon nuclei and the proton spin bath, or segmental motion, or both.

Fitting results: In Table 6.3 and 6.4, the cross-polarization parameters (T_{CP1} , R_1 , T_{CP2} , R_2 , $T_{1\rho\text{H}}$ and b) are presented, obtained by fitting the experimental data with the non-monotonic CP model (Eq. 2.48) for UG8 and WY asphaltenes respectively. The 147.51 ppm signal in UG8, has a large error associated with its R_1 (33.3 ± 33.3 kHz), making the R_1 value unusable to obtain structural information. The same applies to the R_2 value of the 111.59 ppm signal in WY, calculated as 11.1 ± 9.9 kHz.

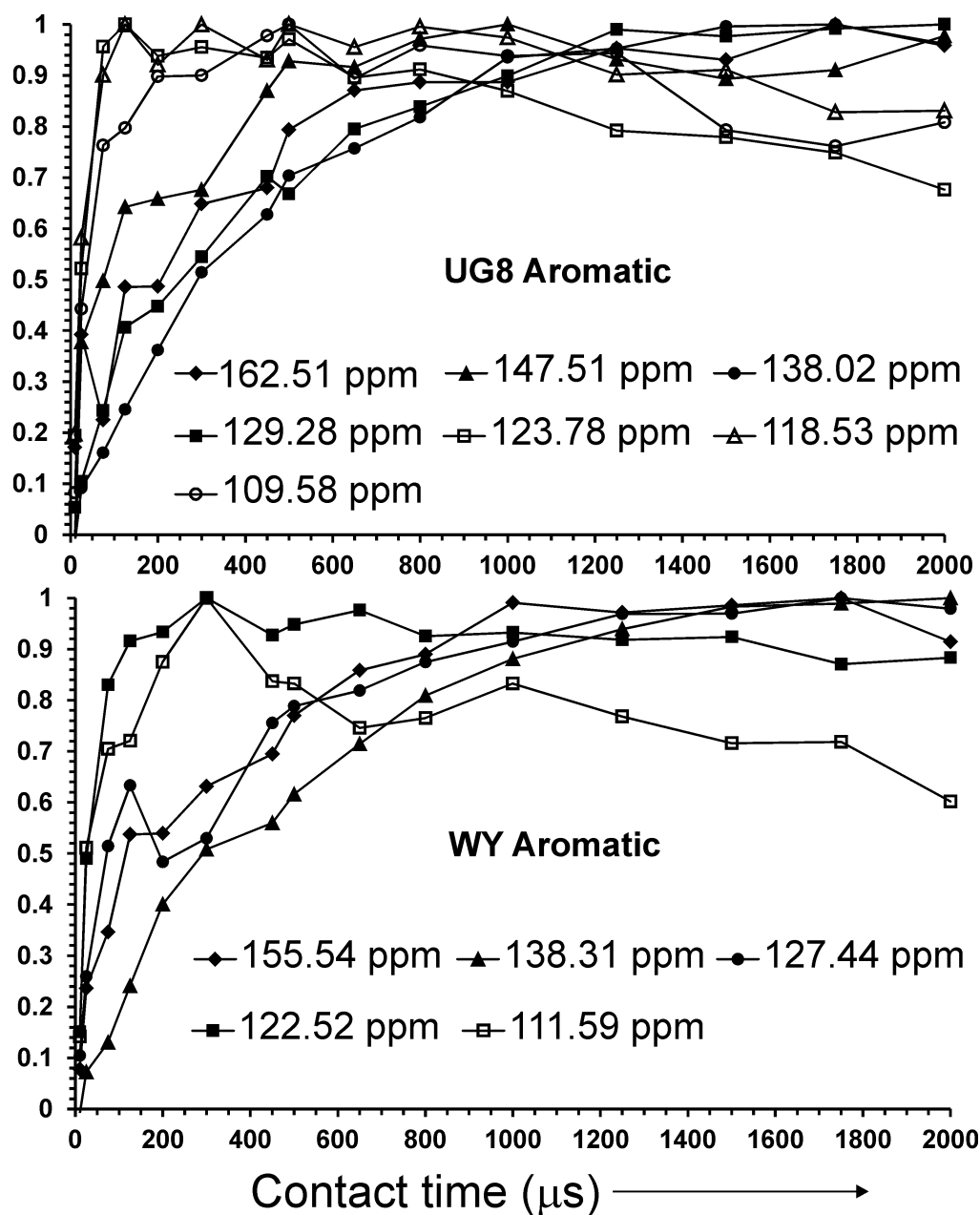


Figure 6.3a. ^1H -to- ^{13}C cross-polarization build-up curves for the deconvolved aromatic peaks of the ^{13}C CP-MAS NMR spectra of UG8 and WY asphaltenes. The normalized intensities are plotted against increasing contact time. The anomeric (O-C-O) carbon signals have been grouped with the aromatic signals

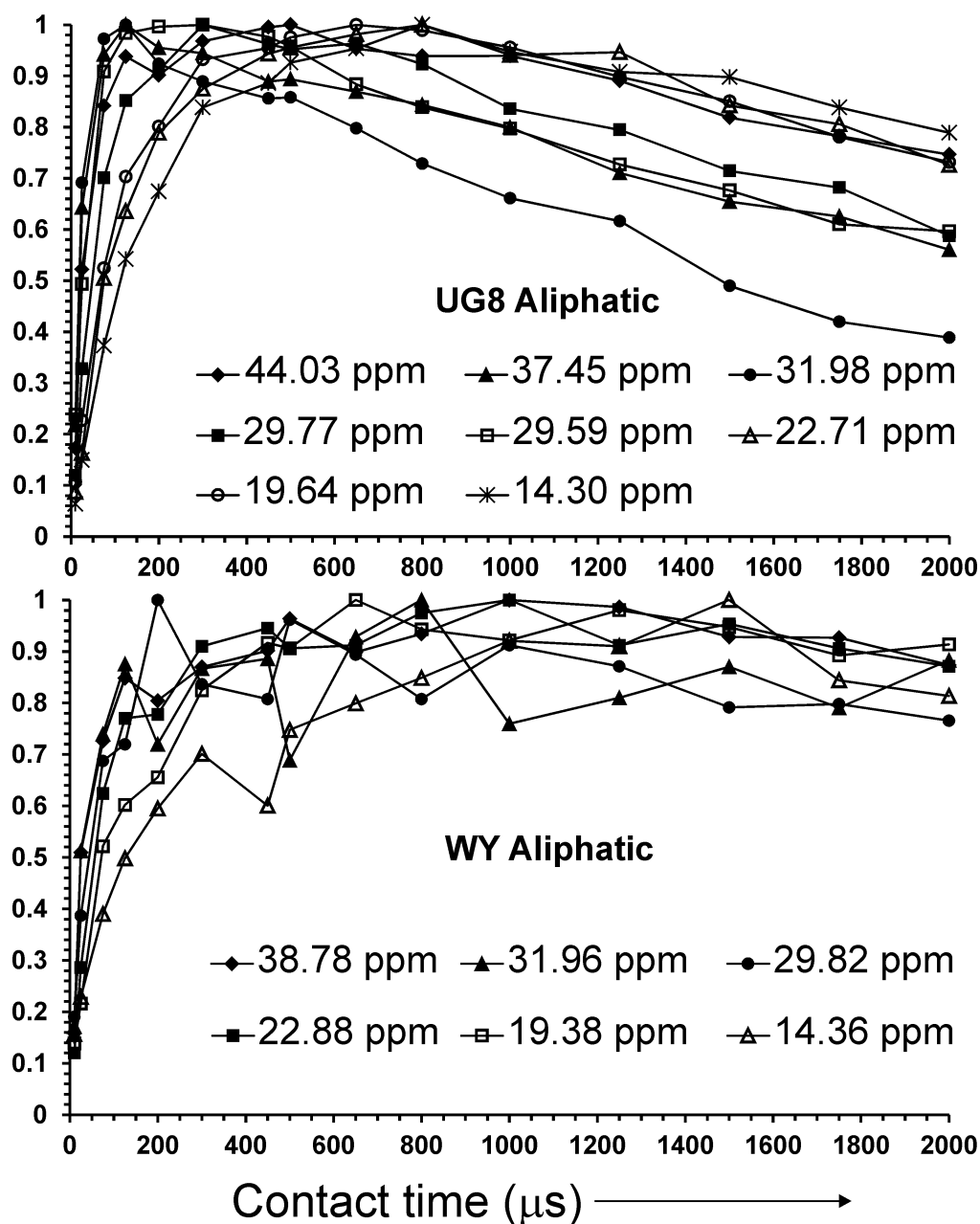


Figure 6.3b. ^1H -to- ^{13}C cross-polarization build-up curves for the deconvolved aliphatic peaks of the ^{13}C CP-MAS NMR spectra of UG8 and WY asphaltenes. The normalized intensities are plotted against increasing contact time.

Although not directly attached to any protons, the ipso-carbons bonded to O and N, ($C_{\text{sub-O-C}}$, $C_{\text{sub-N}}$, $C_{\text{sub-OH}}$) (UG8: 162.5 ppm, WY: 155.54 ppm), have $R_1 \geq 20$ kHz indicating presence of cross-polarizing protons which are very close if not bonded to the said carbon. This could be due to hydrogen bonding interactions which restrict mobility, since the O and

N containing substituents are polar and also because these carbons are exposed to many neighbouring protons, being on the periphery of the aromatic core. This is corroborated by the fact that the peripheral aromatic $-CH$ moieties, $-C_{H,ar}$ (UG8: 123.78, 118.53 ppm, WY: 127.44, 122.52 ppm) also exhibit comparable R_1 values in the range 14-25 kHz. The 147.51 ppm signal in UG8, assigned to aromatic carbons substituted by N-containing groups exhibits the fastest R_2 (12.9 ± 3.4 kHz) among the $C_{sub-O-C}$, C_{sub-N} , C_{sub-OH} carbons, indicating reduced segmental motion in the protons that cross-polarize to these groups, compared to the other heteroatom substitutions discussed above. The rigidity can be ascribed to the nitrogen atoms being in pyrrole/pyrrolidine type rings, which are known to be common in asphaltenes,¹⁵⁹ which can also participate in hydrogen bonding. The significantly smaller R_2 values (0.5 ± 0.2 kHz) of the O-substituted ipso-carbons (UG8: 162.51 ppm, WY: 155.54 ppm) indicate pronounced segmental mobility of the cross-polarizing protons. The alkyl substituted (C_{sub-R}) and double bridgehead (C_{db}) aromatic carbons (UG8: 138.02 ppm, WY: 138.31 ppm) exhibit significantly reduced R_1 (4.0 ± 0.8 and 4.5 ± 0.8 kHz respectively) because of no attached hydrogens. The 127.44 ppm signal in WY coal asphaltenes has a large R_1 (25.0 ± 6.3 kHz) which indicates that a significant fraction of aromatic $-CH$ ($C_{H,ar}$) groups resonate in this region, unlike the corresponding 129.28 ppm UG8 signal with a significantly smaller R_1 of 8.3 ± 0.7 kHz, justifying its assignment only to double and triple bridgehead carbons. The reduced R_2 of both the 127.44 ppm (WY) and 129.28 ppm (UG8) signals, at 0.2 ± 0.1 and 1.0 ± 0.1 kHz respectively, are due to the triple bridgehead carbons (C_{tb}), which are remote from the 1H spin-bath.

The 122.52 ppm signals of WY and the corresponding 123.78 and 118.53 ppm signals of UG8, all have moderately large R_1 and R_2 , both the values being similar, in the range 14-

20 kHz, which means that the dipolar coupling mechanism of CP dominates over spin-diffusion, and that these signals are from $C_{H,ar}$ groups. The majority of the $C_{H,ar}$ of UG8 resonate in the 118-124 ppm region indicating large number of alkyl substitutions, which decrease the chemical shift of adjacent $C_{H,ar}$ groups from the base benzene shift of 128.6 ppm.

Table 6.3. CP dynamics parameters for the deconvolved ^{13}C CP-MAS peaks of UG8 P-asphaltenes

UG8 Petroleum Asphaltenes						
$\delta\{^{13}C\}$ ppm	Assignment	T_{CP1} , ms (R_1 , kHz)	T_{CP2} , ms (R_2 , kHz)	$T_{1\rho H}$, ms	$b/2\pi$, kHz	%C
162.51	$C_{sub-O-C}/$ $C_{sub-O-H}$	0.05±0.02 (20.0±4.0)	1.96±0.73 (0.5±0.2)	14.4 ±10.9	0.5 ±0.2	2.0 ±0.7
147.51	C_{sub-N}	0.03±0.03 (33.3±33.3)	0.77±0.21 (12.9±3.4)	25.1 ±21.8	0.6 ±0.2	3.5 ±0.1
138.02	C_{sub-R}/C_{db}	0.25±0.05 (4.0±0.8)	1.89±0.39 (0.5±0.1)	13.3 ±2.5	0.5±0.2	13.3 ±0.6
129.28	C_{db}/C_{tb}	0.12±0.01 (8.3±0.7)	2.71±0.28 (1.0±0.1)	10.6 ±1.7	0.5 ±0.0	16.3 ±6.5
123.78	$C_{tb}/C_{H,ar}$	0.05±0.01 (20.0±4.0)	0.07±0.01 (14.3±2.0)	5.28 ±0.48	9.5 ±1.6	5.9 ±0.5
118.53	$C_{H,ar}$: 'bay' type and ' α ' to $C_{sub-O/N}$	0.06±0.02 (16.7±5.6)	0.05±0.01 (20.0±4.0)	10.9 ±2.4	15.9 ±4.8	5.5 ±0.2
109.58	anomeric O-C-O	0.19±0.08 (5.3±2.2)	0.06±0.02 (16.7±5.6)	5.8 ±2.0	11.1 ±1.6	2.3 ±0.1
44.03	ali. or cyc. C- S=O/cyclic -CH	0.12±0.02 (8.3±1.4)	0.05±0.01 (20.0±4.0)	5.5 ±0.8	11.1 ±1.6	5.1 ±0.2
37.45	cyclic -CH.	0.05±0.01 (20.0±4.0)	0.05±0.01 (20.0±4.0)	5.3 ±0.2	15.9 ±1.6	5.6 ±0.1
31.98	ali. -CH, -ali./cyc - CH_2 ' α ' to ar.	0.05±0.01 (20.0±4.0)	0.15±0.03 (6.7±1.3)	1.9 ±0.1	19.1 ±0.3	1.8 ±0.0
29.77	ali. - CH_2 not ' α ' to ar. or to term. meth.	0.21±0.00 (4.8±0.1)	0.08±0.04 (12.5±6.3)	2.9 ±0.3	-4.8±0.9	9.7 ±3.1
29.59	ali. - CH_2 /cyc. - CH_2 /cyc. - CH_2 -S-R	0.07±0.01 (14.3±2.0)	0.05±0.01 (20.0±4.0)	3.0 ±0.1	7.9 ±1.6	22.6 ±0.0
22.71	isobut. - CH_3 /- CH_2 ' α ' to term. meth.	0.09±0.02 (11.1±2.5)	1.24±0.77 (0.8±0.5)	2.6 ±0.5	0.3±0.2	2.2 ±0.1
19.64	CH_3 -ar./branched - CH_3	0.07±0.01 (14.3±1.0)	0.67±0.16 (1.5±0.4)	3.3 ±0.3	-0.3±0.2	4.4 ±0.1
14.30	term.- CH_3	0.11±0.02 (9.1±1.7)	0.71±0.69 (1.4±1.4)	4.8 ±2.0	0.5±0.3	3.0 ±0.7

T_{CP1} and T_{CP2} are the CP time constants. R_1 and R_2 are the CP rate constants. $T_{1\rho H}$ is the longitudinal relaxation in the rotating frame. The quantity b is the C-H dipolar coupling constant. The b obtained from the fitting was in radians/s, hence was divided by 2π to obtain the kHz value. The %C values were calculated using Eq. 6.1. $C_{H,ar}$ = aromatic -CH; C_{sub} = substituted/ipso aromatic C; C_{db} = double bridgehead aromatic C; C_{tb} = triple bridgehead aromatic C. ali. = aliphatic; isobut. = isobutyl; meth = methyl; term. = terminal. The assigned carbon types are described in Fig. 6.2 and Table 6.2.

Table 6.4. CP dynamics parameters for the deconvolved ^{13}C CP-MAS peaks of Wyoming CD-asphaltenes.

Wyoming (WY) Coal Derived Asphaltenes						
$\delta\{^{13}\text{C}\}$ ppm	Assignment	T_{CP1} , ms (R_1 , kHz)	T_{CP2} , ms (R_2 , kHz)	$T_{1\rho\text{H}}$, ms	$b/2\pi$, kHz	%C
155.54	$C_{\text{sub-O-H}}/$ $C_{\text{sub-N}}$	0.05±0.01 (20.0±4.0)	1.99±0.28 (0.5±0.1)	18.2 ±6.3	0.6±0.1	7.5 ±0.2
138.31	$C_{\text{sub-R}}/C_{\text{db}}$	0.22±0.04 (4.5±0.8)	2.81±0.56 (0.3±0.1)	13.1 ±3.0	0.5±0.1	25.1 ±1.6
127.44	$C_{\text{tb}}/ C_{\text{H,ar}}$	0.04±0.01 (25.0±6.3)	4.13±1.2 (0.2±0.1)	5.2 ±0.9	0.5±0.1	28.8 ±1.2
122.52	C_{tb} /'bay' type $C_{\text{H,ar}}$	0.07±0.01 (14.3±2.0)	0.05±0.01 (20.0±4.0)	17.8 ±4.1	9.5±2.2	11.7 ±0.3
111.59	anomeric O-C-O/ $C_{\text{H,ar}}$ 'α' to $C_{\text{sub-O/N}}$	0.11±0.04 (9.1±3.3)	0.09±0.08 (11.1±9.9)	5.3±1.7	17.5 ±3.2	6.0 ±0.6
38.78	cyclic -CH.	0.19±0.05 (5.3±1.4)	0.13±0.06 (7.7±3.6)	19.8±15.9	15.9 ±0.6	5.6 ±0.9
31.96	ali. -CH, -ali./cyc - CH_2 'α' to ar.	0.06±0.03 (16.7±8.4)	0.26±0.09 (3.8±2.9)	40.9±103.5	15.9 ±0.8	2.7 ±0.2
29.82	ali. - CH_2 not 'α' to Ar. or term. meth	0.09±0.06 (11.1±7.4)	0.04±0.02 (25.0±12.5)	10.6±6.3	0	4.7 ±0.3
22.88	isobut. - CH_3 / $-CH_2$ 'α' to term. meth.	0.04±0.01 (25.0±6.3)	0.35±0.08 (2.9±0.7)	10.9±6.0	0	3.0 ±0.2
19.38	CH_3 -Ar./branched - CH_3	0.04±0.01 (25.0±6.3)	0.57±0.09 (1.8±0.2)	93.5±149.4	0.9±0.9	2.1 ±0.1
14.36	term.- CH_3	0.04±0.01 (25.0±6.3)	2.11±1.02 (0.5±0.2)	8.3±5.9	0.6±0.6	2.9 ±0.1

T_{CP1} and T_{CP2} are the CP time constants. R_1 and R_2 are the CP rate constants. $T_{1\rho\text{H}}$ is the longitudinal relaxation in the rotating frame. The quantity b is the C-H dipolar coupling constant. The b obtained from the fitting was in radians/s, hence was divided by 2π to obtain the kHz value. The %C values were calculated using Eq. 6.1. $C_{\text{H,ar}}$ = aromatic -CH; C_{sub} = substituted/ipso aromatic C; C_{db} = double bridgehead aromatic C; C_{tb} = triple bridgehead aromatic C. ali. = aliphatic; isobut. = isobutyl; meth = methyl; term. = terminal. The assigned carbon types are described in Fig. 6.2 and Table 6.2.

Conversely, WY CD-asphaltene aromatic carbons are substituted to a lesser extent, evinced by the higher chemical shift (127.44 ppm) of a significant fraction of the $C_{\text{H,ar}}$ groups. The lower chemical shift $C_{\text{H,ar}}$ groups also represent 'bay' type configuration, while those at the higher (>125 ppm) represent 'fjord' type configurations (see Fig 6.2), which shows that while 'bay' regions are present on both the asphaltenes, only WY CD-asphaltenes have 'fjord' motifs. Moreover, the chemical shifts of $C_{\text{H,ar}}$ groups closer to ~130 ppm are characteristic of small aromatic rings which are covalently tethered to a larger PAH, as seen

in hexabenzocoronene derivatives.^{160,161} This shall be investigated further in the following section.

The signals at 109.58 ppm (UG8) and 111.59 ppm (WY) exhibit moderately low R_1 values of 5.3 ± 2.2 and 9.1 ± 3.3 kHz respectively, which indicates that they are from non-protonated carbons. Their chemical shifts, and the large R_2 (rigid) of 16.7 ± 5.6 kHz of the UG8 signal, point to them being cyclic ketal-anomeric (O-CRR'-O) carbons.¹⁶²

All the terminal aliphatic carbons, and the ones which are α , β or γ from free end of a sidechain, exhibit significantly reduced R_1 values in the range 4.8 ± 0.01 to 11.1 ± 2.5 kHz for the UG8 asphaltenes, compared to those in WY asphaltenes, in the range (11.1 ± 7.4 to 25 ± 6.3 kHz) (UG8: 14.30, 22.71, 29.77 ppm, WY: 14.36, 22.88, 29.82 ppm). This is a strong indicator of the UG8 asphaltenes possessing longer, hence more mobile aliphatic sidechains, which diminishes the effective dipolar coupling and reduces CP efficiency. The groups in the middle of the chain (UG8: 22.71, 29.77 ppm, WY: 22.88, 29.82 ppm) also show smaller R_2 values in UG8 (0.8 ± 0.5 to 12.5 ± 6.3 kHz) compared to those on WY (2.9 ± 0.7 to 25 ± 12.5 kHz), which suggests that ^1H spin-diffusion is disrupted by segmental motion, corroborating the above statement. The methyl groups directly attached to the aryl rings in WY asphaltenes (19.38 ppm) have a larger R_1 of 25.0 ± 6.3 kHz, compared to the 14.3 ± 1.0 kHz R_1 in UG8 (19.64 ppm). This is a result of WY asphaltenes having a larger aromatic ^1H spin-bath, and these methyl groups being very close to the aromatic core. The broad UG8 peak at 29.59 ppm exhibits large and similar R_1 and R_2 values, 14.3 ± 2.0 and 20 ± 4.0 kHz respectively, which is coherent with its assignment to alicyclic $-\text{CH}_2$ groups and chain $-\text{CH}_2$ groups α to aryl rings. The rigidity of these groups allow fast magnetization build-up through predominantly the dipolar coupling mechanism.

One of the overall differences between the aliphatic carbon signals of UG8 and WY asphaltenes is that in UG8, most of the signals are comparatively narrower (smaller linewidth) than their WY counterpart, except those assigned to alicyclic groups. A narrower linewidth is characteristic of greater mobility. Also, the comparison of the aliphatic CP build-up curves (Fig. 6.3b) show that the decay of magnetization due to ^1H spin-lattice relaxation in the rotating frame starts occurring earlier in UG8 aliphatic signals across the board. This is evidence that ^1H spin-diffusion is less effective for the UG8 sidechains, likely due to the higher degree of local mobility in them, which is a direct consequence of longer chain lengths. From the assignments, it can also be seen that UG8 asphaltenes have a significantly larger alicyclic fraction and sulfur functionalities, which is consistent with the elemental analysis (UG8: 8.94 wt% S, WY: 0.13 wt% S).

Quantification using CP dynamics: The percentages of the different types of carbon (%C) were calculated using Eq. 6.1:

$$\%C = \frac{I_0^i}{\sum I_0^i} \times 100 \quad \text{Equation 6.1}$$

where I_0^i is the equilibrium magnetization of the i^{th} fitted peak, the value of which was obtained from Eq. 2.44. Equations 2.44 and 2.43 can provide a quantitative I_0 only when the basic CP condition, $T_{\text{CP}} < T_{1\rho\text{H}}$, is valid, as in this case. In other words, if the ^1H spin-lattice relaxation in the rotating frame starts before the completion of ^1H to ^{13}C magnetization transfer, Eq. 2.44 (or Eq. 2.43) cannot be used to study CP dynamics.

Using Eq. 6.1, the percentages of aromatic and aliphatic carbon in both asphaltenes were found to be close to values observed previously via solution-state NMR techniques for the same samples³⁰ and the small differences can be addressed by a specific assignment, namely that of the anomeric carbons. Andrews *et al.*³⁰ reported the aromaticities of UG8 and WY to be 50.1% and 82.2%, respectively, where they defined the aromatic region of the ¹³C NMR spectrum as 108-160 ppm, with protonated carbons in the lower part of that range. In this study, we have assigned the lower ppm values of that range (UG8: 109.58 ppm, WY: 111.59 ppm) to anomeric (O-C-O) carbons instead of aromatic carbons, which yields aromaticity values of 45.0% (UG8) and 73.0% (WY). If these signals were to belong to protonated aromatic carbons, they would show correlations in a ¹H-¹³C heteronuclear correlation spectrum. In a solution-state 2D heteronuclear single quantum coherence (HSQC) experiment (Chapter 5), it was seen that UG8 asphaltenes show no ¹H-¹³C correlations below a ¹³C chemical shift of 115 ppm, supporting the assignment in this chapter. However, the HSQC spectrum for WY shows a weak, but clear correlation around a ¹³C chemical shift of ~111 ppm. Therefore, it is likely that for WY coal asphaltenes, this region contains signals from both aromatic and anomeric carbons, whereas the corresponding resonances for UG8 represent only the anomeric carbons. Nonetheless, the reasonably good agreement with previous quantitative results³⁰ support that this approach can be used to obtain quantitative information from CP experiments on asphaltenes.

Using these quantitative measures of the different carbon moieties, certain important structural parameters can be computed. In the CP NMR spectrum of WY (Fig. 6.1), it was observed that the 14.36 ppm -CH₃ ¹³C peak has significant overlap with the 10.55 ppm spinning sideband, which is much broader and has a larger area under it, making quite likely

to contain contribution from methyl carbons. On inspection of the WY ^{13}C NMR spectrum, it was observed that approximately half of the area of this sideband lies above 10 ppm, where methyl carbons resonate. Thus, half of this sideband was assigned to $-\text{CH}_3$ groups. The average length of aliphatic chains was determined by dividing the fraction of aliphatic $-\text{CH}_3$, $-\text{CH}_2$, $-\text{CH}$ and C by the fraction of $-\text{CH}_3$. Naturally, the average chain length will be fractionally overestimated because all aliphatic carbons are included in the calculation even if they are not chain groups. This is unavoidable due to the large amount of overlapping signals, especially in a broad solid-state spectrum. Nevertheless, it will be overestimated for both the asphaltenes, which makes the values comparable. The average chain lengths calculated in this manner were 7.4 for UG8 and 4.2 for WY, which is coherent with the prevailing notion that petroleum asphaltenes possess longer alkyl chains. Andrews *et al.*³⁰ reported that CD-asphaltenes have a small fraction of alkyl chains that are at least 9 carbons long, but evidence for such long chains was not found in this work, although the above-stated conclusion cannot be completely ruled out since the experiments by Andrews *et al.*³⁰ were performed in the solution-state, which offer better resolution. However, AFM imaging results have shown that CD-asphaltenes are unlikely to have such long chains.⁵⁷ The aromatic condensation index, χ_b ,^{30,58} is usually calculated by dividing the fraction of bridgehead carbons by the aromaticity and provides a measure of the PAH size. However, spectral overlap raises problems in this case as well, since bridgehead and non-bridgehead carbons appear in the same ppm ranges (Tables 6.3 and 6.4). Thus instead of one specific value, upper and lower limits for the χ_b parameter can be calculated by including and excluding, respectively, the peaks that contain contributions from both quaternary and aromatic $-\text{CH}$ carbons. These χ_b limits represent the asphaltene molecules

which have the least (lower limit) and highest (upper limit) bridgehead aromatic carbon fraction. First, since the $C_{\text{sub-R}}$ overlaps with C_{db} , the C_{sub} was calculated from the number of carbons α to the aryl rings and subtracted from the overlapping signal to get C_{db} . For UG8, since the 123.78 ppm signals contains both C_{tb} and $C_{\text{H,ar}}$, the χ_{b} was calculated with and without it to get a range, and the limits were found to be 0.50 and 0.63. The same was done with the 127.44 ppm signal in WY and the χ_{b} limits were calculated as 0.44 and 0.83. These limits include the previously reported value for these asphaltenes,³⁰ and the lower limits correspond to large pericondensed PAH cores with at least 5-6 aromatic rings. On the higher end, larger PAHs can be composed of up to 15-20 aromatic rings (Figure 5 in ref. 30). The larger PAHs are bigger than what was previously believed³⁰ but have also been recently observed through direct molecular imaging using atomic force microscopy (AFM).⁵⁷ It is shown that the UG8 and WY asphaltene aromatic cores can possess between 5-15 and 5-20 condensed aromatic rings, respectively. This demonstrates that both P- and CD-asphaltene PAHs show large variations in size, with the CD-asphaltene containing a fraction of PAHs which are larger than the largest ones found in P-asphaltene. Moreover, since the range of the PAH sizes in UG8 mostly overlaps the range for WY, it is likely that the two different asphaltene have similarly sized aromatic cores. Assuming a single PAH core per molecule, the larger PAHs are bigger than what could be expected if mass limits are considered. But mass spectroscopic studies have reported a high mass tail which can account for these larger systems.²⁸ The fraction of aromatic $-\text{CH}$ groups in the WY asphaltene was also found to be significantly higher, but varying between 11.7 – 40.5%, whereas the UG8 asphaltene vary to a lesser extent, within a smaller range of 5.3 – 11.0%. These values show that the WY asphaltene have a significantly larger spin-bath of

aromatic protons which acts as the primary spin bath for CP through dipolar coupling for the aromatic core carbons, characterized by R_1 . The second ^1H spin-bath for the aromatic core comprises the aliphatic fraction, which is significantly larger in UG8 ($55.0 \pm 0.7\%$) compared to WY ($27.0 \pm 2.5\%$), characterized by R_2 . These spin-baths are depicted in Fig. 6.4

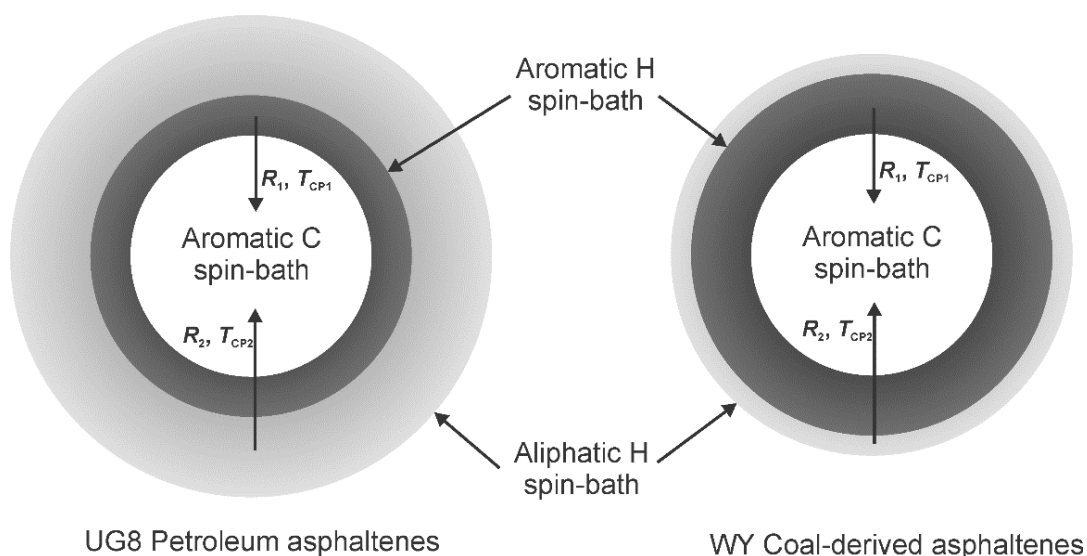


Figure 6.4. Not-to-scale illustration of the relative sizes of the aliphatic and aromatic ^1H spin-baths, with respect to the aromatic core, in UG8 and WY asphaltenes.

The UG8 signal at 29.59 ppm contains most alicyclic signals, but also has contributions from chain $-\text{CH}_2$ groups, which cannot be separated. Thus for UG8, a single value of alicyclic carbon percentage cannot be calculated, but limits of the value can be computed. These parameters, along with a few others are listed in Table 6.5 and average structures constructed on the basis of these parameters are presented in Fig. 6.5. While constructing the models, effort was taken to maintain the H:C atomic ratio close to that obtained from elemental analysis. Two different PAH sizes for each type of asphaltene is shown, to

approximately represent the limits of χ_b . The chemical formula, molecular weight and elemental analysis of each model is also provided in the figure. The assumption that the single core motif dominates asphaltene structure is based on the aromatic condensation index χ_b and the large fraction of double- and triple-bridgehead carbons.

Table 6.5. Structural parameters for UG8 and WY asphaltenes calculated from the % C values obtained from Eq. 6.1.

Structural Parameters	UG8	WY
aromaticity	45.0 ± 8.2%	73.0 ± 3.2%
aliphaticity	55.0 ± 0.7%	27.0 ± 2.5%
$C_{H,ar}^a$	5.3 – 11.0%	11.7 – 40.5%
C_{sub}^a	16.3 ± 0.01%	12.2 ± 0.01%
$C_{db} + C_{tb}^a$	22.7 – 28.4%	32.1 – 60.8%
aromatic condensation index (χ_b) ^a	0.50 – 0.63	0.44 – 0.83
rings in a single core	5 - 15	5 - 20
average alkyl chain length	7.40 ± 0.04	4.2 ± 0.02
alicyclic carbons	7.3 – 29.1%	8.3 ± 1.1%
carbons α to sulfur groups	5.1 ± 0.2%	negligible
anomeric carbons	2.3 ± 0.001%	6.0 ± 0.01
O/N groups	5.3 ± 0.01%	7.5 ± 0.02

^a $C_{H,ar}$ = aromatic –CH; C_{sub} = substituted/ipso aromatic C; C_{db} = double bridgehead aromatic C; C_{tb} = triple bridgehead aromatic C. See Chapter 1 for definition and origin of χ_b .

These values indicate that large, pericondensed cores with 5-20 aromatic rings constitute a PAH core. If two or more of these PAHs (consider those in Fig. 6.5) are linked together via alkyl chains, and if this motif is considered to be the dominating architecture, the average molecular weight, and the weight range, for these asphaltenes would be much higher than what has been reported based on mass spectrometric techniques that do not cause fragmentation.^{28,29,39,55} From these practical considerations, it seems unlikely that the traditional “archipelago” structures have any significant contribution to the overall architecture of asphaltene molecules, and the average structure consists of a single core.

Moreover, these observations are consistent with recent AFM imaging results from Schuler *et al.*⁵⁷ as mentioned earlier, which also show large single core molecules.

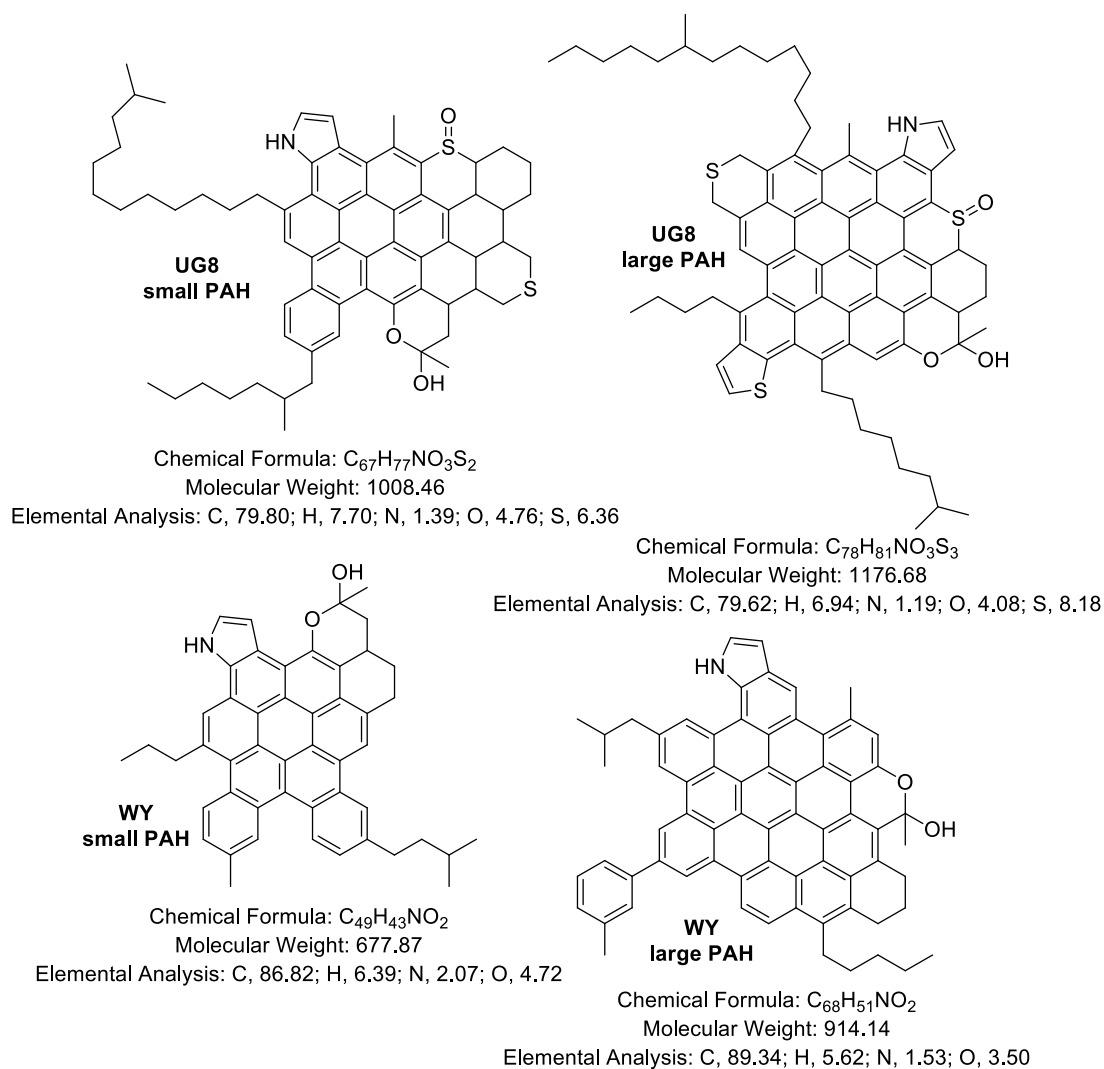


Figure 6.5. Average structures of UG8 P-asphaltenes and WY CD-asphaltenes based on the calculated parameters and elemental analysis. Two different PAH sizes, large and small, have been shown for each to represent the calculated limits.

The $T_{1\rho H}$ relaxation, which is said to govern the decay of the cross-polarized magnetization, is not a fundamental requirement for explaining CP from a thermodynamic perspective, on which the models described by equations 2.43 and 2.44 are based. These

thermodynamic models make the assumption of isolated spin-systems, which is sufficient for describing the CP-behavior, and the relaxation term is included to account for the realistic situation where the spins are not truly isolated. The decay of the CP build-up is not truly governed only by $T_{1\rho\text{H}}$ relaxation, but is better characterized as a balance between magnetization build-up processes and relaxation processes. It has been noted in the literature that $T_{1\rho\text{H}}$ calculated using Eq. 2.43 or Eq.2.44 is usually not very accurate,^{163,164} which also explains the large errors associated some of the $T_{1\rho\text{H}}$ values in Tables 6.3 and 6.4. Unless observations are made up to very long contact times, where decay of the signal is clearly observable and substantial, the $T_{1\rho\text{H}}$ values are likely to be overestimated. However, comparisons can be made since all of them will be overestimated, the error being larger for larger values. As discussed previously in Chapter 4, both highly mobile and rigid moieties have a long $T_{1\rho\text{H}}$, while anything in between have shorter values. The WY aliphatic groups generally appear to have longer values of $T_{1\rho\text{H}}$, ranging from 8.3 ± 5.9 to 19.8 ± 15.9 ms (ignoring the very long values which have errors larger than themselves), compared to those in UG8 ranging from 1.9 ± 0.1 to 5.5 ± 0.8 ms, which once again suggests that WY asphaltenes possess shorter alkyl sidechains. No significant differences in $T_{1\rho\text{H}}$ were observed between the aromatic carbons in UG8 and WY, which indicates similar sizes. The parameter b provides a measure of the dipolar coupling and is normally expected to be zero under magic angle spinning conditions. However, in Table 6.3 and 6.4 we see that most of the signals have non-zero b values. It implies that the $(3\cos^2\theta-1)$ term in the expression for b is non-zero, indicating the presence of residual chemical shift anisotropy (CSA). Not surprisingly, the carbons with attached protons, and the rigid ones, show b values larger (> 7.0 kHz) than those without protons and the mobile groups (< 1.0 kHz), due to larger effective dipolar coupling, lending validation to the fitting calculations. Moreover, the

mobile $-\text{CH}_3$ groups (UG8: 22.71, 19.64, 14.03 ppm; WY: 22.88, 19.38, 14.36 ppm) show smaller b values (< 1 kHz) compared to the other chain and cyclic alkyl groups. The b term quantifies the rate of oscillatory exchange of magnetization between carbons and protons during CP,¹³⁷ which scales with the size of the ^1H spin bath corresponding to the carbon of interest. These oscillations are observable only during the first few tens of microseconds (typically < 50 μs) of CP build-up,¹³⁷ and hence require sampling of a much larger number of contact times under 50 μs . In this work such detailed sampling was not performed due to time constraints, hence these oscillations are not clearly observed. Moreover, in complex spin-systems such as asphaltenes, these oscillations are damped by the destructive interference between oscillations at several different frequencies.

6.3.3. ^{13}C Pre-CP Refocused DIVAM

The pre-CP refocused DIVAM nutation curves are shown in Figs. 6.6a and 6.6b. The more mobile groups show more pronounced oscillations in intensity, and usually have a zero crossing at the smaller excitation angles. Before discussing subtle differences, comparing the nutation curves of the aromatic groups at a glance reveals that in UG8 asphaltenes, the $C_{\text{sub-R}}$, C_{db} , C_{tb} and $C_{\text{H,ar}}$ groups all nutate more coherently than the same groups in WY asphaltenes (UG8: 138.02, 129.28, 123.78, 118.53 ppm, WY: 138.31, 127.44, 122.52 ppm), where the nutation profiles are more disparate. This is an indicator that the most of the aromatic moieties in UG8 asphaltenes are in a similar domain of mobility, while in WY asphaltenes some are more rigid than others. This difference in mobility can be explained in two possible ways: i) that WY coal asphaltenes are composed

of some very large and some much smaller PAHs, or ii) smaller PAHs are tethered to the larger PAHs like in an archipelago structure.

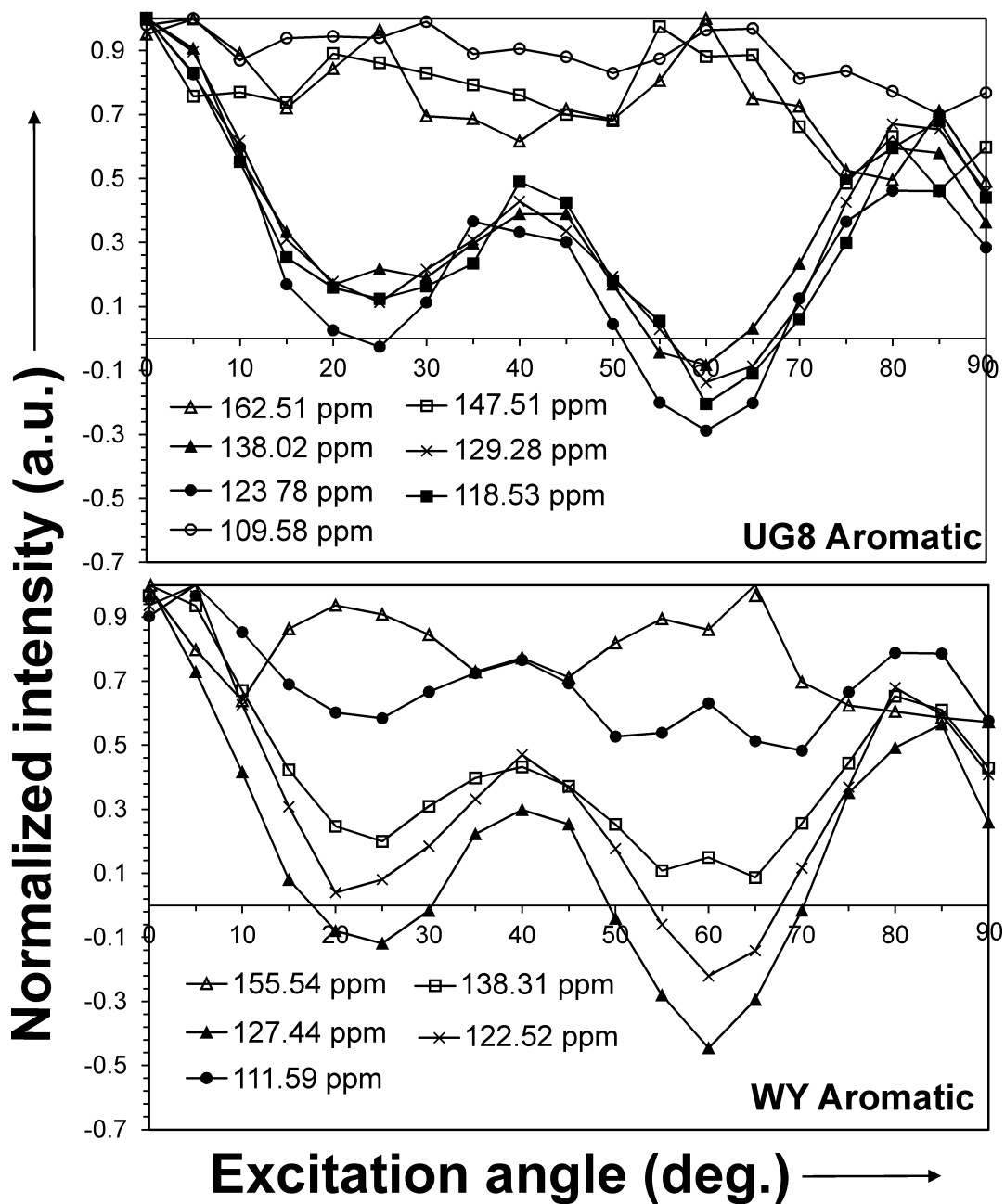


Figure 6.6a. Pre-CP refocused DIVAM nutation curves for the deconvolved aromatic peaks of the ^{13}C CP-MAS NMR spectra of UG8 and WY asphaltenes. The anomeric (O-C-O) carbon signals have been grouped with the aromatic signals

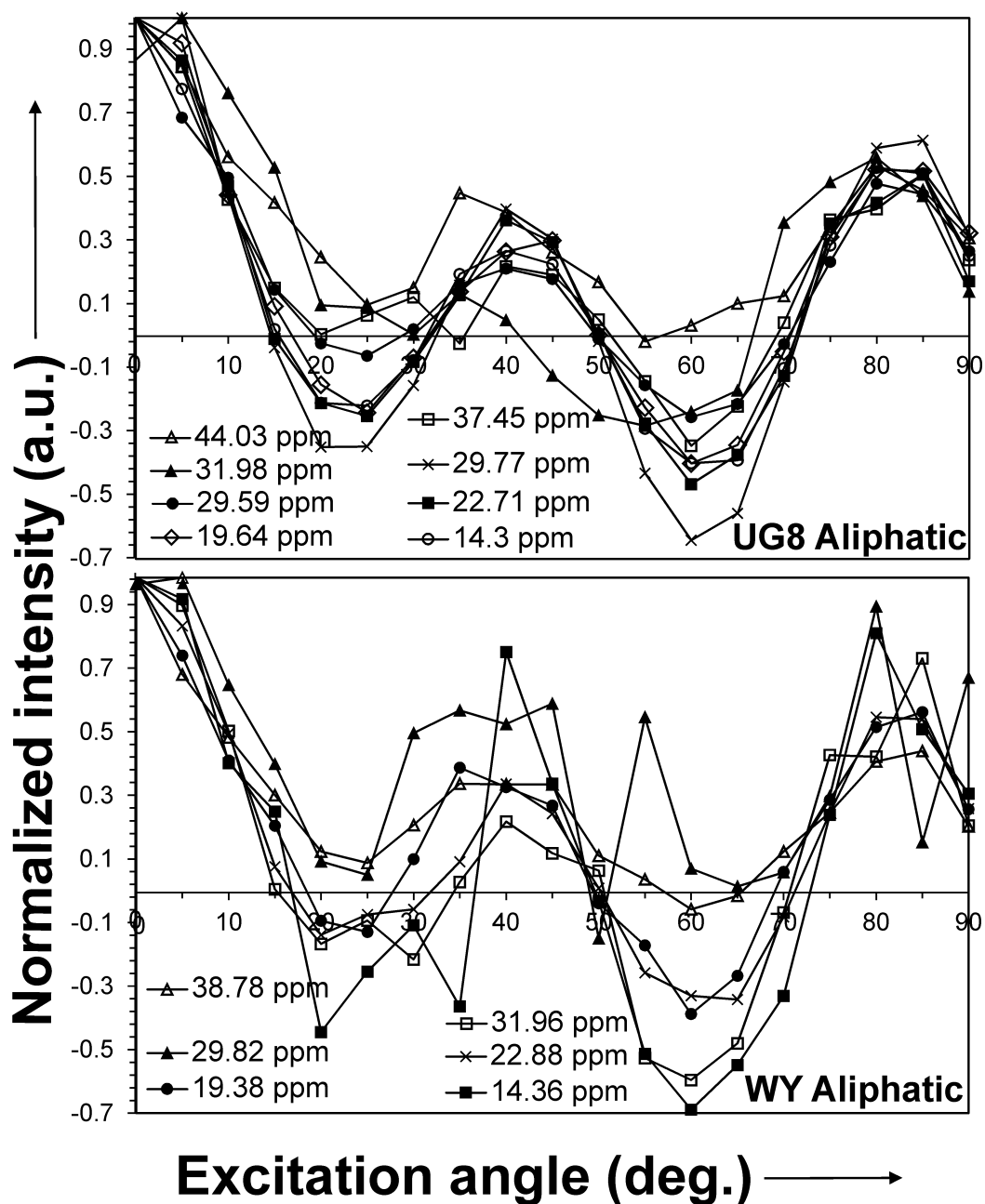


Figure 6.6b. Pre-CP refocused DIVAM nutation curves for the deconvolved aliphatic peaks of the ^{13}C CP-MAS NMR spectra of UG8 and WY asphaltenes.

The WY asphaltene carbons resonating 127.44 ppm, a large fraction of which are $\text{C}_{\text{H,ar}}$ groups, appear to be the most mobile of all the aromatic carbons, including the ones in UG8. As noted in an earlier section, these protonated carbons can belong to smaller aromatic rings connected to a larger PAH system via a single bond and are easily

distinguishable from protonated carbons in the larger PAH from their chemical shifts.^{160,161} Naturally, they can be expected to be more mobile than the carbons in the larger PAH. These observations point towards the presence of archipelago-type motifs in WY coal asphaltenes, where the one large PAH is bound to a much smaller PAH via a single bond. Thus, although archipelago type in nature, these tethers cannot be called ‘aliphatic linkages’ as often shown in a lot of traditional archipelago models.^{43,165} Rather, these can be viewed as a single core but with a discontinuity in the aromatic network, since the “linkage” is still directly between two aromatic carbons. Moreover, Schuler et al.⁵⁷ have recently demonstrated this to be true for a different coal asphaltene. The UG8 petroleum asphaltenes do not appear to have these higher chemical shift $C_{H,ar}$ groups and all the protonated aromatic carbons (123.78 and 118.53 ppm) appear less mobile than those in WY asphaltenes. If the UG8 asphaltenes do possess the pendant aromatic groups, their mobility is likely reduced due to the UG8 clusters being more closely packed than those in WY asphaltenes. The closer packing of the UG8 clusters is likely a result of the longer aliphatic chains that intercalate between the aromatic sheets, which is discussed again below. Thus, although the presence of these pendant aromatics in UG8 cannot be ruled out, no evidence for their presence is observed here.

The signals from the aromatic carbons substituted by O and N groups (UG8: 162.51, 147.51 ppm, WY: 155.54 ppm) and the anomeric carbon signals (UG8: 109.58 ppm, WY: 111.59 ppm) show very little nutation and neither exhibit a zero-crossing, which shows that they are remote from any mobile protons. Among these, the nutation profile for the 111.59 ppm signal in WY CD-asphaltenes is more pronounced, likely because it also contains contributions from $C_{H,ar}$ groups (Table 6.4), which have attached protons. Among the C_{db}

and $C_{\text{sub-R}}$ groups (UG8: 138.02 ppm, WY: 138.31 ppm), the ones in UG8 show more pronounced oscillations and undergo a zero-crossing, while those in WY oscillate to a lesser extent and do not cross zero. This is a direct consequence of UG8 P-asphaltenes having a much greater degree of alkyl substitution. It provides a comparatively more mobile ^1H spin-bath to these carbons in UG8, as manifested in the DIVAM nutation profile, than the ones in WY, whose main spin-bath for CP are the rigid aromatic protons.

Among the aliphatic signals, the chain $-\text{CH}_2$ groups in UG8, especially those not directly attached to aryl rings (22.71, 29.77 ppm), show a greater degree of mobility compared to those in WY (22.88, 29.82 ppm), as evinced by the former's more pronounced nutation profiles. The branched and aryl $-\text{CH}_3$ groups in UG8 (19.64 ppm) also show greater mobility than the same groups in WY (19.38 ppm). These observations are coherent with UG8 P-asphaltenes possessing longer, hence more mobile aliphatic sidechains. The terminal $-\text{CH}_3$ groups in WY (14.36 ppm) show more pronounced oscillations than those in UG8 (14.30 ppm), indicating greater mobility, but its behavior is somewhat erratic at smaller excitation angles. This could simply be an effect of one of the spinning sidebands of the 138.31 ppm signal (see Fig. 6.1) having significant overlap with the 14.36 ppm signal, which adds error to the observed intensity. At larger angles the sideband gets filtered out and the nutation behavior returns to normal. The UG8 terminal methyl groups, interestingly, also appear less mobile than the chain methylene groups. This is only possible when the motion of the methyl groups are restricted by interaction with other groups. In the discussion for CP dynamics, it was hypothesized that alkyl chains can intercalate between the stacked aromatic cores of an aggregate, which would also hinder the motion of terminal groups. Thus, the reduced mobility of terminal $-\text{CH}_3$ groups in UG8 P-asphaltenes

corroborate this hypothesis. This is not the case for WY CD-asphaltenes, where the alkyl chains are too short to have any such interaction. In Chapter 4, we provided evidence for the same intercalation behaviour in bitumen derived asphaltenes, which appear to be structurally similar to P-asphaltenes. These aliphatic-aromatic interactions likely result in more closely packed clusters in UG8 P-asphaltenes, and may have important implications in determining the role of the alkyl sidechains in the aggregation of asphaltenes, but it can only be addressed conclusively by observing asphaltene behavior in a range of concentrations in the solution-state, which shall be covered in a separate study.

The 29.59 ppm UG8 signal shows reduced mobility, agreeing with its assignment to alicyclic carbons. All the other aliphatic carbons in both asphaltenes show reduced mobility, as expected from groups attached to the aromatic core.

In this first study of its kind which uses solid-state NMR spectroscopic techniques to compare petroleum and coal derived asphaltenes, we demonstrate how quantitative information can be properly obtained from cross-polarization experiments on these complex materials. Attempting to quantify a single CP NMR spectrum at one specific contact time, however, will never provide quantitative information for complex materials. An appropriate CP dynamics model should be fit to the experimental variable contact time curves to obtain quantitative information, as long as $T_{1\rho H} > T_{CP}$. It offers a significant time advantage over direct polarization or single pulse excitation, and provides a wider array of structural and dynamic information. The refocused DIVAM experiment offers a novel way to investigate the molecular dynamics of the complex asphaltenes and demonstrates how solid-state NMR pulse sequences originally developed for polymer characterization can also be used to study asphaltenes.

6.4. Conclusions

Solid-state ^{13}C CP-MAS NMR spectroscopic techniques applied to a petroleum asphaltene (UG8) and an asphaltene derived from coal liquids (WY) highlights key structural differences between the two asphaltenes and also provides new information that challenges a few existing ideas, while reinforcing recent AFM imaging results.⁵⁷ Using CP dynamics quantitatively, it was shown, that the asphaltene molecules are dominated by single core PAHs, with the smallest cores in both asphaltenes consisting of at least 5-6 pericondensed aromatic rings, while the largest cores can contain up to 15-20 rings, which is larger than what is currently believed, reinforcing observations made by Schuler *et al.*⁵⁷ The results are also consistent previous NMR studies both in solution³⁰ (Chapter 3) and solid state (Chapter 4) where an average core size of 5-7 rings was reported. Both CP dynamics and CP refocused DIVAM suggest that WY CD-asphaltenes may have archipelago-type structures, where a small PAH is tethered to the larger PAH core via a single bond between aromatic carbons, which makes it different from traditional archipelago models.⁴³ Thus, a single core model still dominates and no evidence for true archipelago structures is found. At this point, no evidence for these tethered groups was observed in UG8 asphaltenes, although they may be present, with their mobility restricted by closer packing of the UG8 clusters. It was also shown that asphaltenes may contain anomeric (O-C-O) groups, the signals of which previously got assigned to aromatic carbons because of chemical shift overlap. The UG8 P-asphaltenes have a greater degree of substitution, longer alkyl chains and a larger fraction of alicyclic groups. On account of the longer length, with an average of ~6 carbons, the alkyl chains in UG8 intercalate between the aromatic rings of adjacent asphaltene aggregates. This is not observed in WY asphaltenes, because of shorter alkyl chains which are ~3 carbons long on average. This is

a major distinction between P- and CD-asphaltenes and may have important implications on the role of alkyl sidechains in asphaltene aggregation. UG8 asphaltenes also have a greater number of sulfur containing groups, including sulfoxide moieties which are absent or present in insignificant amounts in WY asphaltenes. To understand how these structural differences manifest themselves in asphaltene aggregation behavior, solution-state NMR studies at various asphaltene concentrations have been performed and will be the focus of the following chapter.

CHAPTER 7

7. RELATING STRUCTURE TO FUNCTION: CONTRASTING AGGREGATION BEHAVIOR OF PETROLEUM AND COAL DERIVED ASPHALTENES STUDIED USING ^1H T_2 RELAXATION AND 2D-NOESY

7.1. Overview

In the previous chapters, a comprehensive structural comparison of UG8 petroleum (P) asphaltenes and WY coal-derived (CD) asphaltenes was performed. It was observed that the most significant difference between these two asphaltenes was the much lower alkyl content of WY, which manifests itself in short chains and lower number of substitutions. Alicyclic content of UG8 P-asphaltenes was also shown to be much higher, besides possessing more sulfur-containing moieties, which were mostly absent in the WY CD-asphaltenes. The aromatic cores in both asphaltenes were of comparable size, which suggests that in terms of π - π stacking interactions, the asphaltenes should behave similarly, ignoring any other factors that might enhance or hinder stacking. Having established these differences, it is now essential to study how these asphaltenes behave in solution at different concentrations. In this chapter, UG8 and WY asphaltenes are investigated using ^1H T_2 relaxation measurements, performed at asphaltene concentrations ranging from below the critical nanoaggregate concentration to above the cluster forming concentrations (refer to Chapter 1). As discussed previously, relaxation behavior depends on molecular mobility, which is affected by aggregation, and when all other conditions are the same, it is only structure that determines aggregation behavior. Since aggregation and eventually clustering

will bring the asphaltene molecules closer together, interactions between the aliphatic and aromatic fractions, or lack thereof, are important indicators of aggregation behavior. This will be studied using the solution-state 2D NOESY experiment, which reveals the groups that are spatially close to each other.

7.2. Experimental Details

7.2.1. Sample preparation

The asphaltene samples were first dissolved in CDCl_3 to make a stock solution at a concentration of 15 g/L. From this solution, calculated aliquots were drawn, to which the required volume of CDCl_3 was added to obtain the required concentration. Samples at nine different concentrations were prepared in this way: 15, 7.5, 3.0, 1.5, 0.75, 0.38, 0.19, 0.09 and 0.045 g/L. Care was taken to minimize evaporation by preparing the samples only when required and storing them in the freezer or on ice until their use.

7.2.2. NMR spectroscopy parameters

All experiments were performed using a 16.4 T Bruker Avance III HD NMR spectrometer, operating at 700 MHz ^1H Larmor frequency, in 5 mm outer diameter NMR tubes.

The T_2 relaxation measurements were done using a CPMG sequence, with an 8 s relaxation delay and 16 scans. The fixed delay in the CPMG train was 2×2.0 ms, which was looped up to 250 times. The number of scans recorded was based on the concentration, varying between 16 and 128, the lower concentrations requiring more scans and the higher

ones requiring fewer. The decay curves were fitted using a biexponential decay function to calculate the T_2 time constants.

The NOESY experiment was performed only on the sample with the highest concentration (15.0 g/L), since the objective was to observe correlations in the aggregated state. A mixing time of 500 ms was chosen, and 256 transients were recorded to obtain the indirect dimension, with a total acquisition time of 9.14 ms, incremented in steps of 0.07 ms and 32 scans were recorded for each increment. The relaxation delay used was 2 s. For processing, a 10 Hz exponential line-broadening was applied to both dimensions, and the indirect dimension was linear predicted to 1024 points with zero-filling. A 20 ppm spectral width was used in both dimensions, with the transmitter offset centered at 6 ppm.

7.3. Results and Discussions

7.3.1. Concentration dependence of ^1H T_2 relaxation behaviour

In Chapter 1, Section 1.4.4, the concepts of critical nanoaggregate concentration (CNAC) and critical cluster concentration (CCC) were introduced. The CNAC is defined as the lowest concentration at which the nanoaggregate growth stops, and is reported to be in the range 0.05-0.15 g/L for P-asphaltenes.^{7,42} Below ~0.05 g/L, it has been suggested that asphaltenes form smaller multi-mers (dimers, trimers etc.). Beyond the CNAC, a second aggregation step has been proposed to occur where the nanoaggregates further group together to form ‘clusters’, shown to start occurring at concentrations between 2-5 g/L, which is the aforementioned CCC. The variation of T_2 relaxation behavior with increasing concentration of asphaltenes dissolved in CDCl_3 is shown in Fig. 7.1. A biexponential function is fit to a T_2 decay curve when the curve clearly has two components, one decaying faster than the other. The faster decay represents the short T_2 component,

which arises from groups that are more rigid. These could be rigid aromatic or alicyclic protons in aggregates, or alkyl chain protons which have restricted motion due to interaction with neighbouring groups, resulting from crowding or aggregation. The longer T_2 component is attributed to mobile groups, which would be mostly unrestricted alkyl chain protons, and possibly individual asphaltene molecules which are not in an aggregate. The greater the degree of aggregation, more of the groups are expected to have restricted motion. In Fig. 7.1, it is seen that both asphaltenes have two T_2 components at all concentrations. The occurrence of short T_2 components at 0.045 g/L concentration, which is lower than the CNAC, indicates that small aggregates might exist at very low concentrations, which was suggested by Lisitza *et al.*,⁵⁴ but it cannot be said if these aggregates are nanoaggregates that have stopped growing in size or just multi-mers (dimers, trimers etc.). The longer T_2 component at this concentration likely represents the non-aggregated molecules or those in the smallest aggregates.

As concentration is increased up to 15 g/L, the T_2 of the mobile component (longer T_2) of UG8 decreases significantly, from 0.82 ± 0.05 to 0.29 ± 0.02 s, and, along with this decrease, its relative fraction drops from 50.8 ± 1.6 to 26.5 ± 1.8 %. The short T_2 component of UG8, on the other hand, does not show significant reduction in its value as concentration is increased, going from 0.04 ± 0.01 to 0.02 ± 0.00 s. However, their relative fraction increases significantly from 49.2 ± 4.0 to 73.5 ± 2.2 %. Therefore, as the UG8 asphaltene concentration increases, there is a significant increase in the rigid fraction. The rigid fraction is a result of aggregation, suggesting that the UG8 asphaltenes undergo a large degree of aggregation with increasing concentration.

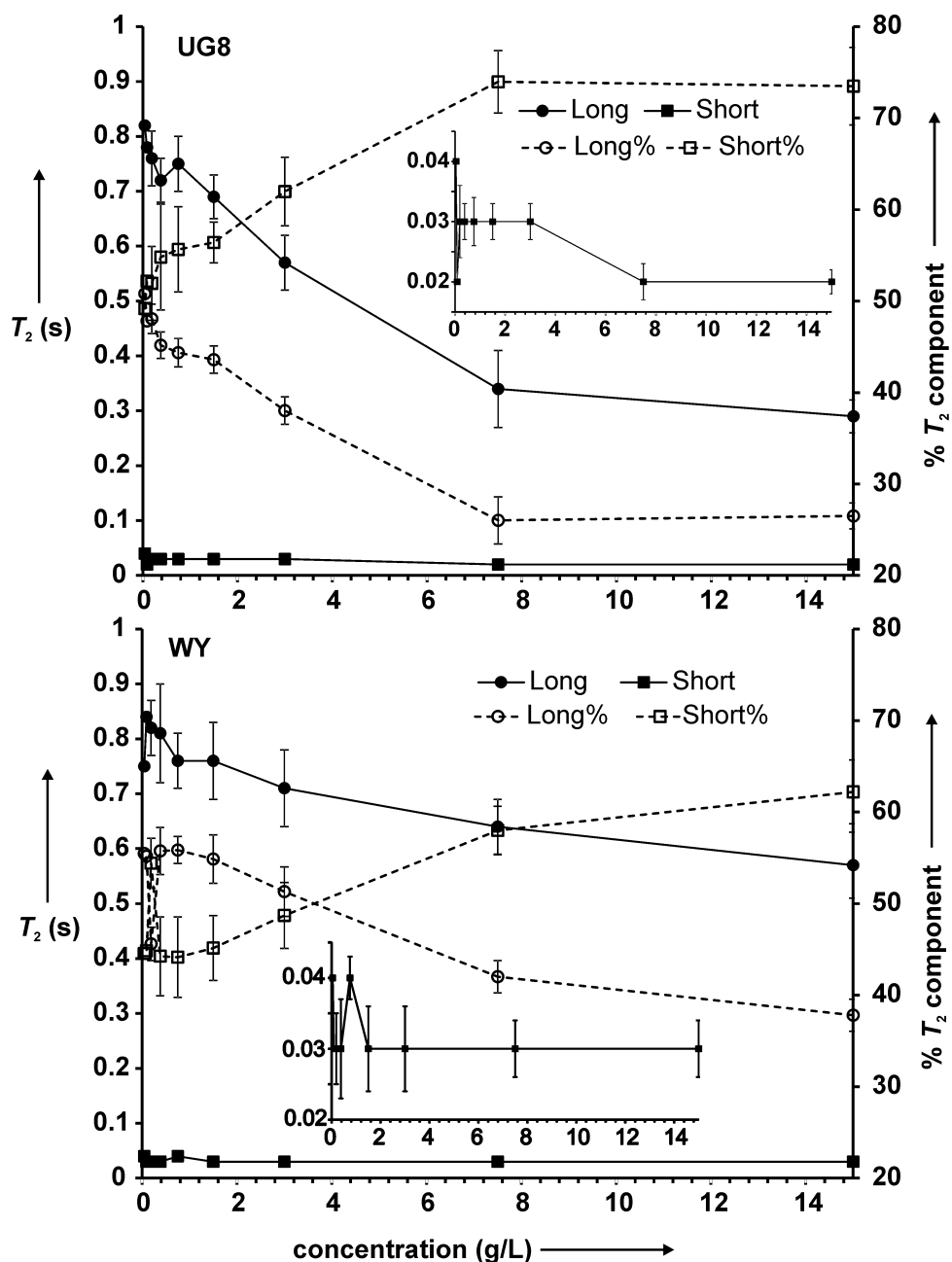


Figure 7.1. The variation of the long and short components of T_2 relaxation time (left y-axis), and their respective percentages (right y-axis), with increasing concentration of UG8 and WY asphaltenes in CDCl_3 . The insets show the vertical expansions of the short T_2 components of the respective plots.

In contrast, the change in the values of the long T_2 component in WY asphaltenes is much less dramatic, decreasing from 0.75 ± 0.05 to 0.57 ± 0.04 s as concentration is

increased from 0.045 to 15.0 g/L. The relative fraction of this component, however, shows a fairly significant reduction from 55.5 ± 1.8 to $37.8 \pm 1.4\%$, which is slightly less than the corresponding T_2 component of UG8. The short T_2 component shows almost no variation, staying steady between 0.03 to 0.04 s, but there is substantial increase in its relative fraction from 44.5 ± 2.7 to $62.2 \pm 2.0\%$. These observations indicate that aggregates likely form with increasing concentration of WY asphaltenes, since there is an increase in the rigid fraction, but the largest aggregates that form are likely smaller or less rigid than the largest aggregates in UG8. Note that at this point, the term ‘aggregate’ is being used in a general sense to describe nanoaggregates and clusters alike, and the specific distinctions will be made as the relaxation behavior is analyzed in greater detail.

Closer inspection of the relaxation behavior of UG8 asphaltenes in Fig. 7.1, reveals that the increase in the rigid fraction of the asphaltenes, i.e., increase in the short T_2 component fraction, is not monotonous, but occurs in two distinct stages. There is a fairly monotonous increase in the rigid, i.e., aggregated fraction of UG8 asphaltenes, up to the concentration 7.5 g/L, increasing from $49.2 \pm 4.0\%$ to $73.9 \pm 2.0\%$. But when the concentration is doubled from 7.5 to 15.0 g/L, the rigid fraction does not show any significant change (73.9 ± 2.0 to $73.5 \pm 2.2\%$). This behavior suggests that whatever aggregation phenomena is occurring, be it the formation of nanoaggregates or clusters, at ~ 7.5 g/L a significant change occurs which keeps the rigid fraction from increasing further. To understand what this change might be, one needs to look at the literature values for CNAC and CCC^{7,42} for petroleum asphaltenes. According the reported CNAC values, nanoaggregate (NA) growth stops around ~ 0.15 g/L, i.e., the NAs stop adding new molecules and thus stop growing in size. As concentration is increased further, molecules form new NAs. These NAs continue to

form until they start to coalesce to form clusters around $\sim 2.0\text{-}5.0$ g/L (CCC), which continue to grow in size as more NAs agglomerate. Hence, there is a gradual increase in the fraction of rigid components, clusters being more rigid than NAs. Thus, at ~ 7.5 g/L as shown in the present study, the majority of UG8 asphaltenes constitute the rigid fraction ($73.5 \pm 2.2\%$), which are likely clusters. If the size of these clusters, i.e., the number of NAs coalesced together, continues to grow as concentration is increased further, the rigid fraction is expected to keep increasing monotonously as before. But as discussed above, no increase in the rigid fraction is observed beyond ~ 7.5 g/L. It suggests that the clusters stop growing in size beyond this concentration, i.e., the existing clusters do not add any more NAs, and as concentration is increased, the non-coalesced NAs form new clusters.

As discussed earlier, the relaxation behavior of WY asphaltenes is significantly different from that of UG8. For WY, while there is a definite and significant increase in the fraction of rigid components, the decrease in rigidity of these components themselves is not as significant as observed for UG8. Up to the concentration of 7.5 g/L, the long T_2 (mobile) values of UG8 decrease much more dramatically compared to WY. What it implies is that NAs are likely forming on increasing WY asphaltene concentration, which increases the rigid fraction, but these NAs do not coalesce further to form clusters like in UG8, which would be more rigid than the NAs themselves. Moreover, the increase in the rigid fraction of the WY asphaltenes is mostly monotonous in nature, without any well-defined inflection point where change in relaxation behavior can be detected. Since, to the best of our knowledge, the aggregation behavior of coal-derived asphaltenes has not been reported in literature, it is not possible at this time to comment on whether there is a specific cut-off concentration at which NA growth stops. However, based on the relaxation behavior

observed here, and the structural differences that have been established in previous chapters, a possible mechanism for the formation of aggregates, NAs and clusters (for UG8) can be formulated (Fig. 7.2).

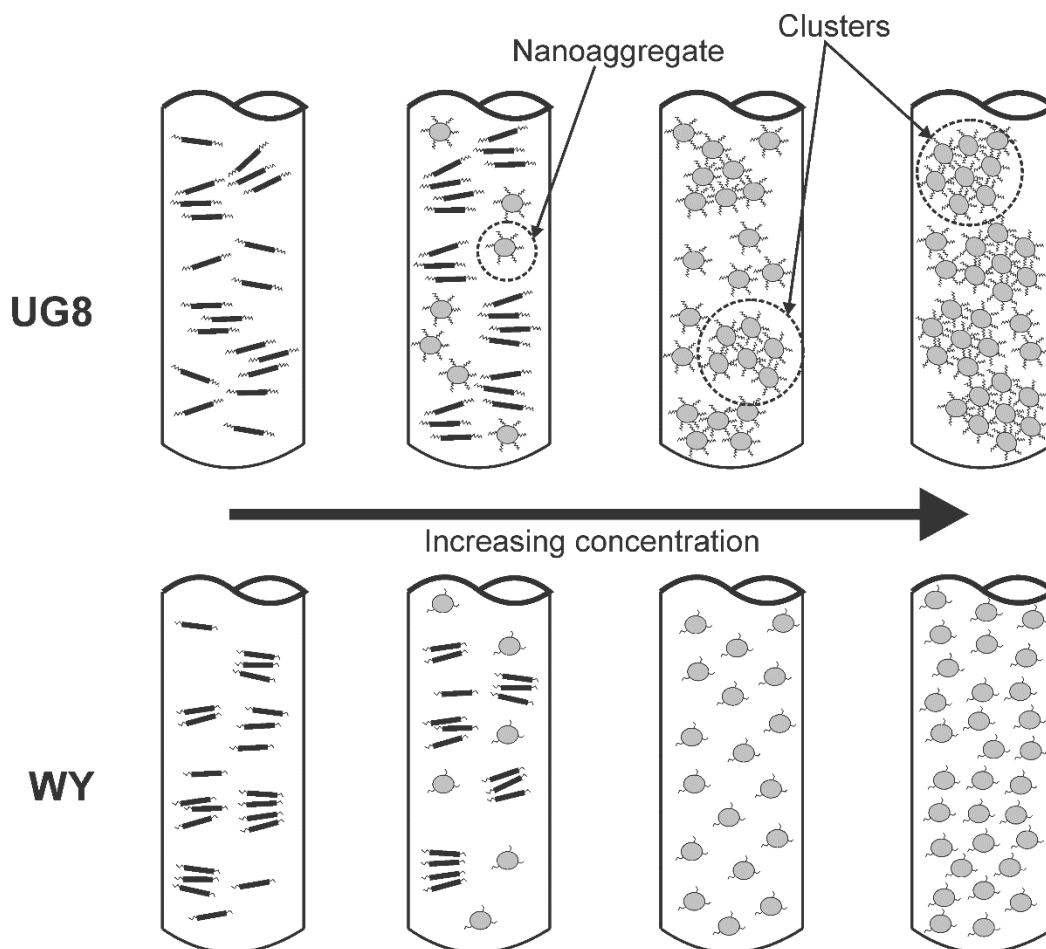


Figure 7.2. Schematic describing the formation of nanoaggregates and clusters in UG8 and WY asphaltene solutions on increasing asphaltene concentration. Note the absence of clusters in WY.

At the lowest concentration used in this study (0.045 g/L), the asphaltene molecules likely exist as small dimers and trimers, i.e., aggregates consisting of two or three molecules, as suggested in literature. (Mullins 2010, 2012) As the concentration increases, NAs begin to form. This initial aggregation, and eventual formation of NAs, occurs mostly through π - π stacking between the aromatic sheets. Since the nature of the aromatic core is

similar in both asphaltenes, other than the greater number of alkyl substitutions in UG8, aggregation via π - π stacking should occur in both UG8 and WY. Now, when NAs form, the aromatic core surface area presented for stacking decreases with the growth of the NA, due to the steric hindrance from the alkyl sidechains. The steric hindrance is greater in UG8 asphaltenes due to the longer and more abundant sidechains, and also a larger alicyclic fraction. Therefore, as concentration is increased, the UG8 NAs eventually attain a size that provides enough steric hindrance to prevent further stacking, and hence stop growing in size. However, the long alkyl sidechains that now occupy the periphery of the UG8 NAs, can also result in strong induced dipole-induced dipole forces (London dispersion forces), that lead to attraction between the NAs. Hence, as concentration increases beyond the CCC, the UG8 NAs coalesce with each other due to the attractive London dispersion forces, forming clusters. In WY asphaltenes, the sidechains are much shorter, less abundant and a smaller alicyclic fraction is present. Therefore, as the WY NAs grow in size, the steric hindrance posed by the alkyl fraction would be lower than that in UG8 and the NAs are likely to add more individual molecules, hence growing larger than those in UG8. Also, the shorter sidechains imply much lower induced dipole-induced dipole attractions between the NAs, if at all. Therefore, it is unlikely that the NAs of WY asphaltenes show the same clustering effect as in UG8, at least at the same concentrations, which is given by the CCC of the petroleum asphaltenes. The clustering behavior of the UG8 NAs manifests as the much more dramatic reduction in the long T_2 values up to 7.5 g/L concentration, compared to WY asphaltenes, where the long T_2 values show a much smaller reduction, most likely due to the continued growth of the NAs. The UG8 asphaltene NAs therefore form clusters on account of being more polarizable, which is consequence of longer, more abundant alkyl sidechains. Additionally, the significantly higher sulfur content of UG8 asphaltenes (8.94%

as opposed to 0.13% of WY) renders them even more polarizable. The short sidechains, along with lower alkyl and sulfur content of WY asphaltenes makes their NAs a lot less polarizable, which precludes cluster formation. For the UG8 asphaltenes, when the concentration reaches ~ 7.5 g/L, the clusters appear to stop growing in size, as discussed earlier. The non-clustered NAs likely continue to coalesce into new clusters beyond this point. The termination of the growth of UG8 asphaltene clusters is likely due to the most polarizable moieties of the NAs occupying the interior of the clusters. The steric bulk of the cluster periphery prevents addition of more NAs to it. From a thermodynamic perspective, the growth of the clusters can continue as long as the associated decrease in entropy of the clusters is less than the increase in entropy of the solvent. Therefore, the size of the clusters will likely depend on the solvent. These observations strongly suggest that from a structural perspective, alkyl sidechains have the most important role to play in the formation of clusters. It may be possible to prevent clustering if the sidechains can be shortened and/or their polarity can be reduced.

7.3.2. ^1H - ^1H Nuclear Overhauser Effect Spectroscopy (NOESY)

In Chapter 6, it was hypothesized that alkyl sidechains in UG8 asphaltenes can get intercalated between stacked aromatic cores. It is suggested that this is a result of clustering, whereby neighbouring nanoaggregates interlock in a ‘Velcro’ like fashion. In this chapter, strong evidence for alkyl sidechains promoting cluster formation has already been presented. A ^1H - ^1H NOESY experiment is used to identify protons that are spatially proximate to each other, but not interacting via J -coupling (refer to section 2.3.6). Hence, it can be potentially used to verify the interaction of sidechains in one nanoaggregate with

neighbouring nanoaggregates. The ^1H - ^1H NOESY spectra of the UG8 and WY asphaltenes are presented in Fig. 7.3. Cross-peaks in a NOESY spectrum appear at the chemical shifts of groups that are spatially close to each other, and for large or rigid molecules or groups of molecules (aggregates is this case), are in the same phase as the diagonal (see section 2.3.6), which is generally phased positive. In the UG8 NOESY spectrum, strong correlations are observed between alkyl protons and aromatic protons, which are distinctly absent in the WY spectrum, even though WY asphaltenes contain a much larger fraction of aromatic protons. However, the absence of correlations does not necessarily imply the absence of interacting protons. The appearance of cross-peaks is predicated on the rotational correlation time (τ_c) of the molecules, which was introduced in Chapter 2, section 2.2.12. Cross-peaks in a NOESY spectrum disappear if the τ_c attains a certain value called the critical rotational correlation time ($\tau_{\text{crit.}}$), which is determined by the Larmor frequency ω_0 (of ^1H in this case), given by:

$$\tau_{\text{crit.}} = \left| \frac{\sqrt{5}}{2\omega_0} \right| \quad \text{Equation 7.1}$$

For large or rigid molecules, $\tau_c \gg \tau_{\text{crit.}}$, and the cross-peaks are in the same phase as the diagonal peaks. If, $\tau_c \ll \tau_{\text{crit.}}$, cross-peaks are phased opposite that of the diagonal or absent if $\tau_c \approx \tau_{\text{crit.}}$. At 700 MHz ^1H Larmor frequency, $\tau_{\text{crit.}} \approx 1.6$ ns, which implies that moieties with $\tau_c \gg 1.6$ ns should show cross-peaks in the same phase as the diagonal, if NOE occurs in them. The correlation time can be estimated by calculating the T_1/T_2 ratio, since the relaxation times can be expressed in terms of the spectral density, which in turn depends on the correlation time (Eqs. 2.38-2.40). A plot showing the dependence of T_1/T_2 on the correlation time at 700 MHz ^1H Larmor frequency is provided in Appendix 5. Therefore,

the T_1/T_2 ratios of the 15 g/L concentration samples of both UG8 and WY asphaltenes were calculated. Since the relaxation behavior was biexponential, two T_1/T_2 values were obtained for each asphaltene. For UG8, these were 57 and 0.55, while for WY these were 43.3 and 0.30. The smaller T_1/T_2 values clearly correspond to moieties in the extreme narrowing limit, with $\tau_c \ll 1.6$ ns. These can be attributed to mobile protons that are located on the periphery of aggregates or in non-aggregated molecules, which are not restricted by any interactions with neighboring groups. Negative cross-peaks are expected if these groups have NOE interactions, which are absent in both the UG8 and WY NOESY spectra. However, it is the rigid fractions with the large T_1/T_2 ratios that are of primary interest, since these represent protons that have restricted motion on account of structural constraints caused by aggregation. For both UG8 and WY asphaltenes, the large T_1/T_2 ratios (UG8: 57, WY: 43.3) correspond to τ_c values around ~11-12 ns, which are about 7 times longer than the τ_{crit} . Therefore, the absence of cross-peaks between alkyl protons and aromatic protons in the WY asphaltene NOESY spectrum is certainly not due to its correlation time, but is a result of the absence of interactions that cause NOE. Whereas, the cross-peaks in the UG8 asphaltene NOESY spectrum clearly show that alkyl protons and aromatic protons exist at close enough proximity to cause NOE.

With respect to a specific UG8 nanoaggregate, these proximal alkyl protons can either belong to itself or to an adjacent nanoaggregate. Therefore, a much larger number of alkyl protons are located close to the aromatic protons in UG8 asphaltenes, which firstly is a result of it containing a large alkyl fraction and of cluster formation, which brings the aliphatic and aromatic protons closer. No alkyl protons in WY asphaltenes are close enough to the aromatic protons to cause NOE, which is a result of low alkyl content and lack of

clustering. For the same reasons, correlations are also observed between alkyl protons ($\text{CH}_n \leftrightarrow \text{CH}_n$ in Fig. 7.3) in UG8 asphaltenes, but not in WY asphaltenes. The only correlations observed for WY asphaltenes are between alkyl protons and phenolic $-\text{OH}$ groups, which are proximal on account of geometry. The schematic in Fig. 7.4 describes the interaction between nanoaggregates, or lack thereof, in the two asphaltenes.

These observations from the NOESY experiments confirm that the nanoaggregates are significantly more closely packed together in UG8, forming clusters, and that the alkyl sidechains play a significant role in cluster formation. These are also the first NOESY spectra of asphaltenes reported, to the best of the author's knowledge. Together with the ^1H T_2 relaxation behavior at different concentrations, this study provides further evidence for the hierarchical Yen-Mullins model, but the model appears to be true only for the petroleum asphaltenes.

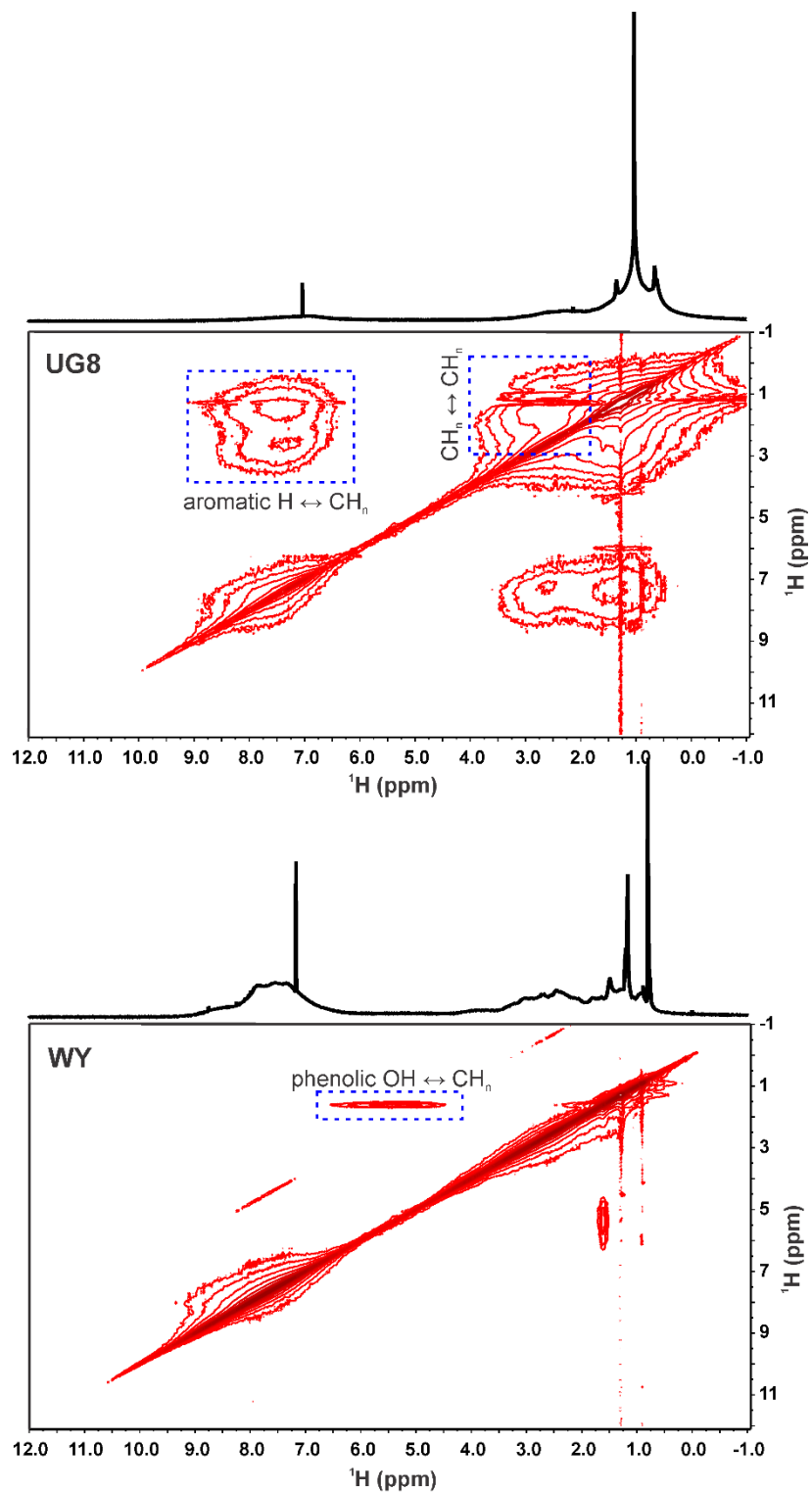


Figure 7.3. Solution-state ^1H - ^1H NOESY spectra of UG8 (top) and WY (bottom) asphaltenes at a concentration of 15 g/L, obtained with a mixing time of 500 ms.

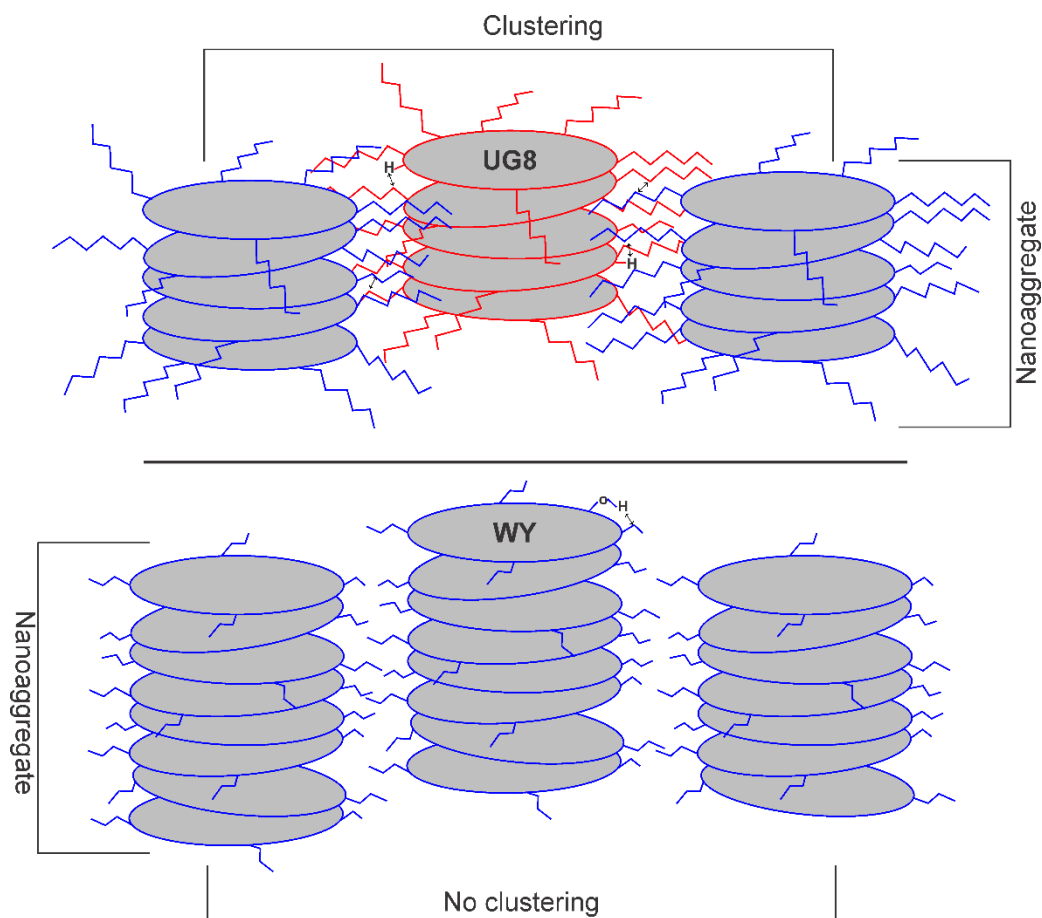


Figure 7.4. Schematic describing the inter- and intra-nanoaggregate interaction of alkyl sidechains that lead to clustering in UG8 asphaltenes. Each disc represents an asphaltene molecule. Note that the WY asphaltene nanoaggregates are shown as more extended, since the shorter sidechains offer less steric resistance to π - π stacking.

7.4. Conclusions

In previous chapters, the fundamental differences between P- and CD-asphaltenes were established, and in this one, it was investigated how these differences manifest themselves when these asphaltene aggregate. The effect of concentration on the aggregation behavior of UG8 and WY asphaltene was studied using ^1H T_2 relaxation experiments. It was conclusively shown that UG8 P-asphaltenes undergo a significantly greater degree of aggregation, evinced by the larger decrease in its mobile components. It is hypothesized

that small aggregates can form in both asphaltenes at concentrations as low as 0.045 g/L. On increasing concentration, the small aggregates coalesce to form nanoaggregates in both the asphaltenes. However, as concentration is increased further, the steric bulk of the longer sidechains in UG8 prevent further growth of the nanoaggregates, by preventing π - π interactions between the aromatic cores. The WY asphaltene nanoaggregates, on the other hand, have considerably less steric bulk due to short sidechains, and can grow to larger sizes, i.e. have more asphaltene molecules per nanoaggregate, compared to UG8. The UG8 nanoaggregates, due to their greater polarizability caused by longer sidechains and more sulfur moieties, attract each other, forming clusters, which continue to grow in size up to a concentration of ~ 7.5 g/L. Beyond this concentration, there is no significant decrease in the longer T_2 component up to 15 g/L, suggesting that the cluster growth is terminated. Meanwhile, no evidence for the formation of clusters is observed in WY asphaltenes, at least up to 15 g/L concentration.

The role of alkyl sidechains in cluster formation was further confirmed by performing a ^1H - ^1H NOESY experiment, which clearly shows that there is far greater number of alkyl-alkyl and alkyl-aromatic interactions in UG8 P-asphaltenes compared to WY CD-asphaltenes. The only correlations observed for WY asphaltenes were between alkyl protons and phenolic $-\text{OH}$ groups.

In the earlier chapters of this thesis, it was suggested that alkyl sidechains have a significant role to play in asphaltene aggregation behavior. This hypothesis finds validation in this study. From a remediation perspective, it can be further hypothesized that clustering, which eventually leads to the blockage of pipelines and reservoirs, can be controlled by reducing the polarizability of the smaller asphaltene aggregates or nanoaggregates. The

polarizability can be tuned by reducing the alkyl content, which in effect implies reducing the length of the sidechains and reducing the sulfur content. These ideas can be tested in the laboratory, by treating asphaltenes thermally, or with reagents, and observing the resultant aggregation behavior. Therefore, this study provides a framework for future work, which may allow the development of on-field remediation techniques.

CHAPTER 8

8. RECENT RESULTS, GENERAL DISCUSSIONS AND FUTURE DIRECTIONS

8.1. Overview

In this closing chapter, a few very recent but key results will be discussed, which open up new avenues for the investigation of complex materials such as asphaltenes. It will be followed by a summary of all the major observations made in this thesis regarding asphaltene structure and finally, the future directions will be discussed.

Up until this point in this dissertation, all the solid-state NMR spectroscopic studies have been performed under a moderately slow MAS rates of 8 kHz. Working at lower speeds is advantageous when performing CP-based experiments, because higher speeds reduce the effective ^1H - ^{13}C dipolar coupling. Also, experiments on complex materials such as asphaltenes require a fairly large sample volume, which necessitates the use of larger rotors, which limits the highest spinning speeds that can be achieved. Larger volumes are required mostly for the experiments observing ^{13}C , which take much longer to provide a good signal-to-noise ratio if the sample volume is insufficient. However, ^1H observed experiments usually do not require a large sample volume, and can be potentially performed in smaller rotors at higher spinning speeds. Since the ^1H solid-state NMR spectrum is inherently broad due to strong homonuclear dipolar coupling (Chapter 4), it lacks any detail and only MAS at very high speeds or specialized filtering techniques (Chapter 4) can reveal finer details in the spectrum. The use of specialized techniques such as dipolar filter were demonstrated in Chapter 4, yielding useful results, but there always remained a curiosity to perform these

experiments under very fast MAS. For the spinning to have a significant effect on the resolution of the ^1H NMR spectrum, the spinning rate needs to be sufficiently high, preferably above 30-40 kHz. However, until very recently, the NMR spectrometers with ultrafast MAS capabilities were not widely available. The recent acquisition of a high-field solid-state NMR spectrometer, along with a 1.3 mm ultrafast MAS probe that can spin at up to 67 kHz enables ultrafast MAS experiments on asphaltenes.

8.2. Experimental details

All experiments were performed on a 16.4 T Bruker Avance III HD NMR spectrometer, operating at 700 MHz ^1H Larmor frequency, using a quadruple resonance 1.3-mm Bruker solid-state MAS probe. The UG8 petroleum asphaltene sample was packed into a 1.7 μL rotor, which was spun at 60 kHz. The temperature was controlled at 22 $^\circ\text{C}$ for all experiments and all ^1H 90° pulses were of 2.5 μs duration.

^1H Dipolar Filter: The dipolar filter sequence described in section 2.3.9 was used. The interpulse delay was varied from 10 to 200 μs , the dipolar filter pulse train was looped five times and 256 scans were recorded for each experiment. The 90° pulses in the 12-pulse train were each of 2.5 μs duration. The total filtering time corresponding to an interpulse delay τ can be calculated as: $5 \times 12 \times (2.5 + \tau) \times 10^{-3}$ ms.

^1H Back-to-Back (BABA) recoupling DQ-MAS: The two rotor-period BABA recoupling sequence described in section 2.3.11 was employed, with the DQ excitation loop repeated two times for each experiment, making the total recoupling period equal to four rotor-periods, i.e., 66.7 μs . A total of 128 transients were collected for the indirect dimension with 32 scans each and the delay being incremented in rotor-synchronized steps of 33.33 μs . In the one-dimensional ^1H NMR spectrum, spinning sidebands of equal intensity

occurred at around 60 kHz from the isotropic peaks, on both sides. Therefore, the DQ dimension is required to be at least double the spectral width used in the SQ dimension, which itself should be at least greater than 120 kHz when centred at the isotropic peaks, to avoid folding of the sidebands. Using a long spectral width in the indirect dimension reduces digital resolution, but this problem can be circumvented by using a DQ spectral width that is $1/2^n$ of the SQ, where n is a positive integer. It folds back the sidebands exactly on to the centre band of the isotropic signals, enhancing its intensity. A spectral width of 30 kHz in the indirect dimension was used in this study.

8.3. Results and Discussions

8.3.1. ¹H Dipolar Filter at 60 kHz MAS

The solid-state ¹H NMR spectrum of AOSA at 8 kHz MAS reported in Chapter 4 was significantly broad in nature and required a dipolar filter to observe the underlying sharper signals. In Fig. 8.1, the 8 kHz MAS ¹H NMR spectrum for UG8 asphaltenes is compared with the same spectrum at 60 kHz MAS. A significant improvement in resolution can be observed, since the aromatic and aliphatic protons are better resolved due to the reduction of broadening caused by homonuclear dipolar coupling. The narrower linewidths open up the possibility of observing the underlying signals with even greater detail when filtering techniques are applied and accurate deconvolution analysis can be performed on the ¹H NMR spectrum.

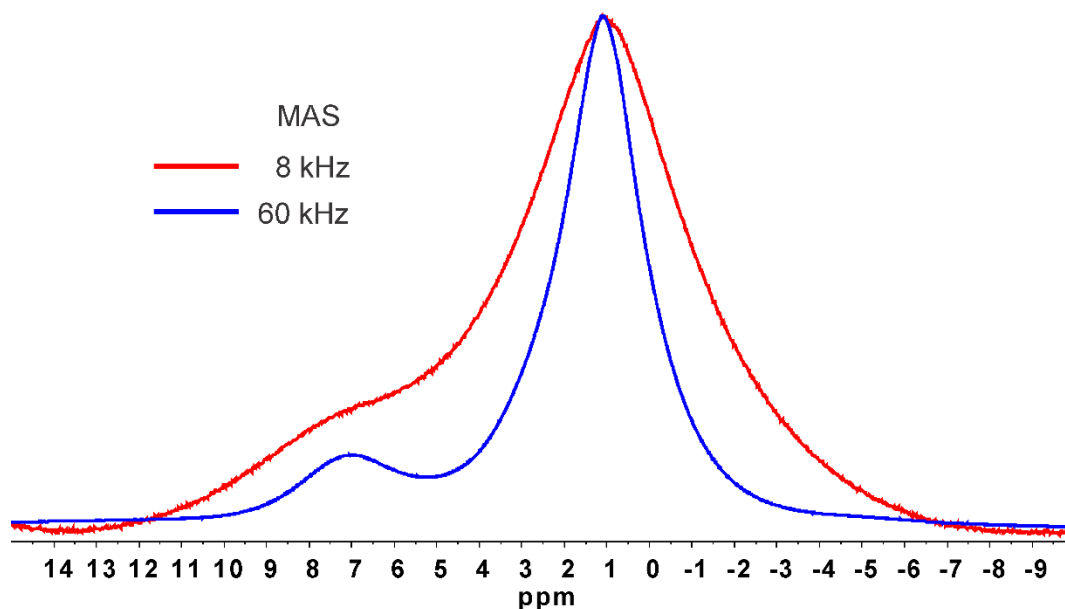


Figure 8.1. Solid-state ^1H NMR spectra of UG8 asphaltenes obtained at MAS speeds of 8 kHz (red) and 60 kHz (blue). The 8 kHz MAS spectrum was obtained at 500 MHz ^1H Larmor frequency in a 4 mm rotor, while the 60 kHz MAS spectrum was obtained at 700 MHz ^1H Larmor frequency in a 1.3 mm rotor.

The ^1H dipolar filtered spectra at different filtering times, corresponding to interpulse delays of 100, 110, 160 and 180 μs , are compared against the unfiltered spectrum at 60 kHz MAS in Fig. 8.2. The filtered spectra have been magnified in intensity for easy investigation, so quantitative deductions should not be made. These filtered spectra show unprecedented detail, especially in the aromatic region, revealing at least five different proton environments, which shall be used later for peak-fitting.

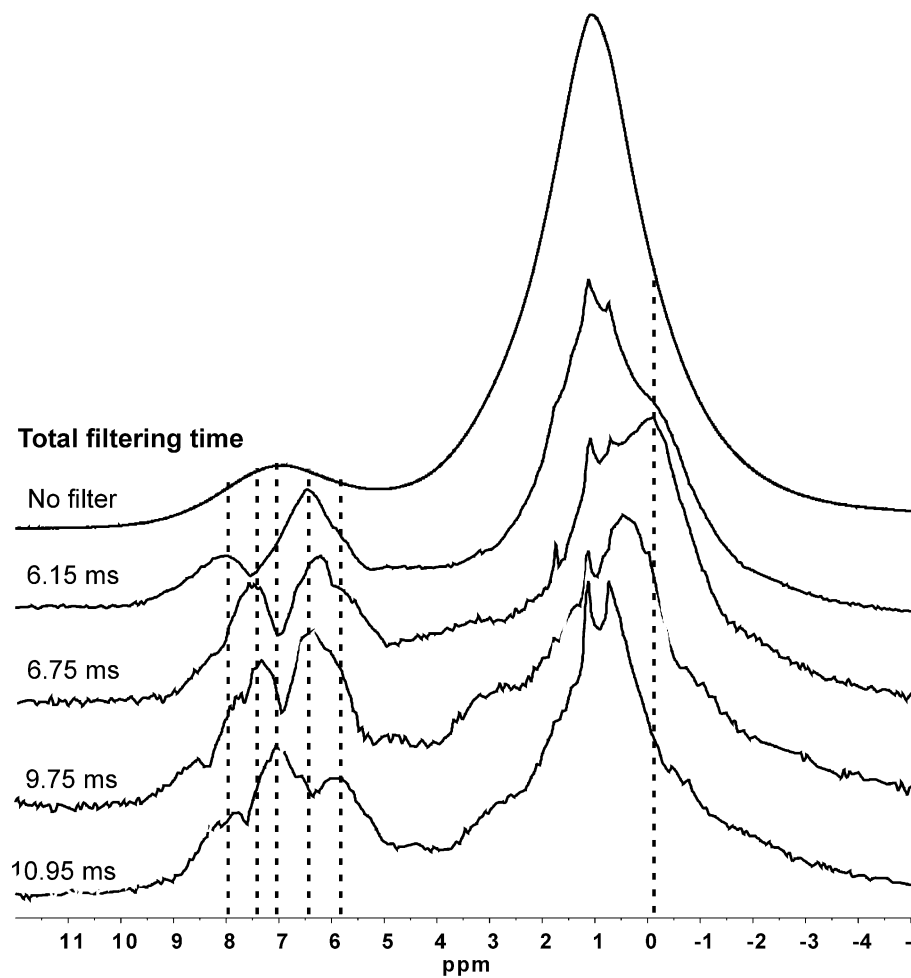


Figure 8.2. The ^1H dipolar filtered NMR spectra at different filtering times obtained at 60 kHz MAS, compared to the unfiltered ^1H NMR spectrum obtained at the same speed.

The aliphatic region also shows the presence of multiple narrow components, overlapping much broader signals. The narrow components arise from protons on mobile aliphatic chains, while the broad ones can be assigned to alicyclic groups and chain aliphatics that have restricted mobility. A definite signal is also observed at a slightly negative chemical shift, which is consistent with a previous study on AOSA (Chapter 4) and will be resolved even further in the following section. This is the first time in asphaltene literature that a solid-state ^1H NMR spectrum with such high degree of detail is reported. The component

signals of the aromatic region are not resolved even in a solution-state NMR spectrum, proving the efficiency and applicability of this technique. However, greater detail in the aliphatic region is desirable, which can be achieved using a T_2 filter, as demonstrated previously in Chapter 4.

8.3.2. ^1H T_2 Filter at 60 kHz MAS

A ^1H Hahn-echo experiment was performed at 60 kHz MAS to reveal the underlying narrow components of the aliphatic region, and also to calculate their respective T_2 relaxation times. Figure 8.3 shows the ^1H NMR spectrum obtained after 6.68 ms of T_2 filtering or Hahn-echo.

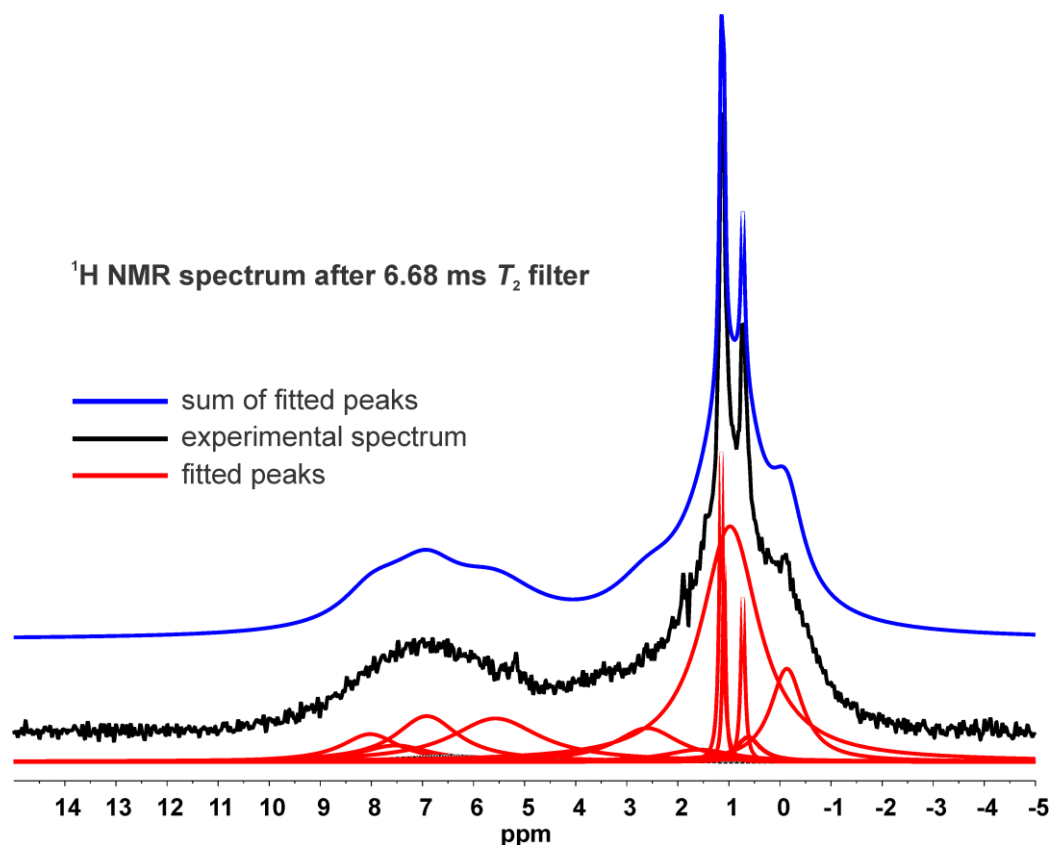


Figure 8.3. The ^1H NMR spectrum of UG8 asphaltenes at 60 kHz MAS, after 6.68 ms of T_2 filter, showing the deconvolved peaks and their sum.

Based on the T_2 filtered spectrum, and the dipolar filtered spectra shown earlier, a peak-fitting (deconvolution) model was constructed which enables the identification of all the components of the ^1H NMR spectrum. The presence of a prominent signal at the chemical shift of -0.13 ppm confirms beyond doubt that negative chemical shifts are indeed present.

Table 8.1. Assignments for the deconvolved peaks of the ^1H NMR spectrum, along with their corresponding calculated T_2 values at 60 kHz MAS.

ppm	assignment	Long T_2 (ms)	Short T_2 (ms)
8.02	'bay'arom. H, arom. H α to heteroatom, pyrrolic H	2.63 \pm 1.61 (24.2%)	0.24 \pm 0.08 (75.8%)
7.52	aromatic H	1.57 \pm 0.19 (39.7%)	0.49 \pm 0.04 (60.3%)
6.91	pendant aromatic	1.24 \pm 0.04 (82.2%)	0.06 \pm 0.02 (17.8%)
6.45	aromatic H/phenolic -OH	2.22 \pm 4.43 (13.9%)	0.94 \pm 0.36 (86.1%)
5.57	phenolic -OH	2.55 \pm 0.84 (21.6%)	0.19 \pm 0.03 (78.4%)
2.60	chain or cyclic -CH _n α to aryl ring	2.55 \pm 1.70 (3.4%)	0.27 \pm 0.01 (96.6%)
1.58	cyclic -CH ₂ /CH, chain CH ₂ on the interior of the clusters	0.92 \pm 0.26 (27.7%)	0.32 \pm 0.05 (72.3%)
1.15	chain -CH ₂ more than α from aryl ring on longer chains, on the exterior of the clusters	27.65 \pm 1.39 (100%)	-
1.09	chain -CH ₂ more than α from aryl ring on shorter chains on the exterior of the clusters	13.50 \pm 0.96 (100%)	-
0.98	cyclic -CH ₂ and rigid chain -CH ₂	1.37 \pm 0.35 (35.2%)	0.50 \pm 0.08 (64.8%)
0.73	-CH ₃ on the periphery of clusters	25.31 \pm 1.11 (100%)	-
0.62	-CH ₃ on the interior of clusters	1.08 \pm 0.22 (32.9%)	0.35 \pm 0.05 (67.1%)
-0.13	intercalated terminal -CH ₃	1.78 \pm 2.09 (13.4%)	0.44 \pm 0.10 (86.6%)

In Table 8.1, the assignments for the deconvolved peaks are shown, along with their corresponding transverse relaxation times. To make the assignments, besides chemical shifts the linewidths and the relaxation times were also considered. Instead of discussing every fitted peak, only those that provide new and important information about asphaltene structure will be elucidated upon. Recall that a longer T_2 implies a more mobile component,

a fact that will be eluded to frequently in the following discussion. The aromatic signal that deserves attention is the one at 6.91 ppm. It arises from protons that are mostly mobile, 82.2% of them having the higher T_2 of 1.24 ± 0.04 ms, while the lower T_2 component of 0.06 ± 0.02 ms constitutes only 17.8% of the signal. Compared to it, all the other aromatic protons (8.02, 7.52 and 6.45 ppm) are mostly rigid, with a greater percentage (60.3-86.1%) of the shorter T_2 components. Therefore, the 6.91 ppm protons likely belong to small aromatic rings that are not condensed with the main core, making them less structurally constrained. Recall that the presence of pendant aromatic rings in Wyoming coal-derived asphaltene was proposed in Chapter 6, but could not be confirmed for UG8 petroleum asphaltene. The ^1H NMR results shown here indicate that UG8 asphaltene also contain similar pendant aromatic rings, attached to the central core via a direct bond between sp^2 aromatic carbons, similar to model hexabenzocoronene derivatives reported by Fechtenkötter *et al.*¹⁶⁰ and Fischbach *et al.*¹⁶¹ These motifs have been reported for UG8 asphaltene in a recent AFM imaging study⁵⁷ and this is the first spectroscopic verification of those results. The intense and broad aliphatic signal at 1.58 ppm is partly assigned to the cycloalkyl groups, with a short T_2 of 0.32 ± 0.05 ms. Their largely rigid (72.3%) nature indicates that they are condensed with the aromatic core. The second component of this signal, with the slightly longer T_2 of 0.92 ± 0.26 ms, but still more rigid than most other alkyl signals, is likely the chain $-\text{CH}_2$ moieties that are located on the interior of the clusters. The very narrow peaks at 1.15 and 1.09 ppm only have single component of T_2 , which is longer than most other signals, at 27.65 ± 1.39 ms and 13.5 ± 0.96 ms respectively. These can be attributed to chain $-\text{CH}_2$ groups that are on the periphery of the asphaltene clusters, which makes them significantly more mobile than those on the interior. Among these, the 1.15 ppm peak has the longer T_2 , which is likely on account of them belonging to longer

chains. It indicates that a distribution of short and long alkyl sidechains exist in UG8 asphaltenes. The signal at 0.73 ppm, with a single component of T_2 at 25.31 ± 1.11 ms, belongs to the mobile terminal $-\text{CH}_3$ groups on the periphery of the clusters, while those at 0.62 ppm arise from those on the interior, since they have a large rigid fraction (67.1%) with a T_2 of 0.35 ± 0.05 ms. The -0.13 ppm peak is assigned to $-\text{CH}_3$ groups that are intercalated between aromatic sheets in an adjacent nanoaggregate, as described previously in Chapter 4. The shift of this methyl signal to lower frequencies is due to the shielding caused by aromatic ring currents, and these groups are largely rigid in nature, evinced by the majority fraction (86.6%) having a short T_2 of 0.44 ± 0.10 ms. Their rigidity attests for their assignment, since the intercalation of these groups inside an aggregate, between aromatic sheets, would restrict their mobility. These results, regarding these aliphatic-aromatic interactions in petroleum asphaltenes, which were also proposed in Chapters 4 and 6, corroborate the previous evidence in a more succinct manner, simply due to the ultrafast spinning speed and the signal dispersion offered by the high magnetic field. This intercalating effect, and also the existence of disparate mobilities among the aliphatic chains, are strong indicators that the UG8 petroleum asphaltenes exist as clusters in the solid state and that the alkyl chains play a significant role in the clustering behavior.

8.3.3. ^1H Back-to-Back Recoupling DQ-MAS Homonuclear Correlation

The back-to-back recoupling technique, referred to as BABA was introduced in Chapter 2. The homonuclear version of this experiment enables the identification of protons that are spatially proximate to each other and interact via dipole-dipole coupling. In brief, the BABA experiment is collected as a 2D spectrum, where the indirect dimension, called the

double quantum (DQ) dimension, has frequencies that are double that of the direct single quantum (SQ) dimension. If two moieties interact via dipole-dipole coupling, they will exhibit two cross peaks, each at the SQ chemical shifts of the respective signals and the DQ chemical shift given by the sum of the SQ shifts. The ^1H DQ-MAS NMR spectrum of UG8 P-asphaltene obtained at 60 kHz MAS is shown in Fig. 8.4.

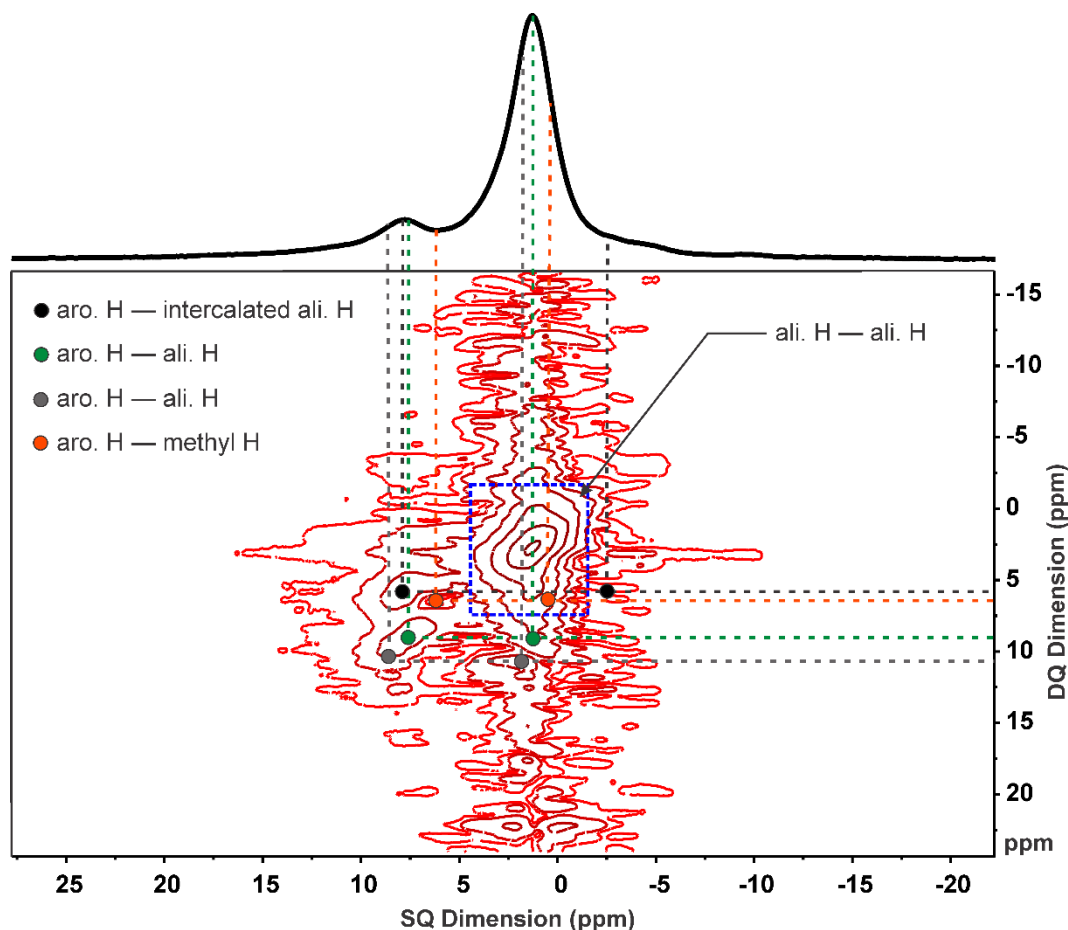


Figure 8.4. ^1H DQ-MAS NMR spectrum of UG8 asphaltene obtained at 60 kHz MAS using the BABA recoupling sequence. (ali. = aliphatic, aro. = aromatic).

The large correlations at the centre represent all the dipolar interactions between aliphatic protons, both chain and cyclic, which is expected since they represent the majority of the protons in the system. Significant correlations can be seen between aromatic protons (7-8

ppm SQ) and alkyl protons (1.2-2 ppm SQ), demonstrating the proximity of these groups (green and grey dots). It is likely that most of these alkyl protons are in the cyclic groups, since these would be more proximate to the aromatic protons, compared to most of the chain protons. Methyl protons in the ~0.6 ppm range correlate with aromatic protons at ~6.0 ppm (orange dots). These methyl protons have been assigned to terminal groups on alkyl chains that are on the interior of the clusters. These correlations confirm this assignment, and reinforces the presence of clusters, which brings these methyl groups close to the aromatic protons. The most interesting correlations are the ones between the aromatic protons and the alkyl protons with negative chemical shifts (black dots). Since one of the interacting groups have a negative chemical shift, the corresponding DQ chemical shift is less than the sum of the SQ chemical shifts. This correlation shows that the negative chemical shift signals in the ^1H solid-state NMR spectrum of UG8 asphaltenes is indeed from alkyl groups that are intercalated between aromatic rings.

8.4. Overall Conclusions, General Discussions

This thesis set out to unravel the molecular structure of asphaltenes using a combination of solution- and solid-state NMR spectroscopic techniques. One of the primary objectives was to address the gaps in the literature with respect to the use of NMR spectroscopy for asphaltene characterization. The broader objective was to understand the intricate details of asphaltene molecular and aggregate structure, and relate the structure to aggregation behavior. Of the various techniques employed for asphaltene characterization, NMR spectroscopy is one of the most versatile, not only providing qualitative and quantitative structural details, but also dynamic information.

First, it was shown that deconvolution of the solution-state ^1H and ^{13}C NMR spectra of Athabasca oil-sands asphaltenes (AOSA) into their component peaks provides a great wealth of information, and avoids the problem of overlapping signals, especially those in the broad regions of the spectra. The overlapping peaks were revealed by using the HSQC experiment. These were also the first detailed deconvolution models reported for the NMR spectra of any asphaltene. Using these models, it was found that the average PAH in AOSA is composed of 6-7 aromatic rings, in agreement with the “island” model architecture. Relaxation parameters T_1 and T_2 were measured for the ^1H signals, which revealed the hierarchical nanoaggregate-cluster motif of asphaltenes, where the clusters were shown to consist of ~6-7 nanoaggregates. The first HSQC spectrum of any asphaltene was reported, along with a modified version of the experiment, which demonstrated that the alicyclic rings remain condensed with the aromatic core. The observations in this study suggest that the Yen-Mullins model represents the predominant molecular architecture of AOSA, with an average molecular weight of ~720 u.

The above solution-state study was followed by a solid-state NMR spectroscopic investigation of AOSA. In this study, deconvolution analysis was once again used to resolve both the ^{13}C CP and DP NMR spectra, where the model was verified by CP build-up and dipolar dephasing (DD) experiments. Using CP dynamics, it was shown that all of the aromatic groups are highly rigid, with no evidence for mobile aromatic rings, ruling out the possibility of pendant aromatic rings attached to the main aromatic core. The predominance of large pericondensed PAH systems was also suggested by cross-polarization dynamics, and was confirmed quantitatively by the ^{13}C DP experiment, which put the number of condensed rings in a PAH between 5 and 7. The DD experiments also

validated the presence of large PAHs, showing that the bridgehead aromatic carbons experience very little C-H dipolar coupling and are dominated by CSA, which indicates their remoteness from the aromatic protons. The ^{13}C CP-DIVAM nutation curves helped differentiate between the mobile and rigid components, showing that the alicyclic groups have similar rigidity to the aromatic core, with which they are condensed. The first well-resolved solid-state ^1H NMR spectrum showing the sharp signals underlying an otherwise broad spectrum was also reported, using a combination of dipolar and T_2 filtering techniques. The very first spectroscopic evidence was provided for alkyl groups occupying the region between stacked aromatic sheets in the solid state and likely interfering with the π - π stacking. The biexponential T_2 relaxation behavior of alkyl groups demonstrated that the nanoaggregate-cluster hierarchy also exists in the solid phase, where the nanoaggregates form interlocking structures. This study provides further evidence for the predominance of the Yen-Mullins model of asphaltene architecture, where the average molecular weight was found to be ~ 960 u.

Having established some of the basic tenets of asphaltene structure, the focus was shifted to relating structure with aggregation behavior. For the purpose of determining the structural features that drive aggregation, petroleum (P) asphaltenes were compared to asphaltenes derived from coal (CD). It is known that CD-asphaltenes are structurally distinct from P-asphaltenes, having lower average molecular weight and generally regarded as less complex, hence easier to study. Three different CD-asphaltenes were compared with two P-asphaltenes, along with AOSA, using two-dimensional multiplicity edited HSQC. This technique enables the differentiation of $-\text{CH}_2$ signals from $-\text{CH}_3$ and $-\text{CH}$ signals, which appear with opposite phases. Qualitative structural differences between P- and CD-

asphaltenes were highlighted. It was shown that the CD-asphaltenes contain mostly short alkyl sidechains, 2-3 carbons long, whereas a larger distribution of sidechain lengths, short and long, is found in P-asphaltenes. The P-asphaltenes were also shown to have a more extended network of alicyclic rings attached to the aromatic core, whereas those in CD-asphaltenes are mostly naphthenic in nature. The P-asphaltene aromatic cores were also found to be substituted to a much larger extent, evinced by the lack of aromatic C-H correlations. This study also hinted at the presence of larger and more rigid aggregates or clusters in UG8 asphaltenes, but it demands further investigation.

A more quantitative comparison of P- and CD-asphaltenes was then performed by selecting one of each kind: UG8 from the P-asphaltenes and WY from CD-asphaltenes. Solid-state ^{13}C CP-MAS NMR spectroscopic techniques were used, which showed that the asphaltene molecules are dominated by single core PAHs, the smallest cores in both asphaltenes consisting of at least 5-6 pericondensed aromatic rings, and the largest cores containing up to 15-20 rings. These PAH sizes were significantly larger than previously hypothesized, but find unambiguous support in AFM imaging results.⁵⁷ These large PAHs rule out the possibility of traditional “archipelago” structures being the dominant architecture, since that would cause the average molecular weight, and the weight range, for these asphaltenes to be much higher than what has been reported by mass spectrometric studies that do not cause fragmentation.^{28,29,39,55} However, both CP dynamics and CP refocused DIVAM suggested that the WY asphaltenes may have small pendant PAHs, attached to the larger core via aryl linkages, making it different from traditional archipelago models. No evidence for these tethered groups was observed for UG8 asphaltenes in this study, although they may be present, with their mobility restricted by closer packing of the

UG8 clusters. It was also shown that asphaltenes may contain anomeric (O-C-O) groups, the signals of which previously got assigned to aromatic carbons because of chemical shift overlap. The UG8 P-asphaltene aromatic cores were shown to be substituted to a greater extent, with longer alkyl sidechains (~6 carbons on average) and a larger fraction of alicyclic groups. They also possess a greater number of sulfur containing groups, including sulfoxide moieties which are absent or present in insignificant amounts in WY asphaltenes. It was proposed that the alkyl chains in UG8 intercalate between the aromatic rings of adjacent asphaltene aggregates on account of their long sidechains, something which is not observed in WY asphaltenes. These interactions were proposed to have important implications on the role of alkyl sidechains in asphaltene aggregation.

In order to investigate the role of structure in aggregation behavior, the UG8 and WY asphaltenes were then studied using solution-state ^1H NMR T_2 relaxation experiments performed at nine different concentrations, ranging from below the critical nanoaggregate concentration (CNAC) to above the critical cluster concentration (CCC). It was observed that on increasing asphaltene concentration, the UG8 P-asphaltenes first form nanoaggregates, which eventually coalesce to form clusters, in agreement with the Yen-Mullins model. However, clustering was not observed among the nanoaggregates in WY asphaltenes, which were hypothesized to grow to larger sizes than the UG8 nanoaggregates. Based on these observations, it was proposed that the longer sidechains, generally higher alkyl content and a larger number of sulfur moieties, make the UG8 asphaltenes a lot more polarizable, which leads to attraction between the nanoaggregates. In contrast, WY asphaltene nanoaggregates have very little polarizability, on account of short alkyl sidechains and insignificant sulfur content. A ^1H - ^1H NOESY experiment on both the

asphaltenes demonstrated that the sidechains in the UG8 asphaltenes indeed interact with each other, and those in WY do not, confirming the role of sidechains in clustering. These results showed that while initial aggregation processes at lower concentrations, where nanoaggregates are formed, are driven by π - π interactions, clustering behavior at higher concentrations appear to be driven by alkyl sidechains and sulfur moieties. This hypothesis provides an experimental handle which allows it to be easily verified by further investigations. Various model-asphaltene compounds of differing sidechain lengths and sulfur content can be studied similarly using relaxation behavior at different concentrations. Computational methods such as molecular dynamics can also be used to study how the above factors affect clustering. If validated, it offers a means for attenuating the clustering behavior in asphaltenes that eventually leads to large scale depositions. Attenuation of clustering can be likely be achieved by reduction of sidechain lengths via chemical or thermal means, or by reducing the sulfur content, or both.

In this final chapter glimpses were provided into the possibilities that solid-state NMR spectroscopy under fast spinning conditions can offer. It was shown that the solid-state ^1H NMR spectrum of asphaltenes that is usually overlooked in literature due to its broad, featureless character, can be resolved into its component peaks using dipolar filter and T_2 filter experiments at 60 kHz MAS. These resolved components clearly show the existence of signals at a negative chemical shift arising from alkyl moieties intercalated between aromatic sheets, unambiguously confirming the observations made previously in Chapter 4. It was also shown that pendant aromatic rings are likely to be present in UG8 asphaltenes as well, for which no evidence was found in Chapter 6. Further evidence for intercalated alkyl sidechains was found using a ^1H - ^1H double-quantum (DQ) correlation experiment at

60 kHz MAS. The high-speed solid-state experiments, especially the two-dimensional DQ-MAS technique, takes the NMR spectroscopic investigation of asphaltenes into uncharted territories.

In summary, the work presented in this thesis provides considerable insight into some of the debates regarding asphaltene molecular architecture. The very first NMR spectroscopic evidence was presented for certain structural features: the alicyclic groups condensed with aromatic core, the alkyl groups intercalated between aromatic cores, the pendant aromatic groups and the interlocked nanoaggregates. It proceeds to correlate asphaltene structure with its aggregation behavior, which is extremely important from an industry perspective. Additionally, the asphaltene structural models proposed here can enable more accurate modelling of reservoirs using DFA measurements, since the measurement of asphaltene gradients with DFA requires detailed understanding of their structure. One of the primary objectives of the thesis was to demonstrate the versatility of NMR spectroscopic techniques, which was successfully achieved in the form of a variety of structural and dynamic information. Several of these techniques were employed for the first time for asphaltene characterization, such as HSQC, NOESY, dipolar filter, DIVAM and BABA DQ-MAS. The most comprehensive analysis of asphaltene CP dynamics was presented, which should serve as a basis for subsequent CP studies on asphaltenes.

8.5. Future Directions

Studies on complex materials such as asphaltenes often raise more questions than they answer. The studies presented in this thesis have established some of the basic tenets of asphaltene structure, and the role structure plays in asphaltene aggregation. However, there

are definitely more experiments that can be performed to validate the observations made in this thesis, and improve upon some of the techniques employed. In this regard, several possible paths that these projects can take in the future are numerated below.

i.) *Using model compounds*: There are several ways in which synthetic model compounds can be employed. To determine asphaltene architecture, i.e. island or archipelago, various model molecules of each type can be studied using solid-state CP-techniques in the same way as Chapters 4 and 6. A wide array of such model compounds can be found in references 29 and 39,^{29,39} which can be either synthesized in the laboratory or are commercially available. An example of a model archipelago compound is 2,5-Bis(2-pyren-1-yl-ethyl)-pyridine, while derivatives of coronene or hexabenzocoronene can be used as model island compounds. The compounds that show similar CP dynamics and dipolar dephasing behavior, similar DIVAM nutation curves or similar relaxation behavior of the dipolar filtered ¹H NMR spectrum (Chapter 4), are likely to constitute the predominant asphaltene architecture. In the footsteps of Chapter 7, the relaxation behavior of these compounds can also be studied at different concentrations to investigate similarities in aggregation behavior with asphaltenes. Model compounds of varying sidechain lengths can be used to test the hypothesis that sidechain length plays a major role in the clustering of nanoaggregates. The role of sulfur moieties can also be investigated in a similar fashion, using model compounds with varying number of sulfur moieties.

ii.) *Computational approach*: Significant insight can be gained using computational methodologies such as molecular dynamics (MD). The hypothetical asphaltene molecules proposed in this thesis can be optimized and then their aggregation behavior studied using MD simulations, to test the feasibility of these models. Ruiz-Morales and co-workers have

used computational techniques to verify the distribution of PAH sizes and set quantitative limits to the size of the PAH.^{166–168} Model systems can be used here as well, to investigate the role of structure on aggregation behavior. Similar approaches have been used in literature by the groups of Pacheco-Sanchez and Bhattacharjee,^{155–158} but the results presented in this work provide specific investigative handles such as sidechain length and sulfur content.

iii.) *Variable temperature studies*: The effect of temperature on asphaltene aggregation behavior has not been studied in this thesis, but it is an important paradigm to consider. Studying how the formation of nanoaggregates and clusters are affected by changing temperature, the role of entropy can be determined. Ideally, relaxation experiments at different temperatures and at different concentrations can be used for this purpose. The ¹H-¹H NOESY experiment can reveal how the interaction between nanoaggregates changes with temperature.

iv.) *Diffusion measurements*: A natural progression of probing relaxation behavior to study asphaltene aggregation is to perform diffusion measurements. Solution-state diffusion ordered spectroscopy (DOSY) is frequently used to distinguish between molecules (or groups of molecules) of different sizes, which makes it a very useful technique to study asphaltenes which have a hierarchical architecture. Petroleum- and coal-derived asphaltenes can be further compared in this way, to correlate structure with function. Model compounds can also find use in these studies.

v.) *Advanced solid-state NMR spectroscopic techniques*: This thesis has already shown the use of solid-state NMR spectroscopic methods that are not mainstream for asphaltene characterization. Numerous other such techniques can prove to be extremely useful for

asphaltene characterization. An example was provided in this chapter in the form of the ^1H DQ-MAS experiment, which can be developed upon further, by first optimizing the parameters using model systems. Two dimensional solid-state heteronuclear correlation techniques can also provide valuable information regarding connectivities in asphaltene molecules. Dipolar recoupling techniques such as REDOR (rotational echo double resonance)¹²³ can potentially measure internuclear distances between different moieties in asphaltenes. A host of spectral editing techniques that can select for specific functional groups have been used in literature for the characterization of humic substances¹⁶⁹ and kerogen.¹⁷⁰ These methods can be extremely useful for the characterization of asphaltenes as well, the only caveat being the requirement of specialized pulse sequences that are not currently implemented at the University of Lethbridge NMR facility. In terms of solid-state NMR spectroscopy, these experiments should be the next step as this project moves forward.

vi.) *Using fluorinated tracer molecules:* An area of interest closely related to asphaltene characterization is the study of how asphaltene molecules interact with the other components of petroleum such as the resins, small aromatics and saturates (maltenes). Model molecules that mimic maltenes can be introduced into asphaltene solutions, and their relaxation and diffusion behavior can be studied using techniques already mentioned. We propose the use of fluorinated tracer molecules, i.e. model maltene molecules which are partially fluorinated or perfluorinated. The fluorine (^{19}F) nucleus as an NMR probe presents the advantage of not having a natural background NMR signal in asphaltenes, and can be studied with convenience. Moreover, fluorine offers much greater sensitivity than ^{13}C and

a wide spectral window. It is also very sensitive to its chemical environment, which makes it ideal for studying intermolecular interactions.

vii.) *Utilizing the high-field NMR spectrometer:* The recently acquired high-field 700 MHz (^1H Larmor frequency) NMR spectrometer at the University of Lethbridge offers the unique advantage of solution- and solid-state capabilities on the same instrument, and its utility has been demonstrated in this thesis. A higher field offers several advantages, including better dispersion, i.e. better frequency separation of the NMR signals and the faster signal acquisition due to requirement of fewer scans. Heteronuclear two-dimensional experiments, which usually require long experimental times at lower fields, can be performed at much shorter times at these high fields. The instrument in question also comes equipped with an automated sample changer which allows for high-throughput experiments in the solution state. Automation is particularly useful for doing experiments where multiple samples are required to be run under the same conditions, such as variable concentration experiments. Moreover, advanced solid-state NMR techniques that require high MAS rates, such as Lee-Goldburg CP (LG-CP)-based experiments¹⁷¹ that enable heteronuclear correlation and distance measurements, can be performed using this facility, adding to the possible investigative pathways to study asphaltenes and related materials in greater detail.

REFERENCES

- (1) *Asphaltenes, heavy oils, and petroleomics* 1st ed; Mullins, O.C., Sheu, E., Hammami, A., Marshall, A., Eds.; Springer: New York, 2007.
- (2) Murphy, D. J.; Hall, C. A. S. *Ann. N. Y. Acad. Sci.* **2010**, *1185*, 102-118.
- (3) Mullins, O. C.; Rodgers, R. P.; Weinheber, P.; Klein, G. C.; Venkataramanan, L.; Andrews, A. B.; Marshall, A. G. *Energy Fuels* **2006**, *20*, 2448-2456.
- (4) Betancourt, S. S.; Dubost, F. X.; Mullins, O. C.; Cribbs, M. E.; Creek, J.; Mathews, S. G. Predicting Downhole Fluid Analysis Logs to Investigate Reservoir Connectivity. Proceedings of the International Petroleum Technology Conference, Dubai, UAE, December 4-6, 2007.
- (5) Hosseini-Dastgerdi, Z.; Tabatabaei-Nejad, S. A. R.; Khodapanah, E.; Sahraei, E. *Asia-Pacific J. Chem. Eng.* **2015**, *10*, 1-14.
- (6) Mullins, O. C. *Annu. Rev. Anal. Chem.* **2011**, *4*, 393-418.
- (7) Mullins, O. C.; Sabbah, H.; Eyssautier, J.; Pomerantz, A. E.; Barré, L.; Andrews, A. B.; Ruiz-Morales, Y.; Mostowfi, F.; McFarlane, R.; Goual, L.; Lepkowitz, R.; Cooper, T.; Orbulescu, J.; Leblanc, R. M.; Edwards, J.; Zare, R. N. *Energy Fuels* **2012**, *26*, 3986-4003.
- (8) Marshall, A. G.; Rodgers, R. P. *Acc. Chem. Res.* **2004**, *37*, 53-59.
- (9) Fan, T.; Buckley, J. S. *Energy Fuels* **2002**, *16*, 1571-1575.
- (10) Speight, J. G. *Chemistry and Technology of Petroleum*; 5th ed.; CRC Press: New York, 2014.
- (11) Akbarzadeh, K.; Hammami, A.; Kharrat, A.; Zhang, D.; Allenson, S.; Creek, J.; Kabir, S.; Jamaluddin, A.; Marshall, A.G.; Rodgers, R.P.; Mullins O.C.; Solbakken, T. *Oilfield Review Summer Ed.* **2007**, 22-43.
- (12) Leontaritis, K.; Mansoori, G. *J. Pet. Sci. Eng.* **1988**, *1*, 229-239.

- (13) Milam, S. N.; Tegelaar, E. W.; Freeman, J. J.; Taylor, R. B. Remediation of asphaltene-induced plugging of wellbores and production lines. U.S. Patent 14/315,054, June 25, 2014.
- (14) Goual, L.; Sedghi, M.; Wang, X.; Zhu, Z. *Langmuir* **2014**, *30*, 5394-5403.
- (15) Goual, L.; Sedghi, M. *J. Colloid Interface Sci.* **2015**, *440*, 23-31.
- (16) Darabi, H.; Sepehrnoori, K. Modeling and Simulation of Near-Wellbore Asphaltene Remediation Using Asphaltene Dispersants. Proceedings of the SPE Reservoir Simulation Symposium; Society of Petroleum Engineers: Houston, USA, 2015.
- (17) Jones, J. L.; Barton, W. R. S.; Saccomando, D. J.; Cook, S. J.; Carney, S. P.; Mayhew, A. Asphaltene dispersant containing lubricating compositions. U.S. Patent 8,877,694, November 4, 2014.
- (18) Gollapudi, U. K.; Bang, S. S.; Islam, M. R. Ultrasonic Treatment for Removal of Asphaltene Deposits During Petroleum Production. Proceedings of the SPE Formation Damage Control Symposium; Society of Petroleum Engineers: Lafayette, USA, 2014.
- (19) Mullins, O. C.; Martínez-Haya, B.; Marshall, A. G. *Energy Fuels* **2008**, *22*, 1765-1773.
- (20) Buenrostro-Gonzalez, E.; Groenzin, H.; Lira-Galeana, C.; Mullins, O. C. *Energy Fuels* **2001**, *15*, 972-978.
- (21) Groenzin, H.; Mullins, O. C. *Energy Fuels* **2000**, *14*, 677-684.
- (22) Groenzin, H.; Mullins, O. C. *J. Phys. Chem. A* **1999**, *103*, 11237-11245.
- (23) Bungler, J. W.; Li, N. C. In *Chemistry of Asphaltenes*; Bungler, J. W.; Li, N. C., Eds.; American Chemical Society: Washington, DC, 1981.
- (24) Sheu, E. Y.; De Tar, M. M.; Storm, D. A.; DeCanio, S. J. *Fuel* **1992**, *71*, 299-302.
- (25) Andersen, S. I.; Speight, J. G. *Fuel* **1993**, *72*, 1343-1344.

- (26) Miller, J. T.; Fisher, R. B.; Thiyagarajan, P.; Winans, R. E.; Hunt, J. E. *Energy Fuels* **1998**, *12*, 1290-1298.
- (27) Boduszynski, M. M. *Energy Fuels* **1988**, *2*, 597-613.
- (28) Pomerantz, A. E.; Hammond, M. R.; Morrow, A. L.; Mullins, O. C.; Zare, R. N. *J. Am. Chem. Soc.* **2008**, *130*, 7216-7217.
- (29) Sabbah, H.; Morrow, A. L.; Pomerantz, A. E.; Mullins, O. C.; Tan, X.; Gray, M. R.; Azyat, K.; Tykwinski, R. R.; Zare, R. N. *Energy Fuels* **2010**, *24*, 3589-3594.
- (30) Andrews, A. B.; Edwards, J. C.; Pomerantz, A. E.; Mullins, O. C.; Nordlund, D.; Norinaga, K. *Energy Fuels* **2011**, *25*, 3068-3076.
- (31) Speight James, G.; Moschopedis Speros, E. In *Chemistry of Asphaltenes; Advances in Chemistry*; American Chemical Society, 2012; Vol. 195, pp. 1–15.
- (32) Zhang, L.; Wang, C.; Zhao, Y.; Yang, G.; Su, M.; Yang, C. *J. Fuel Chem. Technol.* **2013**, *41*, 1328-1335.
- (33) Acevedo, S.; Guzmán, K.; Labrador, H.; Carrier, H.; Bouyssiere, B.; Lobinski, R. *Energy Fuels* **2012**, *26*, 4968-4977.
- (34) Cyr, N.; McIntyre, D. D.; Toth, G.; Strausz, O. P. *Fuel* **1987**, *66*, 1709-1714.
- (35) Storm, D. A.; Edwards, J. C.; DeCanio, S. J.; Sheu, E. Y. *Energy Fuels* **1994**, *8*, 561-566.
- (36) Strausz, O. P.; Mojelsky, T. W.; Lown, E. M. *Fuel* **1992**, *71*, 1355-1363.
- (37) Mojelsky, T. W.; Ignasiak, T. M.; Frakman, Z.; McIntyre, D. D.; Lown, E. M.; Montgomery, D. S.; Strausz, O. P. *Energy Fuels* **1992**, *6*, 83-96.
- (38) Artok, L.; Su, Y.; Hirose, Y.; Hosokawa, M.; Murata, S.; Nomura, M. *Energy Fuels* **1999**, *13*, 287-296.
- (39) Sabbah, H.; Morrow, A. L.; Pomerantz, A. E.; Zare, R. N. *Energy Fuels* **2011**, *25*, 1597-1604.

- (40) Murgich, J.; Abanero, J. A.; Strausz, O. P. *Energy Fuels* **1999**, *13*, 278-286.
- (41) Karimi, A.; Qian, K.; Olmstead, W. N.; Freund, H.; Yung, C.; Gray, M. R. *Energy Fuels* **2011**, *25*, 3581-3589.
- (42) Mullins, O. C. *Energy Fuels* **2010**, *24*, 2179-2207.
- (43) Sheremata, J. M.; Gray, M. R.; Dettman, H. D.; McCaffrey, W. C. *Energy Fuels* **2004**, *18*, 1377-1384.
- (44) Alvarez-Ramírez, F.; Ruiz-Morales, Y. *Energy Fuels* **2013**, *27*, 1791-1808.
- (45) Alshareef, A. H.; Scherer, A.; Tan, X.; Azyat, K.; Stryker, J. M.; Tykwinski, R. R.; Gray, M. R. *Energy Fuels* **2011**, *25*, 2130-2136.
- (46) Zajac, G. W.; Sethi, N. K.; Joseph, J. T. *Scanning Microsc.* **1994**, *8*, 463-470.
- (47) Sharma, A.; Groenzin, H.; Tomita, A.; Mullins, O. C. *Energy Fuels* **2002**, *16*, 490-496.
- (48) Klee, T.; Masterson, T.; Miller, B.; Barrasso, E.; Bell, J.; Lepkowitz, R.; West, J.; Haley, J. E.; Schmitt, D. L.; Flikkema, J. L.; Cooper, T. M.; Ruiz-Morales, Y.; Mullins, O. C. *Energy Fuels* **2011**, *25*, 2065-2075.
- (49) Pinkston, D. S.; Duan, P.; Gallardo, V. A.; Habicht, S. C.; Tan, X.; Qian, K.; Gray, M.; Müllen, K.; Kenttämä, H. I. *Energy Fuels* **2009**, *23*, 5564-5570.
- (50) Wargadalam, V. J.; Norinaga, K.; Iino, M. *Fuel* **2002**, *81*, 1403-1407.
- (51) Badre, S.; Carla Goncalves, C.; Norinaga, K.; Gustavson, G.; Mullins, O. C. *Fuel* **2006**, *85*, 1-11.
- (52) Qian, K.; Edwards, K. E.; Siskin, M.; Olmstead, W. N.; Mennito, A. S.; Dechert, G. J.; Hoosain, N. E. *Energy Fuels* **2007**, *21*, 1042-1047.
- (53) Andrews, A. B.; Guerra, R. E.; Mullins, O. C.; Sen, P. N. *J. Phys. Chem. A* **2006**, *110*, 8093-8097.

- (54) Lisitza, N. V.; Freed, D. E.; Sen, P. N.; Song, Y.-Q. *Energy Fuels* **2009**, *23*, 1189-1193.
- (55) Sabbah, H.; Pomerantz, A. E.; Wagner, M.; Müllen, K.; Zare, R. N. *Energy Fuels* **2012**, *26*, 3521-3526.
- (56) Wu, Q.; Pomerantz, A.; Mullins, O.; Zare, R. *J. Am. Soc. Mass Spectrom.* **2013**, *24*, 1116-1122.
- (57) Schuler, B.; Meyer, G.; Peña, D.; Mullins, O. C.; Gross, L. *J. Am. Chem. Soc.* **2015**, *137*, 9870-9876.
- (58) Solum, M. S.; Pugmire, R. J.; Grant, D. M. *Energy Fuels* **1989**, *3*, 187-193.
- (59) Dwiggin, C. W. *J. Phys. Chem.* **1965**, *69*, 3500-3506.
- (60) Storm, D. A.; Sheu, E. Y.; DeTar, M. M. *Fuel* **1993**, *72*, 977-981.
- (61) Eyssautier, J.; Levitz, P.; Espinat, D.; Jestin, J.; Gummel, J.; Grillo, I.; Barré, L. *J. Phys. Chem. B* **2011**, *115*, 6827-6837.
- (62) Sirota, E. B. *Energy Fuels* **2005**, *19*, 1290-1296.
- (63) Östlund, J. A.; Löfroth, J. E.; Holmberg, K.; Nyden, M. *J. Colloid Interface Sci.* **2002**, *253*, 150-158.
- (64) Durand, E.; Clemancey, M.; Lancelin, J.-M.; Verstraete, J.; Espinat, D.; Quoineaud, A.-A. *Energy Fuels* **2010**, *24*, 1051-1062.
- (65) Barré, L.; Jestin, J.; Morisset, A.; Palermo, T.; Simon, S. *Oil Gas Sci. Technol. - Rev. IFP* **2009**, *64*, 617-628.
- (66) Gray, M. R.; Tykwinski, R. R.; Stryker, J. M.; Tan, X. *Energy Fuels* **2011**, *25*, 3125-3134.
- (67) Friedel, R. *J. Chem. Phys.* **1959**, *31*, 280-281.

- (68) Gardner, R. A.; Hardman, H. F.; Jones, A. L.; Williams, R. B. *J. Chem. Eng. Data* **1959**, *4*, 155-159.
- (69) Williams, R. *Symp. Compos. Pet. Oils, ASTM Spec. Tech. Publ.* **1957**, *224*, 168-194.
- (70) Brown, J. K.; Ladner, W. R.; Sheppard, N. *Fuel* **1960**, *39*, 79-86.
- (71) Botto, R. E. Fossil Fuels. *Encyclopedia of Magnetic Resonance* [Online]; John Wiley & Sons, 1996, Posted March 15, 2007.
<http://dx.doi.org/10.1002/9780470034590.emrstm0175> (accessed Aug 1, 2015).
- (72) Yen, T.; Erdman, J. *Am. Chem. Soc., Div. Pet. Chem. Prepr.* **1962**, *7*, 99-111.
- (73) Friedel, R.; Retcofsky, H. L. *Proceedings of the Fifth Conference on Carbon, Vol 2*; Pergamon Press: London, 1963; pp. 149-165.
- (74) Girdler, R. B. Constitution of asphaltenes and related studies. *Proceedings of the Assoc. Asphalt. Paving Technol Proc. Conference, Vol 34*; February 1965; pp 45-79.
- (75) Ramsey, J. W.; McDonald, F. R.; Petersen, J. C. *I&EC Prod. Res. Dev.* **1967**, *6*, 231-236.
- (76) Yen, T. F.; Wu, W. H.; Chilingar, G. V. *Energy Sources* **1984**, *7*, 275-304.
- (77) Semple, K. M.; Cyr, N.; Fedorak, P. M.; Westlake, D. W. S. *Can. J. Chem.* **1990**, *68*, 1092-1099.
- (78) Knight, S. A. *Chem. Ind.* **1967**, 1920-1923.
- (79) Clutter, D. R.; Petrakis, L.; Stenger, R. L.; Jensen, R. K. *Anal. Chem.* **1972**, *44*, 1395-1405.
- (80) Ignasiak, T.; Kemp-Jones, A. V.; Strausz, O. P. *J. Org. Chem.* **1977**, *42*, 312-320.
- (81) Dereppe, J. M.; Moreaux, C.; Castex, H. *Fuel* **1978**, *57*, 435-441.
- (82) Dickinson, E. M. *Fuel* **1980**, *59*, 290-294.

- (83) Sklenar, V.; Hajek, M.; Sebor, G.; Lang, I.; Suchanek, M.; Starcuk, Z. *Anal. Chem.* **1980**, *52*, 1794-1797.
- (84) Cookson, D. J.; Smith, B. E. *Fuel* **1983**, *62*, 34-38.
- (85) Doddrell, D. M.; Pegg, D. T.; Bendall, M. R. *J. Magn. Reson.* **1982**, *48*, 323-327.
- (86) Calemma, V.; Iwanski, P.; Nali, M.; Scotti, R.; Montanari, L. *Energy Fuels* **1995**, *9*, 225-230.
- (87) Christopher, J.; Sarpal, A. S.; Kapur, G. S.; Krishna, A.; Tyagi, B. R.; Jain, M. C.; Jain, S. K.; Bhatnagar, A. K. *Fuel* **1996**, *75*, 999-1008.
- (88) Desando, M. A.; Ripmeester, J. A. *Fuel* **2002**, *81*, 1305-1319.
- (89) Fossen, M.; Kallevik, H.; Knudsen, K. D.; Sjöblom, J. *Energy Fuels* **2011**, 3552–3567.
- (90) Masuda, K.; Okuma, O.; Nishizawa, T.; Kanaji, M.; Matsumura, T. *Fuel* **1996**, *75*, 295-299.
- (91) Pekerar, S.; Lehmann, T.; Méndez, B.; Acevedo, S. *Energy Fuels* **1998**, *13*, 305-308.
- (92) Desando, M. A.; Lahajnar, G.; Ripmeester, J. A.; Ivan, Z. *Fuel* **1999**, *78*, 31-45.
- (93) Norinaga, K.; Wargardalam, V. J.; Takasugi, S.; Iino, M.; Matsukawa, S. *Energy Fuels* **2001**, *15*, 1317-1318.
- (94) Ancheyta, J.; Centeno, G.; Trejo, F.; Marroquín, G.; García, J. A.; Tenorio, E.; Torres, A. *Energy Fuels* **2002**, *16*, 1121-1127.
- (95) Evdokimov, I. N.; Eliseev, N. Y.; Akhmetov, B. R. *Fuel* **2003**, *82*, 817-823.
- (96) Jestin, J.; Barré, L. *J. Dispers. Sci. Technol.* **2004**, *25*, 341-347.
- (97) Evdokimov, I. N.; Eliseev, N. Y.; Akhmetov, B. R. *Fuel* **2006**, *85*, 1465-1472.

- (98) Durand, E.; Clemancey, M.; Lancelin, J.-M.; Verstraete, J.; Espinat, D.; Quoineaud, A.-A. *Prepr. Symp. - Am. Chem. Soc., Div. Fuel Chem.* **2008**, *53*, 563-564.
- (99) Durand, E.; Clemancey, M.; Lancelin, J.-M.; Verstraete, J.; Espinat, D.; Quoineaud, A.-A. *J. Phys. Chem. C* **2009**, *113*, 16266-16276.
- (100) Zielinski, L.; Saha, I.; Freed, D. E.; Hürlimann, M. D.; Liu, Y. *Langmuir* **2010**, *26*, 5014-5021.
- (101) Morgan, T. J.; Alvarez-Rodriguez, P.; George, A.; Herod, A. A.; Kandiyoti, R. *Energy Fuels* **2010**, *24*, 3977-3989.
- (102) Rane, J. P.; Harbottle, D.; Pauchard, V.; Couzis, A.; Banerjee, S. *Langmuir* **2012**, *28*, 9986-9995.
- (103) da Silva Oliveira, E. C.; Neto, Á. C.; Júnior, V. L.; de Castro, E. V. R.; de Menezes, S. M. C. *Fuel* **2014**, *117*, 146-151.
- (104) Vorapalawut, N.; Nicot, B.; Louis-Joseph, A.; Korb, J.-P. *Energy Fuels* **2015**, *29*, 4911-4920.
- (105) Sarpal, A. S.; Kapur, G. S.; Chopra, A.; Jain, S. K.; Srivastava, S. P.; Bhatnagar, A. K. *Fuel* **1996**, *75*, 483-490.
- (106) Abu-Dagga, F.; Rüegger, H. *Fuel* **1988**, *67*, 1255-1262.
- (107) Dosseh, G.; Rousseau, B.; Fuchs, A. H. *Fuel* **1991**, *70*, 641-646.
- (108) Weinberg, V. L.; Yen, T. F.; Gerstein, B. C.; Murphy, P. D. *Prepr. - Am. Chem. Soc., Div. Pet. Chem.* **1981**, *26*, 816-824.
- (109) Murphy, P. D.; Gerstein, B. C.; Weinberg, V. L.; Yen, T. F. *Anal. Chem.* **1982**, *54*, 522-525.
- (110) Weinberg, V. A.; Yen, T. F.; Murphy, P. D.; Gerstein, B. C. *Carbon N. Y.* **1983**, *21*, 149-156.

- (111) Opella, S. J.; Frey, M. H. *J. Am. Chem. Soc.* **1979**, *101*, 5854-5856.
- (112) Douda, J.; Alvarez, R.; Navarrete Bolaños, J. *Energy Fuels* **2008**, *22*, 2619-2628.
- (113) Daaou, M.; Bendedouch, D.; Bouhadda, Y.; Vernex-Loset, L.; Modaressi, A.; Rogalski, M. *Energy Fuels* **2009**, *23*, 5556-5563.
- (114) Daaou, M.; Bendedouch, D.; Modarressi, A.; Rogalski, M. *Energy Fuels* **2012**, *26*, 5672-5678.
- (115) Bouhadda, Y.; Florian, P.; Bendedouch, D.; Fergoug, T.; Bormann, D. *Fuel* **2010**, *89*, 522-526.
- (116) Kolodziejcki, W.; Klinowski, J. *Chem. Rev.* **2002**, *102*, 613-628.
- (117) Siskin, M.; Kelemen, S. R.; Eppig, C. P.; Brown, L. D.; Afeworki, M. *Energy Fuels* **2006**, *20*, 1227-1234.
- (118) Hauser, A.; Bahzad, D.; Stanislaus, A.; Behbahani, M. *Energy Fuels* **2008**, *22*, 449-454.
- (119) Bloch, F.; Hansen, W. W.; Packard, M. *Phys. Rev.* **1946**, *69*, 127.
- (120) Purcell, E.; Torrey, H.; Pound, R. *Phys. Rev.* **1946**, *69*, 37-38.
- (121) Becker, E. D. *Anal. Chem.* **1993**, *65*, 295A-302A.
- (122) Tjandra, N. *Science* **1997**, *278*, 1111-1114.
- (123) Schaefer, J. REDOR and TEDOR. *Encyclopedia of Magnetic Resonance* [Online]; John Wiley & Sons, 1996, Posted March 15, 2007. <http://dx.doi.org/10.1002/9780470034590.emrstm0448> (accessed Aug 1, 2015).
- (124) Tycko, R.; Dabbagh, G.; Mirau, P. A. *J. Magn. Reson.* **1989**, *85*, 265-274.
- (125) Keeler, J. *Understanding NMR Spectroscopy*; 2nd ed.; John Wiley & Sons: Cambridge, 2010.

- (126) Levitt, M. H. *Spin dynamics*; John Wiley & Sons: Chichester, UK, 2001.
- (127) *Solid state NMR spectroscopy: principles and applications*; Duer, M. J., Ed.; Blackwell Science: Oxford, 2002.
- (128) Borisov, A.; Hazendonk, P.; Hayes, P. J. *Inorg. Organomet. Polym. Mater.* **2010**, *20*, 183-212.
- (129) Silverstein, R. M.; Webster, F. X.; Kiemle, D.; Bryce, D. L. *Spectrometric identification of organic compounds*; John Wiley & Sons: Hoboken, 2014.
- (130) Haeberlen, U. *Advances in magnetic resonance* Vol. 1; Academic Press: New York, 1976.
- (131) Smith, S.; Palke, W.; Gerig, J. *Concepts Magn. Reson.* **1992**, *4*, 107-144.
- (132) Smith, S.; Palke, W.; Gerig, J. *Concepts Magn. Reson.* **1992**, *4*, 181-204.
- (133) Bennett, A. E.; Rienstra, C. M.; Auger, M.; Lakshmi, K. V.; Griffin, R. G. *J. Chem. Phys.* **1995**, *103*, 6951-6958.
- (134) Freeman, R.; Hill, H.; Kaptein, R. *J. Magn. Reson.* **1972**, *7*, 327.
- (135) Meiboom, S.; Gill, D. *Rev. Sci. Instrum.* **1958**, *29*, 688-691.
- (136) Mandal, P. K.; Majumdar, A. *Concepts Magn. Reson. Part A* **2004**, *20A*, 1-23.
- (137) Taylor, R.; Chim, N.; Dybowski, C. *J. Mol. Struct.* **2007**, *830*, 147-155.
- (138) Conte, P.; Piccolo, A.; van Lagen, B.; Buurman, P.; Hemminga, M. A. *Solid State Nucl. Magn. Reson.* **2002**, *21*, 158-170.
- (139) Egger, N.; Schmidt-Rohr, K.; Blümich, B.; Domke, W. D.; Stapp, B. *J. Appl. Polym. Sci.* **1992**, *44*, 289-295.

- (140) Ando, S.; Harris, R. K.; Holstein, P.; Reinsberg, S. A.; Yamauchi, K. *Polymer* **2001**, *42*, 8137-8151.
- (141) Ando, S.; Harris, R. K.; Reinsberg, S. A. *Magn. Reson. Chem.* **2002**, *40*, 97-106.
- (142) Ando, S.; Harris, R. K.; Hazendonk, P.; Wormald, P. *Macromol. Rapid Commun.* **2005**, *26*, 345-356.
- (143) Hazendonk, P.; Harris, R. K.; Ando, S.; Avalle, P. *J. Magn. Reson.* **2003**, *162*, 206-216.
- (144) Borisov, A.; Hazendonk, P.; Hayes, P. *J. Inorg. Organomet. Polym. Mater.* **2008**, *18*, 163-174.
- (145) Hazendonk, P.; de Denus, C.; Iuga, A.; Cahoon, P.; Nilsson, B.; Iuga, D. *J. Inorg. Organomet. Polym. Mater.* **2006**, *16*, 343-357.
- (146) Traficante, D. D. Relaxation: An Introduction. *Encyclopedia of Magnetic Resonance* [Online]; John Wiley & Sons, 1996, Posted March 15, 2007. <http://dx.doi.org/10.1002/9780470034590.emrstm0452> (accessed Aug 1, 2015).
- (147) Feike, M.; Demco, D. E.; Graf, R.; Gottwald, J.; Hafner, S.; Spiess, H. W. *J. Magn. Reson. Ser. A* **1996**, *122*, 214-221.
- (148) Kubo, R. *J. Phys. Soc. Jpn.* **1954**, *9*, 935-944.
- (149) Kontaxis, G.; Stonehouse, J.; Laue, E. D.; Keeler, J. *J. Magn. Reson. Ser. A* **1994**, *111*, 70-76.
- (150) Hansen, P. E. *Prog. Nucl. Magn. Reson. Spectrosc.* **1981**, *14*, 175-295.
- (151) Boek, E. S.; Yakovlev, D. S.; Headen, T. F. *Energy Fuels* **2009**, *23*, 1209-1219.
- (152) Seki, H.; Kumata, F. *Energy Fuels* **2000**, *14*, 980-985.
- (153) Badu, S.; Pimienta, I. S. O.; Orendt, A. M.; Pugmire, R. J.; Facelli, J. C. *Energy Fuels* **2012**, *26*, 2161-2167.

- (154) Brown, S. P. *Solid State Nucl. Magn. Reson.* **2012**, *41*, 1-27.
- (155) Pacheco-Sánchez, J. H.; Zaragoza, I. P.; Martínez-Magadán, J. M. *Energy Fuels* **2003**, *17*, 1346-1355.
- (156) Pacheco-Sánchez, J. H.; Álvarez-Ramírez, F.; Martínez-Magadán, J. M. *Energy Fuels* **2004**, *18*, 1676-1686.
- (157) Jian, C.; Tang, T.; Bhattacharjee, S. *Energy Fuels* **2013**, *27*, 2057-2067.
- (158) Jian, C.; Tang, T.; Bhattacharjee, S. *Energy Fuels* **2014**, *28*, 3604-3613.
- (159) Siddiqui, M. N. *Pet. Sci. Technol.* **2006**, *21*, 1601-1615.
- (160) Fechtenkötter, A.; Saalwächter, K.; Harbison, M.; Müllen, K.; Spiess, H. *Angew. Chem. Int. Ed. Engl.* **1999**, *38*, 3039-3042.
- (161) Fischbach, I.; Pakula, T.; Minkin, P.; Fechtenkötter, A.; Müllen, K.; Spiess, H. W.; Saalwächter, K. *J. Phys. Chem. B* **2002**, *106*, 6408-6418.
- (162) Mao, J. D.; Xing, B.; Schmidt-Rohr, K. *Environ. Sci. Tech.* **2001**, *35*, 1928-1934.
- (163) Marica, F.; Snider, R. F. *Solid State Nucl. Magn. Reson.* **2003**, *23*, 28-49.
- (164) Conte, P.; Berns, A. E. *Anal. Sci.* **2008**, *24*, 1183-1188.
- (165) Acevedo, S.; Castro, A.; Negrin, J. G.; Fernández, A.; Escobar, G.; Piscitelli, V.; Delolme, F.; Dessalces, G. *Energy Fuels* **2007**, *21*, 2165-2175.
- (166) Ruiz-Morales, Y.; Mullins, O. C. *Energy Fuels* **2007**, *21*, 256-265.
- (167) Ruiz-Morales, Y.; Wu, X.; Mullins, O. C. *Energy Fuels* **2007**, *21*, 944-952.
- (168) Ruiz-Morales, Y.; Mullins, O. C. *Energy Fuels* **2009**, *23*, 1169-1177.

- (169) Mao, J.; Chen, N.; Cao, X. *Org. Geochem.* **2011**, *42*, 891-902.
- (170) Cao, X.; Yang, J.; Mao, J. *Int. J. Coal Geol.* **2013**, *108*, 83-90.
- (171) van Rossum, B.-J.; de Groot, C. P.; Ladizhansky, V.; Vega, S.; H.J.M., de G. *J. Am. Chem. Soc.* **2000**, *122*, 3465-3472.

APPENDIX 1

The chemical shielding Hamiltonian can be written in the form

$$\mathbf{H} = C\mathbf{I} \cdot \hat{\sigma} \cdot \mathbf{B}_0$$

where $\hat{\sigma}$ is the shielding tensor and \mathbf{I} and \mathbf{B}_0 are the spin-operator and magnetic field operator, respectively, and C is a constant. The dipolar coupling Hamiltonian can be expressed similarly as

$$\mathbf{H} = C\mathbf{I} \cdot \hat{D} \cdot \mathbf{I}$$

Now, the above expressions are in a product of the form “vector-matrix-vector” (say \mathbf{UMV}), which results in scalar, given by the trace of the resulting matrix, which can be written as $\mathbf{Tr}(\mathbf{UMV})$. The trace is invariant to cyclic permutations of the three components, and hence can be written as an outer product of the two vectors, given by $\mathbf{Tr}(\mathbf{VUM})$. Therefore, both the shielding and coupling Hamiltonians above can be expressed in the following form:

$$\mathbf{H} = C\hat{\mathbf{X}} \cdot \hat{A}$$

where $\hat{\mathbf{X}}$ is the spin-part, given by either $\mathbf{I} \cdot \mathbf{I}$ or $\mathbf{I} \cdot \mathbf{B}_0$, as is the case, and \hat{A} is the space part, which either $\hat{\sigma}$ or \hat{D} . Now, both the spin and space parts are in the Cartesian coordinates, which is not helpful if orientation dependence has to be derived. Both $\hat{\mathbf{X}}$ and \hat{A} can be converted into spherical polar coordinates, which can be further decomposed into components that have rotational symmetry in the same form as spherical harmonics, Y_l^m , allowing them to be expressed in terms of angular momentum components (l, m). The Hamiltonians can therefore be written as

$$\mathbf{H}=\mathbf{C} \sum_l \sum_{m=-l}^l X_l^m A_l^{-m}$$

Just as in the Cartesian coordinates, this spherical harmonic representation also has nine components, but for the chemical shielding case, only three of these components survive when symmetry considerations are taken into account, which is not apparent in the Cartesian representation. These components are proportional to the different quantities associated with the shielding tensor, as follows:

The isotropic chemical shift $\sigma_{\text{iso}} \propto A_0^0 I_z$ [analogous to an s -orbital ($l=0, m=0$)]

The CSA $\delta_{\text{aniso}} \propto A_2^0 I_z$ [analogous to a d_{z^2} -orbital ($l=2, m=0$)]

The asymmetry parameter $\eta \propto A_2^{\pm 2} I_z$ [analogous to the $d_{x^2-y^2}$ and d_{xy} ($l=2, m=\pm 2$) orbitals]

For the dipolar coupling Hamiltonian, only one component survives, which is proportional to the dipolar coupling as

$$D \propto A_2^0 [3\mathbf{I}_z \mathbf{I}_z - \mathbf{I} \cdot \mathbf{I}]$$

Now, the spherical harmonic of the form A_2^0 has an orientation dependence given by

$A_2^0 \propto 3\cos^2\theta - 1$, which imparts the same dependence to the CSA (δ_{aniso}) and the dipolar coupling terms. Therefore, magic angle spinning (MAS), described in Chapter 2, can be used to eliminate or reduce the contribution of both these terms, where θ is set to 54.74° , making $3\cos^2\theta - 1 = 0$.

APPENDIX 2

Quality of fit analysis for the CP dynamics study in Chapter 4, from which T_{CP} and $T_{1\rho H}$ were calculated. R^2 gives the quality or goodness of fit and the confidence interval (CI) provides the accuracy of each data point in the fit. For explanation of error-calculation procedure, refer to: Brown, A. M. *Comput. Methods Programs. Biomed.* **2001**, 65, 191-200.

Peak #	$\delta\{^{13}\text{C}\}$ (ppm)	Standard Error	R^2	\pm Confidence Interval (at 95% Significance Level)
1	14.00	0.03	0.97	0.06
2	20.03	0.02	0.96	0.05
3	22.57	0.01	0.99	0.02
4	29.54	0.01	0.98	0.02
5	30.45	0.01	0.97	0.01
6	36.31	0.04	0.73	0.09
7	42.53	0.02	0.99	0.05
8	123.13	0.01	0.87	0.02
9	128.81	0.01	0.99	0.02
10	138.37	0.02	0.97	0.04

Example fit (128.81 ppm):

$$\frac{I(t)}{I(0)} = \frac{1}{\lambda} \left[1 - \exp\left(-\frac{\lambda t}{T_{CP}}\right) \right] \times \exp\left(-\frac{t}{T_{1\rho H}}\right)$$

$$\lambda = 1 - \frac{T_{CP}}{T_{1\rho H}}$$

$$T_{CP} = 0.23 \text{ ms}, T_{1\rho H} = 64.64 \text{ ms},$$

Contact (μs)	I_{exp}^*	I_{calc}^*	$(I_{\text{exp}} - I_{\text{calc}})^2$	Upper CI*	Lower CI
10	0.028259	0.043327	0.000227	0.06366	0.022994
25	0.105999	0.10481	1.41E-06	0.125143	0.084477
50	0.240937	0.198592	0.001793	0.218925	0.178259
75	0.317444	0.282502	0.001221	0.302835	0.262169
100	0.424104	0.357575	0.004426	0.377908	0.337242
125	0.420257	0.424738	2.01E-05	0.445071	0.404405
150	0.496112	0.48482	0.000128	0.505153	0.464487
175	0.571565	0.538563	0.001089	0.558896	0.51823
200	0.602566	0.586631	0.000254	0.606964	0.566298
250	0.64526	0.668063	0.00052	0.688396	0.64773
300	0.724913	0.733163	6.81E-05	0.753496	0.71283
350	0.741432	0.785177	0.001914	0.80551	0.764844
500	0.817901	0.886219	0.004667	0.906552	0.865886
600	0.876835	0.923886	0.002214	0.944219	0.903553
750	0.936926	0.955731	0.000354	0.976064	0.935398
900	0.966874	0.971004	1.71E-05	0.991337	0.950671
1000	0.94787	0.97614	0.000799	0.996473	0.955807
1250	0.993147	0.980335	0.000164	1.000667	0.960002
1500	0.979253	0.979181	5.15E-09	0.999514	0.958848
1750	1	0.976271	0.000563	0.996604	0.955938
2000	0.990397	0.97279	0.00031	0.993123	0.952457
			$=\sum(I_{\text{exp}} - I_{\text{calc}})^2$	←Minimize	

* I_{exp} = experimental intensity, I_{calc} = calculated intensity, CI = Confidence Interval.

After getting a reasonable fit with sum of squares minimization, maximize R^2 for best fit.
Example below:

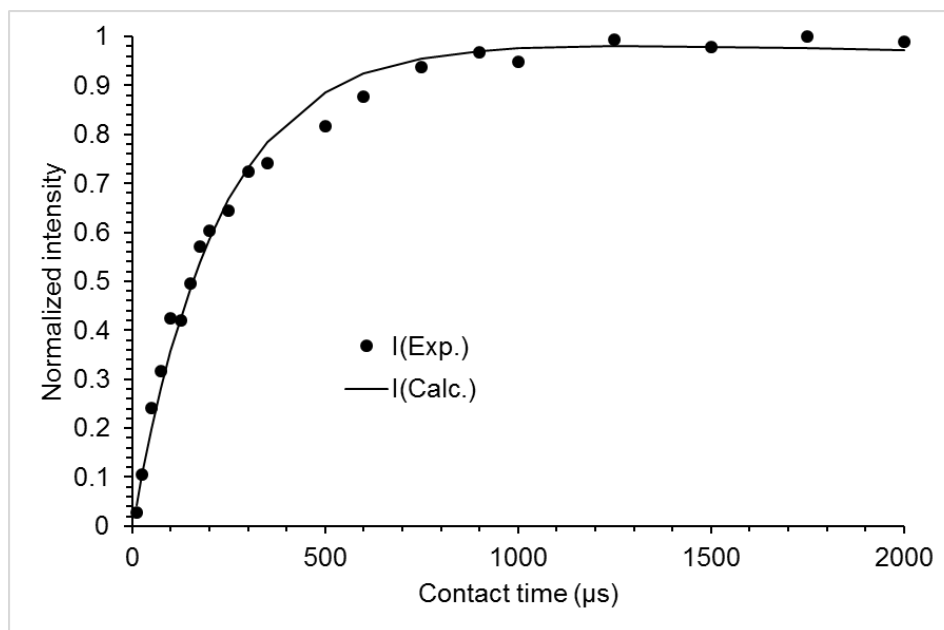


Figure A2. Example fit for the CP build-up curve of the 128.81 ppm deconvolved solid-state ^{13}C NMR signal of AOSA using Eq. 2.43.

APPENDIX 3

Exponential fitting for the ^1H dipolar filter T_2 data in Chapter 4.

The raw data obtained from the relaxation experiment was normalized; natural logs of the data points were taken and plotted against time. For the peaks at $\delta_{1\text{H}} = -0.18, 0.65$ and 1.06 ppm, the resulting log plot was not one linear line, but had at least one inflection point. The slope 'a' of the more prominent linear line with more data points was used to fit the corresponding points in the normalized raw data employing a mono-exponential decay model of the form $I(t) = A\exp(-at)$. This was subtracted from the original normalized raw data curve and the natural log of the difference curve was plotted against time. This gave us a linear plot and its slope 'b' was used to generate the difference curve using a mono-exponential decay model as above. This was then added to the other mono-exponential curve and this trial data was compared with the original data while adjusting the theoretical equilibrium magnetization values (A). Satisfactory fits with high R^2 values were obtained which indicates the bi-exponential model is applicable. If the data were truly multi-exponential, a good fit could not have been achieved. Multi-exponential behavior might definitely be present but occurs over a range narrow enough to allow approximation to a bi-exponential model. The table below shows the R^2 values obtained by non-linear regression analysis between the experimental and calculated data.

$\delta_{1\text{H}}$ (ppm)	R^2	
-0.18	0.99	Bi
0.65	0.97	Bi
1.06	0.99	Bi
1.29	0.96	Mono
1.56	0.96	Mono
4.04	0.97	Mono

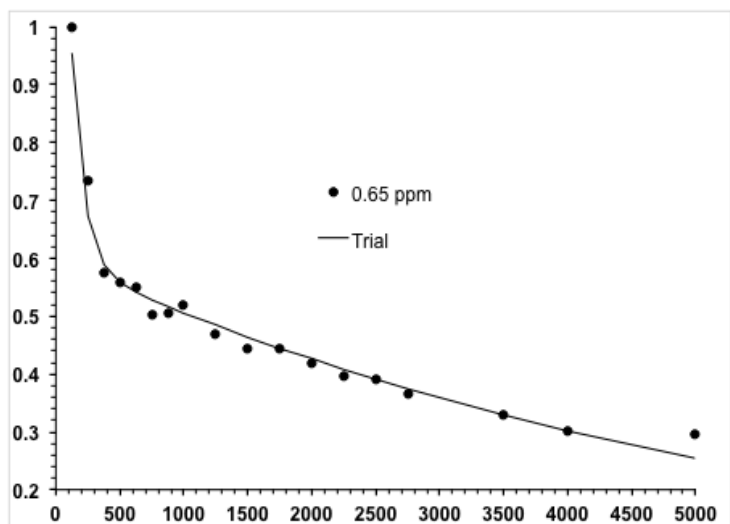
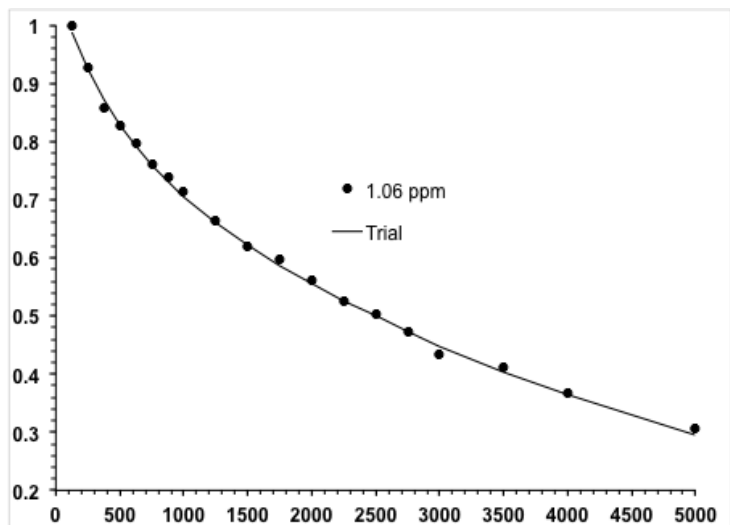


Figure A3. Examples of bi-exponential fits used in Chapter 4.

APPENDIX 4

The deconvolution (peak-fitting) models used for the solid-state ^{13}C NMR spectra of UG8 and WY asphaltenes in Chapter 6.

UG8			WY		
ppm	linewidth	L/G*	ppm	linewidth	L/G*
202.15	1316	1	266.46	2048	1
193.18	1581	1	252.98	1191	1
187.82	1060	1	236.56	1336	1
183.98	949	1	219.59	1949	1
162.51	1647	1	202.50	2048	1
147.51	1450	1	192.00	973	0
138.02	1316	1	186.3	1191	1
129.28	1581	1	174.92	1336	1
123.78	1060	1	155.54	1949	1
118.53	949	1	138.31	2048	1
109.58	1647	1	127.44	973	0
83.53	1450	1	122.52	1191	1
74.77	1316	1	111.59	1336	1
65.49	1581	1	92.51	1949	1
59.13	1060	1	74.81	2048	1
54.68	949	1	63.59	973	0
44.03	1326	1	58.44	1191	1
37.45	1125	1	47.63	1336	1
31.98	230	1	38.78	1510	1
29.77	456	0	31.96	1075	1
29.59	1606	1	29.82	959	1
22.71	372	1	22.88	566	1
19.64	504	1	19.38	699	1
14.30	379	1	14.36	387	1
10.05	1316	1	10.55	2048	1
			-1.65	973	0

*The L/G ratio describes the Lorentzian or Gaussian character of a signal, i.e. the lineshape. L/G = 1 means a completely Lorentzian shape and L/G = 0 means a fully Gaussian shape.

Comparison of the two CP-dynamics models to demonstrate that the $I-I^*-S$ model (Eq. 2.44) provides a better description of the CP dynamics:

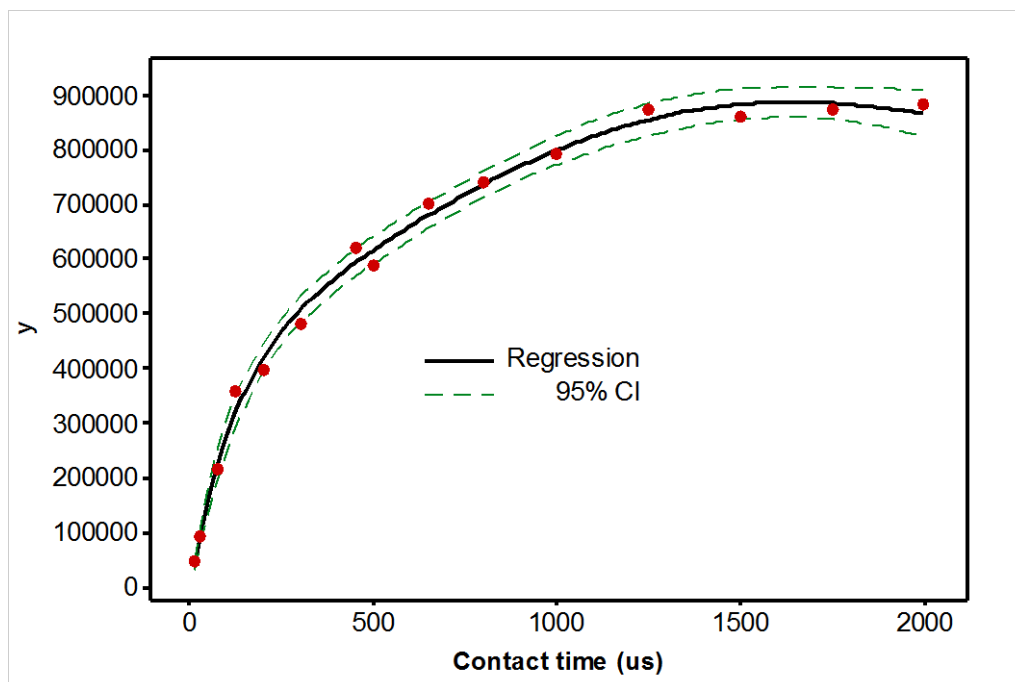


Figure A4. Non-linear regressive line-fitting of the cross-polarization build-up data of the 129.28 ppm ^{13}C signal (Chapter 6) using the non-monotonic $I-I^*-S$ CP model described by Eq. 2.44.

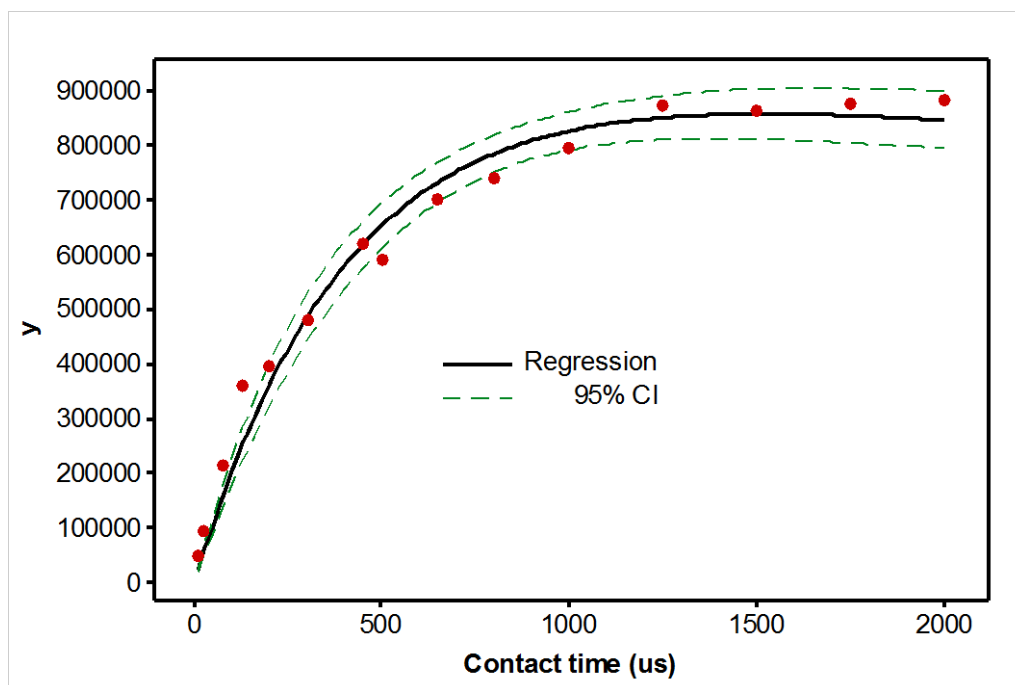


Figure A5. Non-linear regressive line-fitting of the cross-polarization build-up data of the 129.28 ppm ^{13}C signal (Chapter 6) using the classical $I-S$ CP model described by Eq. 2.43.

APPENDIX 5

Tables showing the ^1H T_2 values measured for UG8 and WY asphaltenes, used to generate Figure 7.1 in Chapter 7, along with the corresponding percentages of long and short T_2 .

UG8

g/L	Long T_2 (s)	%Long T_2	Short T_2 (s)	%Short T_2
15.0	0.29±0.02	26.5±1.8	0.02±0.001	73.5±2.2
7.5	0.34±0.03	26.0±1.7	0.02±0.001	74.0±2.0
3.0	0.57±0.03	38.0±1.4	0.03±0.002	62.0±4.2
1.5	0.69±0.07	43.6±2.6	0.03±0.003	56.4±3.4
0.75	0.75±0.05	44.4±1.5	0.03±0.003	55.6±3.8
0.38	0.72±0.04	45.2±1.5	0.03±0.003	54.8±2.2
0.19	0.76±0.05	48.1±1.6	0.03±0.004	51.9±4.7
0.09	0.78±0.04	47.8±1.4	0.02±0.003	52.2±5.8
0.045	0.82±0.05	50.8±1.6	0.04±0.006	49.2±4.0

WY

g/L	Long T_2 (s)	%Long T_2	Short T_2 (s)	%Short T_2
15.0	0.57±0.04	37.8±1.4	0.03±0.002	62.2±2.0
7.5	0.64±0.03	42.0±1.2	0.03±0.002	58.0±1.6
3.0	0.71±0.06	51.3±1.7	0.03±0.004	48.7±3.5
1.5	0.76±0.05	54.9±1.8	0.03±0.004	45.1±2.7
0.75	0.76±0.07	55.9±2.7	0.04±0.006	44.1±3.6
0.38	0.81±0.07	55.8±2.7	0.03±0.006	44.2±3.5
0.19	0.82±0.05	45.6±1.5	0.03±0.003	54.4±4.4
0.09	0.84±0.09	55.2±2.6	0.03±0.007	44.8±4.3
0.045	0.75±0.05	55.5±1.8	0.04±0.005	44.5±2.7

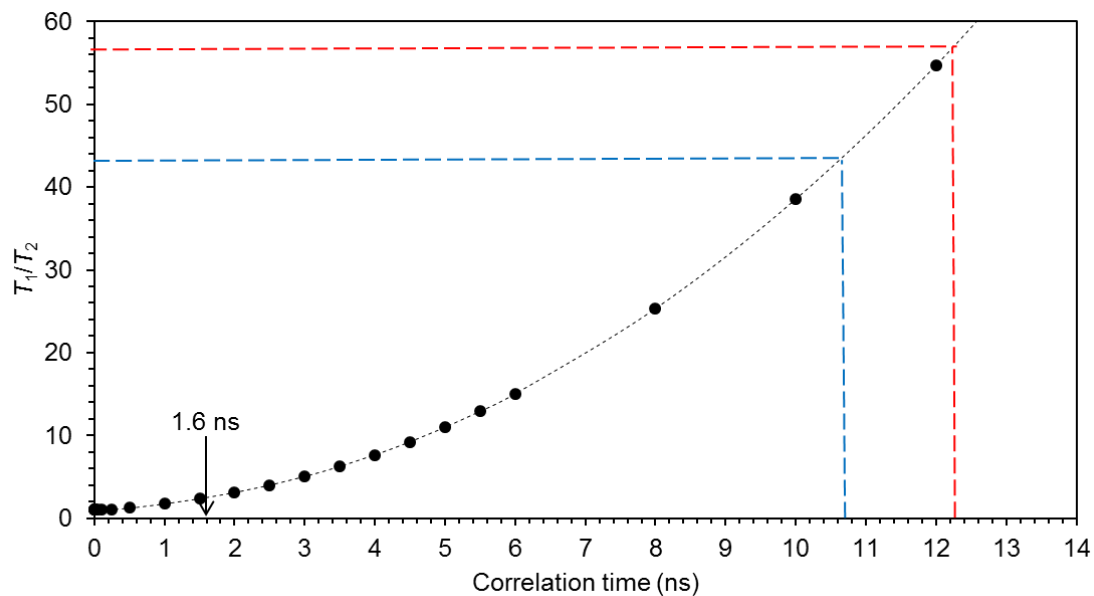


Figure A6. Plot showing the variation of ^1H T_1/T_2 ratio with correlation time at a ^1H Larmor frequency of 700 MHz. The critical correlation time of 1.6 ns, indicated by the arrow, indicates the correlation time for which NOESY correlation peaks disappear (Chapter 7). The dashed lines indicate the T_1/T_2 ratios of the UG8 (red) and WY (blue) asphaltenes at a concentration of 15 g/L, and the corresponding correlation times.